Imperial College London

Novel Tools and Strategies of Nanopore Single-molecule Biosensing

Ren Ren

Department of Chemistry

Imperial College London

A thesis submitted in partial fulfilment of the requirement for the degree of Doctor of Philosophy

August 2019

Abstract

Nanopores have been proved to be promising analytical platforms for label-free single-molecule biosensing. However, the practical application of nanopores, such as early stage diagnosis tools or the DNA sequencing tools, is restricted by several functional defects. The main aim of this work is to explore multiple approaches to improve the sensitivity and selectivity of a nanopipette based nanopore sensing, by a combination of field-effect transistors or molecular carriers.

In the first part of the thesis, a new class of nanoscale sensors – dubbed a nanopore extended field-effect transistor (nexFET) – is fabricated to control and selectively sense the biomolecules. Through real-time feedback controlling electrodeposition, a tuneable polypyrrole nanopore can be formed on a carbon-coated double-barrel nanopipette tip with one barrel filled with carbon nanoelectrodes. The generated nexFET displays outstanding FET performance and pH sensitivity. Combining the advantages of nanopore single-molecule sensing, field-effect transistors, and recognition chemistry, the nexFETs are subsequently employed to probe DNA and protein molecules. By controlling the gate voltage of the nexFET, the transport of DNA can be improved comprehensively; for example, a higher throughput, a longer dwell time, and a higher signal-to-noise ratio can be achieved. The selectivity of the nexFET can be further improved by functionalising with embedded receptors.

Attention is then focussed to explore novel strategies for selective biomolecular sensing using nanopipettes, and molecular carriers and probes. Here, I design probes based on the dimerisation of gold nanoparticles (NP), which can be used for the detection of biological targets. Two strategies are employed: 1) aptamer-modified NP dimers are used to target biomarkers, and 2) antibody-modified NP monomers dimerise and self-assemble based on the binding of an antigen target. Importantly, we demonstrate that nanopore sensing can be utilised with both strategies to quantify bound analytes from unbound ones and, in the process, perform single-molecule binding assays.

In summary, multiple approaches including functionalised nanopores, novel molecular carriers, and novel molecular probes were designed and developed. As they can address various limitations of nanopore-based biosensors, these improved methods are expected to pave the way for the practical application of nanopores in early diagnostics and therapeutics.

Declaration of Originality

I, the author, declare that the work presented in this thesis is original and performed by myself; otherwise it is clearly cited and acknowledged. This work has not previously been submitted in any form to satisfy any degree requirements at this or any other university.

Copyright Declaration

The copyright of this thesis rests with the author and is made available under a Creative Commons Attribution Non-Commercial No Derivatives licence. Researchers are free to copy, distribute or transmit the thesis on the condition that they attribute it, that they do not use it for commercial purposes and that they do not alter, transform or build upon it. For any reuse or redistribution, researchers must make clear to others the licence terms of this work.

Acknowledgments

First and foremost, I would like to express my heartfelt gratitude to my supervisors Prof. Joshua Edel, Prof. Yuri Korchev and Dr. Alex Ivanov for the continuous support of my PhD study and research, for their patience, motivation, and immense knowledge. It is a great honour and privilege to be the PhD student of three nicest supervisors I've ever met. Thanks Joshua and Alex for introducing me to the single molecule biosensing world, for the precious time that we talked about the science, for all the lectures that we presented together in eight universities over China, for all the things I learned from you, not only the science, but also your personality and life physiology. And Yuri, the time that I did experiments with you, that we talked about tons of new ideas, and that we ate the sashimi prepared by you, have become my precious memory.

I also wish to acknowledge all my collaborators. This work would not have been possible without you: Dr. Yanjun Zhang for the nexFET work; Prof. Nicholas Kotov, Prof. Chuanlai Xu, Prof. Hua Kuang, Prof. Maozhong Sun and Dr. Pratibha Goel for the AuNP dimer work; Prof. Yang Yang and Prof. Chenxiang Lin for the DNA origami carrier work.

To all the members in Edel group, Ivanov group and nanomedicine research group, thanks for made it a friendly and enjoyable place to work. To Binoy, Paolo, Jane, Jasmine, Colin and Agnieszka, thanks for your guidance, your help, and all the valuable ideas that you shared with me, and I wish every success in your future career. Ye, Liang, Minkyung, Victoria, Ben, Giulia, Micol, Alex, Alfie, Mike, Long, Yaxian, Lin, Neng, Jinjing, thank you for all the happiness we shared, and good luck to the rest of your PhD. Longhua, it's a great pleasure to meet you, one of the most knowledgeable scientists that I've met, at the end of my PhD journey. Shenglin, I'm happy that you were sitting next to me for the past four years (and it has been proved no one can sit between us). During the PhD, I have the opportunity to supervise two master students. Fangyuan, I hope you good luck in your future career. Xiaoyi, please keep your passion, your commitment and your 'Nanjing style' on your PhD journey. I much appreciate Alex, D-L and Bernice for proofreading part of this thesis. To all of you, I am grateful to share this PhD with you and I will keep our friendship and sincerely wish you the best in your next chapter of life.

To Xin, I wish to express my deepest gratitude for your love, constant support and encouragement. To my little son, I just finished the draft of this thesis when I first time saw your small body (by the ultrasound). Knowing your existence is the happiest moment during this most stressful time.

Finally, I wish to thank my parents. I could not have achieved anything without your unconditional love, support and encouragement. Thanks for taught me the value of hard work and the importance of being a man with integrity and kindness. Thank you everything Mum and Dad!

To my parents

致我的父母

Table of Contents

Abstract....1

Declaration of Originality....2

Copyright Declaration....2

Acknowledgments....3

Table of Contents....4

List of Figures....9

List of Tables....26

Chapter 1

Introduction

1.1 Single-molecule sensing....30

1.2 Nanopores....31

1.2.1 Biological nanopores....32

1.2.2 Solid-state nanopores....34

1.3 Sensing principles in solid-state nanopores....37

1.3.1 Ionic current detection....37

1.3.2 Surface charges in nanopores....39

1.3.3 Current rectification of the nanopore....41

1.3.4 Electrophoretic and electroosmotic flow....43

1.3.5 Conductance modulation by charged molecules....44

1.4 Using solid-state nanopores to sense biomolecules and their limitations....46

1.4.1 Single-molecule biosensing by solid-state nanopores....46

1.4.2 The challenges of nanopore-based sensing techniques....52

1.5 Objective and thesis overview....53

1.6 References....55

Chapter 2

Methodology

2.1 Nanopipette fabrication and characterisation 65
2.1.1 Nanopipette fabrication 65
2.1.2 Microscopic characterisation of the nanopipettes 67
2.1.3 Electrochemical characterisation 68
2.2 Single-molecule translocation experiments 69
2.2.1 Preparation of Ag/AgCl electrodes 69
2.2.2 Buffer preparation 70
2.2.3 Ionic current measurements 71
2.3 Data analysis 72
2.4 References 78

Chapter 3

The nanopore extended field-effect transistor fabrication

3.1 Introduction 80
3.2 Methods 82
3.2.1 Fabrication of carbon-coated dual-barrel nanopipettes with one carbon nanoelectrode 82
3.2.2 PPy deposition with real-time feedback control 83
3.2.3 Electrical characterisation of the nanopore extended field-effect transistor 84
3.3 Result and discussion 84
3.3.1 Fabrication and characterisation of the nexFET 84
3.3.2 nexFET performance 91
3.3.3 The pH sensitivity of the nexFET 93
3.4 Conclusion 95
3.5 References 96

Chapter 4

Using nexFET to control the transport of DNA and sense proteins selectively

4.1 Introduction....100
4.2 Methods....102
4.2.1 The fabrication of insulin-imprinted nexFETs....102
4.2.2 DNA sensing and protein-selective sensing experiment....102
4.3 Result and discussion....102
4.3.1 Single-molecule DNA sensing using a nexFET....102
4.3.2 Selective protein sensing using a nexFET....109
4.4 Conclusion....115
4.5 References....115

Chapter 5

The nanopore sensing of AuNP-based nanostructures

5.1 Introduction....120
5.2 Methods....122
5.2.1 The fabrication of AuNP-based nanostructures....123
5.2.2 Nanostructure translocation experiments....126
5.2.3 Single-molecule SERS detection....126
5.3 Result and discussion....126
5.3.1 Fine-tuned nanopipette....127
5.3.2 Single-molecule sensing of nanoparticle-based nanostructures....131
5.4 Conclusion....138
5.5 References....138

Chapter 6

Two strategies based on AuNP-based nanostructures for single biomolecule detection using nanopores

6.1 Introduction....142
6.2 Methods....144
6.2.1 The fabrication of TBA-modified AuNP dimers....144
6.2.2 The fabrication of the monomer PCT probes....145
6.2.3 UV-Vis measurement....145
6.2.4 Nanostructure translocation experiments....145
6.3 Result and discussion....146
6.3.1 Sensing protein using AuNP dimer protein carriers....146
6.3.2 Sensing small antigens using AuNP monomer antigen probes....150
6.4 Conclusion....155
6.5 References....156

Chapter 7

Conclusion and future work

7.1 Aims and achievements....160
7.2 Future works....161
7.2.1 Improvement of receptor-embedded nexFETs....162
7.2.2 Detecting multiple targets using molecular carriers....165
7.3 Conclusion....167
7.4 References....167
Copyright Permission....169

Appendix: Copyright Permission....169

List of Figures

Chapter 1

Figure 1. 1 Schematic of a conventional Coulter counter. **(a)** The Coulter counter has one (or more) microchannels linking two separate chambers, which are filled with electrolytes and the electrode. **(b)** Ion transport will only contribute to a constant current flow. **(c)** The microparticles passed through the channel and left a resistance pulse on the signal. 31
Figure 1. 2 Molecular graphic images of α-haemolysin. **(a)** A ribbon diagram of the heptameric nanopore. **(b)** A cross-section view of the protein. Figures adapted from reference 32..... 33
Figure 1. 3 A simple workflow of a typical solid-state membrane and nanopore on it. Figures adapted from reference 19..... 35
Figure 1. 4 TEM images of the nanopore. The TEM images of **(a)** the initial membrane, which is approximately 60 nm, and **(b)** the nanopore, which is approximately 1.8 nm after FIB milling. Figures adapted from reference 47..... 35
Figure 1. 5 Schematic of a nanopipette biosensor. The conically shaped nanopipette can be a bridge between the nanoworld and the macroworld, converting the invisible molecules to visualised information either by a single-molecule translocation signal or scanning ion conductance microscopy (SICM) images. Moreover, this unique shape can be utilised to deliver the analytes into cells..... 36
Figure 1. 6 Schematic of a translocation experiment and the parameters of the signals. **(a)** The steady-state current is decreased (or increased) when a molecule blocks the nanopore. **(b)** The translocation can be characterised by the following parameters: dwell time, current amplitude, integral area, sub-peak location, the time between translocation events, and capture rate. 39
Figure 1. 7 Schematic of the distribution of ions around the surface/solution interface monitored by the Gouy-Chapman-Stern model. 40
Figure 1. 8 The ionic current rectification of nanopipettes with different pore sizes. The I-V curve of **(a)** a nanopipette with a 100 nm nanopore and **(b)** a nanopipette with a 15 nm nanopore in 100 mM of KCl. 42
Figure 1. 9 The translocation of avidin under different driving forces. **(a)**The current-time traces and **(b)** a schematic of the electrophoresis and electro-osmosis of the avidin translocation through a Si_3N_4 nanopore under different pHs. The arrow length is scaled by the corresponding zeta potential. Figures adapted from reference 87..... 44

Figure 1. 10 The translocation signal of lambda DNA in different salt concentrations. Three individual translocation events of lambda DNA through a nanopore on nanopipette at KCl concentrations of **(a)** 150 mM and **(b)** 500 mM. Figures adapted from reference 73. 45
Figure 1. 11 A comparison of translocation signals with different salts and concentrations. **(a)** Schematic of DNA detection using a nanopore device. **(b)** The example of a translocation experiment of lambda DNA in different salts and concentrations. Figures adapted from reference 97. 46
Figure 1. 12 Slowing down DNA translocation by a nanofluidic field-effect transistor. **(a)** Side-view of the nanofluidic field-effect transistor. By controlling the gate voltage, the surface charge of the nanopore, which is a layer of Al_2O_3, can be manipulated. **(b)** Scatter plot of lambda DNA translocation in 1 M of KCl under a 1-V bias voltage. The sharp spikes indicate a fast translocation without a gate voltage, where the long events illustrate that the DNA molecules were significantly slowed down with 9 V being applied to the gate. Figures adapted from reference 98..... 47
Figure 1. 13 Sensing 10-bp dsDNA by a hydrogel-filled nanopipette. **(a)** Schematic of sensing 100-bp dsDNA molecules by a hydrogel-filled nanopipette. **(b)** A comparison between the translocation recordings of sensing 100-bp dsDNA using **(i)** a plain nanopipette and **(ii)** a hydrogel-filled nanopipette. Figures adapted from reference 100. 47
Figure 1. 14 Sensing ssDNA by biological-solid-state nanopores. **(a)** a DNA hairpin functionalized SiO_2 nanopore, which is capable of distinguishing between ssDNA which is perfectly complementary (PC DNA) to the hairpin sequence and the ssDNA which has one base mismatch (1 MM DNA) with the hairpin. **(b)** an α-haemolysin inserted solid-state nanopore. The protein pore was led by the dsDNA tail which passed through the solid-state nanopore by electrophoresis and sit on the solid-state nanopore. Figures adapted from reference 105. 48
Figure 1. 15 The selection of current-time traces of the translocation of different analytes. **(a)** The translocation of 37 uM of GFP through a 14 nm nanopore. **(b)** The translocation of 9 uM of FP through a 14 nm nanopore. **(c)** The positive control, which is lambda DNA translocating through a 14 nm nanopore. **(d)** The translocation of 0.6 uM of BSA through a 21 nm nanopore. **(e)** The translocation of 0.6 uM of IgG through a 16 nm nanopore. **(f)** The translocation of 0.6 uM of RNAp 480 through a 13 nm nanopore. All translocation experiments were performed in 1 M of KCl under a bias of 0.5 V. Figures adapted from reference 109. 49
Figure 1. 16 Sensing protein, orientation of protein and the interactions between proteins using solid state nanopores. **(a)** The current blockages show different orientation of the glucose oxidase: The deep current blockage demonstrates that the protein passes through the pore horizontally; the relative smaller blockage represents

the protein translocate vertically. Figure **(a)** adapted from reference 111; Figure **(b)** adapted from reference 113. 50
Figure 1. 17 Selective translocation of His-tagged protein through a bis-NTA nanopore. **(a)** Schematic of the translocation process of His-tagged protein (red) through an NTA (green binding sites) functionalised Au-coated nanopore. **(b)** The protein can be slowed down by the interactions between the ligands on the protein and the NTA on the inner wall of the nanopore. **(c)** Sharp spikes illustrate that the bare nanopore has no selectivity to sense proteins. **(d)** The long-lasting translocation events illustrate the specific binding of the target proteins. Figures adapted from reference 114. 51
Figure 1. 18 Schematic of protein-selective sensing by a lambda DNA protein carrier. **(a)** Schematic of the protein-DNA complex. **(b)** The translocation signatures of the DNA carrier itself and the carrier bound two or three proteins. **(c)** The sequence of each aptamer binding site. Figures adapted from reference 64. 52

Chapter 2

Figure 2. 1 Fabrication of double-barrel nanopipettes using a laser-based pipette puller and a one-step protocol. 65
Figure 2. 2 The double-barrel capillary and a pair of double-barrel nanopipettes after the pulling. **(a)** The double-barrel quartz capillary. From the microscopy image (inset), it is obvious that two barrels with semi-circular column profile are divided by a septum. **(b)** Generated double-nanopipettes after the pulling. Scale bar: inset of **a** 500 μm; **b(ii)** 500 μm; **b(iii)** 100 μm. 66
Figure 2. 3 Fabrication of single-barrel nanopipettes using a laser-based pipette puller and a two-step protocol. 66
Figure 2. 4 The single barrel capillary and a pair of single-barrel nanopipettes after the pulling. **(a)** The double-barrel quartz capillary. **(b)** Generated single-barrel nanopipettes after the pulling. Scale bar: inset of **a** 500 μm; **b(ii)** 500 μm; **b(iii)** 100 μm. 67
Figure 2. 5 The morphology of nanopore characterised by SEM. The side view **(a)** and the cross-section **(b)** of a single barrel nanopipette. Scale bar: **(a)** 10 μm, **(b)** 100 nm. 68
Figure 2. 6 I-V characterisation of a nanopipette. **(a)** I-t measurement of a typical nanopipette under bias from -600 mV to 600 mV in 100 mM of KCl. The grey dashed line represents the time point where the I-V curve was obtained. **(b)** The I-V curve of a nanopipette, which can be used to calculate the conductance and the ionic current rectification of the nanopore. 69
Figure 2. 7 Preparation of Ag/AgCl electrodes. **(a)** The set-up of the AgCl electrodes preparation. **(b)** I-t curve showing Ag oxidation in a 1 M KCl solution under a bias of 2 V. 70

Figure 2. 8 Schematic of a nanopipette set-up for ionic current and molecule translocation measurements. 72
Figure 2. 9 The customised nanopore app interface. 73
Figure 2. 10 The peak selection steps of the translocation analysis. **(a)** A 120-s current-time trace of 300-pM 10-kbp dsDNA translocation in 100 mM of KCl and 10 mM of Tris-EDTA (pH = 8) through a nanopipette with a 18 nm pore size; V = 400 mV. **(b)** Histogram of the ionic current distribution. The red line denotes the open pore current, which was fitted by a Poisson probability distribution function. The dashed line indicates the threshold above which the peak current can be counted. **(c)** The selection of fitted traces with the events above the threshold (black line) and that crossed the cut-off (green line). **(d)** The exported events after the peak selection step. 74
Figure 2. 11 The dwell time of the peak are determined by FWHM **(a)** or the cut-off **(b)**. 75
Figure 2. 12 Statistics of the translocation events from the current-time trace of 10 kbp DNA translocation analysed by the nanopore app. **(a)** Histogram of the dwell time, the integral area, and the current amplitude. The red lines represent the distribution fitting curves. **(b)** The green dashed line indicates the Kernal density of the distributions across three parameters. **(c)** The scatter plots and surface plots of current amplitude/charge along with the dwell time. **(d)** The distribution of the current amplitude and dwell time, with the mean and median of the whole data set. **(e)** The calculation of the capture rate using the stochastic process of the time between the events (delta T). **(f)** The cumulative histogram of the delta T. **(g)** The power spectral density of the current-time trace which is shown in Figure 2.10..... 77

Chapter 3

Figure 3. 1 Label-free FET based biosensors. The FET biosensors for DNA (a) and protein, (b) label-free detection. Figure 3.1a adapted from reference 4, and Figure 3.1b adapted from reference 7. 80
Figure 3. 2 Schematic of the nexFET. The nexFET platform is a functionalised nanopore-based transistor device. The transistor is located on a double-barrel quartz nanopipette tip, with one barrel filled with a carbon nanoelectrode. On the cross-section of the nanopipette, the carbon covers the entire area. Therefore, the PPy can coat the conductive carbon area by electropolymerisation. With the ionic current feedback control, which can be monitored by the current decreasing of the second (open) barrel, the pore size can be precisely tuned. The generated ring-like PPy layer acts as the gate electrode of the FET, whereas the open nanopore acts as the source-to-drain channel.

Controlling the PPy gate voltage via the carbon nanoelectrode, the current between the source and drain can be manipulated. 82
Figure 3. 3 Schematic of carbon pyrolysis in the nanopipette. The time marked in the figure represents the duration each location was heated. 82
Figure 3. 4 Schematic of the PPy electropolymerisation with real-time feedback control. When the carbon deposited dual-barrel nanopipette inserted into the Py electrolyte, the PPy were generated on the conductive surface with V_G = 600. A V_{DS}=100 was used to generate a small drain-source current, which were used to monitor the nanopore size. 84
Figure 3. 5 The fabrication process and the corresponding SEM characterisations of each step. **(a)** The nexFET is fabricated in dual-barrel quartz nanopipettes by a pyrolytic carbon deposition in one of the barrels, followed by electrodepositing of PPy at the carbon-coated nanopipette tip. SEM images at each stage of the fabrication process are shown in **(b)** quartz double barrels after nanopipette pulling (scale bar 100 nm, inset 20 μm). **(c)** One barrel coated with carbon after pyrolytic deposition (scale bar 100 nm) and, **(d)** electropolymerized PPy, acting as a gate electrode, deposited on top of the carbon electrode and surrounding the opening of the nanopore (scale bar 100 nm). Some of the SEM characterisations was conducted by Bernice Akpinar. The figures adapted from reference 26. 85
Figure 3. 6 Optical, SEM, and TEM side-view images of the nanopipette. **(a)** Optical microscopy characterisation and **(b)** SEM characterisation of a representative quartz double-barrel nanopipette after pulling from a dual-barrel quartz capillary. **(c)** Optical microscopy characterisation and **(d, e)** TEM characterisation of a nanopipette after pyrolytic carbon deposition. One barrel is still open, and the other barrel is filled with carbon nanoelectrodes (the black barrel in the optical image and the darker barrel in the TEM image). The 'incision' of the plain dual-barrel nanopipette is sharp and clear, while the cross-section of the nanopipette after the carbon deposition is rough, which may relate to a crown-like carbon layer located around the nanopore. The scale bars of all-optical images are 100 μm, while those of the SEM image is 500 nm, and those of all TEM images are 500 nm, and insets are 200 nm. The TEM characterisation was conducted by Bernice Akpinar..... 85
Figure 3. 7 Linear sweep voltammogram characterisation of the carbon area. **(a)** Schematic diagram of carbon-layer **(i)** uncoated and **(ii)** coated dual-barrel nanopipette tips with one carbon nanoelectrode. **(b)** The LSV for the redox of 1 mM of ferrocene methanol at the carbon surface of the carbon-coated and uncoated nanopipettes. A difference of nearly three times in the current plateau confirmed that the carbon-coated nanopipette owns a larger conductive area around the open barrel for the deposition of the PPy gate..... 86

Figure 3. 8 Elemental analysis of a carbon-deposited nanopipette. **(a-c)** TEM images and elemental analysis of a carbon-deposited nanopipette. For elemental analysis, carbon was over- deposited (higher butane flow-rate and lower argon flow-rate were used during pyrolytic deposition), which confirmed that carbon deposition occurs on the tip of the nanopipette. Here ring-like (or crown-like) carbon structures are observed on the tip of the nanopipette. Element mapping analyses show the existing of **(d)** carbon, **(e)** oxygen, and **(f)** silicon distribution at the tip of the nanopipette. The TEM and elemental mapping characterisation were conducted by Bernice Akpinar. Scale bar: **(a)** 1 µm, **(b)** 200 nm, **(c)** 100 nm, **(d-f)** 1 µm. 87
Figure 3. 9 The current change of each channel during the electrodeposition. **(a)** The gate current and voltage plots and **(b)** the drain-source (or nanopore channel) current and voltage plots in a representative nanopipette monitored overtime during PPy deposition. The gate current gradually increased with each PPy electropolymerized cycle, indicated by number and arrow. The I-Vs of the drain-source (nanopore) channel were also monitored. The conductance of this channel was gradually decreased with each corresponding PPy electropolymerized cycle, indicated by number and arrow. The inset of (b) illustrates that the initial current of the drain-source channel (1) decreased over time with the electropolymerisation process under a 100 mV voltage..... 88
Figure 3. 10 Nanopore characterisation before and after the real-time controlled electropolymerisation. **(a)** The I-V characteristics of five representative nanopores (drain-source), which exhibit varied initial ion transport characteristics, indicated by the differences in the size and morphology of the nanopores. **(b)** By monitoring the current decrease of the drain-source channel over time (at 100 mV of the applied voltage), which demonstrates the decrease in nanopore conductance, the same nexFET devices could be generated when the I_{DS} reached the set-point current (1 nA in this example). **(c)** The I-V characteristics of the five generated devices by using the real-time feedback control of the electrodeposition indicates the high reproducibility of the fabrication. The measurements of the I-V characteristics were performed in 100 mM of KCl, 1 mM of Tris-EDTA, pH 7.4..... 89
Figure 3. 11 Nanopipette characterisation at different stages of nexFET fabrication. SEM images of **(a)** carbon-filled nanopipettes with a 100 nm open barrel, **(b)** nexFET with ~80 nm nanopore after PPy deposition, **(c)** nexFET with ~ 10 nm nanopore after PPy deposition, and **(d)** a fully blocked nexFET after longer polypyrrole deposition. **(e)** representative I-V plots showing the change from an open barrel nanopipette (red colour) to a closed nexFET after 8 seconds of PPy deposition (green colour). **(f)** Nanopore current I_{DS} (at 100 mV applied voltage) was measured over time to monitor decreasing nanopore conductance during PPy deposition until the nanopore was fully closed within 8 seconds. Scale bars: 100 nm..... 90

Figure 3. 12 nexFET ion selectivity characterisation. **(a)** I-V plots, and **(b-c)** ion-selectivity of nexFET nanopore at different steps of PPy deposition on the tip of the nanopipette. The ion selectivity is measured as a reversal potential with a 3 times KCl concentration gradient (inside/outside ratio = 100 mM/ 33.3 mM) across the nexFET. The deposition steps are colour coded identically in all plots. Step 0 is the initial drain-source I-V of the open-barrel of the nanopipette before PPy deposition. Following deposition of PPy on the tip, the ion current rectification ratio and ion selectivity increases, while nanopore conductance decreases. 91
Figure 3. 13 Ionic transport (nanopore) dependence on applied gate voltage in the nexFET. I_{DS}-V_{DS} characteristics were measured at KCl concentration of (a) 1 mM, (b) 10 mM, (c) 100 mM, and (d) 1 M, respectively..... 92
Figure 3. 14 Ionic transport and ionic current rectification of the nexFET under different salt concentrations. **(a–d)** Contour plots of the ionic transport dependence on the applied gate voltage under different KCl concentrations (from 1 mM to 1 M), corresponding to the I-V curves in Figure 3.13. **(e)** The ionic current rectification dependence on the applied gate voltage (V_G), calculated from the I-V curves in Figure 3.13. Error bars represent the standard deviation of three independent experimental repeats with different nexFET devices. 93
Figure 3. 15 Ionic transport of the nexFET, dependent on the pH. **(a–h)** The I-V (drain-source) characteristics of the nexFET at different gate voltages under different pHs. The I-V measurements were performed in 100 mM of KCl with a Tris-HCl buffer from pH 1 to pH 8 (a–h) at gate potentials (V_G) ranging from -400 to +400 mV. 94
Figure 3. 16 Ionic transport of the nexFET, dependent on the pH. (contour plots). **(a–h)** Contour plots of the ionic transport's dependence on the applied gate voltage under different pHs, corresponding to the I-V curves in Figure 3.15. The measurements were performed in 100 mM of KCl with a Tris-HCl buffer from pH 1 to pH 8 (a–h) at gate potentials (V_G) ranging from -400 to +400 mV. 94
Figure 3. 17 The pH response of nexFET as a pH sensor. (a) The ICR of nexFET under different pH. The measurements are performed in 100 mM of KCl with a Tris-HCl buffer from pH 1 to pH 8. (b) The response time of pH change. The starting test point is pH=1. The quick I-V was measured when the buffer was switched to next pH. The response time was recorded as the time between switch buffer and stabilization of the I-V curves. Error bars represent the standard deviation of three independent experimental repeats with different nexFET devices. 95

Chapter 4

Figure 4. 1 Using a nexFET to sense DNA and protein. The nexFET platform is a functionalised nanopore-based FET. The transistor is located on a double-barrel quartz nanopipette tip, with one barrel filled with a carbon nanoelectrode. The nanopore provides a drain-source channel, and the PPy gate layer acts as the gate of the FET. By controlling the gate voltage through the carbon nanoelectrode, the transport properties and capture rate of biomolecules can be efficiently controlled at the single-molecule level. Moreover, by embedding some artificial receptors, the nexFET can detect biomolecules with high sensitivity and selectivity.....101
Figure 4. 2 Bias voltage study of DNA translocation through a nexFET. **(a)** The voltage dependence of DNA translocation through a quartz nanopore (approximately 100 nm) located on a bare dual-barrel nanopipette and the PPy nanopore located on the nexFET are indicated by the black traces on the top and coloured traces on the bottom, respectively. The translocation of 100 pM, 3 kbp dsDNA is measured in 100 mM of KCl and a 1 mM Tris-EDTA buffer, pH 7 solution. All traces are 10 s long and filtered by a low-pass Bessel filter with a cut-off frequency of 10 kHz. Horizontal scale bar: 1 s; vertical scale bar: 10 pA. **(b)** The I-V characteristics of the nanopore before and after PPy deposition, corresponding to the schematic above. Before PPy modification, the pore size is too large to sense the target DNA, which results in no events observed. **(c)**The capture rate, **(d)**the translocation time, and **(e)** the current blockage versus applied V_{DS} without any gate voltage (V_G). The nexFET behaves similarly to conventional nanopores. Error bars represent the standard deviation of three independent experimental repeats with different nexFETs. 104
Figure 4. 3 Gate voltage dependence on dsDNA translocation through the nexFET. (a) Representative translocation recordings are shown for 300 pM 3 kbp dsDNA in 100 mM KCl and a 1 mM Tris-EDTA buffer, pH 8 with V_{DS} = 700 mV and V_G, equal to (i) -400 mV, (ii) -200 mV, (iii) 0 mV, (iv) 200 mV, and (v) 400 mV. All measurements were conducted at least three times. I-t traces are shown for a 60 s duration as well as a 4 s inset. Note that the number of events (N) is for the plotted traces. In all cases, the traces were filtered using a Bessel filter with a cut-off frequency of 10 kHz. The main trace scale bar: 5 s; partial traces scale bar: 0.5 s) The scatter plots, along with peak amplitude and translocation time histograms, are also included. Note that the count of event numbers (N) is only for the plotted traces. All measurements were conducted at least three times.....105
Figure 4. 4 The gate voltage dependence of DNA translocation through the nexFET. The **(a)** capture rate, **(b)** translocation dwell time, **(c)** current blockage, and **(d)** signal-to-noise ratio of 300 pM, 3 kbp dsDNA translocation versus gate voltage are measured in 100 mM of KCl and a 1 mM Tris-EDTA buffer under a 700 mV drain-source voltage. The rate of change (based on V_G = 0) in each parameter is also marked. Error bars

represent the standard deviation of three independent experimental repeats with different nexFETs.....106
Figure 4. 5 The ratio of translocation events with multi-steps in all translocation events at different gate voltages. **(a)** Representative ionic translocation recordings demonstrate different single- or multi-step events of the 3 kbp dsDNA molecules with a 700 mV drain-source voltage and different gate voltages from -400 mV to 400 mV (from top to bottom). The measurements were conducted in 100 mM of KCl and a 1 mM Tris-EDTA buffer, pH 8, and they were recorded with a low-pass Bessel filter with a cut-off frequency of 10 kHz. Scale bars: 0.5 s. **(b)** Increasing the gate voltage results in more multi-step events. With the gate voltage increased from -400 mV to 400 mV, the ratio of multi-step events in all translocation events increased linearly. Error bars represent the standard deviation of three independent experimental repeats with different nexFETs.....107
Figure 4. 6 The detection of single 18-mer ssDNA using a nexFET. **(a)** Representative ionic translocation traces of 1 nM of ssDNA (18 mer) and **(b)** partially magnified traces indicate that the small oligonucleotides can be detected using a nexFET at the single-molecule level. The translocation was measured in 100 mM of KCl and a 1 mM Tris-EDTA (pH = 8) buffer with V_{DS} = 700 mV. The **(c)** distribution of translocation time and **(d)** peak current histograms. All measurements were conducted at least three times. 109
Figure 4. 7 The characterisation of a nexFET and an insulin-embedded nexFET. **(a)** Schematic of an insulin-embedded nexFET and a plain nexFET. **(b)** The I-V (drain-source) characteristics of an insulin-embedded nexFET and a plain nexFET in 100 mM of KCl and a 1 mM Tris-EDTA buffer, pH 8. Fluorescence images, which were superimposed on optical microscopy images of the nanopipette, validate that **(c)** the insulin-embedded nexFET can bind the anti-insulin antibody selectively by using a dye tagged secondary antibody, while **(d)** the plain nexFET is not able to bind the target antibody selectively.....110
Figure 4. 8 Using an insulin-embedded nexFET to sense an anti-insulin IgG antibody. **(a–d)** Schematic of the nexFET translocation and corresponding 60 s I-t records: **(a)** the translocation of 1 nM of an anti-insulin IgG antibody through a plain nexFET, **(b)** the translocation of 1 nM of an isotype IgG antibody through an insulin-modified nexFET, **(c)** the translocation of 200 pM of an anti-insulin IgG antibody through an insulin-modified nexFET, and **(d)** the translocation of 1 nM of an anti-insulin IgG antibody through an insulin-embedded nexFET. All above translocations were measured in 100 mM of KCl, 1mM TE, pH = 7 buffer with a -800 mV drain-source voltage and recorded using a low-pass Bessel filter with a cut-off frequency of 10 kHz. For all translocation traces, the all-point data analysis is shown, including **(e)** the

histogram of the pore closure ratio; **(f)** the capture rate, along with time; and **(g)** the translocation time. 111
Figure 4. 9 A full translocation trace of 200 pM of an anti-insulin IgG antibody through an insulin-modified nexFET. A 1,200 s full translocation trace is demonstrated for the sensing of 200 pM of an anti-insulin IgG antibody by using an insulin-modified nexFET. This translocation experiment was conducted in 100 mM of KCl, 1 mM TE, pH = 7 buffer under a -800 mV drain-source bias voltage. The top panel illustrates the 1,200 s full trace, and the remaining 20 panels depict magnified 60 s successive traces. The initial (0–60 s), the middle (570–630 s), and the end (1,140–1,200 s) segments of the trace are presented in Figure 4.8c. The histograms of the nanopore closure ratio (Figure 4.8e); the capture rate, along with translocation time (Figure 4.8f); and the dwell time (Figure 4.8g) for 200 pM of an anti-insulin IgG antibody were calculated from this full trace. 113
Figure 4. 10 A full translocation trace of 1 nM of an anti-insulin IgG antibody through an insulin-modified nexFET. A 600 s full translocation trace is demonstrated for the sensing of 1 nM of an anti-insulin IgG antibody by using an insulin-modified nexFET. This translocation experiment was conducted in 100 mM of KCl, 1 mM TE, pH = 7 buffer under a -800 mV drain-source bias voltage. The top panel illustrates the 600 s full trace, and the remaining 10 panels depict magnified 60 s successive traces. The initial (0–60 s), the middle (270–330 s), and the end (540–600 s) segments of the trace are presented in Figure 4.8d. The histograms of the nanopore closure ratio (Figure 4.8e); the capture rate, along with translocation time (Figure 4.8f); and the dwell time (Figure 4.8g) for 200 pM of an anti-insulin IgG antibody were calculated from this full trace. 114

Chapter 5

Figure 5. 1 A single-nucleotide polymorphism detection assay that integrates nanoparticle-based superstructures and a solid-state nanopore sensing platform. Different ionic signals represent different nanostructures. Figure adapted from reference 19.....121
Figure 5. 2 Schematic of single-molecule detection of nanoparticle-based superstructures. From an AuNP monomer and AuNP symmetrical dimers to trimers, a range of nanoparticle-based superstructures were fabricated and sensed by the nanopore platform incorporating a high-bandwidth amplifier. The sub-peaks of the ionic translocation signal represent the sub-structures of the nanoparticle-based superstructures. In addition, single-molecule SERS detection was also applied by

integrating gold-coated nanopores, SERS, and Raman reporter tagged AuNP dimers. 122
Figure 5. 3 The details of AuNP-based nanostructures. **(a)** AuNP monomer: one 17 nm AuNP modified by an ssDNA. **(b)** AuNP symmetrical dimers: two 17 nm AuNPs linked by a DNA bridge (35 bases long). **(c)** AuNP symmetrical dimers with a long linker: two 17 nm AuNPs linked by a DNA bridge (115 bases long). **(d)** AuNP asymmetrical dimers: one 20 nm AuNP and one 10 nm AuNP linked by a DNA bridge (35 bases long). **(e)** AuNP trimers: three AuNPs linked by two DNA bridges (35 bases long). **(f)** The AuNP symmetrical dimers with Raman reporter. Two 4-aminothiophenol modified 35 nm AuNPs linked by a DNA bridge (35 bases long). All fabrication details are described in the method part. 123
Figure 5. 4 The SEM images of a representative nanopipette. The SEM image of **(a)** a side view (scale bar: 10 μm) and **(b)** a cross-section (scale bar: 100 nm) of a nanopipette. From the images, the conical shape of the nanopipette and the nanopore located on the tip can be observed. 127
Figure 5. 5 The I-V characterisation of nanopores. Electrical nanopipette characterisation from 18 nanopipettes. The quartz nanopipettes were pulled from quartz capillaries by a laser-based pipette puller. The current-voltage curves indicate the conductance of quartz nanopores to be 15.3 ± 2.4 nS (n = 18). The measurements of the I-V characterisation were performed in 100 mM of KCl, 10-mM of Tris-EDTA, pH 8. 128
Figure 5. 6 Schematic representation of a nanopipette. **(a)** The model of the conical nanopore for effective length calculation. **(b)** The real nanopore shape model. 129
Figure 5. 7 The SEM of the nanopore and tip angle measurement. **(a)** SEM image depicts the tip length and geometry, (scale bar 100 μm, inset 20 μm) **(b–s)** The side view of the nanopore and the semi-angle of the first 100 nm of the nanopipette (scale bar 1 μm, inset 50 nm).....130
Figure 5. 8 Calculation of the nanopipette's effective length. The ratio of the resistance of 18 conical nanopores from length x to 500 nm, which is considered to reach the whole resistance. Considering the majority resistance (75%–80%) in our calculation, the effective length can be calculated.....131
Figure 5. 9 The TEM images, current-time traces, individual events, and statistics of a series of AuNP-based nanostructures. The TEM (scale bar: 100 nm), current-time traces (scale bar: vertical 50 pA, horizontal 5 s), individual events (scale bar: vertical 50 pA, horizontal 20 μs), and statistics for **(a)** AuNP monomers, **(b)** AuNP symmetrical dimers (35-mer linker), **(c)** AuNP asymmetrical dimers, and **(d)** AuNP symmetrical dimers (115-mer linker). The schematic and TEM images in **(i)** indicate a clear geometry of the molecules. The typical translocation traces and individual translocation

events of each molecule are also depicted in **(ii)**, as their signatures can be distinguished easily from others. All the translocation experiments were performed in 50 mM of KCl, 10 mM of Tris-EDTA, and at a potential of -600 mV. Each current-time trace was recorded at a 1-us sampling rate and filtered using a low-pass Bessel filter with a cut-off frequency of 100 kHz. The statistics of translocation are illustrated in **(iii)**, including the translocation dwell time, peak current, and normalised peak position. Surface plots along with peak current and normalised peak position histograms are also presented, and they clearly indicate that the translocation signal is capable of simulating the nanostructure, the size/charge of each molecule, and even the distance between them. 132

Figure 5. 10 Schematic of a nanopore sensing the sub-structures of the dimer. With applied potential, the negatively charged molecule is driven by an electrophoretic force and thus moves to the anode. **(a)** When it approaches but does not enter the nanopore sensing area, only the current baseline can be recorded. **(b)** When the first AuNP dominates the sensing part, the local conductivity is increased by the heavy, negatively charged particle. **(c)** Then, the DNA bridge passes through the sensing area, generating a trough. **(d)**The second AuNP enhances the signal again when it passes the sensing area. **(e)**The whole event finishes after the molecule is pushed out of the nanopipette. 133

Figure 5. 11 The voltage dependence of AuNP symmetrical dimers. **(a)** The current-time traces of the AuNP symmetrical dimers with biases of 500, 600, 700, and 800 mV. **(b)** The decreasing of mean dwell times, **(c)** the increasing of mean peak currents, and **(d)** the increasing of event frequency is observed as the voltage is increased. All the translocation experiments were performed in 50 mM of KCl and 10 mM of Tris-EDTA. Each current-time trace was recorded at a 1-μs sampling rate and filtered using a low-pass Bessel filter with a cut-off frequency of 100 kHz. Error bars represent the standard deviation of three independent experimental repeats with different nanopipettes.....134

Figure 5. 12 The TEM images, current-time traces, individual events, and statistics of a series of AuNP trimers. The **(a)** TEM (scale bar: 100 nm), **(b)** current-time traces (scale bar: vertical 50 pA, horizontal 5 s), **(c)** individual events (scale bar: vertical 50 pA, horizontal 20 μs) for AuNP trimers. The translocation experiments were performed in 50 mM of KCl, 10 mM of Tris-EDTA, and at a potential of -600 mV. The current-time trace was recorded at a 1-μs sampling rate and filtered using a low-pass Bessel filter with a cut-off frequency of 100 kHz. 134

Figure 5. 13 The SEM images of Au-coated nanopipette. SEM images of nanopipette after Au 10 nm layer deposition: **(a)** side view (scale bar: 10 μm), **(b)** top-view (scale bar: 200 nm). The size of the nanopore at the tip was approximately 60 nm. A 10 nm

layer of Au was deposited on the nanopore prior to translocation to enhance the SERS signal.....135
Figure 5. 14 Customised electrical detection set-up with integrated laser optics to enable Raman measurement. 136
Figure 5. 15 The single-molecule Raman detection of a 4-ATP tagged AuNP symmetrical dimer. **(a)** The SERS spectrum of the 4-ATP modified AuNP symmetrical dimer in bulk solution. SERS spectrum of 4-ATP dye present in the nanogap of the AuNP symmetrical dimer. This spectrum indicates a significant enhancement of the 1,138, 1,387, and 1,571 cm^{-1} vibrational bands of 4-ATP. **(b)** Raman spectra demonstrate the translocation of the dimers. The top panels illustrate a 4.05-ms translocation using a -800-mV potential at an 810-µs acquisition time. These spectra demonstrate that a single AuNP dimer is translocating through the nanopore over a period of 4.05 ms. **(c)** The Raman spectra of a PEG-modified 4-ATP loaded Au dimer using +800 mV potential. There is a small enhancement in vibrational bands, indicating that the Au dimer moves away from the nanopore, and no translocation takes place. 136
Figure 5. 16 Translocation of a PEG-stabilised 35 nm AuNP dimer functionalised with 4-ATP dye. **(a)** The current-time trace (scale bar: vertical 50 pA, horizontal 5 s) and statistics for a 1 nM Raman sample (35 nm AuNP dimer functionalised with 4-ATP dye, protected by SH-PEG). All the translocation experiments were performed in 100 mM of KCl and 10 mM of Tris-EDTA. The current-time trace was recorded at a 10-us sampling rate and filtered using a low-pass Bessel filter with a cut-off frequency of 10 kHz. **(b)** The dwell time distribution of the electrical translocation of the dimer. The translocation duration of this sample is much longer than others in this work because the PEG-modified molecules have high viscidity. Moreover, the charge of the particles is shielded, so they move slowly, and some unpredictable rotation may occur when the electric field is applied. **(c)** The amplitude statistics of the translocation. 137

Chapter 6

Figure 6. 1 Schematic of AuNP dimer protein carrier and AuNP antigen probes. **(a)** The dimer carrier is based on a dumbbell system where two Au nanoparticles (17–20 nm) are linked by a ~115-mer DNA bridge, which is engineered to contain an aptamer sequence that binds to target protein molecules. **(b)** For the second strategy, two monomer AuNP probes are modified with different antibodies. These form a dimer in

the presence of the target antigen. In both strategies, the bound dimers are transported by the applied electric field from inside the nanopipette to outside. Bound analytes are identified at the single-molecule level by changes in the shape of individual events. Counting statistics of these individual signatures can reveal significant information on the fraction of bound vs unbound analytes, and the analyte concentration. 144
Figure 6. 2 Details of the AuNP dimer thrombin carrier. The AuNP dimer thrombin carrier is self-assembled by an AuNP with a 115-mer ssDNA containing a 15-mer TBA sequence and an AuNP with the complementary part to the sequence aside from the aptamer part. After self-assembling, the protein carrier can be used to sense the thrombin selectively in complex solutions. It is noteworthy that there are eight random bases close to the aptamer sequence to minimise the steric hindrance. The binding affinity between two DNA are strong enough so there's no need of ligation. 145
Figure 6. 3 The sensing of 1 nM thrombin natively. The current-time trace of thrombin (1 nM) nanopore sensing (scale bar: vertical 50 pA, horizontal 5 s) at a bias of -600 mV. The translocation experiments were performed in 50 mM of KCl, 10 mM of Tris-EDTA, and at a potential of -600 mV. The current-time trace was recorded at a 1-μs sampling rate and filtered using a low-pass Bessel filter with a cut-off frequency of 100 kHz. No events were observed under these circumstances because of a fast transient and a low capture rate.....146
Figure 6. 4 The UV-vis spectrum of thrombin/dimer complexes. **(a)** By adding 4 nM of thrombin to 1 nM of AuNP dimer thrombin carrier dispersions with 50 mM of KCl and 10 mM of Tris-EDTA at pH 8, the AuNP-based molecules started oligomerisation as a result of the weakening of the whole charge of the molecule. **(b)** The pristine AuNP dimer molecules of the same ionic strength would not aggregate until the concentration of thrombin reached 100 nM, which masked the surface of the dimer molecules. ...147
Figure 6. 5 Nanopore sensing of thrombin with AuNP dimer thrombin carriers. **(a)** Schematic of the dimer carriers, which were engineered to contain aptamer sequences, delivering and sensing the target protein. **(b—c)** The representative current-time trace (scale bar: vertical 50 pA, horizontal 5 s), individual translocation events (scale bar: vertical 50 pA, horizontal 20 μs), and statistics (translocation dwell time, and the scatter plot, along with peak current and normalised peak position histograms) for AuNP dimer thrombin carriers and AuNP dimers with thrombin complex. The translocation experiments were performed in 50 mM of KCl, 10 mM of Tris-EDTA, and at a potential of -600 mV. Each trace is recorded at a 1-us sampling rate and filtered using a low-pass Bessel filter with a cut-off frequency of 100 kHz.....148
Figure 6. 6 The binding assay for thrombin using AuNP dimer thrombin carriers through nanopipettes. **(a)** The normalised peak position of the dimer carriers or the carrier and target protein complexes, under different concentrations of thrombin (from top to bottom, 0 nM, 0.2 nM, 0.5 nM, 1 nM, and 2 nM). **(b)** Binding assay for a 1 nM

dimer carrier concentration incubated with increasing thrombin concentrations ranging from 0 to 2 nM. Error bars represent the standard deviation of three independent experimental repeats with different nanopipettes. 149
Figure 6. 7 The control experiment of AuNP dimer thrombin carrier. **(a)** The current-time trace (scale bar: vertical 50 pA, horizontal 5 s), individual events (scale bar: vertical 50 pA, horizontal 20 μs), and **(b–d)** statistics for 1 nM of AuNP dimer thrombin carrier incubated with 1 nM of lysozyme. All the translocation experiments were performed in 50 mM of KCl and 10 mM of Tris-EDTA. The current-time trace was recorded at a 1-μs sampling rate and filtered using a digital low-pass Bessel filter with a cut-off frequency of 100 kHz. There are no triple-peak events; however, double-peak events are present, corresponding to unbound thrombin carriers. 150
Figure 6. 8 The sensing of 1 nM PCT natively. The current-time trace of PCT (100 nM) nanopore sensing (scale bar: vertical 50 pA, horizontal 5 s). The translocation experiments were performed in 50 mM of KCl, 10 mM of Tris-EDTA, and at a potential of -600 mV. The current-time trace was recorded at a 1-us sampling rate and filtered using a low-pass Bessel filter with a cut-off frequency of 100 kHz. Even with this high concentration of PCT, there is no translocation signal, because of the poor signal-to-noise ratio. The PCT molecules are too small to be detected natively.....151
Figure 6. 9 Nanopore sensing of PCT via a pair of AuNP monomer probes. **(a)** Schematic of two AuNP monomer probes with different antibodies self-assembling to a dimer in the presence of an antigen (PCT). **(b–c)** The representative current-time trace (scale bar: vertical 50 pA, horizontal 5 s), individual translocation events (scale bar: vertical 50 pA, horizontal 20 μs), and statistics (the translocation dwell time, and the scatter plot, along with peak current and normalised peak position histograms) of conjugated dimers, which are linked by antibody-antigen-antibody sandwich bridges. All the translocation experiments were performed in 50 mM of KCl, 10 mM of Tris-EDTA, and at a potential of -600 mV. The data was recorded at a 1-μs sampling rate and filtered using a low-pass Bessel filter with a cut-off frequency of 100 kHz.....152
Figure 6. 10 The control experiment of AuNP monomer PCT probes. The current-time trace (scale bar: vertical 50 pA, horizontal 5 s), individual events (scale bar: vertical 50 pA, horizontal 20 μs), and statistics for 1 nM of AuNP monomer PCT probes incubated with 1 nM of insulin. All the translocation experiments were performed in 50 mM of KCl and 10 mM of Tris-EDTA. The current-time trace was recorded at a 1-μs sampling rate and filtered using a low-pass Bessel filter with a cut-off frequency of 100 kHz. While there are no double-peak events, single-peak events occurred, corresponding to free PCT probes.....153
Figure 6. 11 The binding assay for thrombin by using AuNP monomer probes through nanopipettes. **(a)** The normalised peak position of the monomer probe and conjugated dimer with different concentrations of PCT (from top to bottom: 0 nM, 80 pM, 20 nM,

40 nM, 100 nM, and 200 nM). **(b)** The binding curve of 1 nM of AuNP monomer PCT probes incubating with PCT ranging from 0 to 400 nM. The inset is the sensing of PCT in a clinical diagnostic range. The error bars of the binding ratio analysis represent the standard deviation of three independent experimental repeats. 153
Figure 6. 12 The TEM of AuNP monomer probes incubating with different levels of PCT. The TEM images (scale bars: 200 nm) of AuNP monomer probes incubated with **(a)** no PCT or **(b)** 40 pM, **(c)** 80 pM, **(d)** 400 pM, **(e)** 4 nM, **(f)** 20 nM, **(g)** 40 nM, **(h)** 100 nM, and **(i)** 200 nM PCT.....154
Figure 6. 13 The binding assay confirmed by translocation and TEM counting statistics. The binding assay of 1 nM of PCT monomer probes with PCT ranging from 0 to 200 nM. **(a)** The binding ratio calculated from the percentage of double-peak translocation signatures in all signals. Error bars represent the standard deviation of three independent experimental repeats with different nanopipettes. **(b)** The binding ratio achieved by counting the dimer out of all particles. Error bars represent the standard deviation of three independent experimental repeats. 155

Chapter 7

Figure 7. 1 Schematic of a TBA-embedded nexFET. This nexFET is a nanopore-based transistor, which is located on a dual-barrel nanopipette tip. By applying the voltage from the carbon nanoelectrode, the drain-source current across the nanopipette can be changed. The nanopore sensing area, which is the TBA-modified PPy nanopore inner wall, is capable of identifying and detecting thrombin selectively. The detection of thrombin by plain glass nanopore is always challenging due to its small size, heterogeneous charge, and fast translocation. This is the limitation I can address by the TBA-embedded nexFET.....162
Figure 7. 2 The I-V characteristics of different nexFETs. **(a)** Schematic of the plain nexFET, the insulin-embedded nexFET, and the TBA-embedded nexFET. **(b)** The I-V measurements of those three types of nexFETs in a solution of 100 mM of KCl and 10 mM of Tris-EDTA (pH = 8). 163
Figure 7. 3 Thrombin single-molecule sensing by using a TBA-embedded nanopore. **(a)** The translocation recordings of 30 nM thrombin translocation through **(i)** a 15 nm plain quartz nanopipette and **(ii)** a TBA-embedded nexFET, with 100 mM of KCl and 10 mM of Tris-EDTA (pH = 8), V_{DS} = 700 mV. Scale bar: horizontal 1 s; vertical 20 pA. **(b)** The scatter plot (peak current along with dwell time) of the thrombin translocation. 164
Figure 7. 4 The FET performance of two types of TBA-embedded nexFETs. The I_{DS}-V_{DS} characteristics with different gate voltages in **(a)** a one-layer TBA-embedded

nexFET and **(b)** a two-layer TBA-embedded nexFET. The I-V measurements were conducted in a solution of 100 mM of KCl and 10 mM of Tris-EDTA (pH = 7). 165
Figure 7. 5 Schematic of a DNA origami protein carrier. The main carrier is a six-helix-bundle DNA origami with a biotinylated end. In the protein carrier, four different aptamers were engineered on the DNA origami carrier to bind specific proteins. The proteins can be identified by the sub-peaks of the translocation signal. The origami sample was provided by Prof. Yang Yang (Shanghai Jiaotong University, China) and Prof. Chenxiang Lin (Yale University, US). 166
Figure 7. 6 The translocation of unmodified six-helix-bundle DNA origami molecules. **(a)** Schematic of the DNA origami, which is a cylindrical shape that is 400 nm long. **(b) (i)** The translocation recording trace and **(ii)** randomly picked events of 200 pM DNA origami in 2 M of LiCl and 10 mM of Tris-EDTA (pH = 8) under 600 mV. Scale bar: **(i)** horizontal 5 s, vertical 50 pA and **(ii)** horizontal 0.2 μs; vertical 50 pA. **(c)** The dwell time and peak current of the translocation of DNA origami. 166

List of Tables

Table 2. 1 Parameters for pulling the pipettes using a laser-based puller. 67

Table 2. 2 Buffer solutions prepared in this thesis. 71

Abbreviation

AFM	Atomic Force Microscopy
AFP	Alpha-fetoprotein
Au	Gold
AuNP	Gold nanoparticle
BSA	Bovine serum albumin
CMOS	Complementary metal-oxide-semiconductor
CV	Cyclic voltammetry
DNA	Deoxyribonucleic acid
dsDNA	double strand DNA
EDS	Energy Dispersive X-ray Spectrometry
EDTA	Ethylenediaminetetraacetic acid
ELISA	Enzyme-linked immunosorbent assay
EOF	Electroosmotic flow
EP	Electrophoretic
FET	Field effect-transistor
FIB	Focused ion beam
FRET	Förster resonance energy transfer
ICR	Ionic current rectification

IHL	Inner Helmholtz layer
ISFET	Ion-sensitive field-effect transistor
LPCVD	Low pressure chemical vapor deposition
nexFET	Nanopore extended field-effect transistor
NP	Nanoparticle
OHL	Outer Helmholtz layer
PCR	Polymerase chain reaction
PPy	Polypyrrole
Py	Pyrrole
RIE	Reactive ion etching
SECM	Scanning electrochemical microscopy
SELEX	Systematic evolution of ligands by exponential enrichment
SEM	Scanning electron microscope
SERS	Surface-enhanced Raman scattering
SICM	Scanning ion conductance microscopy
ssDNA	single strand DNA
TBE	Tris-Borate-EDTA
TE	Tris-EDTA
TEM	Transmission electron microscopy

CHAPTER 1

Introduction

Synopsis

In this initial chapter single molecules sensing is briefly introduced in the context of solid state nanopores. The origins, and working principles of nanopore sensors and latest relevant literature are discussed. The applications relevant to this work, as well as the limitations, of solid-state nanopores in sensing DNA and proteins, are also introduced. The aims and objectives of the entire PhD work are illuminated with an outline of this thesis.

1.1 Single-molecule sensing

With the rapid development in chemistry, biotechnology, and nanotechnology, people have never understood the biological world as well as they do today. In the last century, many epoch-making methods have been employed to explore biomolecules, and some of them are still widely used, such as the polymerase chain reaction (PCR)[1, 2] and the enzyme-linked immunosorbent assay (ELISA)[3]. However, biologists and analytical chemists are not satisfied with studying the bulk collection of biomolecules by using conventional structural or biological methods, since they lack effective information regarding individual molecules and are limited by many factors, such as low concentration of the analytes, elaborate sample preparation, and time consumption. Instead of characterising molecules in a large ensemble, single-molecule science provides an approach to study the morphology, properties, and dynamics of individual molecules rather than attaining an averaged result over the entire molecular population.

During the past two decades, research concerning single-molecule methods has increased exponentially and has been widely recognised, and some techniques have even been applied practically. Fluorescence, a widely used and mature technology that has been studied for decades, joined the family of single-molecule science in the late 1980s. A large number of studies about single-molecule fluorescence emerged based on the utilisation of dye localisation[4], the quenching effect[5, 6], fluorescence anisotropy[7], or alternatively, fluorescence resonance energy transfer (FRET)[8, 9]. Atomic force microscopy (AFM), as another method by which to study analytes at the single-molecule level, allows for the visualisation of one molecule in three dimensions[10-12]. Other single-molecule sensing methods, such as optical tweezers[13, 14] and magnetic tweezers[15, 16], also emerged. However, these valuable techniques do have limitations; for single-molecule fluorescence detection, the target analytes are required to be chemically modified with the dye, which may interfere with the molecule structure. AFM needs analytes to be immobilised on a flat surface. For optical and magnetic tweezer-based measurements, the beam should be engineered to the analytes specifically and, as such, requires careful optimisation.

In comparison with the described technologies, a nanopore[17-19], which is a small hole with an internal diameter of the order of 1 nanometre, is the youngest member in the single-molecule techniques family. The principle of nanopore-based single-molecule sensing is straightforward: a detectable current change will be generated when a target analyte passes through the nanopore. This analytic is label-free and does not need the analytes to be immobilised on the surface. Therefore, nanopore technology

attracts much attention because of their apparent ascendency among different single-molecule techniques. Moreover, this technology has also demonstrated the potential for DNA sequencing with higher speeds and lower cost[20, 21], compared to conventional methods such as capillary electrophoresis (CE). One example of such sequencing is a biological nanopore-based DNA sequencing device that has been developed and commercialised by Oxford Nanopore Technologies[22].

1.2 Nanopores

The origins of the nanopore can be traced back to the mid-20th century when the concept of Coulter counting was put forward[23]. Then, the primitive concept of a nanopore was built after the employment of the single-channel theory, which was established in the 1970s[24, 25].

A Coulter counter is an analytical device that can count the number of targets and measure their size. The objectives can be in a wide range of micro-sized analytes, such as particles, bacteria, and prokaryotic/eukaryotic cells. **Figure 1.1** illustrates the working principle of a typical Coulter counter, which contains two chambers separated by a membrane and filled with electrolytes and connected by a microscale channel. A transmembrane potential was then applied by a potentiostat via the electrodes located in both chambers (**Figure 1.1a**). A constant current flow can be recorded as the ion is transported through the microchannel (**Figure 1.1b**), whereas the resistance of the channel will drop if a molecule blocks the channel temporarily. The number of targets can thus be counted, and the size can be estimated, as the extent of the resistance drop is related to the blocked proportion of the channel (**Figure 1.1c**). Since the concept was accepted and widely used[26], the Coulter-counting resistive-pulse sensing techniques have become the cornerstone of nanopore-based single-molecule analytics.

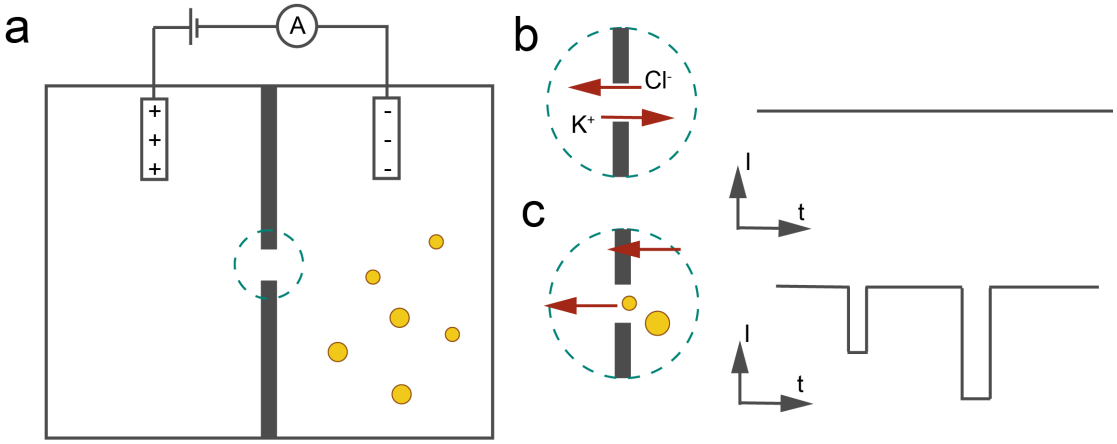


Figure 1. 1 Schematic of a conventional Coulter counter. **(a)** The Coulter counter has one (or more)

microchannels linking two separate chambers, which are filled with electrolytes and the electrode. **(b)** Ion transport will only contribute to a constant current flow. **(c)** The microparticles passed through the channel and left a resistance pulse on the signal.

The single-channel recording technology – also known as patch-clamp technology – was pioneered in the 1970s by Neher and Sakmann, who were awarded the Nobel Prize in Physiology or Medicine in 1991 because of their discoveries in the function of single ion channels in cells[25]. The novelty of this technique was the usage of small pipettes to ‘‘patch’’ a small membrane area thereby reducing the background noise and achieving a sufficiently high resistivity, a prerequisite for the observation of single channel activities. Inspired by this discovery, scientists explored a wide range of ion channels embedded in natural lipid bilayers. These small ion channels are tiny biological structures where the lumen is capable of transporting ions passing through the membrane[27, 28]. As a result, this interest in ion-channel electrophysiology gave the birth of the nanopore another critical push.

Finally, the first nanopore translocation experiment, which detected single synthetic polymer molecule translocation through a natural nanopore located on a bilayer lipid membrane, was implemented in 1994[29]. Later, the translocation experiments of biopolymer molecules were also performed using α-haemolysin channels[30]. In this experiment, not only was the RNA and DNA molecules were observed at the single-molecule level, but the length of those molecules was also characterised as a result of the different translocation durations.

With nearly thirty years of development, nanopore-based single-molecule sensing technology has been growing in leaps and bounds. From microscales to nanoscales, and from detecting large cells to sensing individual nucleotides, nanopore-based analytical methods are overcoming the limits and helping researchers understand the biological world better. During this time, biological and nanomaterial scientists have explored a wide range of nanopores, which can be divided into two categories: biological nanopores and solid-state nanopores. In this section, both types of nanopores will be introduced along with nanopipettes, which comprise a branch of solid-state nanopores and are the type used in this thesis.

1.2.1 Biological nanopores

While being the oldest type of nanopores, natural protein channels are still appealing because of several unique advantages. For instance, the small pore size of biological nanopores is on a similar scale to most essential analytes, contributing to high sensitivity and high resolution. Moreover, protein nanopores can be engineered

using a wide range of methods, such as the incorporation of specific adaptors or site-directed mutagenesis.

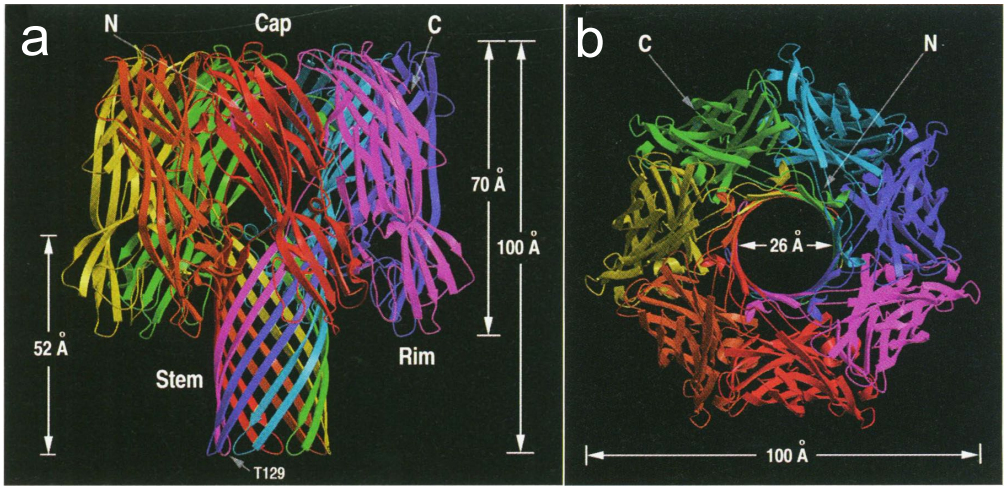


Figure 1. 2 Molecular graphic images of α-haemolysin. **(a)** A ribbon diagram of the heptameric nanopore. **(b)** A cross-section view of the protein. Figures adapted from reference 32.

α-haemolysin, a bacterial toxin protein, is one of the oldest and most commonly used biological nanopores[31, 32] (**Figure 1.2**). This mushroom-shaped and transmembrane nanopore is created by a self-assembly process of seven monomers in a lipid bilayer. By sitting in a lipid membrane, the protein channel can be fully functional; the analytes can enter the channel from the vestibule (diameter of the mouth is 2.6 nm, and the wide lumen is 4.6 nm) located on the cis side of the membrane, and they can exit the channel through the β-barrel (2 nm in diameter and 5 nm in length) to the trans side of the membrane. In the middle part, the constriction to 1.4 nm gives the whole channel a critical nanopore size. In 1996, Kasianowicz et al. successfully observed transient current modulations when single-strand DNA (ssDNA) and RNA molecules passed through an α-haemolysin driven by electrophoresis.[30] Novel nucleotide sensing experiments were recently performed by the Bayley group using a truncated-barrel mutant α-haemolysin nanopore incorporated into adaptor molecules[33].

Another commonly used protein nanopore is mycobacterium smegmatis porin A (MspA), which exhibits a tapered funnel shape with a smaller constriction part (1.2 nm width and 0.6 nm length) compared with that of α-haemolysin. The short sensing region makes the sensing of single nucleotides possible, as has been demonstrated by MspA-based DNA sequencing devices[22, 34].

Apart from these two frequently used protein channels, several biological nanopores of different sizes have been explored, such as Aerolysin (AeL), Phi29 Motor, Cytolysin A (ClyA), and Outer membrane protein G (OmpG). These biological nanochannels have been utilised in a variety of fields, such as in the detection of nucleic

acids[30, 33, 35, 36], in the sensing of proteins[37-39], in the examination of small molecules and polymers[40-42], in dynamic process studies[43, 44], and even in DNA sequencing[22, 34, 45, 46].

Despite these valuable achievements, biological nanopore biosensors have their limitations. For example, the detection of many proteins and other large molecules is always achieved by indirect methods because the size of the analytes is larger than the biological pore size, which is not tuneable.In addition, inserting the protein nanopore into the lipid bilayer is challenging because of lateral diffusion. Moreover, the lifetime of the biological nanopore is related to the stability of the fragile lipid membrane, which is easily ruptured or broken by the high ionic strength that is often necessary for DNA-sequencing experiments to achieve a reasonable signal-to-noise ratio and a decrease in electroosmosis.

1.2.2 Solid-state nanopores

To overcome the limits of biological nanopores, scientists have designed and fabricated solid-state nanopores, which possess several advantages, such as a tuneable size and shape, and mechanical robustness. In addition, solid-state nanopores demonstrate superior chemical and thermal stability even under harsh temperatures, ionic concentrations, and pH conditions that would destroy most biological nanopores. Moreover, the advanced nanofabrication process allows researchers to reach multiple identical nanopores with sophisticated structures.

The most classical fabrication procedure is to drill one or multiple nanoholes on a fabricated solid-state membrane[19], as illustrated in **Figure 1.3**: (1) On each side of a silicon wafer a layer of silicon nitride thin film is deposited using low-pressure chemical vapour deposition (LPCVD). (2) The membrane features are defined by standard photolithographic techniques. (3) The designated patterns can be opened using reactive ion etching (RIE) of the Si_3N_4 membrane. (4) The exposed silicon can then be removed by anisotropic wet etching (i.e. potassium hydroxide electrolyte). (5) The nanopore will then be generated by the electron or the ion beam drilling a nano-scaled hole on the thin membrane.

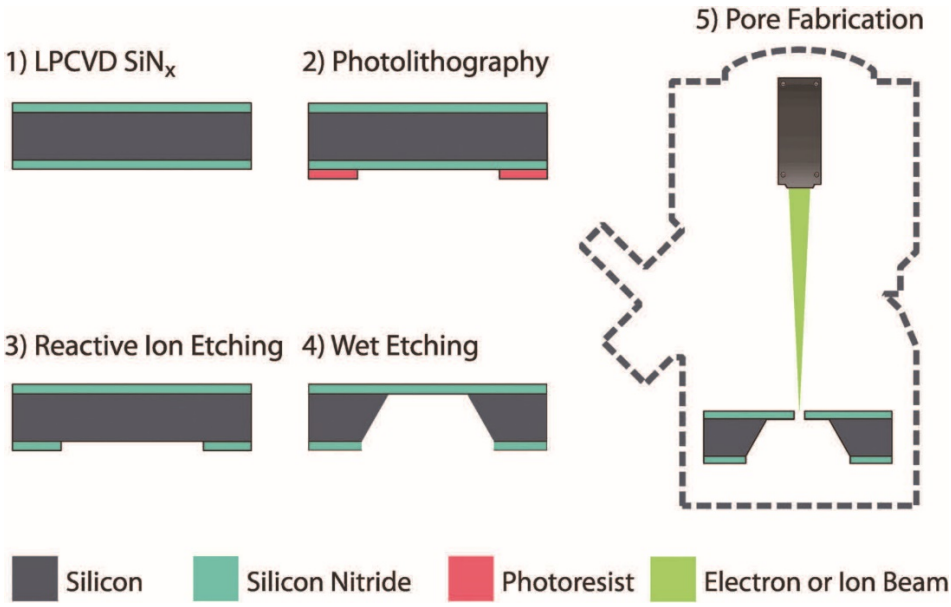


Figure 1. 3 A simple workflow of a typical solid-state membrane and nanopore on it. Figures adapted from reference 19.

Li *et al.* pioneered the fabrication of a 1.8 nm nanopore by using a focused ion beam (FIB) milling technique in 2001, as depicted in **Figure 1.4**[47]. To date, several solid-state nanopores with a wide range of materials have been fabricated using similar procedures under a variety of ion beam sources such as Ga^+, He^+, Ne^+, Kr^+, and Xe^+[48]. More recently, the trend in the solid-state nanopore community is fabricating ultra-thin nanopores to improve the readout. These nanopores can be created by replacing the conventional Si_3N_4 materials with 2D nanomaterials such as Graphene and MoS_2.

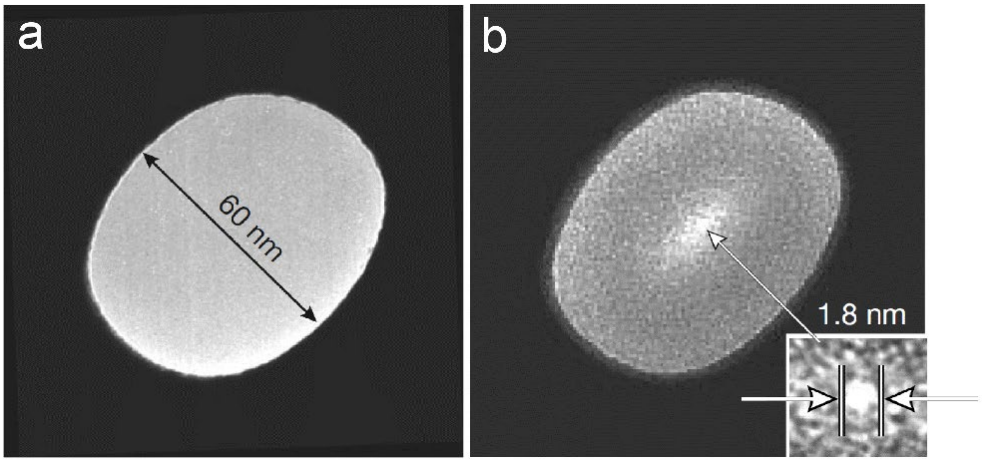


Figure 1. 4 TEM images of the nanopore. The TEM images of **(a)** the initial membrane, which is approximately 60 nm, and **(b)** the nanopore, which is approximately 1.8 nm after FIB milling. Figures adapted from reference 47.

Different solid-state nanopores have been widely used in sensing nucleic acids, proteins, and other molecules. The Dekker group performed the translocation of linear

double-strand DNA (dsDNA) with markers via a Si_3N_4 nanopore.[49] They also revealed the DNA detection by a graphene nanopore.[50] Farimani *et al.* reported using a nanopore located on MoS_2 to detect DNA bases.[51] Wang *et al.* utilised Al_2O_3-coated conical nanochannels to detect single bovine serum albumin (BSA) directly.[52] Li *et al.* monitored the single-molecule signals of a variety of proteins, such as avidin, lysozyme, and IgG antibody, via a glass nanopore[53].

However, the fabrication of conventional solid-state nanopores is time-consuming, and the generated nanopores require careful optimisation. Therefore, a sub-class of the solid-state nanopore, namely nanopipettes, which can be achieved by a simple and low-cost fabrication process, attracts much attention.

1.2.2.1 Nanopipettes

Nanopipettes, which form a sub-class of solid-state nanopores, with most of their tip orifices ranging from around 10 nm to 100 nm, have found numerous applications in analytical chemistry, nanotechnology, and neurosciences. The ancestor of the nanopipette, the micropipette, was first used as an intracellular microelectrode in 1902.[54] After that, glass micropipettes were widely used in biology and analytical chemistry, especially in cell physiology. A famous experiment, as I described previously, was carried out by Neher and Sakmann, who performed the patch-clamp experiment via a glass pipette in 1976.[25] With the growth in demand for miniature, sensitive, and portable biosensors, nanopipettes are attracting more attention because of their essential role bridging the macroworld and the nanoworld (**Figure 1.5**).

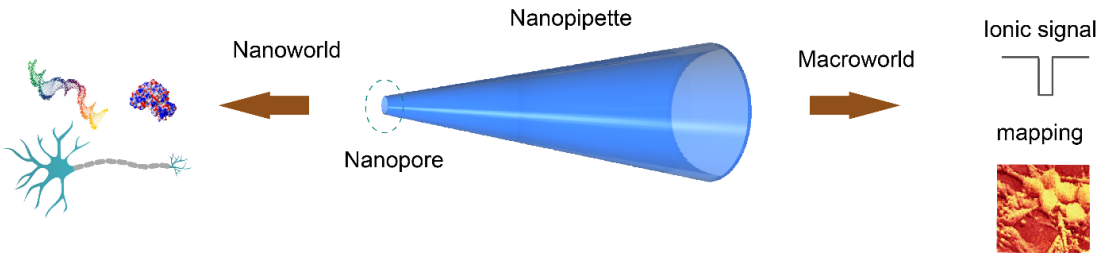


Figure 1. 5 Schematic of a nanopipette biosensor. The conically shaped nanopipette can be a bridge between the nanoworld and the macroworld, converting the invisible molecules to visualised information either by a single-molecule translocation signal or scanning ion conductance microscopy (SICM) images. Moreover, this unique shape can be utilised to deliver the analytes into cells.

To date, nanopipettes are widely used because of their unique advantages, such as low noise[55], high mechanical stability[56], multiplexed detection ability[57], and compatibility with other sensing techniques[58, 59]. Among these advantages, the most attractive one is the simple and low-cost fabrication process, which involves simply pulling a borosilicate or quartz capillary by a laser-based pipette puller. Additionally, the size and geometry of nanopipettes can be fine-tuned by adjusting the parameters of

the pulling protocol. The downside brought about by this quick fabrication process is that the pore sizes of the nanopipettes are always larger than 5 nm. These nanopores can, fortunately, be further tuned to a smaller size by the nanofabrication or functionalisation on the nanopipette[60, 61].

Given their unique features, nanopipettes have been used as single-molecule biosensors to detect a wide range of molecules, such as DNA[62, 63], proteins[53, 64], and other molecules[65, 66]. Moreover, because of their needle-like geometry and portable properties, nanopipettes are also utilised to image some soft samples in liquid, especially cells or tissues, by incorporating the nanopipettes into scanning electrochemical microscopy (SECM)[67, 68] or scanning ion conductance microscopy (SICM)[69, 70].

1.3 Sensing principles in solid-state nanopores

After the comparison of various nanopores, the journey toward single-molecule biosensing has just begun. In this section, the principle of this type of biosensing using a nanopore will be discussed. To study this, we first need to know how the open pore current is generated, how the electrical double layer interferes with the ionic channel, and which forces can drive the molecules.

1.3.1 Ionic current detection

1.3.1.1 Open-pore current

In a typical translocation experiment set-up, the electrolyte (typically KCl, NaCl, or LiCl) is filled in two reservoirs, which are separated by an insulating membrane. Two non-polarised electrodes (typically Ag/AgCl when the anion of the electrolyte salt is Cl^-), which provide a driving force for the ions and analytes, are placed on both sides of the membrane. The nanopore, is located on the membrane, providing a channel by which the ions and analytes can be transported from one reservoir to the other. With a transmembrane electrical potential applied, a steady current flow, which is known as an ‘open pore current’, is generated through the nanochannel. In the nanopore sensing experiment, this current flow is always recorded along with time, usually referred to as ‘current-time translocation traces’.

In detail, this steady current flow is provided by the ions transported through the nanopore. Taking the most commonly used electrolyte, KCl, as an example, free anions (Cl^-) and cations (K^+) are in the solutions. If a potential is applied, then a constant redox

reaction occurs on each Ag/AgCl electrode: On the cathode, the given electrons can aid in the reductions of the AgCl to Ag, as indicated in **Equation 1.1**. On the other side, the Ag on the positively charged anode is oxidised to AgCl, as seen in **Equation 1.2**. The generated electrons are transported from the anode to the cathode via measurement electronics, while the Cl^- is transported from the cathode to the anode through the electrolyte. The different electrochemical potentials drive the K+ and Cl^- to the oppositely charged electrodes. Given their closely matched ion mobilities in aqueous solutions, K^+ and Cl^- move with the same speed and thus generate a steady current across the nanopore.

$$AgCl + e^- \rightarrow Ag + Cl^- \quad (\mathbf{1.1})$$

$$Ag + Cl^- \rightarrow AgCl + e^- \quad (\mathbf{1.2})$$

As is known, the electric field of a conventional symmetrical nanopore set-up is an 'hourglass' shape, where the geometry of the central constriction, nanopore, is closely related to the conductance. The open-pore conductance, G_0, for a cylindrical solid-state nanopore can be estimated by considering the combinations of the ions in bulk concentration and the cations shielding the negatively charged nanopore internal walls, as presented in **Equation 1.3**[71, 72]:

$$G_0 = \frac{\pi {d_{pore}}^2}{4L_{pore}}((\mu_{K^+} + \mu_{Cl^-})c_{KCl}F + \frac{4\sigma}{d_{pore}}\mu_{K^+}) \quad (\mathbf{1.3})$$

where μ_{K^+} and μ_{Cl^-} denote the electrophoretic (EP) mobility of the cations and anions, c_{KCl} is the electrolyte concentration filling in the lumen of the nanopore, d_{pore} and L_{pore} represent the diameter and the length of the nanopore respectively, σ is the surface charge density of the nanopore, and F is the Faraday constant.

However, the **Equation 1.3** can only be used for calculating the conductance in symmetrical solid-state nanopores rather than asymmetrical nanopores, such as the conical nanopores on nanopipettes. Similar with the current through the symmetrical nanopore, the total current through a conical nanopore is still a composition of the bulk concentration of the ions and the counter ions which shield the surface charge of the nanopore. Herein, the adjusted conductance for the conical nanopore can be estimated by **Equation 1.4**[73]:

$$G_0 = \frac{\pi {d_{pore}}^* {D_{base}}^*}{4({L_{pore}}^* + \pi/8({d_{pore}}^* + {D_{base}}^*))}((\mu_{K^+} + \mu_{Cl^-})c_{KCl}F + \frac{4\sigma}{{d_{pore}}^*}\mu_{K^+}) \quad (\mathbf{1.4})$$

Where ${d_{pore}}^*$, ${D_{base}}^*$ and ${L_{pore}}^*$ represent the inner diameter of the conical nanopore, the inner diameter at the base and the length between the pore and the base.

1.3.1.2 Blockade current change

Unlike the transport of ions contributing to a steady current flow, the translocation of analytes results in a current transient change – either an enhancement or a depletion. **Figure 1.6a** illustrates this translocation process and the corresponding transient signal. To depict how the analyte passes through the nanopore, two parameters of this translocation signal are essential. The first one is the dwell time, or translocation duration, which represents the time that the molecule spends in the nanopore. The other parameter is the peak current, or amplitude, which represents the extent to which the conductance of the nanopore is changed by the analyte.

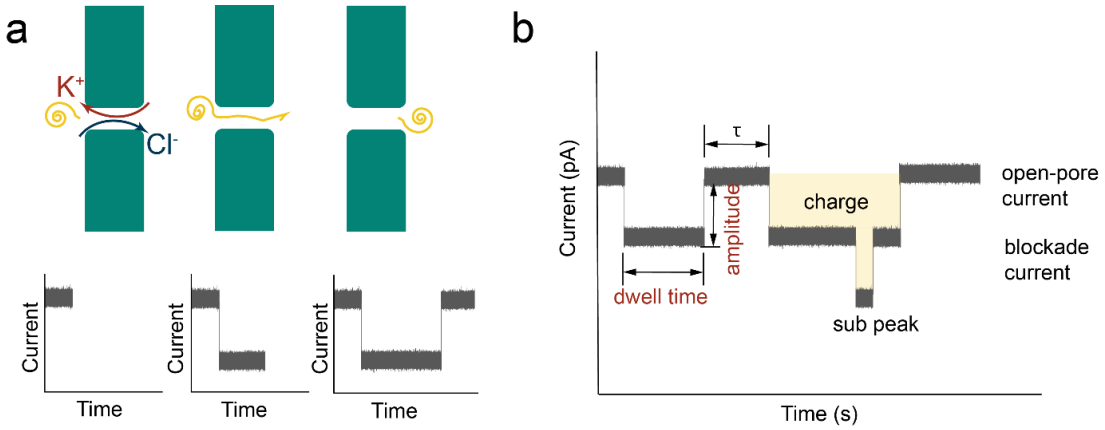


Figure 1. 6 Schematic of a translocation experiment and the parameters of the signals. **(a)** The steady-state current is decreased (or increased) when a molecule blocks the nanopore. **(b)** The translocation can be characterised by the following parameters: dwell time, current amplitude, integral area, sub-peak location, the time between translocation events, and capture rate.

These two parameters can be used to determine the physical properties of the analytes, including size and charge[74]. Apart from the dwell time and peak current, other parameters are also important in specific cases, as presented in **Figure 1.6b**. The time between two translocation events (τ) and the capture rate (or event frequency) can be used to study the concentration of the analytes and molecule dynamics under the electrophoretic or electroosmotic forces[62]. The integral area gives the equivalent charges of the analytes[74]. Sub-peak identification is mainly used to study complex structures, such as protein-bounded DNA molecules[64].

1.3.2 Surface charges in nanopores

Although the majority of the movements of analytes are current-induced, local electrostatics also contributes, especially when the analytes are close to the charged surface of the nanopore[75]. As with other solid-state surfaces, the inner wall of the nanopore carries some charges when immersed in a polar solvent. These surface

charges may be attributed to the protonation of surface groups or the ionisation of functional groups at the surface. Then, the free ions in the electrolyte carrying opposite charges will be electrostatically absorbed onto the charged solid-state surface, resulting in an electrical double-layer system.

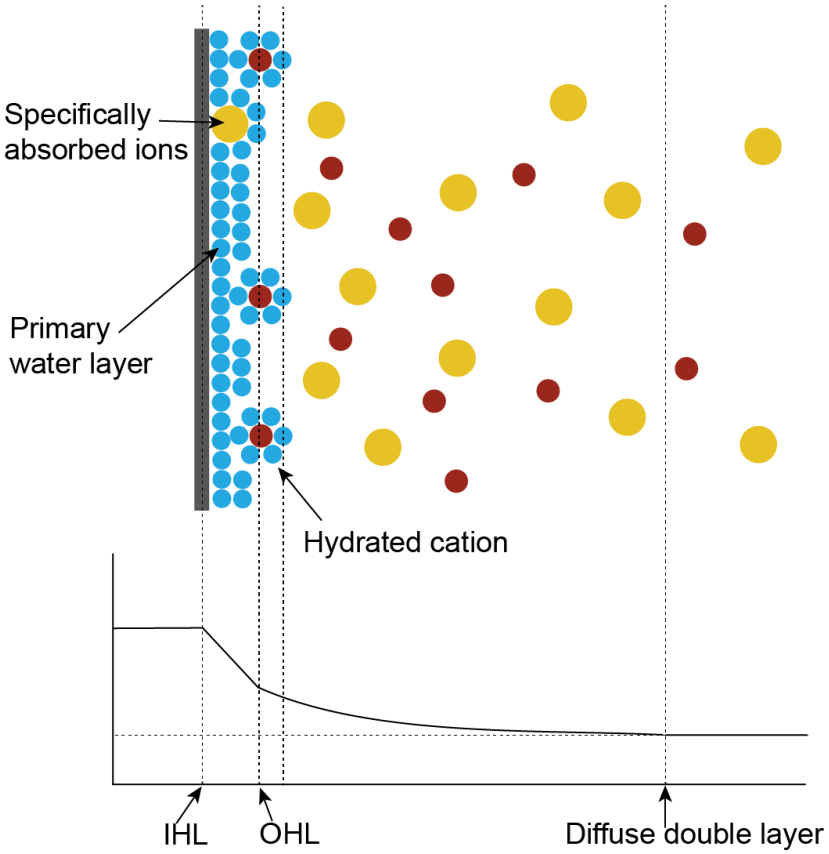


Figure 1. 7 Schematic of the distribution of ions around the surface/solution interface monitored by the Gouy-Chapman-Stern model.

At the surface/electrolyte interfaces, the electrical double layer forms and can be described by a Gouy-Chapman-Stern model[76], which is a combination of the Helmholtz model and the Gouy-Chapman model. The Helmholtz model, which was established in 1853[77], described the charge separations at the interface of the surface/solution, while the Gouy-Chapman model introduced a diffuse layer in this system in 1913[78]. The Gouy-Chapman-Stern model combines two previous models by adapting the compact layer and the diffuse layer together, as illustrated by **Figure 1.7**. The innermost layer, as the well-known inner Helmholtz layer (IHL) or Stern layer, is formed by immobilised solvent molecules and ions, which are absorbed specifically on the solid-state surfaces. The outer layer, which is the outer Helmholtz layer (OHL) or diffuse layer, is formed by solvated ions, which are mobile because of the non-specific absorption and long-range electrostatic interactions between the ions and the charged surface. Given the thermal motion in the electrolyte, these solvated ions can spread to

the diffuse double-layer region, whose length is approximately equal to the Debye length (λ_D), which can be calculated from **Equation 1.5**[79, 80]:

$$\lambda_D = \sqrt{\frac{\varepsilon_0 \varepsilon_r k_B T}{2en^2}} \qquad (\mathbf{1.5})$$

where n is the electrolyte concentration, e is the electronic charge, ε_0 is the permittivity of free space, T is the temperature in Kelvin, and ε_r and k_B are the relative dielectric constant and the Boltzmann constant respectively.

Although the Gouy-Chapman-Stern model is capable of illustrating the ions and charge distributions around a surface/solution interface, it is limited in several ways; for example, the model can only be used in low ionic strength environments. The limitations are a result of the simplified assumptions on which the model builds, such as point ions, homogeneously charged surfaces, and a continuum solvent.[81]

The surface charges of the majority of solid-state nanopores – either conventional Si_3N_4 nanopores or glass/quartz nanopipettes – are negative when immersed in a polar solution, such as KCl, NaCl, or LiCl.[82] This is mainly because of the dissociation of terminal silanol groups of the silica and silicate surfaces, which can be explained by **Equation 1.6**[83]:

$$S_s - OH + H_2O \rightarrow S_s - O^- + H_3O^- \qquad (\mathbf{1.6})$$

where S_s represents the silicon surface, which is a neutral oxide that can dissociate or protonate.

Furthermore, the electrostatic interactions between the cations and the negatively charged nanopore inner walls contribute to the formation of the electrical double layer. The mobilised diffuse layer is the origin of the electroosmotic flow (EOF), which is an important driving force or resistance in the nanopore sensing experiment, as I will discuss later in this chapter. Interestingly, the surface charges of some nanopores (i.e. nanopipettes and conical-shaped Si_3N_4 nanopores) result in an asymmetrical current-voltage curve, which implies that the ionic current is undergoing rectification.

1.3.3 Current rectification of the nanopore

Ionic current rectification (ICR) is a phenomenon observed in many nano-scaled channels, characterised by the non-linear relationship of the I-V dependence, as illustrated in **Figure 1.8b**. In this thesis, ICR was calculated by **Equation 1.7**:

$$ICR = \left| \frac{I^+_{(V=+v)}}{I^-_{(V=-v)}} \right| \qquad (\mathbf{1.7})$$

where I^+ is the current at a given positive voltage, and I^- is the current at a negative voltage, which is the same value as the positive one.

To date, many efforts have been made to explain the ICR phenomenon. Among them, the most widely accepted opinion is that the ions are selectively transported through an asymmetrically shaped nanochannel if the thickness of the diffused layer is comparable with the diameter of the pore open. For example, when a positive potential is applied inside the nanopipette, some cations will be trapped on the negatively charged surface by the electrostatic force, whereas the cations can pass through freely when a negative potential is applied, which is described by the Ratchet model[84, 85]. Therefore, the decay of the positive current results in the non-linear I-V characteristics.

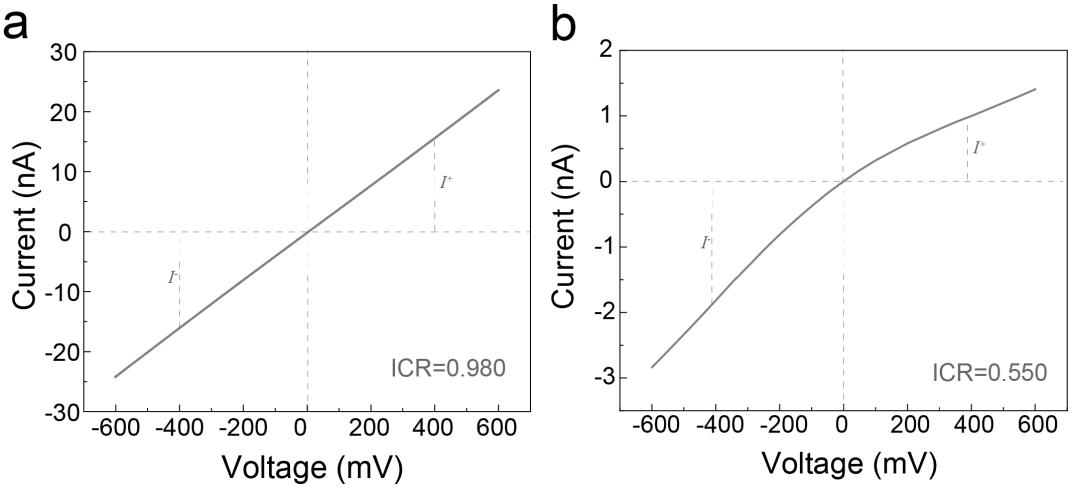


Figure 1. 8 The ionic current rectification of nanopipettes with different pore sizes. The I-V curve of **(a)** a nanopipette with a 100 nm nanopore and **(b)** a nanopipette with a 15 nm nanopore in 100 mM of KCl.

Although the mechanism of ICR is still inconclusive, many factors have demonstrated the ability to affect the extent of the rectification. These factors include size, geometry, and the surface charge of the nanopore. In addition, the pH and concentration of the electrolyte also play key roles in affecting ICR. Since ICR only occurs when the thickness of the electrical double layer is comparable with the nanopore dimensions, this rectification is most sensitive to the diameter of the nanopore. **Figure 1.8a** depicts the linear I-V characteristics of an approximately 100 nm nanopore, and **Figure 1.8b** pictures the current negatively rectified through an approximately 15 nm nanopore. In addition, as described previously, the Debye length (the thickness of the diffused layer) is inversely proportional to the ionic strength, resulting in a strong ICR in low concentration and no ICR effect in a highly concentrated salt solution.[86] Another way in which to change the ICR, and to even obtain a complete reversal, is to functionalise the surface of the nanopore, which will be described in **Chapter 3**.

1.3.4 Electrophoretic and electroosmotic flow

In the translocation experiment, many forces, mainly including electrophoresis, electro-osmosis, and the diffusion effect, contend with one another to lead the analytes to pass through the nanopore.[87] The charged analytes are intrinsically driven by the EP force to the biased electrode with opposite polarity. The EP force is closely related to the charge of the molecule, where the velocity v_{EP} can be described using a Helmholtz–Smoluchowski equation:[87]

$$v_{EP} = \frac{\varepsilon_0 \varepsilon_r}{\eta} \xi_{molecule} E \qquad (\mathbf{1.8})$$

where ε_0 and ε_r are the electrical permittivity of a vacuum and the relative dielectric constant respectively. Moreover, E represents the external electrical field, and η is the viscosity of the electrolyte. Finally, $\zeta_{molecule}$ is the zeta potential of the target molecule.

However, when the molecules are close to the charged nanopore surface, the motion of the double electrical layer begins to interfere with the movement of the analytes by EOF. This phenomenon occurs when the diffuse layer is parallel to the electrical field.[88, 89] The electro-osmotic velocity v_{EOF} can be described by **Equation 1.9**[90]:

$$v_{EOF} = -\frac{\varepsilon_0 \varepsilon_r}{\eta} \xi_{nanopore} E \qquad (\mathbf{1.9})$$

where the $\zeta_{nanopore}$ is the zeta potential of the nanopore inner wall.

Electroosmosis is a force that cannot be ignored, as it can enhance, counteract, or reverse the electrophoresis, especially when the target molecule is moderately charged, such as with proteins. Combining **Equation 1.8** and **Equation 1.9**, the effective velocity of molecule transport under these two forces can be calculated[87]:

$$v = v_{EP} + v_{EOF} = \frac{\varepsilon_0 \varepsilon_r}{\eta} \left(\xi_{molecule} - \xi_{nanopore}\right) E \qquad (\mathbf{1.10})$$

Figure 1.9 presents an example of the translocation of avidin through a Si_3N_4 nanopore, of which the surface charge can be tuned by different pHs.[87] At pH 2, even slightly weakened by EOF, the EP flow still dominated. At pH 4, where $\zeta_{molecule}$ approximately equals to $\zeta_{nanopore}$, the EOF counterbalanced the EP flow. Therefore, the protein translocation was mainly caused by diffusion in this environment. At pH of 6 and 8, the high throughput was because of electrophoresis enhanced by electro-osmosis. At pH 10, the basic environment led to deprotonation of the amino group on the protein, thereby reversing the surface charge of the avidin. The EOF dominated and drove the weakly charged protein to pass through the nanopore.

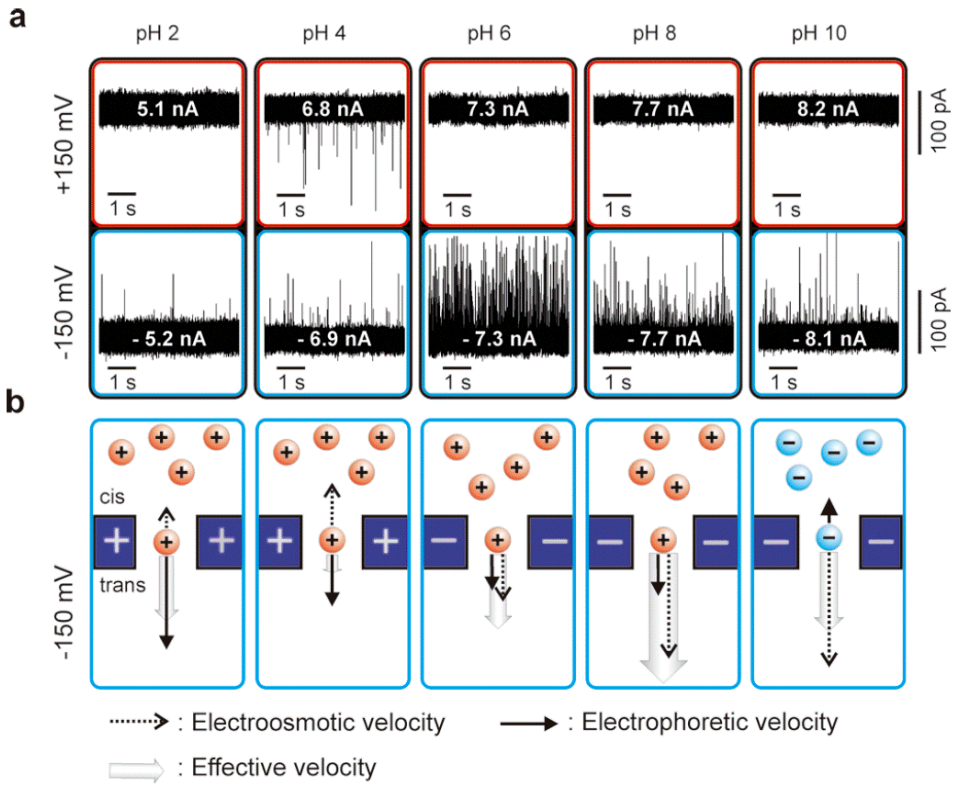


Figure 1. 9 The translocation of avidin under different driving forces. **(a)**The current-time traces and **(b)** a schematic of the electrophoresis and electro-osmosis of the avidin translocation through a Si_3N_4 nanopore under different pHs. The arrow length is scaled by the corresponding zeta potential. Figures adapted from reference 87.

1.3.5 Conductance modulation by charged molecules

The nature of nanopore detection is based on the nanopore conductance change when charged analytes are passing through. Interestingly, for different molecules under various conditions (e.g. electrolyte concentration and nanopore size), the translocation signals sometimes demonstrated that the current was blocked, while others represented an increase in the channel conductance. These are the results of two competing effects: When the molecule occupies the nanochannel, the original ions would be squeezed out, leading to a conductance drop (G_{block}); meanwhile, the ions attached to the charged analyte by electrostatic interactions contribute to a conductance enhancement (G_{charge}). Taking both effects into account, the nanopore conductance changed by a charged analyte can be expressed as follows:[71, 91]

$$\Delta G = -G_{block} + G_{charge} \qquad (\mathbf{1.11})$$

In a conventional nanopore set-up with a KCl electrolyte, if the molecule is cylindrical, then the conductance change can be further calculated by **Equation 1.12**[71, 72]:

$$\Delta G = -(\mu_{K^+} + \mu_{Cl^-})c_{KCl}F\frac{\pi {d_{analyte}}^2}{4L_{pore}} + \frac{\lambda_q}{L_{pore}}\mu_{K^+(Cl^-)} \qquad (\mathbf{1.12})$$

where μ_{K+} and μ_{Cl-} represent the EP mobility of the cations and anions respectively, c_{KCl} is the electrolyte concentration, $d_{analyte}$ is the molecule diameter, L_{pore} is the nanopore length, λ_q is the effective charge per unit length of the counterions (either K+ or Cl-) screening the nanorod wall, and F represents the Faraday constant.

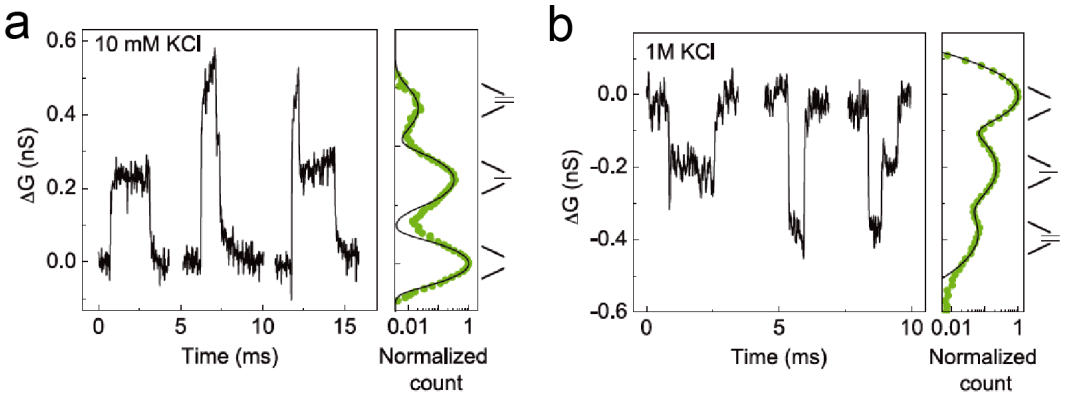


Figure 1. 10 The translocation signal of lambda DNA in different salt concentrations. Three individual translocation events of lambda DNA through a nanopore on nanopipette at KCl concentrations of **(a)** 150 mM and **(b)** 500 mM. Figures adapted from reference 73.

From the equation, it is evident that the concentration of electrolytes plays a crucial role in nanopore conductance modulation. Keyser group observed current enhancement signals when translocating lambda DNA in 10 mM of KCl through a quartz nanopipette (**Figure 1.10a**). In contrast, current blockades were revealed when the KCl concentration was increased to 1 M (**Figure 1.10b**).[73] Smeets *et al.* observed similar trend on silicon nitride nanopore .They also found that the translocation and calculation results illustrate that approximately 370 mM of KCl was the critical concentration between the enhancement and blockage.[71] Other conditions, such as nanopore size and geometry, can also affect the direction of the current transient. From the equation, it seems that the nanopore dimensions are irrelevant to the ΔG. However, the electrical double layer of the nanopore inner wall could interfere with the ion distribution on the charged molecules when the molecules pass through a narrow nanochannel. Zanjani *et al.* found that the translocation of gold nanorod through a relatively large nanopore and a narrow nanopore exported reverse transient signals.[72] In this case, when the positively charged nanorod close to the negatively charged wall, the surface charge of the molecule was shielded entirely, which was equivalent to increasing the G_{charge}.

1.4 Using solid-state nanopores to sense biomolecules and their limitations

1.4.1 Single-molecule biosensing by solid-state nanopores

Since the first demonstration of dsDNA translocation through a silicon nitride membrane[47], solid-state nanopores were shown to be powerful analytical tools for single-molecule biosensing. To date, nanopore analytics has been utilised to sense a wide range of analytes at the single-molecule level.

1.4.1.1 Applications in the detection of nucleic acids

DNA molecules, the essential biological polyelectrolytes, have been studied using nanopores at the single-molecule level for decades. During the last twenty years, several solid-state nanopores have been fabricated and demonstrated to sense DNA molecules; for example silicon-based nanopores[92-94], graphene nanopores[50, 95], and nanopipettes[62, 63, 74]. However, due to the strongly charged biopolymer chain and poor interaction between the DNA and the negatively charged nanopore, the fast translocation speed, resulting in limited translocation event information (from several μs to approximately 1 ms), has become the bottleneck in nanopore sensing.[94, 96] Moreover, the sensing of short DNA fragments, as well as micro RNA molecules, is significantly challenged by their ultra-fast transient times.

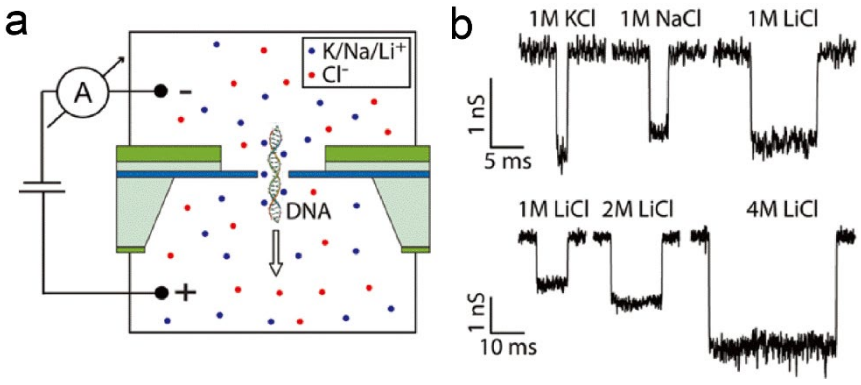


Figure 1. 11 A comparison of translocation signals with different salts and concentrations. **(a)** Schematic of DNA detection using a nanopore device. **(b)** The example of a translocation experiment of lambda DNA in different salts and concentrations. Figures adapted from reference 97.

The Dekker group reported a solution to slow down DNA translocation by using different salts and ionic strengths, as illustrated in **Figure 1.11**.[97] The dwell time of 48.5 kbp dsDNA was elongated 4.8 times when the KCl was replaced by LiCl, where the Li^+ bound to the DNA more tightly than K^+. As a result, the charge of the biopolymer

was neutralised more by the counterions in LiCl, resulting in a decrease in EP force. Another efficient method to slow down DNA translocation was implemented by a nanofluidic field-effect transistor (FET), reported by Liu *et al.* – see **Figure 1.12**.[98] By applying a positive voltage to the gate, the surface charge of the nanopore was successfully reversed to positive, leading an attracted electrostatic interaction between the nanopore and DNA molecules.

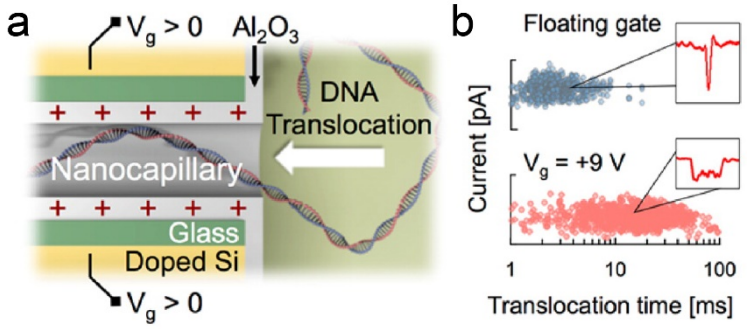


Figure 1. 12 Slowing down DNA translocation by a nanofluidic field-effect transistor. **(a)** Side-view of the nanofluidic field-effect transistor. By controlling the gate voltage, the surface charge of the nanopore, which is a layer of Al_2O_3, can be manipulated. **(b)** Scatter plot of lambda DNA translocation in 1 M of KCl under a 1-V bias voltage. The sharp spikes indicate a fast translocation without a gate voltage, where the long events illustrate that the DNA molecules were significantly slowed down with 9 V being applied to the gate. Figures adapted from reference 98.

Small DNA fragment signals were also recently reached by multiple methods. Fraccari *et al.* reported that 100-bp dsDNA molecules were successfully detected by using a wide-bandwidth CMOS amplifier with a high filter and sampling rate and low noise.[99] In another work, Sulaiman and co-worker observed clear and long 100-bp dsDNA single-molecule events by using a hydrogel-filled nanopipette, which can slow down the translocation of analytes 10,000 times by the multiple layers of grid structures, as illustrated in **Figure 1.13**.[100]

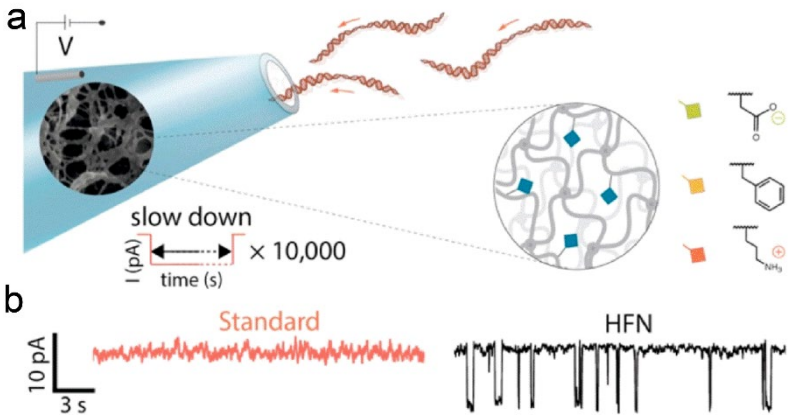


Figure 1. 13 Sensing 10-bp dsDNA by a hydrogel-filled nanopipette. **(a)** Schematic of sensing 100-bp dsDNA molecules by a hydrogel-filled nanopipette. **(b)** A comparison between the translocation

recordings of sensing 100-bp dsDNA using **(i)** a plain nanopipette and **(ii)** a hydrogel-filled nanopipette. Figures adapted from reference 100.

In addition, a number of studies regarding DNA translocation dynamics emerged, revealing the velocity of each step when the long biopolymers pass through the nanopore.[49, 101] Moreover, the detection of single nucleic acids could be realised by incorporating the tunnelling junction into solid-state nanopores,[102, 103], which makes these nanopores a promising DNA sequencing platform.

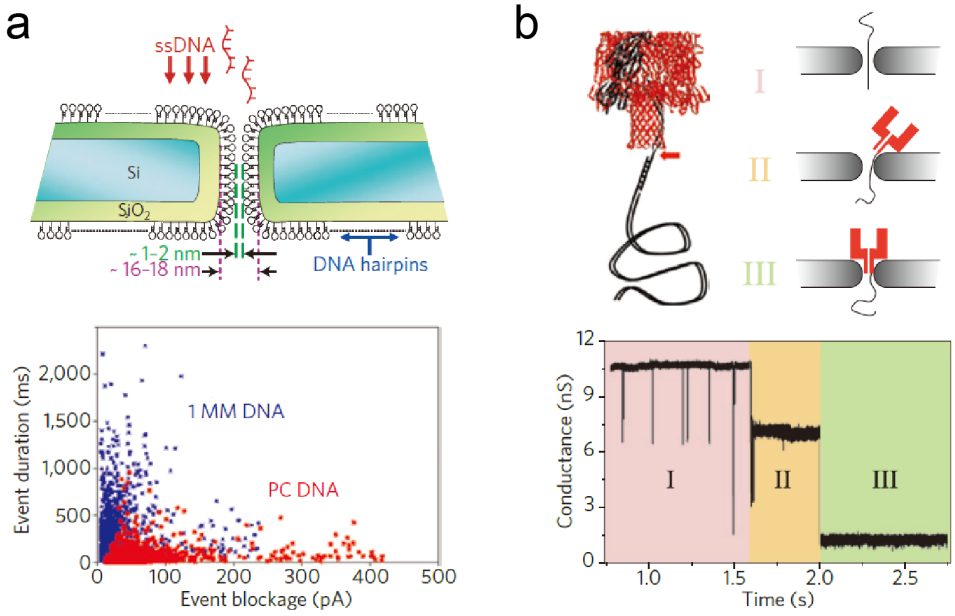


Figure 1. 14 Sensing ssDNA by biological-solid-state nanopores. **(a)** a DNA hairpin functionalized SiO_2 nanopore, which is capable of distinguishing between ssDNA which is perfectly complementary (PC DNA) to the hairpin sequence and the ssDNA which has one base mismatch (1 MM DNA) with the hairpin. **(b)** an α-haemolysin inserted solid-state nanopore. The protein pore was led by the dsDNA tail which passed through the solid-state nanopore by electrophoresis and sit on the solid-state nanopore. Figures adapted from reference 105.

More valuable design of functionalized solid-state nanopore emerged to sense the nucleic tides efficiently. Bashir group reported a DNA hairpin functionalized SiO_2 nanopore which can discriminate perfectly matched ssDNA and the nucilic acids with one base mismatch, demonstrating the potential of this technique to detect single-nucleotide polymorphism (SNP), see **Figure 1.14a**.[104, 105] Alternatively, a biological nanopore, which has higher resolution compare with conventional solid-state nanopore, has been engineered on a SiN_x solid state nanopore, resulting successful ssDNA translocation detection, shown in **Figure 1.14b**.[105, 106]

1.4.1.2 Applications in the detection of proteins

Other appealing, but also troublesome targets are protein molecules, which are essential biomolecules of living organisms. Studying these molecules at the single-molecule level is crucial because of their key role in early diagnosis. However, compared with the nanopore sensing of DNA, the nanopore sensing of proteins becomes significantly challenging because of their small size, heterogeneous charge, fast translocation, and low signal-to-noise ratio.

According to the simulation,[107, 108] to detect small protein molecules (< 100 kDa) by using a conventional nanopore (> 10 nm) set-up incorporating an amplifier (10-kHz bandwidth), only approximately 0.1% slowest events can be detected. Catching the protein directly using nanopores can be achieved by either increasing the protein concentration or using high-bandwidth instruments. Steinbock et al. successfully detected a wide range of highly concentrated proteins by using a glass nanopore.[109] In this experiment, the different sizes of proteins, from 12-kDa ComEA to 480-kDa RNAp, were reflected by the current amplitude, as depicted in **Figure 1.15**. The fast translocation of protein can be also recorded by high-bandwidth amplifier. Wanunu group successfully detected sub-30 kDa proteins by using ultrathin HfO_2 nanopores incorporating with a high bandwidth amplifier.[110] Alternatively, Li *et al.* performed translocation experiments for a wide range of proteins, including lysozyme (14 kDa), avidin (66 kDa), bovine β-lactoglobulin (18 kDa), ovalbumin (42 kDa), BSA (66 kDa), rabbit immunoglobulin G (IgG) (150 kDa), and β-galactosidase (465 kDa), by utilising a high-bandwidth amplifier.[53]

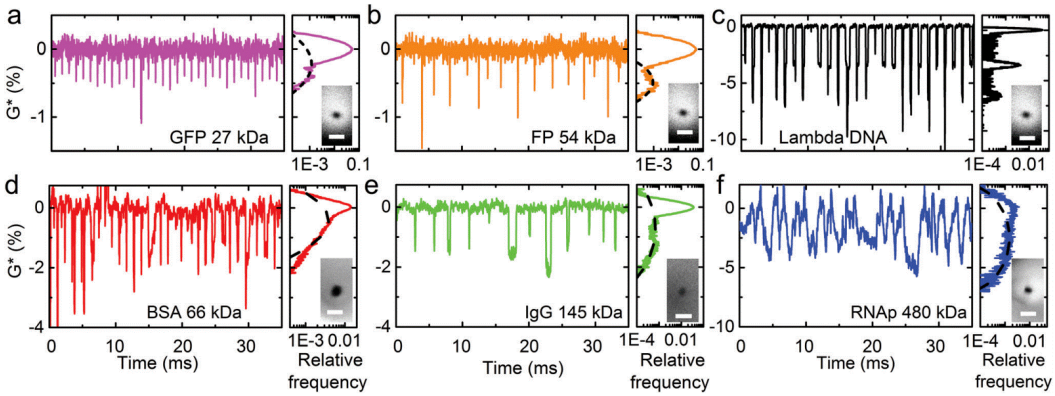


Figure 1. 15 The selection of current-time traces of the translocation of different analytes. **(a)** The translocation of 37 uM of GFP through a 14 nm nanopore. **(b)** The translocation of 9 uM of FP through a 14 nm nanopore. **(c)** The positive control, which is lambda DNA translocating through a 14 nm nanopore. **(d)** The translocation of 0.6 uM of BSA through a 21 nm nanopore. **(e)** The translocation of 0.6 uM of IgG through a 16 nm nanopore. **(f)** The translocation of 0.6 uM of RNAp 480 through a 13 nm nanopore. All translocation experiments were performed in 1 M of KCl under a bias of 0.5 V. Figures adapted from reference 109.

Recently, solid-state nanopores are also utilised to study the rotation of the proteins. Long group screen the orientation change of the glucose oxidase by using amino group functionalized Au nanopore. When the interactions between the carboxyl group on glucose oxidase and the amino group on Au nanopore were activated by the common protein cross-linkers, N-(3-(dimethylamino)propyl)-N′-ethylcarbodimide (EDC)/N-hydroxysuccinimide (NHS), a long translocation of glucose oxidase and its rotation can be observed, **Figure 1.16a**.[111] Houghtaling *et al.* demonstrates that low-noise silicon nitride nanopores in combination with high-bandwidth current recordings can detect the molecular volume, approximate shape, and event dipole moment of single native proteins.[112]

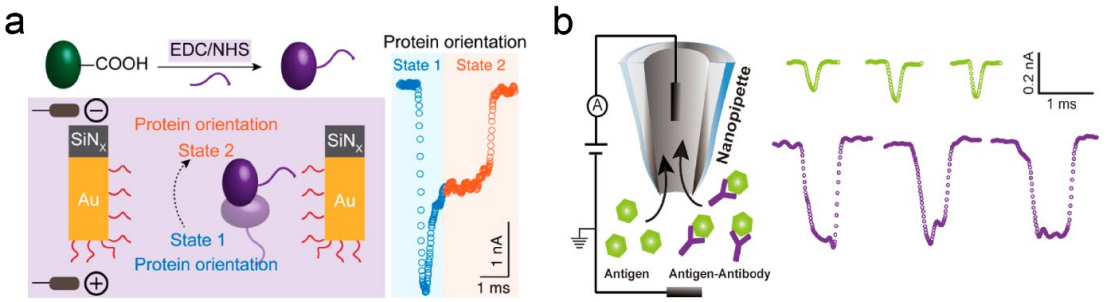


Figure 1. 16 Sensing protein, orientation of protein and the interactions between proteins using solid state nanopores. **(a)** The current blockages show different orientation of the glucose oxidase: The deep current blockage demonstrates that the protein passes through the pore horizontally; the relative smaller blockage represents the protein translocate vertically. Figure **(a)** adapted from reference 111; Figure **(b)** adapted from reference 113.

Impressively, the immunoreaction between single Alpha-fetoprotein (AFP) and its specific antibody without any labelling has been monitored by Long group, **Figure 1.16b**.[113] The translocation signal of antigen itself and antigen-antibody complex were screened respectively, demonstrating the potential of this approach to study single protein and protein-protein interactions.

1.4.1.3 Sensing analytes selectively

Although the direct detection of single nucleic acids or protein signals has been achieved, nanopore biosensing is still limited by a lack of selectivity. The principle of nanopore sensing limits itself: if there are two molecules of similar sizes and charges, then the generated current transient signal would be similar. Among millions of biomolecules, many of them translocate through a nanopore with an indistinguishable current change, which is an unacceptable defect for an analytical biosensor.

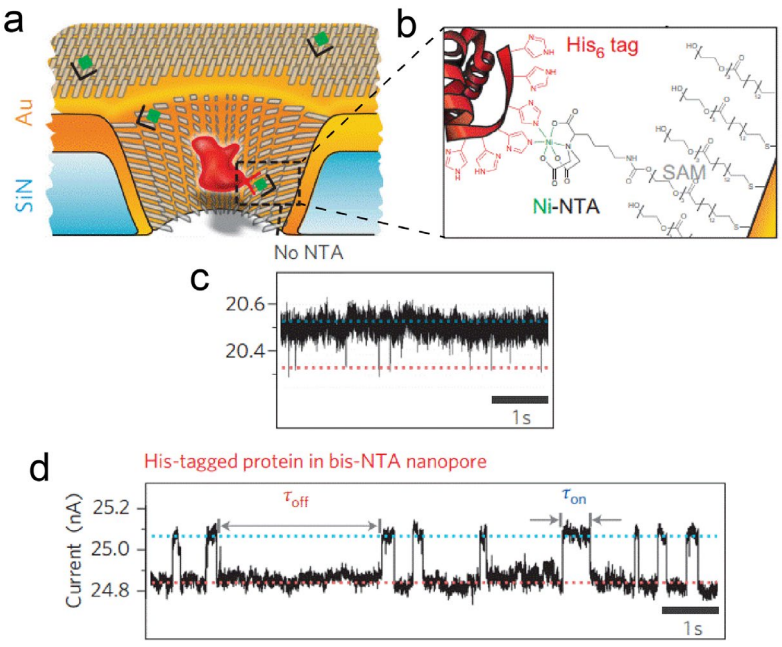


Figure 1. 17 Selective translocation of His-tagged protein through a bis-NTA nanopore. **(a)** Schematic of the translocation process of His-tagged protein (red) through an NTA (green binding sites) functionalised Au-coated nanopore. **(b)** The protein can be slowed down by the interactions between the ligands on the protein and the NTA on the inner wall of the nanopore. **(c)** Sharp spikes illustrate that the bare nanopore has no selectivity to sense proteins. **(d)** The long-lasting translocation events illustrate the specific binding of the target proteins. Figures adapted from reference 114.

One way in which to improve selectivity is to engineer a nanopore with receptors, which can bind to the target molecules specifically. Wei et al. observed protein translocation with a long dwell time by using a receptor-bound silicon nitride nanopore, **Figure 1.17**.[114] When the His-tagged proteins passed through the bis-NTA modified nanopore, the movement of the analytes could be slowed down significantly as a result of the interactions between the binding sites and the analytes (ligands).

Alternatively, the molecular carrier also contributes to lab-free selective single-molecule biosensing. This approach involves employing artificial, engineered structures as carriers to identify and deliver the targets selectively by force between the carrier binding sites and the target molecules, such as antibody-antigen or protein-aptamer interactions. Sze et al. reported that a lambda DNA-based molecular carrier, including three aptamer overhangs (two on each end, and one in the middle), was capable of sensing up to three proteins specifically and simultaneously in the serum, **Figure 1.18**.[64] Similar to this approach, Kong et al. designed a two-step assay by using a complex DNA structure encoded with aptamers to detect multiple targets specifically.[115]

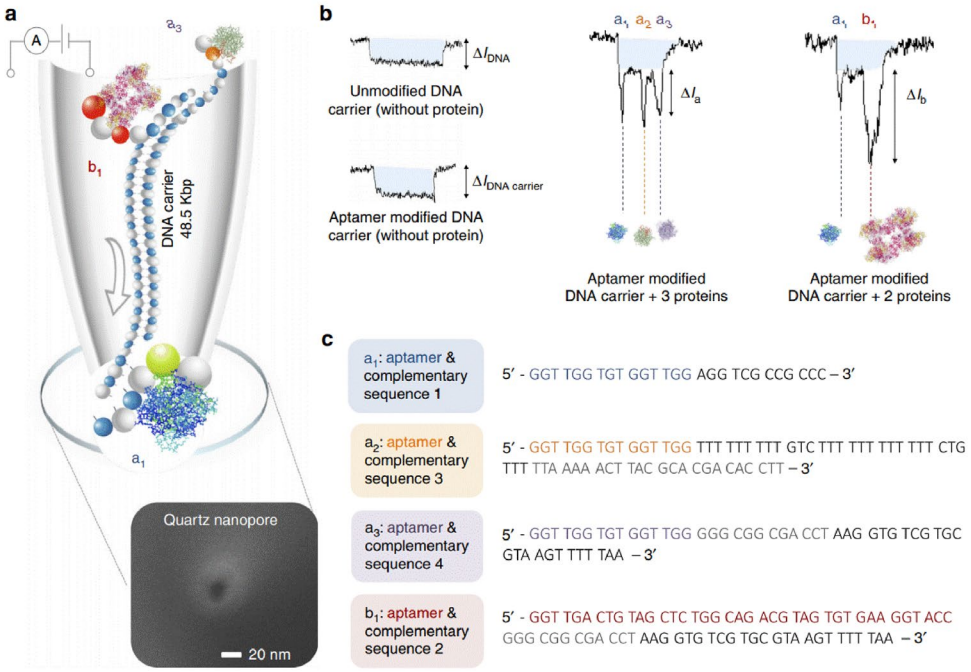


Figure 1. 18 Schematic of protein-selective sensing by a lambda DNA protein carrier. **(a)** Schematic of the protein-DNA complex. **(b)** The translocation signatures of the DNA carrier itself and the carrier bound two or three proteins. **(c)** The sequence of each aptamer binding site. Figures adapted from reference 64.

1.4.2 The challenges of nanopore-based sensing techniques

Researchers have long been aware of the sensitivity and selectivity issues regarding nanopore biosensing, and they have designed a series of valuable methods to address the limitations, as described previously. However, the challenges of nanopore sensing still exist.

The fast transient of analytes, either short DNA fragments or proteins, could be slowed down by a high ionic strength (above 1 M KCl).[53, 109, 116, 117] However, these highly concentrated salt solutions dramatically deviate from the intracellular ionic strength, which makes in vivo detection impossible. Moreover, under such a highly concentrated salt environment, properties, such as binding effects and the confirmation of biomolecules, especially proteins, become unstable and elusive.

Alternatively, high-bandwidth amplifiers were also used to record the fast translocation of the small molecules.[53, 110, 118] However, the signal and noise are unfortunately, always the double-edged swords of ion-based detection. With a higher sampling rate and a higher low-pass filter, the fast transient may be recorded or may be submerged in the increased noise level. Therefore, the use of high-bandwidth instruments acts as a secondary method.

Another approach is to use an extremely high concentration of biomolecules to increase throughput.[53, 109, 119] As described in the previous section, to observe the translocation of small proteins, the concentration of analytes must be over 10–100 s nM, which was predicted by the Smoluchowski rate equation.[107] Therefore, many studies of nanopore protein detection were conducted in highly concentrated protein solutions, including the examples presented before. However, this seemingly effective approach betrays the aims of nanopore single-molecule sensing, which is expected to be a method of effective early diagnosis, requiring the ability to sense trace amounts of target biomarkers.

The functionalisation of nanopores seems to be a promising approach to increase sensitivity and selectivity.[98, 114, 120] However, many such methods only improve the translocation process one-sidedly. Some of them can only increase the translocation duration, while others can only increase the capture rate. These designs are undeniably valuable; however, they are still far from achieving a comprehensive biosensor. Moreover, the complicated fabrication process and the requirement of careful optimisation challenge these approaches.

As with any other scientific techniques, molecular carrier methods[64, 115, 121] are also challenging because of their defects. In this case, the worst enemy is the molecule carrier itself, as it can generate false-positive signals. For DNA-protein complex detection, the sub-peaks indicate the presence of the target protein. However, the soft biopolymers, especially if their length is above 10 kbp, can be screened to similar signatures when they are partially folding. Therefore, detecting the biomolecules using label-free solid-state nanopores, with high sensitivity and selectivity, remains a challenge.

Herein, an urgent need exists to fabricate a comprehensive nanopore with a facile and effective functionalisation process. Alternatively, novel molecular carriers should be designed for accurate, generic, and label-free single-molecule detection.

1.5 Objective and thesis overview

This thesis aims to explore multiple approaches to improve the sensitivity and selectivity of nanopore analytics, and thus increase the practicality of nanopore single-molecule biosensing towards early-stage diagnosis. These approaches include developing novel nanopore-extended devices (**Chapter 3, Chapter 4**) and novel single-molecule biosensing strategies (**Chapter 5, Chapter 6**).

Chapter 2 describes the primary materials, instruments, and methods across this thesis, including the fabrication of nanopipettes, the microscopy characterisation and electrochemistry characterisation of nanopipettes, the set-up of the single-molecule translocation experiments, and the data analysis.

Chapter 3 presents a novel device, namely the nanopore extended FET (nexFET), which is a combination of a solid-state nanopore and a FET. Unlike conventional functionalised nanopores, this device is expected to be fabricated by a facile and low-cost approach with high repeatability. In this device, the polypyrrole (PPy) thin layer, which can easily be deposited on the nanopipette tip by electropolymerisation, acts as the gate and the nanopore sensing part. During the fabrication process, the nanopore size can be tuned precisely by real-time controlled electrodeposition. By applying the voltage to the conductance polymer, the surface charge of the nanopore and local electric field can be affected, thereby leading to a change in the ionic current.

In **Chapter 4**, using the fabricated nexFETs and their derivatives, we tackle the problems in nanopore biosensing. By controlling the gate voltage of the nexFET, the translocation signal of DNA through the PPy gated nanopore can be comprehensively improved; for example, a higher capture rate, a longer dwell time, and a larger signal-to-noise ratio can be achieved. As a result of the positively charged PPy nanopore inner wall, the nexFET is also able to screen the translocation of ultra-short nucleic acids (e.g. 18-base ssDNA). Furthermore, the selective sensing of specific proteins at a picomolar concentration is also achieved by receptor-embedded nexFETs, where the PPy layer is an ideal substrate to support binding sites to identify and slow down analytes selectively.

Chapter 5 presents the screening of the sub-structures of multiple gold nanoparticle (AuNP)-based molecular carriers. Unlike previous reports on the discrimination of different nanostructures by current amplitude, which may lead to a misreading, this study can identify the nanostructures by the sub-peaks of the translocation events, which are undoubtedly. To achieve this, the finely tuned nanopipette incorporating high-bandwidth instruments is utilised to provide a sufficient resolution for screening different nanostructures, including AuNP monomers, dimers, and trimers. In addition, the Surface-enhanced Raman scattering (SERS) enhancement effect between the two AuNPs is also studied at the single-molecule level.

In **Chapter 6**, we address the limitations of the molecule carrier in single-molecule biosensing by using the AuNP-based nanostructures. To detect a wide range of biomolecules, two strategies are designed. The first strategy – for transporting and identifying relatively larger single proteins (> 35 kDa) specifically – is implemented by a protein carrier, which is an AuNPs dumbbell system incorporating an aptamer located in the middle of the DNA linker. The second strategy – for detecting tiny antigen

molecules (< 15 kDa) – is achieved by a pair of monomer probes, including an AuNP with corresponding antibodies to a target antigen and the other AuNP with its complementary secondary antibody. Both strategies are fully flexible by simply changing the aptamer sequence or antibody to the target.

Chapter 7 summarises the conclusion of this thesis, and it illuminates the improved tools and strategies based on the previous work. More elaborate nanopore extended devices, which are protein aptamer embedded nexFETs, and more comprehensive molecule carriers, which are DNA origami based molecular carriers with multiple binding sites, have been designed.

1.6 References

1. Bartlett, J. M. S.; Stirling, D., A short history of the polymerase chain reaction. *Methods in molecular biology (Clifton, N.J.)* **2003,** *226*, 3-6.

2. Mullis, K. B.; Erlich, H. A.; Arnheim, N.; Horn, G. T.; Saiki, R. K.; Scharf, S. J., PROCESS FOR AMPLIFYING DETECTING AND-OR CLONING NUCLEIC ACID SEQUENCES US PATENT-4683195. JULY 28 1987. *Official Gazette of the United States Patent and Trademark Office Patents* **1987,** *1080* (4), 1960-1960.

3. Weiland, G., ENZYME-LINKED IMMUNOSORBENT ASSAY (ELISA) - NEW SERODIAGNOSTIC METHOD FOR DETECTION OF PARASITIC INFECTIONS. *Munchener Medizinische Wochenschrift* **1978,** *120* (44), 1457-&.

4. Ha, T., Single-molecule fluorescence methods for the study of nucleic acids. *Current Opinion in Structural Biology* **2001,** *11* (3), 287-292.

5. Marme, N.; Knemeyer, J.-P., Sensitive bioanalysis - combining single-molecule spectroscopy with mono-labeled self-quenching probes. *Analytical and Bioanalytical Chemistry* **2007,** *388* (5-6), 1075-1085.

6. Zhu, P. Z.; Clamme, J. P.; Deniz, A. A., Fluorescence quenching by TEMPO: A sub-30 angstrom single-molecule ruler. *Biophysical journal* **2005,** *89* (5), L37-L39.

7. Axelrod, D., Total internal reflection fluorescence microscopy in cell biology. *Biophotonics, Pt B* **2003,** *361*, 1-33.

8. Weiss, S., Fluorescence spectroscopy of single biomolecules. *Science* **1999,** *283* (5408), 1676-1683.

9. Weiss, S., Measuring conformational dynamics of biomolecules by single molecule fluorescence spectroscopy. *Nature Structural Biology* **2000,** *7* (9), 724-729.

10. Binnig, G.; Quate, C. F.; Gerber, C., ATOMIC FORCE MICROSCOPE. *Physical review letters* **1986,** *56* (9), 930-933.

11. Hinterdorfer, P.; Dufrene, Y. F., Detection and localization of single molecular recognition events using atomic force microscopy. *Nature Methods* **2006,** *3* (5), 347-

355.

12. Zlatanova, J.; Lindsay, S. M.; Leuba, S. H., Single molecule force spectroscopy in biology using the atomic force microscope. *Progress in Biophysics & Molecular Biology* **2000,** *74* (1-2), 37-61.

13. Visscher, K.; Block, S. M., Versatile optical traps with feedback control. *Molecular Motors and the Cytoskeleton, Pt B* **1998,** *298*, 460-489.

14. Leuba, S. H.; Bennink, M. L.; Zlatanova, J., Single-molecule analysis of chromatin. *Chromatin and Chromatin Remodeling Enzymes, Pt B* **2004,** *376*, 73-105.

15. Charvin, G.; Strick, T. R.; Bensimon, D.; Croquette, V., Tracking topoisomerase activity at the single-molecule level. *Annual Review of Biophysics and Biomolecular Structure* **2005,** *34*, 201-219.

16. Zlatanova, J.; McAllister, W. T.; Borukhov, S.; Leuba, S. H., Single-molecule approaches reveal the idiosyncrasies of RNA polymerases. *Structure* **2006,** *14* (6), 953-966.

17. Wanunu, M., Nanopores: A journey towards DNA sequencing. *Physics of life reviews* **2012,** *9* (2), 125-58.

18. Meller, A.; Nivon, L.; Branton, D., Voltage-Driven DNA Translocations through a Nanopore. *Physical review letters* **2001,** *86* (15), 3435-3438.

19. Miles, B. N.; Ivanov, A. P.; Wilson, K. A.; Dogan, F.; Japrung, D.; Edel, J. B., Single molecule sensing with solid-state nanopores: novel materials, methods, and applications. *Chemical Society reviews* **2013,** *42* (1), 15-28.

20. Branton, D.; Deamer, D. W.; Marziali, A.; Bayley, H.; Benner, S. A.; Butler, T.; Di Ventra, M.; Garaj, S.; Hibbs, A.; Huang, X.; Jovanovich, S. B.; Krstic, P. S.; Lindsay, S.; Ling, X. S.; Mastrangelo, C. H.; Meller, A.; Oliver, J. S.; Pershin, Y. V.; Ramsey, J. M.; Riehn, R.; Soni, G. V.; Tabard-Cossa, V.; Wanunu, M.; Wiggin, M.; Schloss, J. A., The potential and challenges of nanopore sequencing. *Nature biotechnology* **2008,** *26* (10), 1146-1153.

21. Haque, F.; Li, J.; Wu, H.-C.; Liang, X.-J.; Guo, P., Solid-state and biological nanopore for real-time sensing of single chemical and sequencing of DNA. *Nano Today* **2013,** *8* (1), 56-74.

22. Deamer, D.; Akeson, M.; Branton, D., Three decades of nanopore sequencing. *Nature biotechnology* **2016,** *34* (5), 518-524.

23. Coulter, W. H. Means for counting particles suspended in a fluid. 1953.

24. Hladky, S. B.; Haydon, D. A., DISCRETENESS OF CONDUCTANCE CHANGE IN BIMOLECULAR LIPID MEMBRANES IN PRESENCE OF CERTAIN ANTIBIOTICS. *Nature* **1970,** *225* (5231), 451-&.

25. Neher, E.; Sakmann, B., SINGLE-CHANNEL CURRENTS RECORDED FROM MEMBRANE OF DENERVATED FROG MUSCLE-FIBERS. *Nature* **1976,** *260* (5554), 799-802.

26. Leng, S.; Chaves, P.; Koenig, K.; Walston, J., Serum interleukin-6 and hemoglobin as physiological correlates in the geriatric syndrome of frailty: A pilot

study. *Journal of the American Geriatrics Society* **2002,** *50* (7), 1268-1271.

27. Single-channel recording, Second edition. *Single-channel recording, Second edition* **1995**, xxvii+700p-xxvii+700p.

28. Stevens, C. F., ION CHANNEL RECONSTITUTION - MILLER,C. *Science* **1986,** *234* (4779), 1016-1016.

29. Bezrukov, S. M.; Vodyanoy, I.; Parsegian, V. A., COUNTING POLYMERS MOVING THROUGH A SINGLE-ION CHANNEL. *Nature* **1994,** *370* (6487), 279-281.

30. Kasianowicz, J. J.; Brandin, E.; Branton, D.; Deamer, D. W., Characterization of individual polynucleotide molecules using a membrane channel. *Proceedings of the National Academy of Sciences of the United States of America* **1996,** *93* (24), 13770-13773.

31. Howorka, S.; Siwy, Z., Nanopore analytics: sensing of single molecules. *Chemical Society reviews* **2009,** *38* (8), 2360-2384.

32. Song, L. Z.; Hobaugh, M. R.; Shustak, C.; Cheley, S.; Bayley, H.; Gouaux, J. E., Structure of staphylococcal alpha-hemolysin, a heptameric transmembrane pore. *Science* **1996,** *274* (5294), 1859-1866.

33. Ayub, M.; Stoddart, D.; Bayley, H., Nucleobase Recognition by Truncated alpha-Hemolysin Pores. *ACS nano* **2015,** *9* (8), 7895-7903.

34. Derrington, I. M.; Butler, T. Z.; Collins, M. D.; Manrao, E.; Pavlenok, M.; Niederweis, M.; Gundlach, J. H., Nanopore DNA sequencing with MspA. *Proceedings of the National Academy of Sciences of the United States of America* **2010,** *107* (37), 16060-16065.

35. Cao, C.; Ying, Y. L.; Hu, Z. L.; Liao, D. F.; Tian, H.; Long, Y. T., Discrimination of oligonucleotides of different lengths with a wild-type aerolysin nanopore. *Nature nanotechnology* **2016,** *11* (8), 713-+.

36. Butler, T. Z.; Pavlenok, M.; Derrington, I. M.; Niederweis, M.; Gundlach, J. H., Single-molecule DNA detection with an engineered MspA protein nanopore. *Proceedings of the National Academy of Sciences of the United States of America* **2008,** *105* (52), 20647-20652.

37. Kukwikila, M.; Howorka, S., Nanopore-Based Electrical and Label-Free Sensing of Enzyme Activity in Blood Serum. *Analytical Chemistry* **2015,** *87* (18), 9149-9154.

38. Wang, L.; Han, Y. J.; Zhou, S.; Guan, X. Y., Real-time label-free measurement of HIV-1 protease activity by nanopore analysis. *Biosensors & Bioelectronics* **2014,** *62*, 158-162.

39. Zhou, S.; Wang, L.; Chen, X. H.; Guan, X. Y., Label-Free Nanopore Single-Molecule Measurement of Trypsin Activity. *Acs Sensors* **2016,** *1* (5), 607-613.

40. Campos, E. J.; McVey, C. E.; Astier, Y., Stochastic Detection of MPSA-Gold Nanoparticles Using a alpha-Hemolysin Nanopore Equipped with a Noncovalent Molecular Adaptor. *Analytical Chemistry* **2016,** *88* (12), 6214-6222.

41. Krasilnikov, O. V.; Rodrigues, C. G.; Bezrukov, S. M., Single polymer molecules in a protein nanopore in the limit of a strong polymer-pore attraction. *Physical review letters* **2006,** *97* (1).

42. Li, T.; Liu, L.; Li, Y.; Xie, J.; Wu, H.-C., A Universal Strategy for Aptamer-Based Nanopore Sensing through Host-Guest Interactions inside -Hemolysin. *Angewandte Chemie-International Edition* **2015,** *54* (26), 7568-7571.

43. Lee, J.; Bayley, H., Semisynthetic protein nanoreactor for single-molecule chemistry. *Proceedings of the National Academy of Sciences of the United States of America* **2015,** *112* (45), 13768-13773.

44. Pulcu, G. S.; Mikhailova, E.; Choi, L.-S.; Bayley, H., Continuous observation of the stochastic motion of an individual small-molecule walker. *Nature nanotechnology* **2015,** *10* (1), 76-83.

45. Kumar, S.; Tao, C.; Chien, M.; Hellner, B.; Balijepalli, A.; Robertson, J. W. F.; Li, Z.; Russo, J. J.; Reiner, J. E.; Kasianowicz, J. J.; Ju, J., PEG-Labeled Nucleotides and Nanopore Detection for Single Molecule DNA Sequencing by Synthesis. *Scientific Reports* **2012,** *2*.

46. Manrao, E. A.; Derrington, I. M.; Laszlo, A. H.; Langford, K. W.; Hopper, M. K.; Gillgren, N.; Pavlenok, M.; Niederweis, M.; Gundlach, J. H., Reading DNA at single-nucleotide resolution with a mutant MspA nanopore and phi29 DNA polymerase. *Nature biotechnology* **2012,** *30* (4), 349-U174.

47. Li, J.; Stein, D.; McMullan, C.; Branton, D.; Aziz, M. J.; Golovchenko, J. A., Ion-beam sculpting at nanometre length scales. *Nature* **2001,** *412* (6843), 166-169.

48. Cai, Q.; Ledden, B.; Krueger, E.; Golovchenko, J. A.; Li, J. L., Nanopore sculpting with noble gas ions. *Journal of Applied Physics* **2006,** *100* (2).

49. Plesa, C.; van Loo, N.; Ketterer, P.; Dietz, H.; Dekker, C., Velocity of DNA during Trans location through a Solid-State Nanopore. *Nano letters* **2015,** *15* (1), 732-737.

50. Schneider, G. F.; Kowalczyk, S. W.; Calado, V. E.; Pandraud, G.; Zandbergen, H. W.; Vandersypen, L. M.; Dekker, C., DNA translocation through graphene nanopores. *Nano letters* **2010,** *10* (8), 3163-7.

51. Farimani, A. B.; Min, K.; Aluru, N. R., DNA Base Detection Using a Single-Layer MoS2. *ACS nano* **2014,** *8* (8), 7914-7922.

52. Wang, C. M.; Fu, Q. B.; Wang, X. W.; Kong, D. H.; Sheng, Q.; Wang, Y. G.; Chen, Q.; Xue, J. M., Atomic Layer Deposition Modified Track-Etched Conical Nanochannels for Protein Sensing. *Analytical Chemistry* **2015,** *87* (16), 8227-8233.

53. Li, W.; Bell, N. A. W.; Hernandez-Ainsa, S.; Thacker, V. V.; Thackray, A. M.; Bujdoso, R.; Keyser, U. F., Single Protein Molecule Detection by Glass Nanopores. *ACS nano* **2013,** *7* (5), 4129-4134.

54. Brown, K. T.; Flaming, D. G., *Advanced Micropipette Techniques for Cell Physiology*. Wiley: 1986.

55. Levis, R. A.; Rae, J. L., THE USE OF QUARTZ PATCH PIPETTES FOR LOW-NOISE SINGLE-CHANNEL RECORDING. *Biophysical journal* **1993,** *65* (4),

1666-1677.

56. White, R. J.; Ervin, E. N.; Yang, T.; Chen, X.; Daniel, S.; Cremer, P. S.; White, H. S., Single ion-channel recordings using glass nanopore membranes. *Journal of the American Chemical Society* **2007,** *129* (38), 11766-11775.

57. Bell, N. A. W.; Thacker, V. V.; Hernandez-Ainsa, S.; Fuentes-Perez, M. E.; Moreno-Herrero, F.; Liedl, T.; Keyser, U. F., Multiplexed ionic current sensing with glass nanopores. *Lab on a Chip* **2013,** *13* (10), 1859-1862.

58. Pitchford, W. H.; Kim, H.-J.; Ivanov, A. P.; Kim, H.-M.; Yu, J.-S.; Leatherbarrow, R. J.; Albrecht, T.; Kim, K.-B.; Edel, J. B., Synchronized Optical and Electronic Detection of Biomolecules Using a Low Noise Nanopore Platform. *ACS nano* **2015,** *9* (2), 1740-1748.

59. Gibb, T. R.; Ivanov, A. P.; Edel, J. B.; Albrecht, T., Single Molecule Ionic Current Sensing in Segmented Flow Microfluidics. *Analytical Chemistry* **2014,** *86* (3), 1864-1871.

60. Sze, J. Y. Y.; Kumar, S.; Ivanov, A. P.; Oh, S.-H.; Edel, J. B., Fine tuning of nanopipettes using atomic layer deposition for single molecule sensing. *The Analyst* **2015,** *140* (14), 4828-4834.

61. Steinbock, L. J.; Steinbock, J. F.; Radenovic, A., Controllable Shrinking and Shaping of Glass Nanocapillaries under Electron Irradiation. *Nano letters* **2013,** *13* (4), 1717-1723.

62. Ivanov, A. P.; Actis, P.; Jonsson, P.; Klenerman, D.; Korchev, Y.; Edel, J. B., On-demand delivery of single DNA molecules using nanopipets. *ACS nano* **2015,** *9* (4), 3587-3595.

63. Freedman, K. J.; Otto, L. M.; Ivanov, A. P.; Barik, A.; Oh, S. H.; Edel, J. B., Nanopore sensing at ultra-low concentrations using single-molecule dielectrophoretic trapping. *Nat.Commun.* **2016,** *7*, 10217.

64. Sze, J. Y. Y.; Ivanov, A. P.; Cass, A. E. G.; Edel, J. B., Single molecule multiplexed nanopore protein screening in human serum using aptamer modified DNA carriers. *Nature Communications* **2017,** *8*.

65. Lin, X. Y.; Ivanov, A. P.; Edel, J. B., Selective single molecule nanopore sensing of proteins using DNA aptamer-functionalised gold nanoparticles. *Chemical Science* **2017,** *8* (5), 3905-3912.

66. Lan, W. J.; Holden, D. A.; Zhang, B.; White, H. S., Nanoparticle Transport in Conical-Shaped Nanopores. *Analytical Chemistry* **2011,** *83* (10), 3840-3847.

67. Amemiya, S.; Bard, A. J.; Fan, F.-R. F.; Mirkin, M. V.; Unwin, P. R., Scanning Electrochemical Microscopy. In *Annual review of analytical chemistry*, 2008; Vol. 1, pp 95-131.

68. Macpherson, J. V.; Unwin, P. R., Combined scanning electrochemical-atomic force microscopy. *Analytical Chemistry* **2000,** *72* (2), 276-285.

69. Korchev, Y. E.; Gorelik, J.; Lab, M. J.; Sviderskaya, E. V.; Johnston, C. L.; Coombes, C. R.; Vodyanoy, I.; Edwards, C. R. W., Cell volume measurement using scanning ion conductance microscopy. *Biophysical journal* **2000,** *78* (1), 451-457.

70. Takahashi, Y.; Shevchuk, A. I.; Novak, P.; Murakami, Y.; Shiku, H.; Korchev, Y. E.; Matsue, T., Simultaneous Noncontact Topography and Electrochemical Imaging by SECM/SICM Featuring Ion Current Feedback Regulation. *Journal of the American Chemical Society* **2010,** *132* (29), 10118-10126.

71. Smeets, R. M. M.; Keyser, U. F.; Krapf, D.; Wu, M. Y.; Dekker, N. H.; Dekker, C., Salt dependence of ion transport and DNA translocation through solid-state nanopores. *Nano letters* **2006,** *6* (1), 89-95.

72. Zanjani, M. B.; Engelke, R. E.; Lukes, J. R.; Meunier, V.; Drndic, M., Up and down translocation events and electric double-layer formation inside solid-state nanopores. *Physical Review E* **2015,** *92* (2).

73. Steinbock, L. J.; Lucas, A.; Otto, O.; Keyser, U. F., Voltage-driven transport of ions and DNA through nanocapillaries. *Electrophoresis* **2012,** *33* (23), 3480-3487.

74. Cadinu, P.; Nadappuram, B. P.; Lee, D. J.; Sze, J. Y. Y.; Campolo, G.; Zhang, Y.; Shevchuk, A.; Ladame, S.; Albrecht, T.; Korchev, Y.; Ivanov, A. P.; Edel, J. B., Single Molecule Trapping and Sensing Using Dual Nanopores Separated by a Zeptoliter Nanobridge. *Nano letters* **2017,** *17* (10), 6376-6384.

75. Wadhawan, J. D.; Compton, R. G., Electrochemistry: Nanosystems Electrochemistry. - P001.

76. Edel, J. B.; Albrecht, T., *Engineered Nanopores for Bioanalytical Applications*. William Andrew Publishing: Oxford, 2013; p 1-30.

77. Helmholtz, H., Ueber einige Gesetze der Vertheilung elektrischer Ströme in körperlichen Leitern mit Anwendung auf die thierisch-elektrischen Versuche. *Annalen der Physik* **1853,** *165* (6), 211-233.

78. Bard, A. J.; Faulkner, L. R., *Electrochemical Methods: Fundamentals and Applications, 2nd Edition*. John Wiley & Sons: 2000.

79. Singh, K. P.; Kumar, M., Effect of Nanochannel Diameter and Debye Length on Ion Current Rectification in a Fluidic Bipolar Diode. *Journal of Physical Chemistry C* **2011,** *115* (46), 22917-22924.

80. Liu, S. J.; Dong, Y. T.; Zhao, W. B.; Xie, X.; Ji, T. R.; Yin, X. H.; Liu, Y.; Liang, Z. W.; Momotenko, D.; Liang, D. H.; Girault, H. H.; Shao, Y. H., Studies of Ionic Current Rectification Using Polyethyleneimines Coated Glass Nanopipettes. *Analytical Chemistry* **2012,** *84* (13), 5565-5573.

81. Torrie, G. M.; Valleau, J. P., ELECTRICAL DOUBLE-LAYERS .4. LIMITATIONS OF THE GOUY-CHAPMAN THEORY. *Journal of Physical Chemistry* **1982,** *86* (16), 3251-3257.

82. Behrens, S. H.; Grier, D. G., The charge of glass and silica surfaces. *Journal of Chemical Physics* **2001,** *115* (14), 6716-6721.

83. Lowe, B. M.; Skylaris, C.-K.; Green, N. G., Acid-base dissociation mechanisms and energetics at the silica-water interface: An activationless process. *Journal of Colloid and Interface Science* **2015,** *451*, 231-244.

84. Siwy, Z.; Heins, E.; Harrell, C. C.; Kohli, P.; Martin, C. R., Conical-nanotube ion-current rectifiers: The role of surface charge. *Journal of the American Chemical*

Society **2004,** *126* (35), 10850-10851.

85. Siwy, Z. S., Ion-current rectification in nanopores and nanotubes with broken symmetry. *Advanced Functional Materials* **2006,** *16* (6), 735-746.

86. Wei, C.; Bard, A. J.; Feldberg, S. W., Current rectification at quartz nanopipet electrodes. *Analytical Chemistry* **1997,** *69* (22), 4627-4633.

87. Firnkes, M.; Pedone, D.; Knezevic, J.; Doblinger, M.; Rant, U., Electrically Facilitated Translocations of Proteins through Silicon Nitride Nanopores: Conjoint and Competitive Action of Diffusion, Electrophoresis, and Electroosmosis. *Nano letters* **2010,** *10* (6), 2162-2167.

88. Schmid, G., Electrochemistry of capillary systems with narrow pores. II. Electroosmosis. *Journal of Membrane Science* **1998,** *150* (2), 159-170.

89. Schoch, R. B.; Han, J.; Renaud, P., Transport phenomena in nanofluidics. *Reviews of Modern Physics* **2008,** *80* (3), 839-883.

90. Experton, J.; Wu, X. J.; Martin, C. R., From Ion Current to Electroosmotic Flow Rectification in Asymmetric Nanopore Membranes. *Nanomaterials* **2017,** *7* (12).

91. Fan, R.; Karnik, R.; Yue, M.; Li, D. Y.; Majumdar, A.; Yang, P. D., DNA translocation in inorganic nanotubes. *Nano letters* **2005,** *5* (9), 1633-1637.

92. Min, S. K.; Kim, W. Y.; Cho, Y.; Kim, K. S., Fast DNA sequencing with a graphene-based nanochannel device. *Nature nanotechnology* **2011,** *6* (3), 162-165.

93. Storm, A. J.; Chen, J. H.; Zandbergen, H. W.; Dekker, C., Translocation of double-strand DNA through a silicon oxide nanopore. *Physical Review E* **2005,** *71* (5).

94. Storm, A. J.; Storm, C.; Chen, J. H.; Zandbergen, H.; Joanny, J. F.; Dekker, C., Fast DNA translocation through a solid-state nanopore. *Nano letters* **2005,** *5* (7), 1193-1197.

95. Merchant, C. A.; Healy, K.; Wanunu, M.; Ray, V.; Peterman, N.; Bartel, J.; Fischbein, M. D.; Venta, K.; Luo, Z. T.; Johnson, A. T. C.; Drndic, M., DNA Translocation through Graphene Nanopores. *Nano letters* **2010,** *10* (8), 2915-2921.

96. Ghosal, S.; Sherwood, J. D.; Chang, H. C., Solid-state nanopore hydrodynamics and transport. *Biomicrofluidics* **2019,** *13* (1).

97. Kowalczyk, S. W.; Wells, D. B.; Aksimentiev, A.; Dekker, C., Slowing down DNA Translocation through a Nanopore in Lithium Chloride. *Nano letters* **2012,** *12* (2), 1038-1044.

98. Liu, Y. F.; Yobas, L., Slowing DNA Translocation in a Nanofluidic Field-Effect Transistor. *ACS nano* **2016,** *10* (4), 3985-3994.

99. Fraccari, R. L.; Carminati, M.; Piantanida, G.; Leontidou, T.; Ferrari, G.; Albrecht, T., High-bandwidth detection of short DNA in nanopipettes. *Faraday Discussions* **2016,** *193*, 459-470.

100. Al Sulaiman, D.; Cadinu, P.; Ivanov, A. P.; Edel, J. B.; Ladame, S., Chemically Modified Hydrogel-Filled Nanopores: A Tunable Platform for Single-Molecule Sensing. *Nano letters* **2018,** *18* (9), 6084-6093.

101. Bell, N. A. W.; Chen, K.; Ghosal, S.; Ricci, M.; Keyser, U. F., Asymmetric dynamics of DNA entering and exiting a strongly confining nanopore. *Nature Communications* **2017,** *8*.

102. Ivanov, A. P.; Instuli, E.; McGilvery, C. M.; Baldwin, G.; McComb, D. W.; Albrecht, T.; Edel, J. B., DNA tunneling detector embedded in a nanopore. *Nano letters* **2011,** *11* (1), 279-85.

103. Tsutsui, M.; Taniguchi, M.; Yokota, K.; Kawai, T., Identifying single nucleotides by tunnelling current. *Nature nanotechnology* **2010,** *5* (4), 286-290.

104. Iqbal, S. M.; Akin, D.; Bashir, R., Solid-state nanopore channels with DNA selectivity. *Nature nanotechnology* **2007,** *2* (4), 243-248.

105. Venkatesan, B. M.; Bashir, R., Nanopore sensors for nucleic acid analysis. *Nature nanotechnology* **2011,** *6* (10), 615-624.

106. Hall, A. R.; Scott, A.; Rotem, D.; Mehta, K. K.; Bayley, H.; Dekker, C., Hybrid pore formation by directed insertion of alpha-haemolysin into solid-state nanopores. *Nature nanotechnology* **2010,** *5* (12), 874-877.

107. Plesa, C.; Kowalczyk, S. W.; Zinsmeester, R.; Grosberg, A. Y.; Rabin, Y.; Dekker, C., Fast Translocation of Proteins through Solid State Nanopores. *Nano letters* **2013,** *13* (2), 658-663.

108. Pedone, D.; Firnkes, M.; Rant, U., Data Analysis of Translocation Events in Nanopore Experiments. *Analytical Chemistry* **2009,** *81* (23), 9689-9694.

109. Steinbock, L. J.; Krishnan, S.; Bulushev, R. D.; Borgeaud, S.; Blokesch, M.; Feletti, L.; Radenovic, A., Probing the size of proteins with glass nanopores. *Nanoscale* **2014,** *6* (23), 14380-14387.

110. Larkin, J.; Henley, R. Y.; Muthukumar, M.; Rosenstein, J. K.; Wanunu, M., High-Bandwidth Protein Analysis Using Solid-State Nanopores. *Biophysical journal* **2014,** *106* (3), 696-704.

111. Li, Q.; Ying, Y. L.; Liu, S. C.; Lin, Y.; Long, Y. T., Detection of Single Proteins with a General Nanopore Sensor. *Acs Sensors* **2019,** *4* (5), 1185-1189.

112. Houghtaling, J.; Ying, C. F.; Eggenberger, O. M.; Fennouri, A.; Nandivada, S.; Acharjee, M.; Li, J. L.; Hall, A. R.; Mayer, M., Estimation of Shape, Volume, and Dipole Moment of Individual Proteins Freely Transiting a Synthetic Nanopore. *ACS nano* **2019,** *13* (5), 5231-5242.

113. Yu, R. J.; Ying, Y. L.; Hu, Y. X.; Gao, R.; Long, Y. T., Label-Free Monitoring of Single Molecule Immunoreaction with a Nanopipette. *Analytical Chemistry* **2017,** *89* (16), 8203-8206.

114. Wei, R.; Gatterdam, V.; Wieneke, R.; Tampe, R.; Rant, U., Stochastic sensing of proteins with receptor-modified solid-state nanopores. *Nature nanotechnology* **2012,** *7* (4), 257-263.

115. Kong, J.; Zhu, J.; Chen, K.; Keyser, U. F., Specific Biosensing Using DNA Aptamers and Nanopores. *Advanced Functional Materials* **2019,** *29* (3), 1807555.

116. Oukhaled, A.; Cressiot, B.; Bacri, L.; Pastoriza-Gallego, M.; Betton, J. M.;

Bourhis, E.; Jede, R.; Gierak, J.; Auvray, L.; Pelta, J., Dynamics of Completely Unfolded and Native Proteins through Solid-State Nanopores as a Function of Electric Driving Force. *ACS nano* **2011,** *5* (5), 3628-3638.

117. Talaga, D. S.; Li, J. L., Single-Molecule Protein Unfolding in Solid State Nanopores. *Journal of the American Chemical Society* **2009,** *131* (26), 9287-9297.

118. Rosenstein, J. K.; Wanunu, M.; Merchant, C. A.; Drndic, M.; Shepard, K. L., Integrated nanopore sensing platform with sub-microsecond temporal resolution. *Nature Methods* **2012,** *9* (5), 487-U112.

119. Freedman, K. J.; Haq, S. R.; Fletcher, M. R.; Foley, J. P.; Jemth, P.; Edel, J. B.; Kim, M. J., Nonequilibrium Capture Rates Induce Protein Accumulation and Enhanced Adsorption to Solid-State Nanopores. *ACS nano* **2014,** *8* (12), 12238-12249.

120. Yusko, E. C.; Johnson, J. M.; Majd, S.; Prangkio, P.; Rollings, R. C.; Li, J. L.; Yang, J.; Mayer, M., Controlling protein translocation through nanopores with bio-inspired fluid walls. *Nature nanotechnology* **2011,** *6* (4), 253-260.

121. Loh, A. Y. Y.; Burgess, C. H.; Tanase, D. A.; Ferrar, G.; McLachlan, M. A.; Cass, A. E. G.; Albrecht, T., Electric Single-Molecule Hybridization Detector for Short DNA Fragments. *Analytical Chemistry* **2018,** *90* (23), 14063-14071.

CHAPTER 2

Methodology

Synopsis

This chapter outlines the primary materials, instruments, methods, and data analysis for the experiments in this thesis. The fabrication, microscopy characterisation, and electrochemistry characterisation of nanopipettes, including single-barrel and double-barrel, are illustrated. We also introduce the set-up of ionic current measurements and the data analysis of the translocation recordings.

2.1 Nanopipette fabrication and characterisation

2.1.1 Nanopipette fabrication

The nanopipettes were made from quartz capillaries. The experiments described in this thesis relied on two types of quartz capillaries: double-barrel quartz theta capillaries (o.d., 1.2 mm, i.d., 0.9 mm, Intracell) in **Chapter 3** and **Chapter 4**, and single-barrel quartz capillaries (o.d., 1.0 mm, i.d., 0.7 mm, Intracell) in **Chapter 5** and **Chapter 6**. Both types of capillaries contain filaments, which contribute to the capillary action in order to easily assist in filling the barrel with electrolytes. All capillaries were cleaned for at least 20 mins using a plasma cleaner (Harrick Plasma), which utilises ionised gas to remove most of the contaminates on the quartz surface.

2.1.1.1 Double-barrel nanopipette fabrication

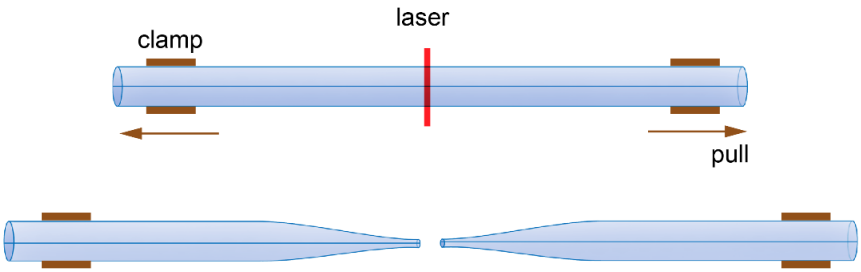


Figure 2. 1 Fabrication of double-barrel nanopipettes using a laser-based pipette puller and a one-step protocol.

After plasma cleaning, the double-barrel capillaries were carefully loaded into a laser-based pipette puller (Sutter Instrument, P-2000) without touching the middle part, where the tips of the nanopipettes would be generated. It is worth noting that, to avoid a stretched pore shape after pulling, the nanopipettes should be loaded as the septum is horizontal. Then, the capillary was heated and pulled to generate a pair of double-barrel nanopipettes, as illustrated in **Figure 2.1**. The parameters of the one-step protocol are listed in **Table 2.1**, Protocol 1. It should be noted that the parameters of the pulling protocols are instrument specific and sensitive to both the temperature and humidity of the room.[1, 2] By pulling one double-barrel quartz capillary (**Figure 2.2a**), a pair of double barrel nanopipettes can be generated (**Figure 2.2b**).

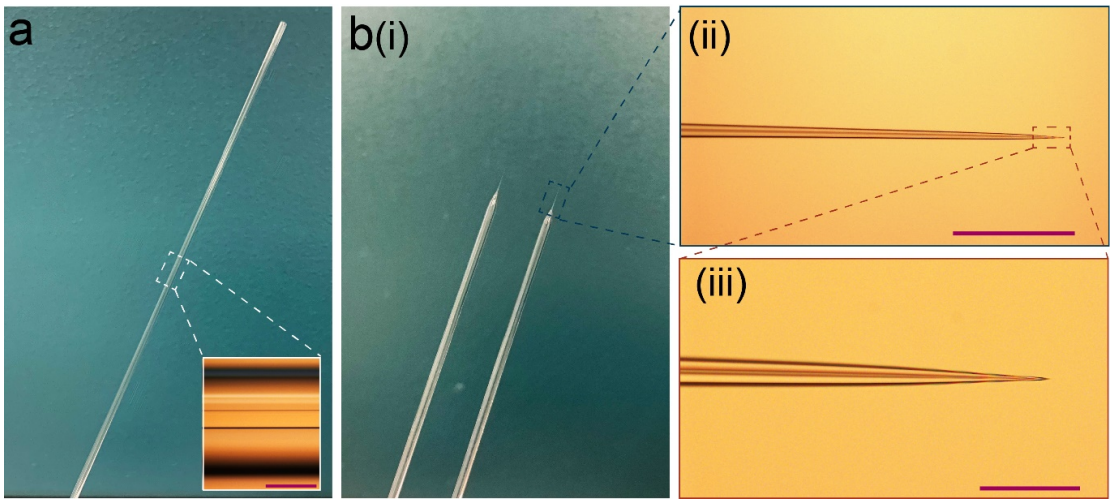


Figure 2. 2 The double-barrel capillary and a pair of double-barrel nanopipettes after the pulling. **(a)** The double-barrel quartz capillary. From the microscopy image (inset), it is obvious that two barrels with semi-circular column profile are divided by a septum. **(b)** Generated double-nanopipettes after the pulling. Scale bar: inset of **a** 500 µm; **b(ii)** 500 µm; **b(iii)** 100 µm.

2.1.1.2 Single-barrel nanopipette fabrication

After plasma cleaning, the single-barrel capillaries were loaded into a laser-based pipette puller. Different from the protocol for pulling double-barrel capillaries, the protocol that we used to pull the single-barrel capillaries is a two-line protocol[3], as listed in **Table 2.1**, Protocol 2 and Protocol 3. In the first step, the capillary was heated and pulled gently, which resulted in an hourglass shape. In the second step, the narrowest part of the capillary was further heated by the laser and then cut into two identical nanopores, as depicted in **Figure 2.3**. By pulling one single barrel quartz capillary (**Figure 2.4a**), a pair of single barrel nanopipettes can be generated (**Figure 2.4b**).

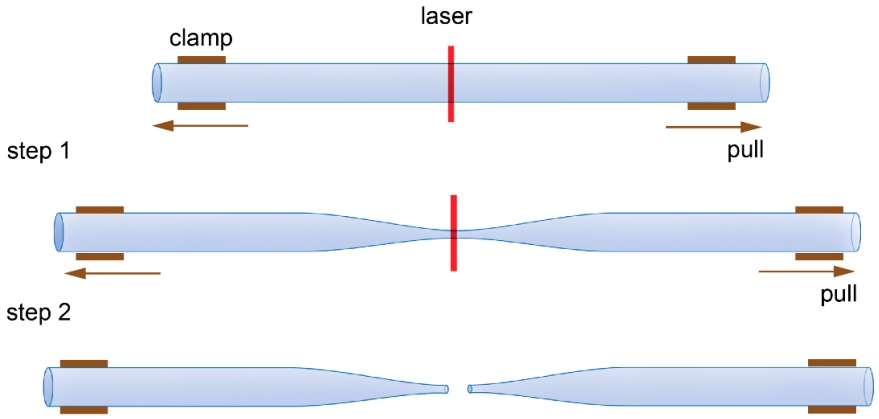


Figure 2. 3 Fabrication of single-barrel nanopipettes using a laser-based pipette puller and a two-step protocol.

The decision regarding whether to use a one-line or a two-line protocol to pull the capillaries is mainly dependent on the size and purpose of the generated nanopipettes.

In this thesis, the double-barrel nanopipette, with two approximately 100 nm pores, was used as the substrate of the polypyrrole nanopore. Therefore, a one-step protocol is sufficient. However, for single-barrel nanopipette, typically a two-line protocol is needed to produce smaller pores which allow analytes to be detected directly.

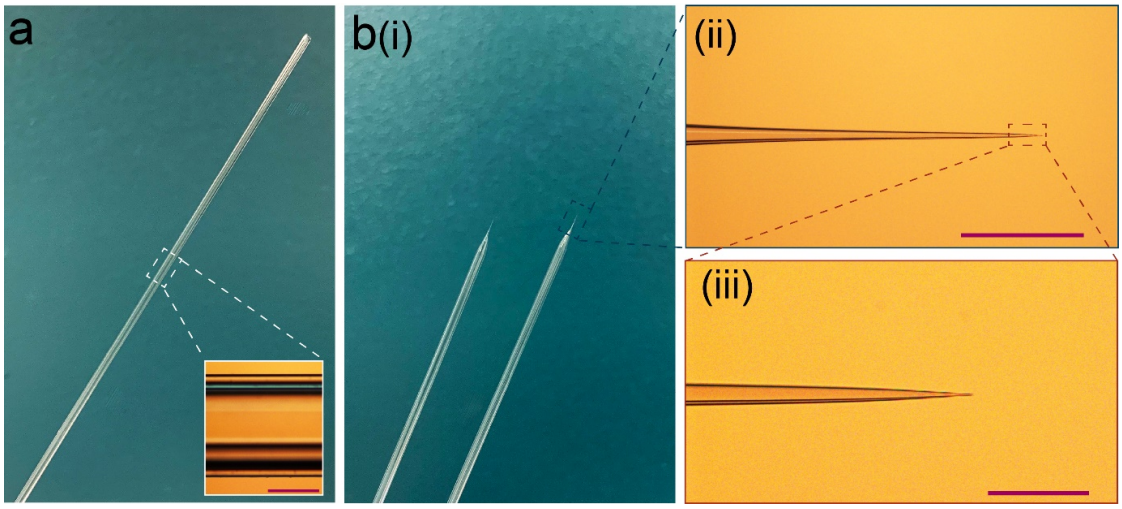


Figure 2. 4 The single barrel capillary and a pair of single-barrel nanopipettes after the pulling. **(a)** The double-barrel quartz capillary. **(b)** Generated single-barrel nanopipettes after the pulling. Scale bar: inset of **a** 500 µm; **b(ii)** 500 µm; **b(iii)** 100 µm.

Table 2. 1 Parameters for pulling the pipettes using a laser-based puller.

	Capillary type	Line	Heat	Filament	Velocity	Delay	Pull	Expected pore size	Pulling time
Protocol 1	Double barrel	Line 1	700	3	45	130	93	100	9 s
Protocol 2	Single barrel	Line 1	800	4	30	170	80	35	3.5 s
		Line 2	825	3	20	145	180		
Protocol 3	Single barrel	Line 1	775	4	30	170	80	42	3.8 s
		Line 2	825	3	20	145	180		

2.1.2 Microscopic characterisation of the nanopipettes

2.1.2.1 Optical microscopy

After pulling, the nanopipettes were quickly checked using an optical microscope (Olympus BX51, Japan). The nanopipettes were placed horizontally on the mechanical stage by a customised holder. It is important to ensure that each objective lens does not touch the tip area. For double-barrel nanopipette imaging, it is worth noting that the septum should be vertical, so two barrels can be observed. The image can be obtained by microscopy software (Olympus, Japan).

2.1.2.2 Scanning electron microscopy (SEM)

The precise geometry and size of the fabricated nanopipettes are characterised by a high-resolution scanning electron microscope: Leo Gemini 1525 SEM (Carl Zeiss AG, Germany). To increase the conductivity, the nanopipettes were coated with 5 nm chromium by a sputtering instrument (Quorum Technologies Ltd) and held by conductive carbon tape on the sample stage. An example is shown in **Figure 2.5**.

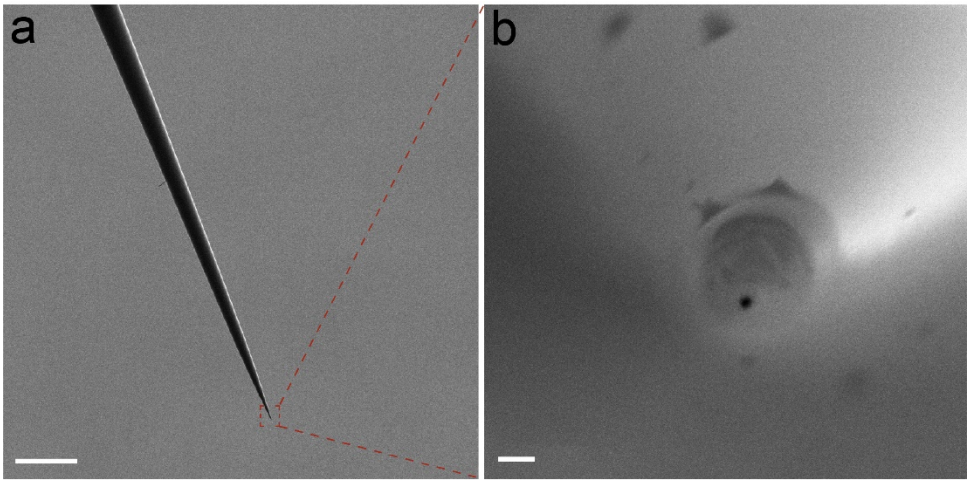


Figure 2. 5 The morphology of nanopore characterised by SEM. The side view **(a)** and the cross-section **(b)** of a single barrel nanopipette. Scale bar: **(a)** 10 μm, **(b)** 100 nm.

2.1.2.3 Transmission electron microscopy (TEM)

The transmission electron microscopy (TEM) imaging and element mapping of double-barrel nanopipettes were performed by Ms Bernice Akpinar, a PhD candidate, under the supervision of Prof. Joshua Edel (Imperial College London) and Prof. Bart Hoogenboom (University College London).

A high-resolution TEM (JEOL STEM/TEM 2100 Plus) with energy-dispersive X-ray spectroscopy (Oxford Instruments) was used to determine the elemental composition of the nanopipette tip. The nanopipette was cut and placed on a TEM copper grid without carbon film. Note, to observe both channels of a double-barrel nanopipette, the septum of the nanopipette should be perpendicular to the TEM grid surface.

2.1.3 Electrochemical characterisation

After nanopipette fabrication, the fastest and easiest way in which to estimate the pore size is to measure its conductance, which is closely related to the geometry of the

nanopore, as described previously. The conductance of the nanopore can be obtained by simply plotting the *I-V* curve, as indicated in **Equation 2.1**:

$$G = \frac{1}{R} = \frac{I}{V} \qquad (\mathbf{2.1})$$

where G and R are the conductance and resistance of the nanopore, respectively. Furthermore, V represents the applied voltage, and I is the corresponding ionic current.

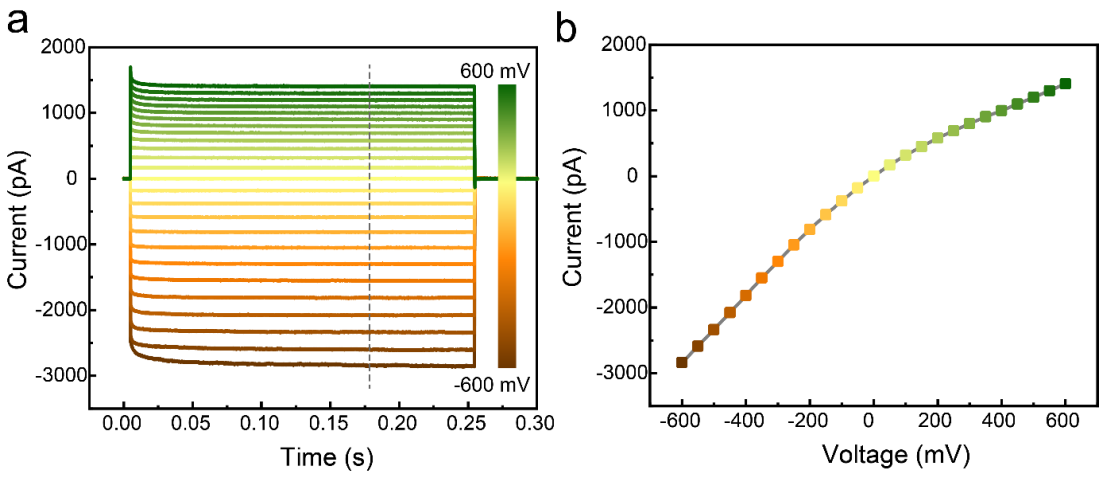


Figure 2. 6 *I-V* characterisation of a nanopipette. **(a)** I-t measurement of a typical nanopipette under bias from -600 mV to 600 mV in 100 mM of KCl. The grey dashed line represents the time point where the *I-V* curve was obtained. **(b)** The I-V curve of a nanopipette, which can be used to calculate the conductance and the ionic current rectification of the nanopore.

I-V characterisation was performed using an AxoPatch 200B patch-clamp amplifier (Molecular Devices, US) and 1440A digitiser (Molecular Devices, US). The ionic current under each voltage can be measured using a protocol, as illustrated in **Figure 2.6a**. The *I-V* curves can then be plotted by choosing the stable current point under each bias – see **Figure 2.6b**. In 100 mM KCl, the nanopipette always show a non-linear *I-V* characteristic. Herein, to use Ohm's law to calculate the conductance, we only choose the area between -50 mV and 50 mV, which shows a linear ohmic region.

2.2 Single-molecule translocation experiments

2.2.1 Preparation of Ag/AgCl electrodes

In this thesis, Ag/AgCl electrodes were used in all measurements. These electrodes are non- polarisable with negligible capacitive current at the electrode/electrolyte interface[4] and were fabricated by electro-oxidation of Ag in a highly concentrated chloride electrolyte[5], which can be described by **Equation 2.2**:

$$Ag + Cl^- \rightarrow AgCl + e^- \quad (2.2)$$

Two types of silver wire with different diameters were used. For the ionic current measurement in the double-barrel nanopipettes (**Chapter 3, Chapter 4**), 0.125 mm Ag wire (Goodfellow Cambridge, UK) was used, and for the ionic current measurement in the single-barrel nanopipettes (**Chapter 5, Chapter 6**), 0.25 mm Ag wire (Goodfellow Cambridge, UK) was used.

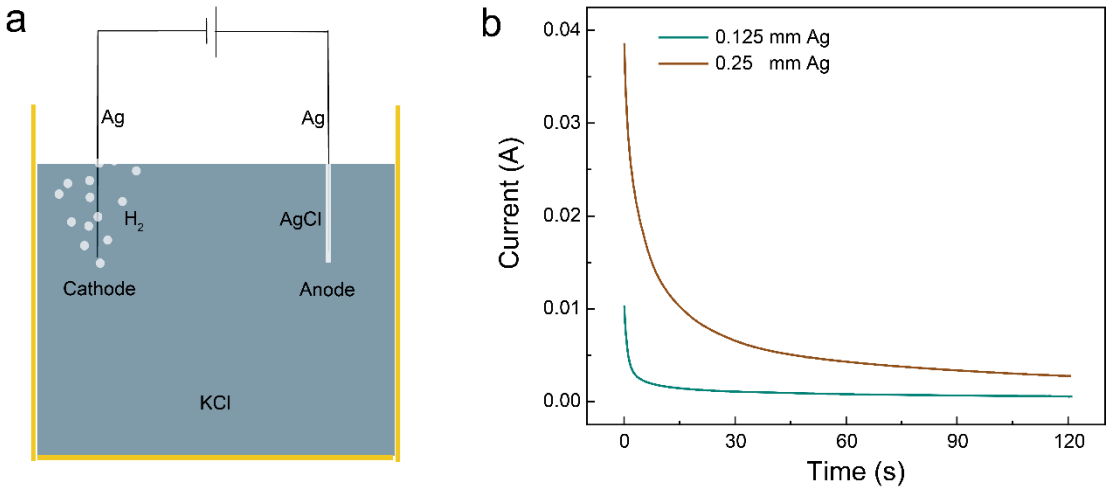


Figure 2. 7 Preparation of Ag/AgCl electrodes. **(a)** The set-up of the AgCl electrodes preparation. **(b)** I-t curve showing Ag oxidation in a 1 M KCl solution under a bias of 2 V.

Approximately 2 cm of Ag wires was immersed into a 1 M KCl solution, as illustrated in **Figure 2.7a**. A 2-V bias was applied using a CHI 760 C potentiostat (CH Instruments). The current-time curves could be monitored to control the quality of the electrodes (**Figure 2.7b**). The whole process took approximately 2 mins. Formation of AgCl could be observed by the loss of shine from the Ag wire and bubble formation from at the cathode. Reactions at both anode and cathode are explained with the flowing equations:

$$\text{Anode: } Ag + Cl^- \rightarrow AgCl + e^- \quad (2.3)$$

$$\text{Cathode: } 2H^+ + 2e^- \rightarrow H_2 \quad (2.4)$$

After oxidation, the generated Ag/AgCl electrodes were flushed with DI water to remove the salt residue. In this thesis, the Ag/AgCl electrodes were all prepared freshly for ionic current measurements.

2.2.2 Buffer preparation

Most buffer solutions used in the experiments of the thesis were made up of 10 mM of Tris-HCl, 1 mM of EDTA (Sigma-Aldrich), and KCl (Sigma-Aldrich) electrolyte.

The pH and salt concentrations varied with experiments, as listed in **Table 2.2**. All buffers were freshly prepared using DI water and further purified using a 0.2-μm syringe filter (Life Sciences, UK) before translocation experiments. The conductivity and pH of the buffer solutions were determined by a conductivity/pH meter (Mettler-Toledo, UK).

Table 2. 2 Buffer solutions prepared in this thesis.

No.	Electrolyte		Buffer		Chapter	Experiment	Related figures
	Salt	Concentration (mM)	Buffer type	pH			
1	KCl	100		6	3	Carbon nanoelectrode characterisation	3.5
2	KCl	100	Tris-EDTA	7.4		*I-V* characterisation	3.8; 3.9
3	KCl	33.3/10	Tris-EDTA	6		Ion selectivity measurements	3.1
4	KCl	1/10/100/1,000		6		FET performance measurements	3.11; 3.12
5	HCl	100		1		pH sensitivity measurements	3.13; 3.14
6	KCl	100	Tris-HCl	2 – 8		pH sensitivity measurements	3.13; 3.14
7	KCl	100	Tris-EDTA	7	4	DNA translocations	4.2
8	KCl	100	Tris-EDTA	8		DNA translocations	4.3; 4.5
9	KCl	100	Tris-EDTA	7		Protein translocations	4.8; 4.9; 4.10
10	KCl	100	Tris-EDTA	8	5	*I*-characterisations	5.4
11	KCl	50	Tris-EDTA	8		NP translocations	5.9; 5.10; 5.11
12	KCl	100	Tris-EDTA	8		SERS measurements	5.15; 5.16
13	KCl	50	Tris-EDTA	8	6	NP translocations	5.3 – 5.11

2.2.3 Ionic current measurements

The electrolyte was filled inside the nanopipettes via a Microfil needle (MF34G, World Precision Instruments, UK). It is important to ensure that no air bubbles are present on the tip. If bubbles exist, they can be removed by rubbing the pipette gently using a tweezer or by applying a negative air pressure using a syringe. The other electrode was filled inside a glass vial (bath). The freshly made Ag/AgCl electrodes were inserted into the nanopipettes and the bath, **Figure 2.8**. In this thesis, three amplifiers were used to measure the *I-V* characteristics of the nanopipette. Firstly, in **Chapter 3** and **Chapter 4**, an AxoPatch 700B Multiclamp amplifier (Molecular Devices, US) and DigiData 1322A digitiser (Molecular Devices, US) were utilised. Secondly, in **Chapter 5** and **Chapter 6**, an AxoPatch 200B patch-clamp amplifier (Molecular Devices, US) and DigiData 1440A digitiser (Molecular Devices, US) were used. Thirdly, for high-bandwidth measurements, a Chimera amplifier VC100 (Chimera Instruments, UK) was employed. Data measured by AxoPatch devices was

filtered and recorded by pClamp 10.5 software (Molecular Devices, US) while the data measured by Chimera was recorded using a Matlab-based GUI (Chimera Instruments, UK).

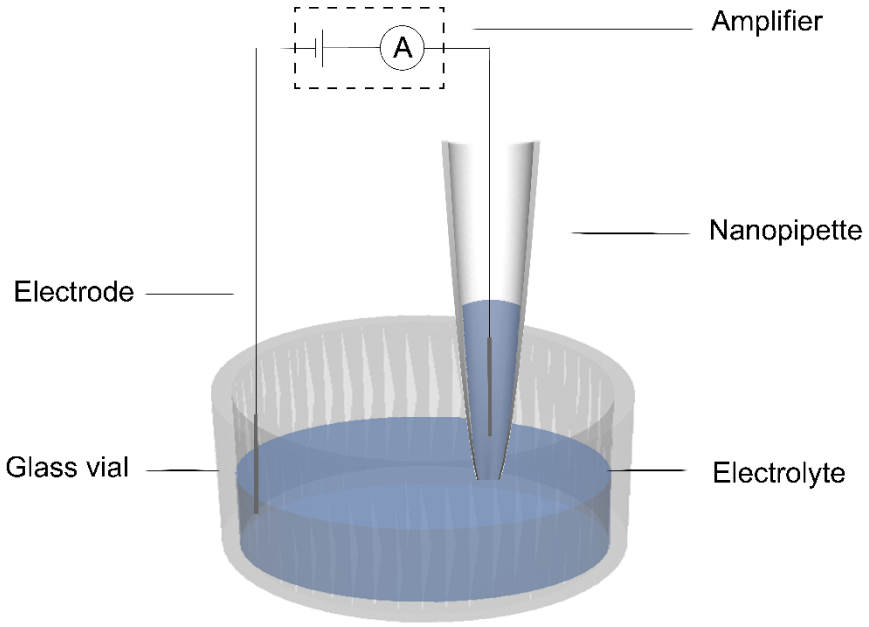


Figure 2. 8 Schematic of a nanopipette set-up for ionic current and molecule translocation measurements.

2.3 Data analysis

All translocation data were analysed using a custom-written Matlab App written by Prof. Joshua Edel (Imperial College London, UK) where translocation events can be selected and analysed accordingly – see **Figure 2.9**. In this section, the example DNA translocation experiments were carried out using 300 pM, 10 kbp dsDNA (New England Biolab, UK) in 100 mM of KCl with a Tris-EDTA (pH = 8) buffer. DNA was loaded in the nanopipette (cis) and the buffer with the same composition as that loaded in the bath (trans). The example translocation trace was recorded under -400 mV.

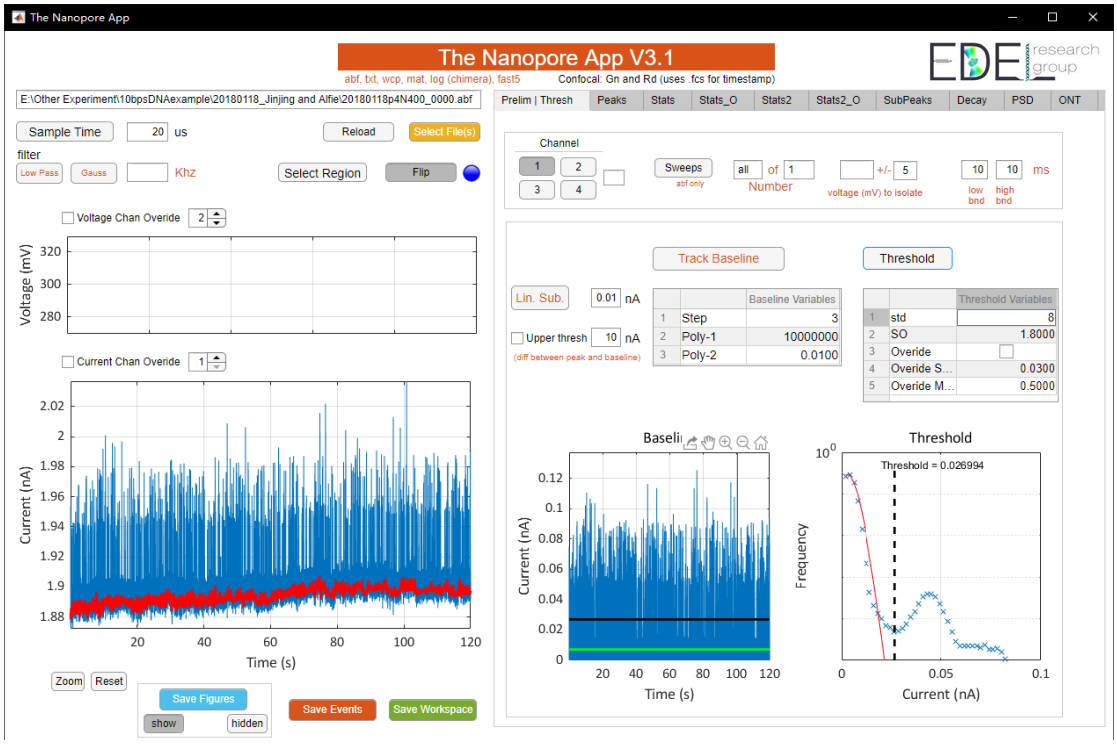


Figure 2. 9 The customised nanopore app interface.

The workflow is as follows:

1. Loading data. The translocation data should first be loaded into the app. Both of the Axon Binary files (.abf), which were recorded by AxoPatch amplifiers, and the Chimera files (.log), which were recorded by Chimera high-bandwidth amplifier, can be opened directly.

2. Digital refiltering and resampling. When translocation traced recorded, we always tended to use a high filter (100 kHz for Axon and 200 kHz for Chemira) and high sampling rate (5 μs for Axon and 1 μs for Chemira) to ensure the information of the peaks were not distorted. Using the app, the trace can be refiltered or resampled as needed, for example, for better-visualized purpose or higher signal-to-noise ratio.

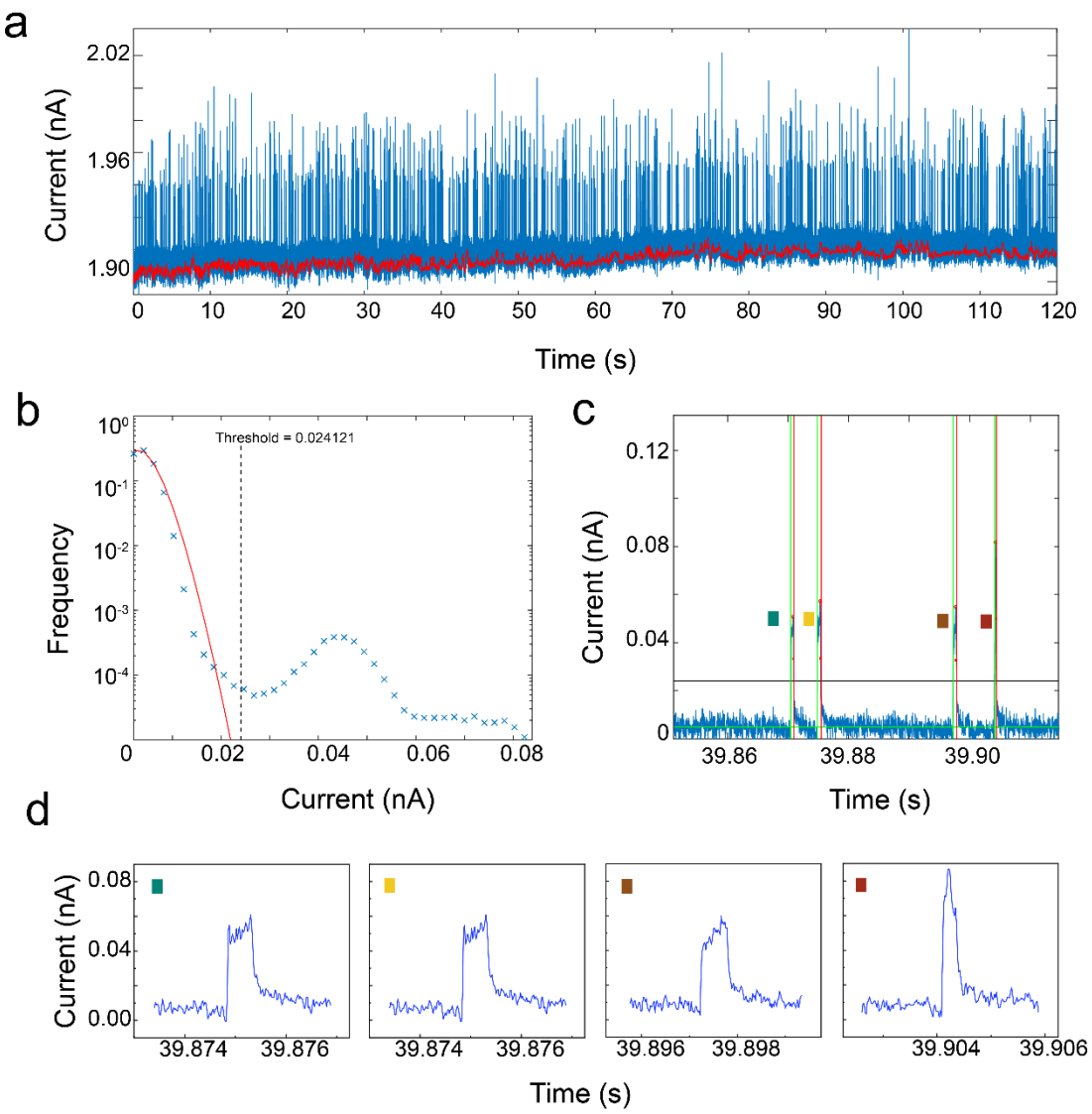


Figure 2. 10 The peak selection steps of the translocation analysis. **(a)** A 120-s current-time trace of 300-pM 10-kbp dsDNA translocation in 100 mM of KCl and 10 mM of Tris-EDTA (pH = 8) through a nanopipette with a 18 nm pore size; V = 400 mV. **(b)** Histogram of the ionic current distribution. The red line denotes the open pore current, which was fitted by a Poisson probability distribution function. The dashed line indicates the threshold above which the peak current can be counted. **(c)** The selection of fitted traces with the events above the threshold (black line) and that crossed the cut-off (green line). **(d)** The exported events after the peak selection step.

3. Fitting the baseline. A baseline can be adjusted automatically by polynomial fitting with appropriate parameters, as indicated in **Figure 2.10a**. For some translocation traces (such as the recordings in **Chapter 4**), if the duration of a single event is too long, then the baseline sampling rate (referring to the 'step' in the app interface) should be adjusted to avoid incorrect fitting. After the generation of the baseline, the whole ionic current trace was corrected using an asymmetric least square smoothing algorithm.

4. Applying a threshold. An ionic current histogram was generated with the open pore current and fitted using a Poisson probability distribution function, as illustrated in **Figure 2.10b**. A threshold, which was typically larger than six times that of the background signal (σ), can be applied by inputting the 'std' parameters (referring to standard deviation), as presented in **Figure 2.9**. Similarly, a cut-off, which was normally between 1σ and 2σ, can be generated by inputting the value after the 'SO' – see **Figure 2.9**.

5. Finding peaks. The events with peak currents above the threshold were selected. Several conditions can be imposed to help with the selection of peaks. For example, normally, the event time is defined by using a full width at half maximum (FWHM) of the translocation signal (**Figure 2.11a**). However, in some cases, especially in high salt condition[6], the 'tail', which corresponds to the ionic current signal returns to baseline following an exponential profile, is too long to neglect. The dwell time of such events was defined as the segments of time where the current exceeds the cut-off (**Figure 2.11b**). Other conditions for peak selection include lower time, upper time, and upper current.

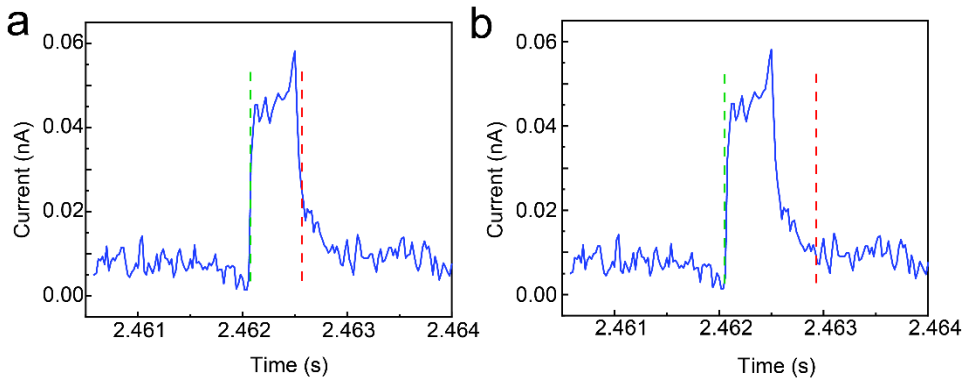


Figure 2. 11 The dwell time of the peak are determined by FWHM **(a)** or the cut-off **(b)**.

6. Exporting statistical results. After finding the peaks, event statistics can be generated.

The distributions of the most important information regarding translocation (dwell time, charge, and peak current) are depicted in **Figure 2.12a–b**. In **Figure 2.12a**, the probability distributions of dwell time, equivalent charge and the amplitude were identified using known parametric distributions such as Gaussian, Ling, and exponential distributions (solid line). However, when the distributions are wide, and they cannot be fitted a proper distribution function (this phenomenon sometimes happens when using the functionalized nanopores[7]), the probability of the distribution than can be estimated by the Kernel density curve (dash line), **Figure 2.12b**. In this example, it is evident that there are two populations in the dwell time and amplitude

where the unfolded DNA passed through the nanopore with longer dwell time and smaller peak current, while the folded DNA translocated with a shorter duration and a higher peak amplitude. This can be seen more clearly in the scatter/surface plots in **Figure 2.12c**. **Figure 2.12d** presents a more intuitive distribution of the amplitude and dwell time.

The capture rate, or the frequency of the translocation, is another important information, which can describe the analytes that approach the nanopore and successfully pass through. The rate of events can be roughly estimated by the counting the number of events (N) over a long time T:

$$r = \frac{N}{T} \tag{2.5}$$

If the time interval becomes extremely short (ΔT), the probability of finding an event can be calculated as r ΔT. Herein, the probability that no event can be found in ΔT is 1- r ΔT. If the trace with a period T can be divided into n numbers of ΔT (T=n ΔT), the probability of no events in this period can be calculated by the equation:

$$P_0(T) \approx (1 - r\,\Delta T)^n \tag{2.6}$$

Herein, if the time period is long enough which means n is big enough, the equation can be written as:

$$P_0(T) \approx \lim_{n\to\infty}(1 - r\,\Delta T)^n = e^{-rt} \tag{2.7}$$

The probability of having 1 pulse intervals of length *t* can be further calculated by:

$$l_1(t)dt = P_0(T) * rdt \tag{2.8}$$

Combining **Equation 2.7** and **Equation 2.8**, the distribution of intervals between successive events can be illustrated by the following equation:

$$l_1(t) = re^{-rt} \tag{2.9}$$

Where l_1(t) is the probability of having 1 pulse intervals of length *t*. *r* represents the capture rate, and *t* is a given time length.

The plot of this function is shown in **Figure 2.12e**. Therefore, the capture rate can be calculated. The density of the events in the trace can be further illustrated by a cumulative histogram, **Figure 2.12f**.

It is essential to assess the noise level in nanopore experiment. Both the nanopores and the patch-clamp amplifier are the sources of ionic current noise, such as thermal noise, shot noise, surface protonation noise, flicker noise, dielectric noise and input

capacitance noise. These noises have different frequency where a power spectrum density (PSD) can be used to assess each of them, **Figure 2.12g**.

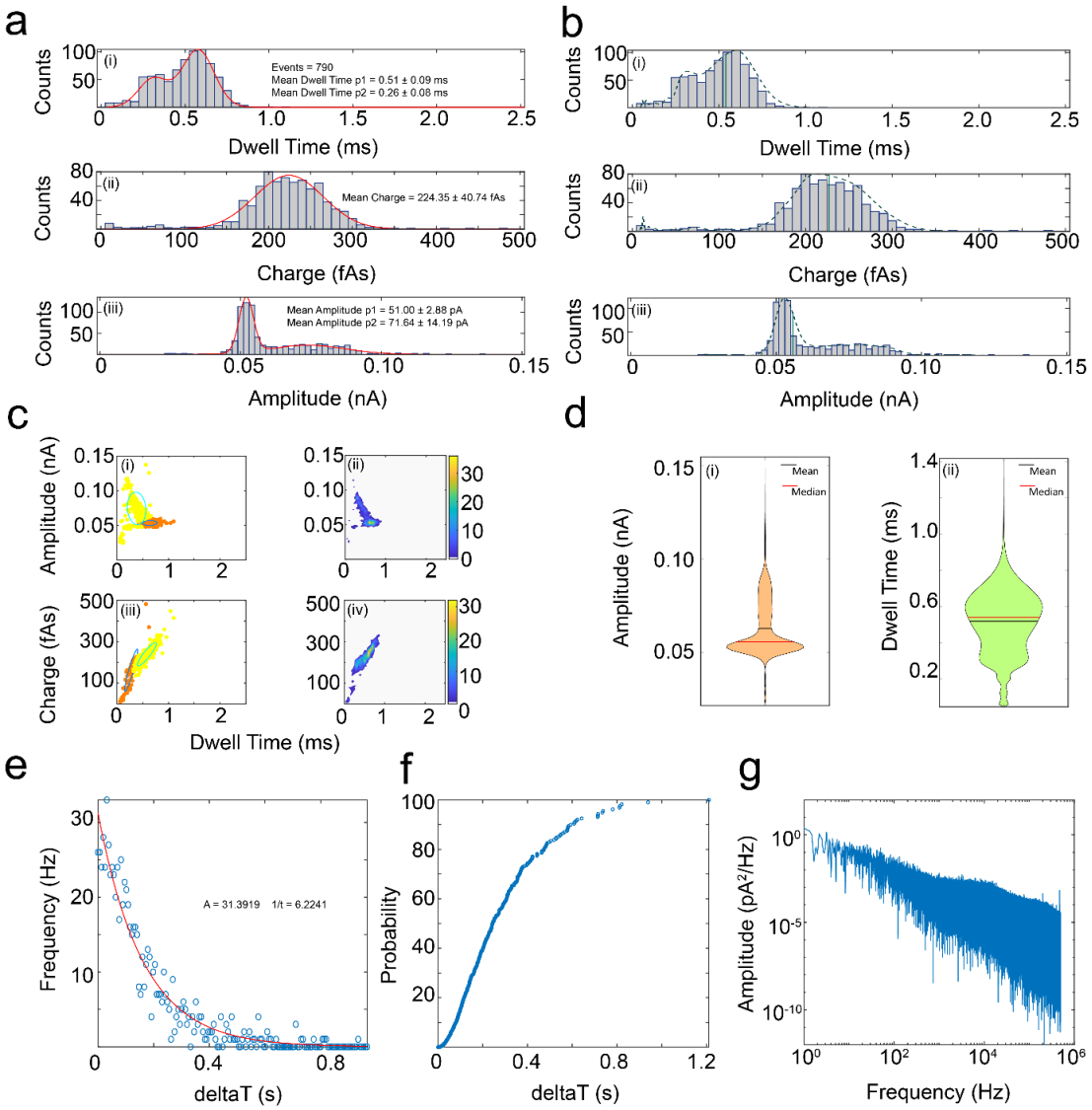


Figure 2. 12 Statistics of the translocation events from the current-time trace of 10 kbp DNA translocation analysed by the nanopore app. **(a)** Histogram of the dwell time, the integral area, and the current amplitude. The red lines represent the distribution fitting curves. **(b)** The green dashed line indicates the Kernal density of the distributions across three parameters. **(c)** The scatter plots and surface plots of current amplitude/charge along with the dwell time. **(d)** The distribution of the current amplitude and dwell time, with the mean and median of the whole data set. **(e)** The calculation of the capture rate using the stochastic process of the time between the events (delta *T*). **(f)** The cumulative histogram of the delta *T*. **(g)** The power spectral density of the current-time trace which is shown in Figure 2.10.

2.4 References

1. Wang, Y. X.; Velmurugan, J.; Mirkin, M. V.; Rodgers, P. J.; Kim, J.; Amemiya, S., Kinetic Study of Rapid Transfer of Tetraethylammonium at the 1,2-Dichloroethane/Water Interface by Nanopipet Voltammetry of Common Ions. *Analytical Chemistry* **2010,** *82* (1), 77-83.

2. Gong, X. Q.; Patil, A. V.; Ivanov, A. P.; Kong, Q. Y.; Gibb, T.; Dogan, F.; deMello, A. J.; Edel, J. B., Label-Free In-Flow Detection of Single DNA Molecules using Glass Nanopipettes. *Analytical Chemistry* **2014,** *86* (1), 835-841.

3. Steinbock, L. J.; Otto, O.; Chimerel, C.; Gornall, J.; Keyser, U. F., Detecting DNA Folding with Nanocapillaries. *Nano letters* **2010,** *10* (7), 2493-2497.

4. Wanunu, M., Nanopores: A journey towards DNA sequencing. *Physics of life reviews* **2012,** *9* (2), 125-58.

5. East, G. A.; del Valle, M. A., Easy-to-make Ag/AgCl reference electrode. *Journal of Chemical Education* **2000,** *77* (1), 97-97.

6. Cadinu, P.; Campolo, G.; Pud, S.; Yang, W. N.; Edel, J. B.; Dekker, C.; Ivanov, A. P., Double Barrel Nanopores as a New Tool for Controlling Single-Molecule Transport. *Nano letters* **2018,** *18* (4), 2738-2745.

7. Al Sulaiman, D.; Cadinu, P.; Ivanov, A. P.; Edel, J. B.; Ladame, S., Chemically Modified Hydrogel-Filled Nanopores: A Tunable Platform for Single-Molecule Sensing. *Nano letters* **2018,** *18* (9), 6084-6093.

CHAPTER 3

The nanopore extended field-effect transistor fabrication

Synopsis

This chapter presents a novel device, namely the nanopore extended field-effect transistor (nexFET), which is a combination of a solid-state nanopore and a field-effect transistor (FET). In this device, a thin polypyrrole (PPy) thin layer is deposited on the nanopipette tip by electropolymerisation and acts as an electrical gate at the nanopore. During the fabrication process, the nanopore size can be tuned precisely by real-time controlled electrodeposition. The gate layer can be operated by applying a voltage to the conductance polymer, where the surface charge of the nanopore and local electric field can be affected, leading to a change in the ionic current and modulation of the transport properties of the nanopore.

Part of this chapter has been published as **Ren R**, Zhang YJ, Nadappuram BP, Akpinar B, Klenerman D, Ivanov AP, Edel JB, Korchev Y (2017) Nanopore extended field-effect transistor for selective single-molecule biosensing. Nature Communications 8, Article number: 586 (2017), doi:10.1038/s41467-017-00549-w.

3.1 Introduction

Development of ultrasensitive micro/nano biosensors has been gaining in prominence in part due to the need to develop strategies for early-stage clinical diagnosis. Improvements in instrumentation and methods are undergoing a revolutionary transition from electrochemical/optical to nano-electronic technologies. Apart from nanopores (as discussed in **Chapter 1**), FET-based biosensors have attracted considerable attention because of their potential for miniaturisation, parallel sensing (e.g. sensing arrays), fast response times, and facile integration with electronic circuits and systems, such as complementary metal-oxide semiconductors (CMOS)[1, 2].

FETs consists of drain and the source electrodes and a semiconductor channel between them. The conductivity of this semiconductor channel can be modulated by another electrode, the gate. Almost all FET-based devices work on the following principle: When an applied potential on the gate is changed, the electric field induces band bending of the semiconductor channel. Depending on the material, the change in the gate voltage results in the change of channel carrier concentration, such as accumulation, depletion, or enhancement. In biosensors that based on an ion-sensitive FET (ISFET)[3], the charge of the gate can be modulated by other factors, such as the charge of biomolecules or solution potentials (e.g. pH value). These factors influence the status of channel carriers and make the current-voltage characteristics shift positively or negatively. To date, a variety of label-free FET biosensors have been developed to sense DNA[4-6] and proteins[7-9] – see **Figure 3.1**.

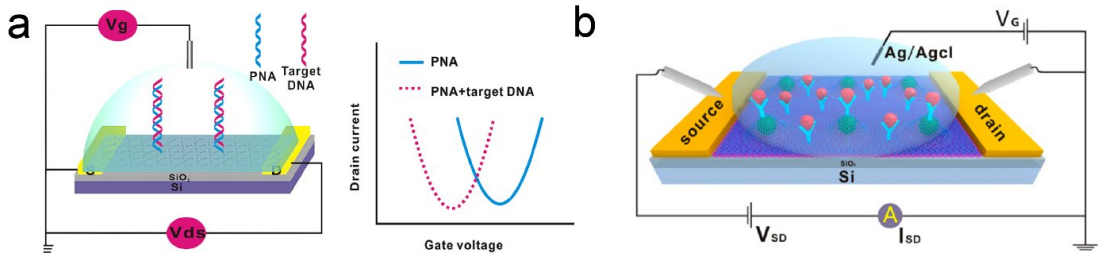


Figure 3. 1 Label-free FET based biosensors. The FET biosensors for DNA (a) and protein, (b) label-free detection. Figure 3.1a adapted from reference 4, and Figure 3.1b adapted from reference 7.

However, FET biosensors are often diffusion-limited and rely on passive transport. Furthermore, the detection sensitivity for large biomolecules is also hampered by the Debye screening length.[10-12] Unlike FETs, nanopore biosensors have additionalbenefits of allowing active transport, enabling the capture of biomolecules to the lumen of the sensor head once the analyte is confined within the capture radius.[13-15] However, active and effective nanopore detection of small biomolecules has still been remarkably

elusive due to their size and fast transport through the nanopore.[16] Some of these limitations can be addressed by functionalising the nanopore surface with hydrophobic, and positively or negatively charged residues acting as binding sites at the nanopore.[17-20] These functional sites can be used not only to slow down transport molecular transport (and hence increase signal to noise ratios and limits of detection), but also allow greater selectivity. However, functionalisation strategies are often challenging and require careful optimisation. It is therefore still a fundamental challenge to develop easy methods to fabricate and functionalise label-free biosensors which can target and measure elusive biological molecules such as nucleic acids, and proteins, with high sensitivity and selectivity while at the same time addressing the limitations described above.

Recently, there has been increasing interest in bringing together both FETs and nanopores to develop ionic-FETs to undertake this challenge.[21-24] The physical principles of ionic FETs are similar to that of the more conventional semiconductor FETs with the exception that the gate medium is made up of ions rather than electrons or holes. A potential advantage of using such platforms is that it could enable improved selectivity and controllable molecular transport; however, challenges remain including fabrication, operational stability and ease of functionalisation. A step towards achieving this goal has been in the development of conducting polypyrrole (PPy) FET nanosensors on the tips of multi-barrel nanopipette.[25]

In this chapter, the possibility to combine the advantages from both FET and nanopore platforms, using a novel nanopipette-based PPy ionic-FET, dubbed Nanopore Extended Field Effect Transistor (nexFET)[26] is discussed. I describe the fabrication process and characterise the nexFET (**Figure 3.2**). The sensing element of the nexFET is located on the tip of a double-barrel nanopipette. Through real-time current control, the nanopore size of the nexFET can be tuned to a wide range of sizes, which can match different targets. By controlling the gate voltage of the device, the current between the drain and source can be modulated.

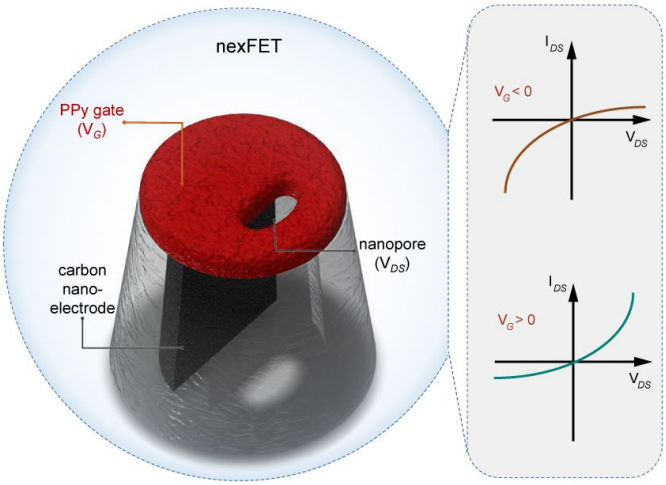


Figure 3. 2 Schematic of the nexFET. The nexFET platform is a functionalised nanopore-based transistor device. The transistor is located on a double-barrel quartz nanopipette tip, with one barrel filled with a carbon nanoelectrode. On the cross-section of the nanopipette, the carbon covers the entire area. Therefore, the PPy can coat the conductive carbon area by electropolymerisation. With the ionic current feedback control, which can be monitored by the current decreasing of the second (open) barrel, the pore size can be precisely tuned. The generated ring-like PPy layer acts as the gate electrode of the FET, whereas the open nanopore acts as the source-to-drain channel. Controlling the PPy gate voltage via the carbon nanoelectrode, the current between the source and drain can be manipulated.

3.2 Methods

3.2.1 Fabrication of carbon-coated dual-barrel nanopipettes with one carbon nanoelectrode

Initially dual barrel was pulled using the method described in **Chapter 2** and characterised by SEM and TEM.

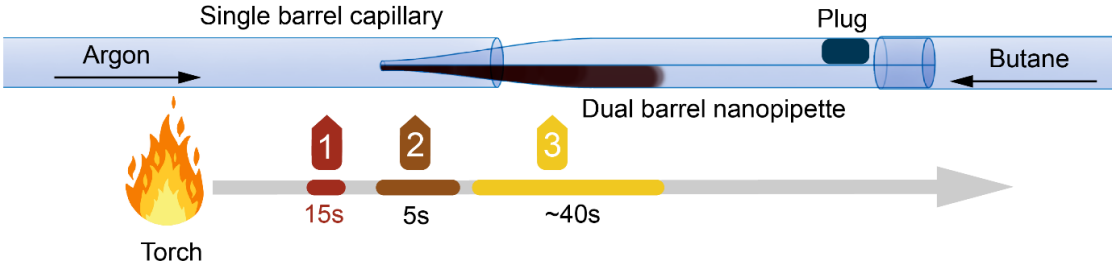


Figure 3. 3 Schematic of carbon pyrolysis in the nanopipette. The time marked in the figure represents the duration each location was heated.

In this experiment, I improved the fabrication protocol that was previously published by our group.[27] Specifically, to deposit carbon only in one barrel, a plug was used to seal off the 2nd barrel. Then, a flow of butane/propane was filled in the barrel and heated with a butane torch under a convective Argon flow, which prevented the deposited carbon from being oxidised by the air under high temperatures. Within the inert atmosphere and high temperature, butane/propane can be pyrolysed to form a conductive solid layer made up of carbon. To coat the whole cross-section of the nanopore rather than only one barrel, it is essential to heat location 1 for at least 15 s initially and then gradually move closer to the tip area (location 2 and 3), as illustrated in **Figure 3.3**. The entire fabrication process took approximate 60 s.

After fabrication, the open nanopore was assessed by cyclic voltammetry (CV) to characterise the approximate pore size in 100 mM of KCl (Sigma-Aldrich) before PPy polymerisation. The carbon nanoelectrode was examined by linear sweep voltammogram (LSV) to check the carbon quality and area by use of the redox mediator ferrocenemethanol (Sigma-Aldrich) in 100 mM KCl.

3.2.2 PPy deposition with real-time feedback control

Pyrrole (Py, Sigma-Aldrich) was stored under an inert atmosphere, and the quality was always checked before use. The colour of the liquid should be transparent. Otherwise the pyrrole needs to be purified by column chromatography (using Al_2O_3). PPy was electropolymerised on the conductive surface of the carbon-coated dual-barrel nanopipettes by applying a 600 mV bias (This was determined by the voltage of the oxidation peak on the CV scan from -800 mV to 800 mV) on the carbon nanoelectrode using a solution of 500 mM Py, 200 mM of lithium perchlorate ($LiClO_4$, Sigma-Aldrich), and 100 mM of perchloric acid ($HClO_4$, Sigma-Aldrich) in DI water. At the same time, the open barrel was filled with 100 mM of KCl, and a small bias (100 mV) was applied to monitor the open pore current, **Figure 3.4**. Real-time feedback control is crucial as the conductivity of the nanopore is tightly linked to its size. Using this approach, it is ensured that the PPy did not over polymerise and cover the pore and were able to ensure that the nexFET was fabricated with a controllable and reproducible size nanopore. After the PPy polymerisation, the nexFET was stabilised in 100 mM HCl. A CV was performed between -300 mV and 300 mV until the current was steady.

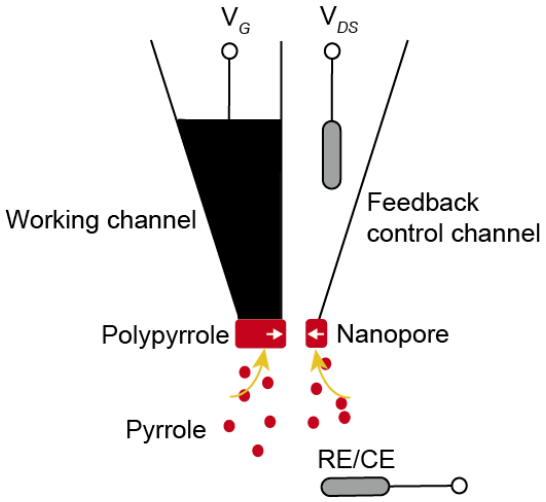


Figure 3. 4 Schematic of the PPy electropolymerisation with real-time feedback control. When the carbon deposited dual-barrel nanopipette inserted into the Py electrolyte, the PPy were generated on the conductive surface with V_G = 600. A V_{DS}=100 was used to generate a small drain-source current, which were used to monitor the nanopore size.

3.2.3 Electrical characterisation of the nanopore extended field-effect transistor

The *I-V* characteristics and the FET behaviour of the nexFET were measured using a Multiclamp 700B amplifier (Molecular Devices). The working electrode made up Ag/AgCl was used to apply the drain-source voltage and inserted inside the open barrel of the nexFET. The counter electrode was also made from Ag/AgCl, and it was placed into the bath. A silver wire was incorporated into the carbon and was used to bias the PPy gate. All characterisation experiments were performed in Tris-EDTA pH-buffered KCl electrolytes. The methods used in data recording and analysis is described in **Chapter 2**, **Section 2.3**.

3.3 Result and discussion

3.3.1 Fabrication and characterisation of the nexFET

The nexFET was fabricated using real-time feedback controlling PPy deposition process on a double-barrel nanopipette tip whose one barrel was filled with carbon nanoelectrodes. **Figure 3.5** illustrates the schematics and the SEM images of each step.

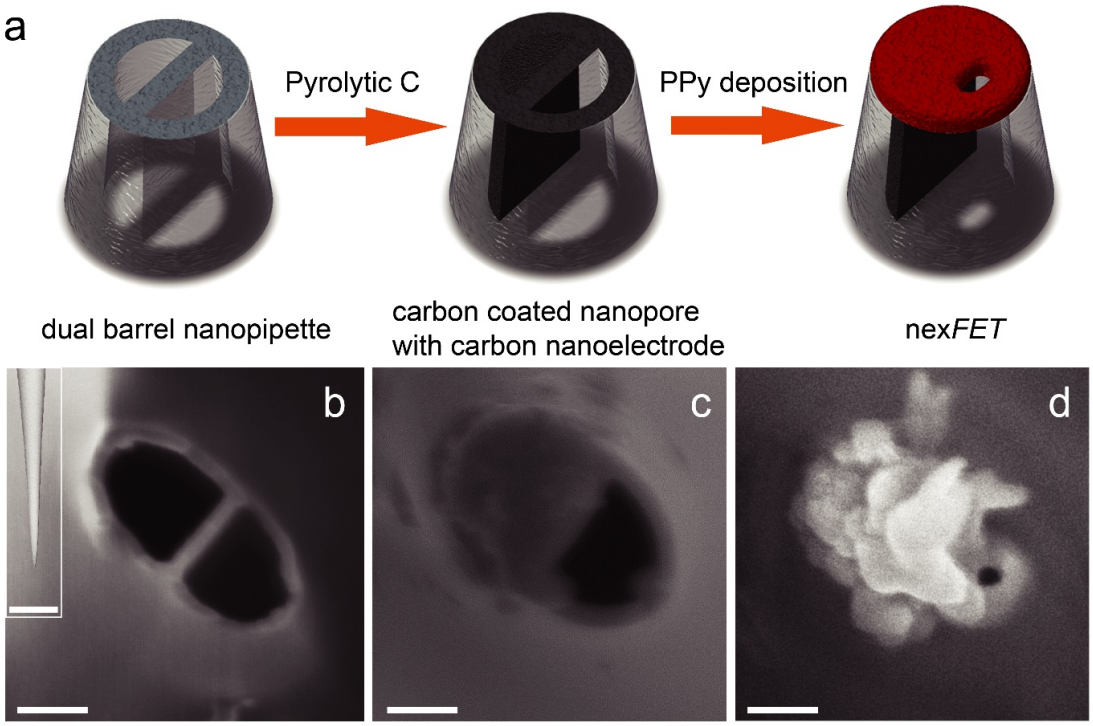


Figure 3. 5 The fabrication process and the corresponding SEM characterisations of each step. **(a)** The nexFET is fabricated in dual-barrel quartz nanopipettes by a pyrolytic carbon deposition in one of the barrels, followed by electrodepositing of PPy at the carbon-coated nanopipette tip. SEM images at each stage of the fabrication process are shown in **(b)** quartz double barrels after nanopipette pulling (scale bar 100 nm, inset 20 µm). **(c)** One barrel coated with carbon after pyrolytic deposition (scale bar 100 nm) and, **(d)** electropolymerized PPy, acting as a gate electrode, deposited on top of the carbon electrode and surrounding the opening of the nanopore (scale bar 100 nm). Some of the SEM characterisations was conducted by Bernice Akpinar. The figures adapted from reference 26.

3.3.1.1 Pyrolytic carbon deposition

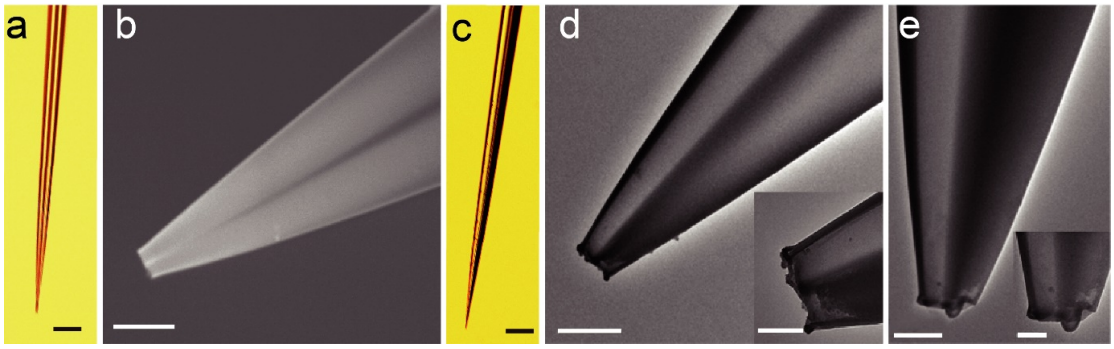


Figure 3. 6 Optical, SEM, and TEM side-view images of the nanopipette. **(a)** Optical microscopy characterisation and **(b)** SEM characterisation of a representative quartz double-barrel nanopipette after pulling from a dual-barrel quartz capillary. **(c)** Optical microscopy characterisation and **(d, e)** TEM characterisation of a nanopipette after pyrolytic carbon deposition. One barrel is still open, and the other barrel is filled with carbon nanoelectrodes (the black barrel in the optical image and the darker barrel in the TEM image). The 'incision' of the plain dual-barrel nanopipette is sharp and clear, while the cross-section of the nanopipette after the carbon deposition is rough, which may relate to a crown-like carbon layer located around the nanopore. The scale bars of all-optical images are 100 µm, while those of the

SEM image is 500 nm, and those of all TEM images are 500 nm, and insets are 200 nm. The TEM characterisation was conducted by Bernice Akpinar.

The nanopipette was pulled from quartz capillaries by a laser-based nanopipette puller, and the shape was checked using an optical microscope (**Figure 3.6a**). The diameter of each barrel of the nanopipette was approximately 100 nm, which was characterised by SEM imaging (**Figure 3.6b, Figure 3.6b**). Then, I filled one barrel of the nanopipette with carbon and 'smoked' the cross-section to generate a ring-like shape by pyrolysis of the butane (**Figure 3.5c, Figure 3.6d–e**).

In our previous study[27], one barrel of the double-barrel nanopipette was filled with pyrolytic carbon by the pyrolysis of the butane gas (**Figure 3.7a[i]**). However, the following PPy deposition step would generate a bulb-shaped polymer due to the limited conductive area. The resulting device lacked the gating control, as the drain-source channel would still be dominated by the glass wall rather than the PPy gating layer. For this reason, the whole nanopipette cross-section must be coated by carbon (**Figure 3.7a[ii]**). This allows for PPy to be coated along with the surroundings of the nanopore. The improved pyrolytic carbon deposition process is described in the method section, as I changed the heating position, heating time, argon flow, and butane flow.

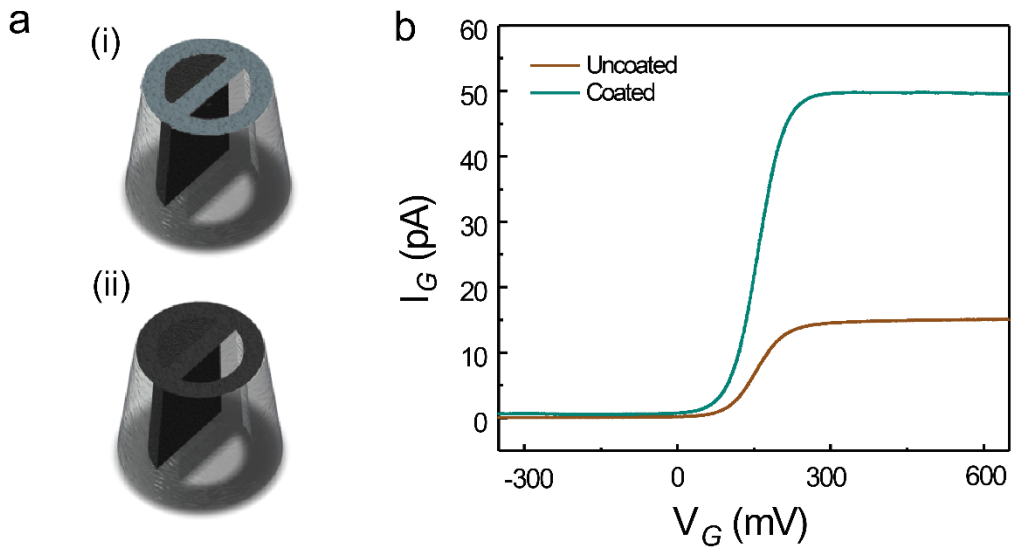


Figure 3. 7 Linear sweep voltammogram characterisation of the carbon area. **(a)** Schematic diagram of carbon-layer **(i)** uncoated and **(ii)** coated dual-barrel nanopipette tips with one carbon nanoelectrode. **(b)** The LSV for the redox of 1 mM of ferrocene methanol at the carbon surface of the carbon-coated and uncoated nanopipettes. A difference of nearly three times in the current plateau confirmed that the carbon-coated nanopipette owns a larger conductive area around the open barrel for the deposition of the PPy gate.

The steady-state limiting current in electrochemical measurements was used (**Figure 3.7b**) to validate whether the nanopipette was filled with the carbon electrode and coated with a carbon layer. The smooth and steady curve of the ferrocene methanol

redox on the carbon electrode by linear sweep voltammograms indicates that the generated amorphous carbon was smooth and homogenous. The carbon surface, which is the electrochemically active area, can be calculated by **Equation 3.1**[28, 29]:

$$r = \frac{I_{steady-state}}{4.64nFCD} \qquad (\mathbf{3.1})$$

In this equation, r is the radius of the electrode area, n is the number of electrons transferred in the ferrocenemethanol oxidation process (1-electron reduction), F is the faraday constant, C is the concentration of ferrocenemethanol (1 mM), and D is its diffusion coefficient in 100 mM of KCl. This equation estimates the nanoelectrode active area, which is equal to the carbon surface, indicating that the carbon area of the carbon-coated (or 'smoked') nanopipette is approximately threefold to the uncoated nanopipette's.

To further confirm the ring-like carbon shape on the nanopipette tip, the TEM and energy-dispersive X-ray spectroscopy (EDS) were utilised to characterise an over-smoked nanopipette (**Figure 3.8**). From the TEM images, it is evident that the carbon-filled one barrel and brimmed over the nanopipette. The roughness of the cross-section demonstrates that the smooth glass surface is covered by the pyrolytic carbon. From element analysis, it is also clear that carbon dominates in one of the barrels and along the tip area.

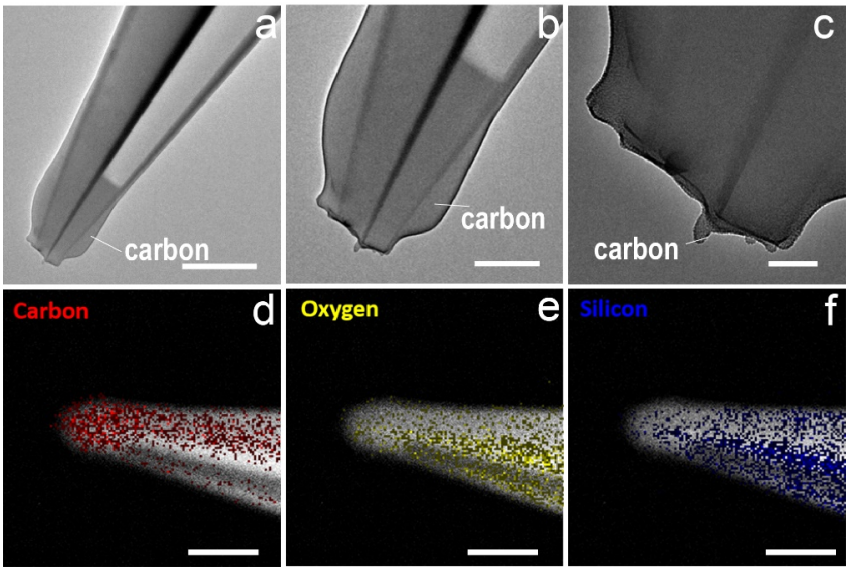


Figure 3. 8 Elemental analysis of a carbon-deposited nanopipette. **(a-c)** TEM images and elemental analysis of a carbon-deposited nanopipette. For elemental analysis, carbon was over- deposited (higher butane flow-rate and lower argon flow-rate were used during pyrolytic deposition), which confirmed that carbon deposition occurs on the tip of the nanopipette. Here ring-like (or crown-like) carbon structures are observed on the tip of the nanopipette. Element mapping analyses show the existing of **(d)** carbon, **(e)** oxygen, and **(f)** silicon distribution at the tip of the nanopipette. The TEM and elemental mapping characterisation were conducted by Bernice Akpinar. Scale bar: **(a)** 1 µm, **(b)** 200 nm, **(c)** 100 nm, **(d-f)** 1 µm.

Having demonstrated the conductive surface of the nanopipette with carbon nanoelectrodes, I next use it as the electrode and substrate to control the growth of a PPy layer.

3.3.1.2 Polypyrrole deposition

Considering that the PPy layer acts not only as of the gate of the FET but also as the nanopore, precise control of the polymer deposition is essential. To achieve this, real-time feedback control was applied, so that the electropolymerisation process can be stopped at any stage to generate nanopores of different sizes. The current in the open barrel (I_{DS}) was used to monitor the extent of how much the nanopore decreases in size in real-time. Therefore, the potential applied to the carbon electrode, which was used to oxidise Py to PPy, could be cut off precisely when the pore size decreased to the expected value. **Figure 3.4** presents a schematic of the set-up: the dual barrel nanopipette with one carbon nanoelectrode and carbon-coated surface was immersed in the electrolyte containing Py; one working electrode (Ag) linked the carbon nanoelectrode, while the other working electrode (AgCl) was placed inside the open barrel, and the counter/reference electrode (AgCl) was placed outside of the nanopipette. With more PPy deposited on the nanopipette, the current on the carbon electrode increased as a result of enlargement of the conductive area, while the current on the open barrel decreased because of the decrease in pore size (**Figure 3.9**).

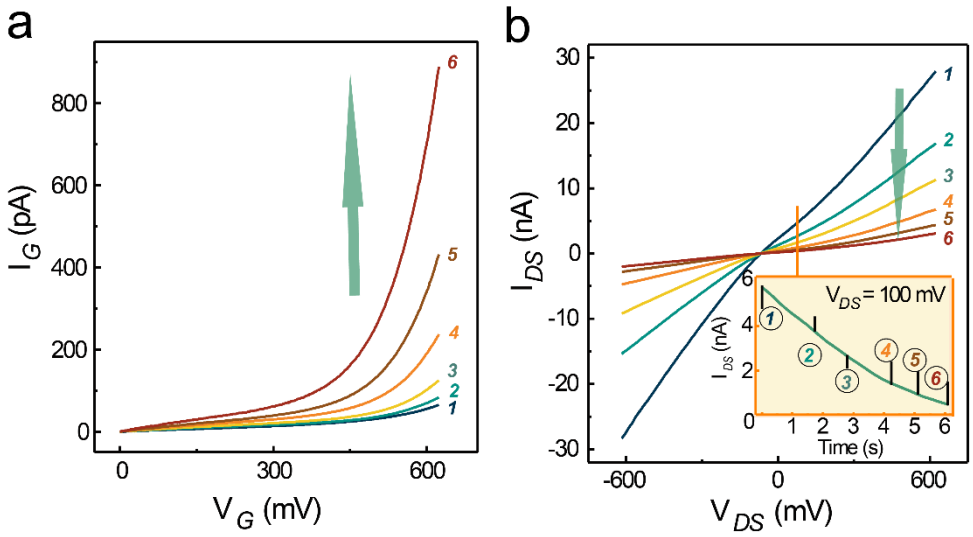


Figure 3. 9 The current change of each channel during the electrodeposition. **(a)** The gate current and voltage plots and **(b)** the drain-source (or nanopore channel) current and voltage plots in a representative nanopipette monitored overtime during PPy deposition. The gate current gradually increased with each PPy electropolymerized cycle, indicated by number and arrow. The *I-V*s of the drain-source (nanopore) channel were also monitored. The conductance of this channel was gradually decreased with each corresponding PPy electropolymerized cycle, indicated by number and arrow. The inset of (b) illustrates that the initial current of the drain-source channel (1) decreased over time with the electropolymerisation process under a 100-mV voltage.

This method with real-time feedback control allows me to fabricate nexFETs with similar characteristics. For example, *I-V* curves for five nanopipettes before PPy deposition show that the initial nanopores varied in size and geometry, which is caused by the pulling process (**Figure 3.10a**). PPy electropolymerisation was performed until the feedback current reached the set point. For example, the feedback current of the five nanopipettes kept decreasing under a 100-mV bias and finally reached the setpoint, which is 1 nA (**Figure 3.10b**). Finally, it can be seen in **Figure 3.10c** that the open pore current post polymerisation is very similar.

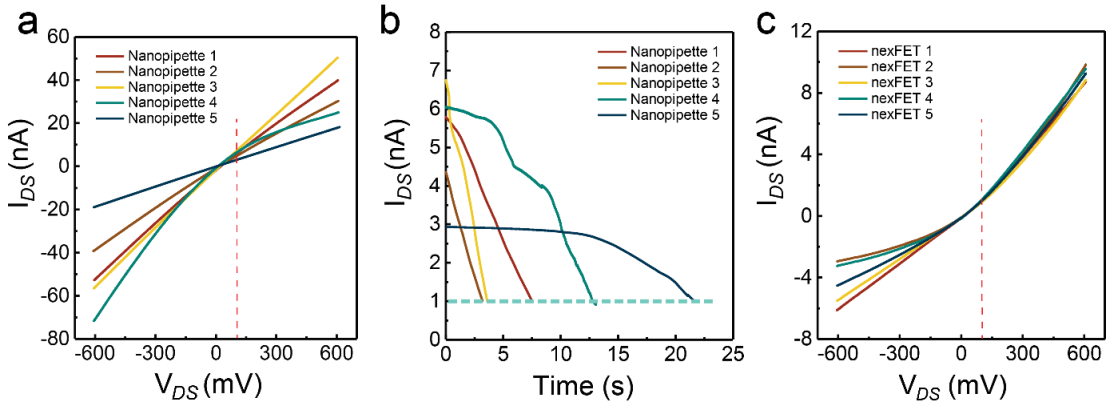


Figure 3. 10 Nanopore characterisation before and after the real-time controlled electropolymerisation. **(a)** The *I-V* characteristics of five representative nanopores (drain-source), which exhibit varied initial ion transport characteristics, indicated by the differences in the size and morphology of the nanopores. **(b)** By monitoring the current decrease of the drain-source channel over time (at 100 mV of the applied voltage), which demonstrates the decrease in nanopore conductance, the same nexFET devices could be generated when the I_{DS} reached the set-point current (1 nA in this example). **(c)** The *I-V* characteristics of the five generated devices by using the real-time feedback control of the electrodeposition indicates the high reproducibility of the fabrication. The measurements of the I-V characteristics were performed in 100 mM of KCl, 1 mM of Tris-EDTA, pH 7.4.

Being able to decrease the pore size is a useful feature. For example, the initially pulled nanopipette had a nanopore of approximately 100 nm in diameter (**Figure 3.11a**), which is too large to detect most biomolecules. PPy deposition could bring the nanopore size down to 20 nm (**Figure 3.11**). The *I-V* characteristic and the *I-t* feedback curve demonstrate that this PPy deposition/pore shrink process is fully controllable and tuneable. The actual pore size can be validated by SEM images. However, the majority of resistance drops and ion transport through the nanopore are mainly dependent on the narrowest part, which is difficult to visualise with SEM, especially when the pore is sub-20 nm.

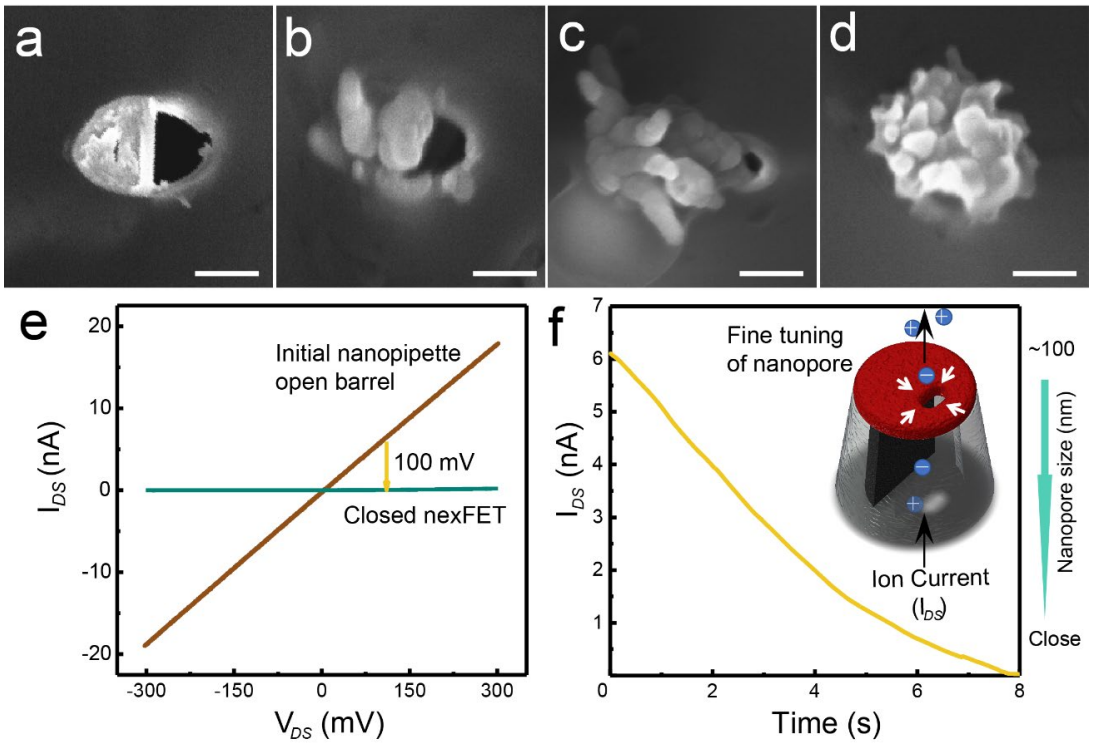


Figure 3. 11 Nanopipette characterisation at different stages of nexFET fabrication. SEM images of **(a)** carbon-filled nanopipettes with a 100 nm open barrel, **(b)** nexFET with ~80 nm nanopore after PPy deposition, **(c)** nexFET with ~ 10 nm nanopore after PPy deposition, and **(d)** a fully blocked nexFET after longer polypyrrole deposition. **(e)** representative *I-V* plots showing the change from an open barrel nanopipette (red colour) to a closed nexFET after 8 seconds of PPy deposition (green colour). **(f)** Nanopore current I_{DS} (at 100 mV applied voltage) was measured over time to monitor decreasing nanopore conductance during PPy deposition until the nanopore was fully closed within 8 seconds. Scale bars: 100 nm.

A unique way in which to characterise a nanochannel of such a small size is to measure ion selectivity (cations versus anions) across the nanopore. In detail, if a nanopore is large, then the thickness of the double layer is much less than the nanochannel diameter, and the transport of cations and anions is equal. In contrast, if a nanopore is small, the double layer on the nanochannel/solution interface will affect ion transport and thus contribute to ionic permselectivity (i.e., co-ions are repelled, whereas counter-ions are easily passed through).[30, 31] In our case, ion selectivity can be used to estimate the size of the small nanopore. To examine the ion selectivity, the potential reversal V_{Rev}, which compensates the net current to zero, was measured based on the well-known Goldman-Hodgkin-Katz (GHK) model.[32-34] The reversal potential is related to the selectivity of the pore via the GHK voltage equation:

$$V_{\mathrm{Rev}} = \frac{k_B T}{e} \ln\left(\frac{(Sc_{High}) + c_{Low}}{(Sc_{Low}) + c_{High}}\right) \qquad (\mathbf{3.2})$$

where S is the selectivity ratio of the cations versus anions, c_{high} and c_{low} are the solution concentrations on both sides of the nanopore, T is the electrolyte temperature,

k_B is the Boltzmann constant, and e is the electron charge. In our case, c_{high} is 100 mM of KCl filled inside the nanopipette, whereas c_{low} is 33.3 mM of KCl outside of the nanopore. If a whole PPy deposition was divided into four steps, then the high ion selectivity of the generated nanopore began to appear after the second PPy deposition step (**Figure 3.12**). The nanopore size could then be further estimated by conductivity. Unlike SEM characterisation, this method does not break or contaminate the nanopipette and remains functional.

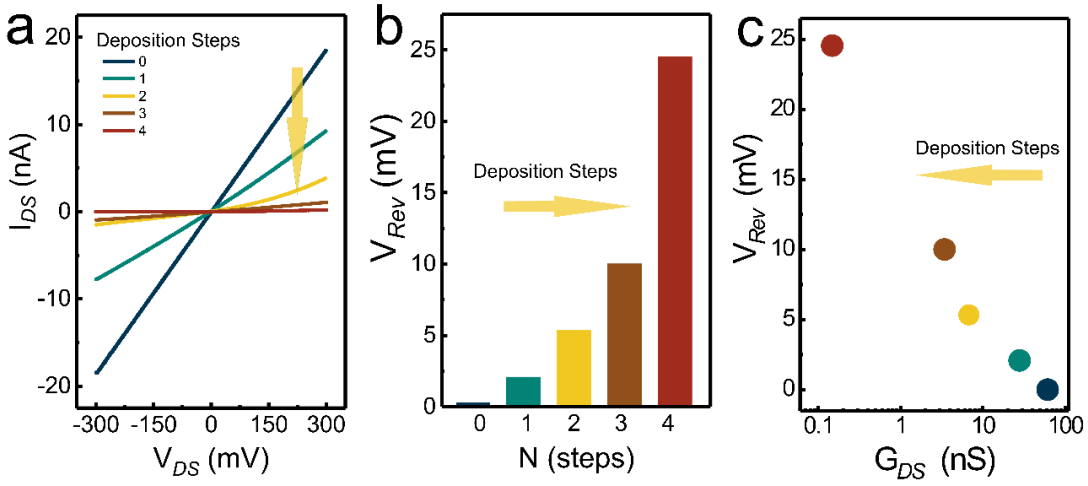


Figure 3. 12 nexFET ion selectivity characterisation. **(a)** I-V plots, and **(b-c)** ion-selectivity of nexFET nanopore at different steps of PPy deposition on the tip of the nanopipette. The ion selectivity is measured as a reversal potential with a 3 times KCl concentration gradient (inside/outside ratio = 100 mM/ 33.3 mM) across the nexFET. The deposition steps are colour coded identically in all plots. Step 0 is the initial drain-source *I-V* of the open-barrel of the nanopipette before PPy deposition. Following deposition of PPy on the tip, the ion current rectification ratio and ion selectivity increases, while nanopore conductance decreases.

3.3.2 nexFET performance

The gating behaviour of a nexFET was demonstrated by monitoring the ICR of the nanopore channel. Theoretically, the distributions of the ions on the electrical diffusion layer can be manipulated by the gate voltage, V_G. The ICR of the nanopore channel (or drain-source channel) can thus be affected. **Figure 3.13** illustrates the *I-V* characteristics of the drain-source channel under different gate voltages at different ionic strengths. It is obvious that in each electrolyte, the drain-source current, I_{DS}, can move from negative to positive rectification by manipulating the V_G from negative to positive, which corresponds to n-type FET behaviour.

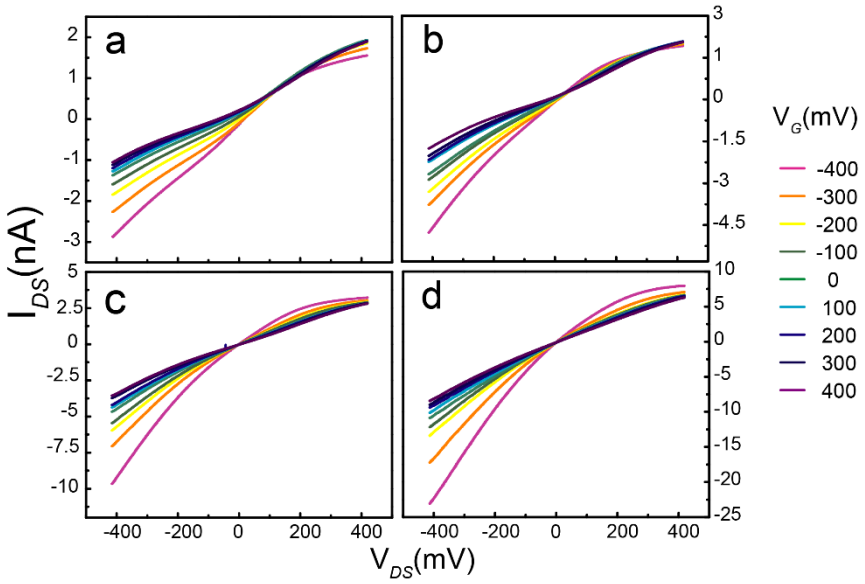


Figure 3. 13 Ionic transport (nanopore) dependence on applied gate voltage in the nexFET. I_{DS}-V_{DS} characteristics were measured at KCl concentration of (a) 1 mM, (b) 10 mM, (c) 100 mM, and (d) 1 M, respectively.

To further validate the FET behaviour, experiments were performed at varying V_G and V_{DS} at different salt concentrations (**Figure 3.13, Figure 3.14**). In this measurement, the fabricated nexFET was filled with 1 mM KCl as well as the bath filled with same electrolyte. Then, the I_{DS}-V_{DS} curves under each gate voltage were obtained. To observe the FET behaviour under different ionic strength, I measured the I-V characteristics of the nexFET also in 10 mM, 100 mM and 1 M electrolyte.

It is known that conventional transistors have a stronger field effect at low ionic strength solutions. The reason is that the thickness of the electrical diffusion layer is approximately equal to the Debye length, which is affected by the environmental ion concentration (details have been discussed in **Chapter 1**). In short, the diffusion layer is inversely proportional to the salt concentration. An approximate relationship can be represented by the following equation: [35, 36]

$$\sigma = \frac{0.3}{\sqrt{c}} \qquad (3.3)$$

where σ is the Debye length (in nm), and c is the salt concentration (in mol/L). From this equation, the Debye length is about 0.3 nm at 1 M KCl, whereas the layer can reach 9.5 nm at 1 mM KCl. This means in the low ionic strength environment; the gating effect is stronger than in a solution with higher salt concentration. The experimental data is also in line with the calculation (**Figure 3.14).** It is evident that the gating control in a lower salt concentration is more efficient, which is reflected by a larger change of the ICR.

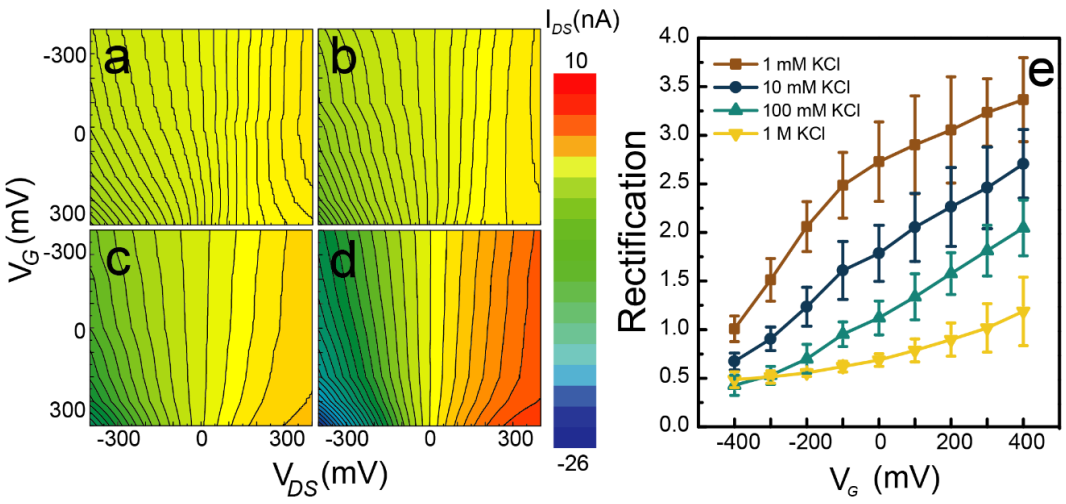


Figure 3. 14 Ionic transport and ionic current rectification of the nexFET under different salt concentrations. **(a–d)** Contour plots of the ionic transport dependence on the applied gate voltage under different KCl concentrations (from 1 mM to 1 M), corresponding to the I-V curves in Figure 3.13. **(e)** The ionic current rectification dependence on the applied gate voltage (V_G), calculated from the I-V curves in Figure 3.13. Error bars represent the standard deviation of three independent experimental repeats with different nexFET devices.

3.3.3 The pH sensitivity of the nexFET

Although nexFETs display similar features to conventional FETs, these nanodevices possess some unique advantages. Polypyrrole can be used as a material for use as a potentiometric pH sensor. This is due to the facile protonation and deprotonation of the amino groups in the polymer. However, these PPy-based pH sensors have limitations, such as poor reproducibility and long response times. These weaknesses are mainly caused by the slow protonation and deprotonation process and the difficult transmission of electrons across multiple polymer layers. However, a nexFET can overcome the challenges described above. **Figure 3.15** illustrates the I-V characteristic of the nanopore channel a varying pH. It is clear that in an acidic environment, the I_{DS} displays positive rectification due to the positive surface charge, as is a result of the protonation of PPy. It is worth noting that at each pH, the gate voltage can still be used to modulate ion transport through the drain-source channel.

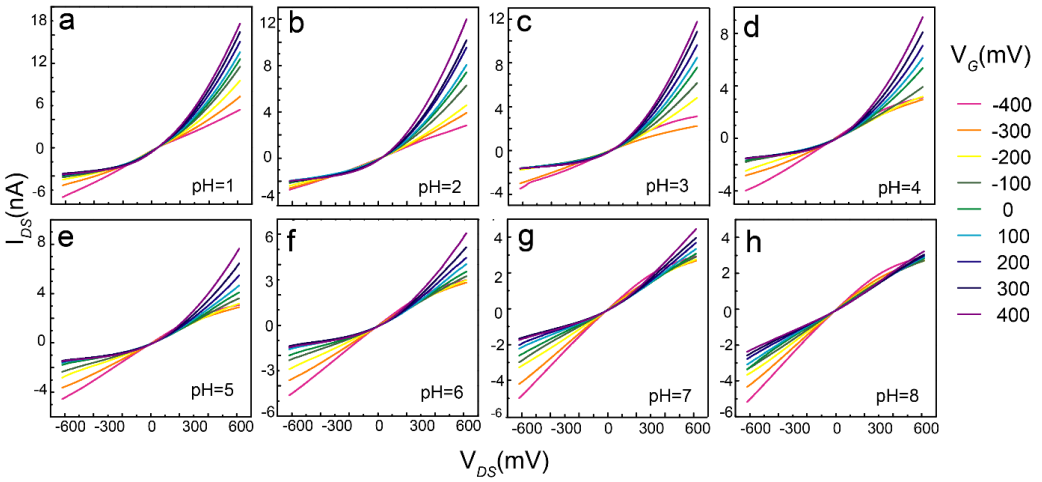


Figure 3. 15 Ionic transport of the nexFET, dependent on the pH. **(a–h)** The *I-V* (drain-source) characteristics of the nexFET at different gate voltages under different pHs. The *I-V* measurements were performed in 100 mM of KCl with a Tris-HCl buffer from pH 1 to pH 8 (a–h) at gate potentials (V_G) ranging from -400 to +400 mV.

Figure 3.16 further reveals how this potentiometric pH sensor works. The nexFET can quickly respond to the pH change; this is a valuable feature for pH sensors. The principle of conventional PPy-based pH sensors is to utilise the electrode to detect the change of polymer charge in different acidic/basic solutions. This process contains protonation or deprotonation, electron transmission, and electrode detection. Herein, the response time of conventional polymer based pH sensor is often several minutes.[37] Different from this conventional process, which is limited by the thickness and quality of the PPy layer, the working principle of a nexFET pH sensor is based on the ICR change of the open channel. In this process, protonation/deprotonation occurs on the ultra-thin PPy layer, which is instantaneous and restorable. The surface charge is then immediately changed; this is reflected in the ICR change. **Figure 3.17** shows a quick response (several seconds) of the nexFET as a highly sensitive pH sensor.

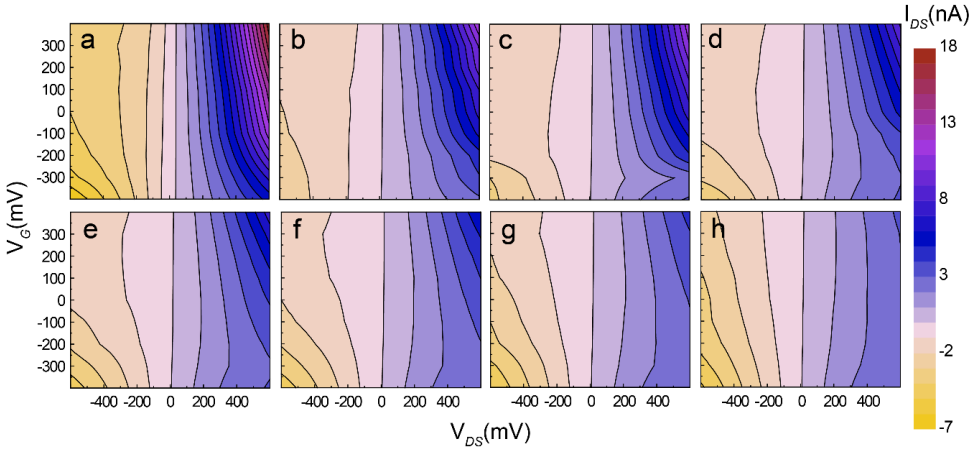


Figure 3. 16 Ionic transport of the nexFET, dependent on the pH. (contour plots). **(a–h)** Contour plots of the ionic transport's dependence on the applied gate voltage under different pHs, corresponding to the

I-V curves in Figure 3.15. The measurements were performed in 100 mM of KCl with a Tris-HCl buffer from pH 1 to pH 8 (a–h) at gate potentials (V_G) ranging from -400 to +400 mV.

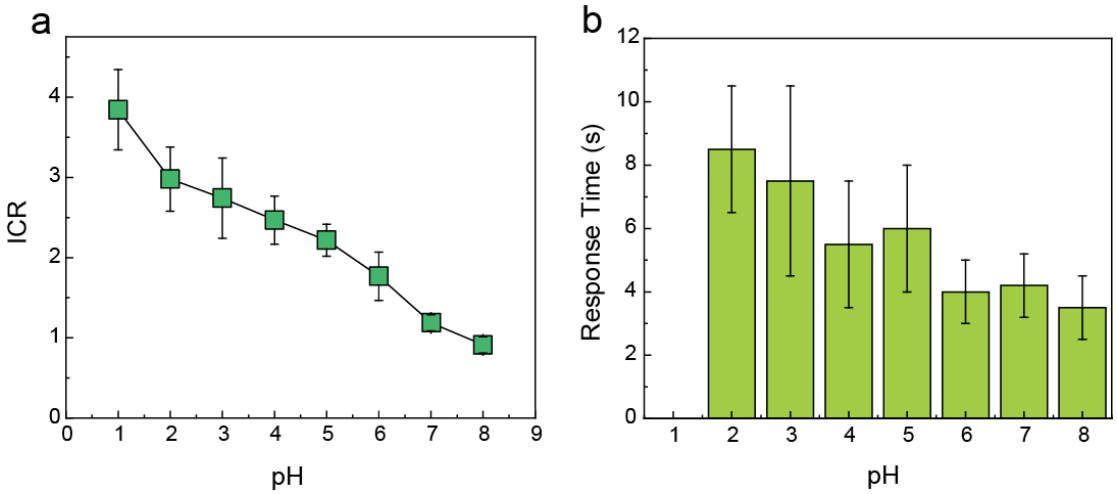


Figure 3. 17 The pH response of nexFET as a pH sensor. (a) The ICR of nexFET under different pH. The measurements are performed in 100 mM of KCl with a Tris-HCl buffer from pH 1 to pH 8. (b) The response time of pH change. The starting test point is pH=1. The quick *I-V* was measured when the buffer was switched to next pH. The response time was recorded as the time between switch buffer and stabilization of the *I-V* curves. Error bars represent the standard deviation of three independent experimental repeats with different nexFET devices.

3.4 Conclusion

In this chapter, I reported on the design and fabrication of the nexFET platform. One barrel of the nanopipette was filled with a carbon nanoelectrode, while the second barrel was empty. A ring-like PPy layer, which acts as both a gate and a nanopore, was deposited and shrank the open nanopore channel. By recording the open pore current, the extent of polymerisation of the PPy layer can be monitored, and the size of the generated nanopore channel can thus be controlled precisely. We have demonstrated that even with different initial nanopores, the nanopore of final generated nexFETs can be shrunk to the same size by using real-time feedback control.

The FET performance of the nexFETs was also validated in different solutions with a wide range of salt concentrations and pHs. The nexFETs exhibited a strong capability of controlling ionic transport by applying bias through the gate electrodes under different conditions. However, I did not fully explore the nanopore character of the nexFET in this chapter. As is known, the adaptable pore size of the nanopore is crucial to detect analytes of different sizes. The nexFET, with fully controllable pore size,

provides a promising platform for sensing a variety of biomolecules at the single-molecule level. Moreover, the biomolecules can be manipulated by the gate electric field. Therefore, in the next chapter, the aim is to maximise the potential of the nexFET in practice, I utilise the nexFET platform to sense DNA and proteins at the single-molecule level with high sensitivity and selectivity.

3.5 References

1. Schoning, M. J.; Poghossian, A., Recent advances in biologically sensitive field-effect transistors (BioFETs). *The Analyst* **2002,** *127* (9), 1137-1151.

2. Poghossian, A.; Schoning, M. J., Label-Free Sensing of Biomolecules with Field-Effect Devices for Clinical Applications. *Electroanalysis* **2014,** *26* (6), 1197-1213.

3. Bergveld, P., DEVELOPMENT OF AN ION-SENSITIVE SOLID-STATE DEVICE FOR NEUROPHYSIOLOGICAL MEASUREMENTS. *Ieee Transactions on Biomedical Engineering* **1970,** *BM17* (1), 70-&.

4. Cai, B. J.; Wang, S. T.; Huang, L.; Ning, Y.; Zhang, Z. Y.; Zhang, G. J., Ultrasensitive Label-Free Detection of PNA-DNA Hybridization by Reduced Graphene Oxide Field-Effect Transistor Biosensor. *ACS nano* **2014,** *8* (3), 2632-2638.

5. Campos, R.; Borme, J.; Guerreiro, J. R.; Machado, G.; Cerqueira, M. F.; Petrovykh, D. Y.; Alpuim, P., Attomolar Label-Free Detection of DNA Hybridization with Electrolyte-Gated Graphene Field-Effect Transistors. *Acs Sensors* **2019,** *4* (2), 286-293.

6. Gao, Z. L.; Xia, H.; Zauberman, J.; Tomaiuolo, M.; Ping, J. L.; Zhang, Q. C.; Ducos, P.; Ye, H. C.; Wang, S.; Yang, X. P.; Lubna, F.; Luo, Z. T.; Ren, L.; Johnson, A. T. C., Detection of Sub-fM DNA with Target Recycling and Self-Assembly Amplification on Graphene Field-Effect Biosensors. *Nano letters* **2018,** *18* (6), 3509-3515.

7. Zhang, C.; Xu, J. Q.; Li, Y. T.; Huang, L.; Pang, D. W.; Ning, Y.; Huang, W. H.; Zhang, Z. Y.; Zhang, G. J., Photocatalysis-Induced Renewable Field-Effect Transistor for Protein Detection. *Analytical Chemistry* **2016,** *88* (7), 4048-4054.

8. Ahn, J. H.; Choi, S. J.; Han, J. W.; Park, T. J.; Lee, S. Y.; Choi, Y. K., Double-Gate Nanowire Field Effect Transistor for a Biosensor. *Nano letters* **2010,** *10* (8), 2934-2938.

9. Hammock, M. L.; Knopfmacher, O.; Naab, B. D.; Tok, J. B. H.; Bao, Z. A., Investigation of Protein Detection Parameters Using Nanofunctionalized Organic Field-Effect Transistors. *ACS nano* **2013,** *7* (5), 3970-3980.

10. Lee, C. S.; Kim, S. K.; Kim, M., Ion-Sensitive Field-Effect Transistor for Biological Sensing. *Sensors* **2009,** *9* (9), 7111-7131.

11. Stern, E.; Wagner, R.; Sigworth, F. J.; Breaker, R.; Fahmy, T. M.; Reed, M.

A., Importance of the debye screening length on nanowire field effect transistor sensors. *Nano letters* **2007,** *7* (11), 3405-3409.

12. Matsumoto, A.; Miyahara, Y., Current and emerging challenges of field effect transistor based bio-sensing. *Nanoscale* **2013,** *5* (22), 10702-10718.

13. Ivanov, A. P.; Actis, P.; Jonsson, P.; Klenerman, D.; Korchev, Y.; Edel, J. B., On-demand delivery of single DNA molecules using nanopipets. *ACS nano* **2015,** *9* (4), 3587-3595.

14. Freedman, K. J.; Otto, L. M.; Ivanov, A. P.; Barik, A.; Oh, S. H.; Edel, J. B., Nanopore sensing at ultra-low concentrations using single-molecule dielectrophoretic trapping. *Nat.Commun.* **2016,** *7*, 10217.

15. Wanunu, M.; Morrison, W.; Rabin, Y.; Grosberg, A. Y.; Meller, A., Electrostatic focusing of unlabelled DNA into nanoscale pores using a salt gradient. *Nature nanotechnology* **2010,** *5* (2), 160-165.

16. Carson, S.; Wanunu, M., Challenges in DNA motion control and sequence readout using nanopore devices. *Nanotechnology* **2015,** *26* (7), 074004.

17. Luan, B.; Stolovitzky, G.; Martyna, G., Slowing and controlling the translocation of DNA in a solid-state nanopore. *Nanoscale* **2012,** *4* (4), 1068-1077.

18. Keyser, U. F., Controlling molecular transport through nanopores. *J.R.Soc.Interface* **2011,** *8* (63), 1369-1378.

19. Wei, R. S.; Gatterdam, V.; Wieneke, R.; Tampe, R.; Rant, U., Stochastic sensing of proteins with receptor-modified solid-state nanopores. *Nature nanotechnology* **2012,** *7* (4), 257-263.

20. Tan, S. W.; Wang, L.; Yu, J. J.; Hou, C. R.; Jiang, R.; Li, Y. P.; Liu, Q. J., DNA-functionalized silicon nitride nanopores for sequence-specific recognition of DNA biosensor. *Nanoscale Research Letters* **2015,** *10*.

21. Haywood, D. G.; Saha-Shah, A.; Baker, L. A.; Jacobson, S. C., Fundamental Studies of Nanofluidics: Nanopores, Nanochannels, and Nanopipets. *Analytical Chemistry* **2015,** *87* (1), 172-187.

22. Nam, S. W.; Rooks, M. J.; Kim, K. B.; Rossnagel, S. M., Ionic Field Effect Transistors with Sub-10 nm Multiple Nanopores. *Nano letters* **2009,** *9* (5), 2044-2048.

23. Siwy, Z. S.; Powell, M. R.; Petrov, A.; Kalman, E.; Trautmann, C.; Eisenberg, R. S., Calcium-induced voltage gating in single conical nanopores. *Nano letters* **2006,** *6* (8), 1729-1734.

24. Xie, P.; Xiong, Q. H.; Fang, Y.; Qing, Q.; Lieber, C. M., Local electrical potential detection of DNA by nanowire-nanopore sensors. *Nature nanotechnology* **2012,** *7* (2), 119-125.

25. Zhang, Y.; Clausmeyer, J.; Babakinejad, B.; Cordoba, A. L.; Ali, T.; Shevchuk, A.; Takahashi, Y.; Novak, P.; Edwards, C.; Lab, M.; Gopal, S.; Chiappini, C.; Anand, U.; Magnani, L.; Coombes, R. C.; Gorelik, J.; Matsue, T.; Schuhmann, W.; Klenerman, D.; Sviderskaya, E. V.; Korchev, Y., Spearhead Nanometric Field-Effect Transistor Sensors for Single-Cell Analysis. *Acs Nano* **2016,** *10* (3), 3214-3221.

26. Ren, R.; Zhang, Y. J.; Nadappuram, B. P.; Akpinar, B.; Klenerman, D.; Ivanov, A. P.; Edel, J. B.; Korchev, Y., Nanopore extended field-effect transistor for selective single-molecule biosensing. *Nature Communications* **2017,** *8*.

27. Takahashi, Y.; Shevchuk, A. I.; Novak, P.; Zhang, Y.; Ebejer, N.; Macpherson, J. V.; Unwin, P. R.; Pollard, A. J.; Roy, D.; Clifford, C. A.; Shiku, H.; Matsue, T.; Klenerman, D.; Korchev, Y. E., Multifunctional Nanoprobes for Nanoscale Chemical Imaging and Localized Chemical Delivery at Surfaces and Interfaces. *Angewandte Chemie-International Edition* **2011,** *50* (41), 9638-9642.

28. Lefrou, C.; Cornut, R., Analytical Expressions for Quantitative Scanning Electrochemical Microscopy (SECM). *Chemphyschem* **2010,** *11* (3), 547-556.

29. Actis, P.; Tokar, S.; Clausmeyer, J.; Babakinejad, B.; Mikhaleva, S.; Cornut, R.; Takahashi, Y.; Cordoba, A. L.; Novak, P.; Shevchuck, A. I.; Dougan, J. A.; Kazarian, S. G.; Gorelkin, P. V.; Erofeev, A. S.; Yaminsky, I. V.; Unwin, P. R.; Schuhmann, W.; Klenerman, D.; Rusakov, D. A.; Sviderskaya, E. V.; Korchev, Y. E., Electrochemical Nanoprobes for Single-Cell Analysis. *ACS nano* **2014,** *8* (1), 875-884.

30. Cervera, J.; Schiedt, B.; Neumann, R.; Mafe, S.; Ramirez, P., Ionic conduction, rectification, and selectivity in single conical nanopores. *Journal of Chemical Physics* **2006,** *124* (10).

31. Tagliazucchi, M.; Szleifer, I., Transport mechanisms in nanopores and nanochannels: can we mimic nature? *Materials Today* **2015,** *18* (3), 131-142.

32. Schultz, S. G., INTERNATIONAL UNION OF PURE AND APPLIED BIOPHYSICS BIOPHYSICS SERIES VOL. 2. BASIC PRINCIPLES OF MEMBRANE TRANSPORT. *Schultz, S. G. Iupab (International Union of Pure and Applied Biophysics) Biophysics Series, Vol. 2. Basic Principles of Membrane Transport. Xii+144p. Cambridge University Press: New York, N.Y., USA; London, England. Illus* **1980**, XII+144P-XII+144P.

33. Hille, B., Ion channels of excitable membranes. Edition 3. *Ion channels of excitable membranes. Edition 3* **2001**, i-xviii, 1-814.

34. Rollings, R. C.; Kuan, A. T.; Golovchenko, J. A., Ion selectivity of graphene nanopores. *Nature Communications* **2016,** *7*.

35. Deng, X. L.; Takami, T.; Son, J. W.; Kang, E. J.; Kawai, T.; Park, B. H., Effect of concentration gradient on ionic current rectification in polyethyleneimine modified glass nano-pipettes. *Scientific Reports* **2014,** *4*.

36. Pu, Q. S.; Yun, J. S.; Temkin, H.; Liu, S. R., Ion-enrichment and ion-depletion effect of nanochannel structures. *Nano letters* **2004,** *4* (6), 1099-1103.

37. Korostynska, O.; Arshak, K.; Gill, E.; Arshak, A., Review on state-of-the-art in polymer based pH sensors. *Sensors* **2007***, 7(12): 3027–3042.*

CHAPTER 4

Using nexFET to control the transport of DNA and sense proteins selectively

Synopsis

In this chapter, we explore the application of nanopore extended field-effect transistors (nexFETs) in single-molecule biosensing, where the targets include dsDNA and ssDNA of different lenghts, and IgG antibodies. By controlling the gate bias of the nexFET, the translocation behaviour of analytes can be modulated efficiently. By applying a positive gate voltage, the dsDNA molecules pass through the nanopore with longer dwell time and a higher signal-to-noise ratio. Moreover, the clear translocation signal of ultra-short nucleic acids (e.g. 18-base ssDNA) are observed as a result of the high affinity between analytes and the nanopore inner wall. In addition, the selective sensing of specific proteins at a picomolar concentration is also achieved by a receptor-embedded nexFET.

Part of this chapter has been published as **Ren R**, Zhang YJ, Nadappuram BP, Akpinar B, Klenerman D, Ivanov AP, Edel JB, Korchev Y (2017) Nanopore extended field-effect transistor for selective single-molecule biosensing. Nature Communications 8, Article number: 586 (2017), doi:10.1038/s41467-017-00549-w.

4.1 Introduction

Since the concept of biosensors, which are series of analytical devices incorporating a biological sensing element, was proposed in the 60s[1], the related technologies have attracted much attention due to their outstanding capabilities[2-4]. Most biosensors can be grouped into the following categories: calorimetric, electrical, optical, and mechanical. Over the past two decades, the development of novel biosensing strategies has been gaining in prominence, largely as a result of new tools and techniques offering heightened sensitivity. Among the different biosensors reported, nanopores[5-8] have attracted significant attention because of their ability to detect biomarkers, such as DNA[6, 9-12], RNA[13, 14], and proteins,[15-18] at the single-molecule level. However, the detection of these biomolecules is often limited by the low concentration in biological samples, the fast translocation time of the analytes, poor analyte selectivity, and a low signal-to-noise ratio. Some of these fundamental limitations can be solved by using functionalised nanopores, whose surfaces are decorated by positively or negatively charged binding sites[19-22]. These binding sites, such as antibodies, aptamers, or other chemical residues, are capable of slowing down the transport of the target molecule. Moreover, the binding sites encoded nanopores can gain selectivity, much like natural receptors and engineered biological nanopores. However, these functionalisation strategies are still challenging to perform and require careful optimisation. Therefore, the development of selective label-free micro/nano biosensors is an ongoing research direction, actively being pursued by the analytical community.

As discussed in the previous chapter, the current between the drain and source of a FET device can be regulated by the voltage applied to the gate. More specifically, this current-control mechanism of the FET is based on an electric field generated by the voltage applied to the gate. This electric field controls the amount of charge in the drain-source channel, and it thus determines the local conductivity of the channel. Utilising this feature, the translocation signal of the charged biomolecules can be improved. In this regard, a nanopore incorporated into a FET can address the limitations described above. Scientists are already combining FETs and nanopores to develop novel devices.[23-26] However, they often entail complex fabrication processes, difficult functionalisation, and low operational stability. In addition, the FET biosensors are limited in concentration range since their sensing range is much larger than the single molecule regime. As discussed before, nanopores, the single molecule biosensor can actively transport molecules, can make up for the FETs' deficiencies.

In **Chapter 3**, we reported on an easy and efficient fabrication method for designing a nanopore-based transistor, the nanopore extended field-effect transistor (nexFET). In this chapter, we use this platform to control the transport of DNA, and we use a receptor-embedded nexFET to sense biomolecules selectively (**Figure 4.1**). By controlling the gate voltage of the nexFET, the capture rate, dwell time, and signal-to-noise ratio of DNA translocation can be modulated. We also demonstrate that it is possible to utilise the features of the nexFET, such as high sensitivity and elongation of the dwell time, to sense short oligonucleotides. In addition, we show that the PPy gate layer is easy to functionalise with biological receptors. For example, in this chapter, we embed insulin into the PPy gate layer to sense anti-insulin IgG antibodies.

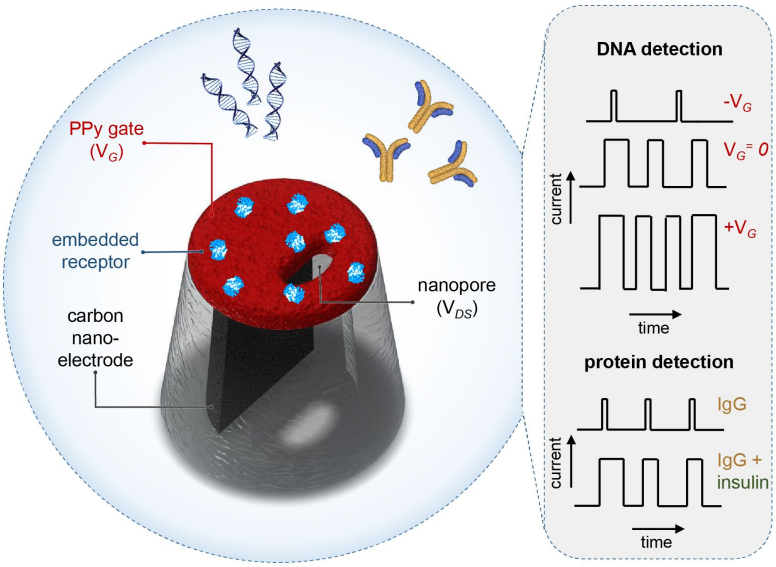


Figure 4. 1 Using a nexFET to sense DNA and protein. The nexFET platform is a functionalised nanopore-based FET. The transistor is located on a double-barrel quartz nanopipette tip, with one barrel filled with a carbon nanoelectrode. The nanopore provides a drain-source channel, and the PPy gate layer acts as the gate of the FET. By controlling the gate voltage through the carbon nanoelectrode, the transport properties and capture rate of biomolecules can be efficiently controlled at the single-molecule level. Moreover, by embedding some artificial receptors, the nexFET can detect biomolecules with high sensitivity and selectivity.

4.2 Methods

4.2.1 The fabrication of insulin-imprinted nexFETs

The details of the fabrication of the plain nexFET were presented in **Chapter 3**. Compared with the standard nexFET fabrication protocol, the insulin-embedded nexFET was fabricated simply by adding the insulin into the original polymerisation electrolyte. In detail, the PPy deposition solution consisted of 100 μM of human insulin (Sigma-Aldrich), 500 mM of Py (Sigma-Aldrich), and 100 mM of KCl with a Tris-EDTA buffer (pH = 6). After electropolymerisation, the insulin-embedded nexFET was washed several times with the Tris-EDTA buffer to remove residual Py and insulin.

4.2.2 DNA sensing and protein-selective sensing experiment

Drain-source voltage-dependent and gate voltage-dependent DNA translocation experiments were carried out using 300 pM, 3 kbp dsDNA (Thermo-Fisher) in 100 mM of KCl with a Tris-EDTA (pH = 8) buffer. ssDNA translocation was performed using 1 nM, 18-mer ssDNA (Thermo-Fisher) in 100 mM of KCl with a Tris-EDTA (pH = 8) buffer. Protein-selective sensing translocation experiments were performed using 200 pM or 1 nM of an anti-insulin IgG antibody (BSA- and azide-free, ab46707, Abcam) in 100 mM of KCl with a Tris-EDTA pH 7 buffer. With each experiment, the target analytes (dsDNA, ssDNA, or the anti-insulin IgG antibody) were loaded in the bath (cis) and the buffer with the same composition as that loaded in the open barrel of the nexFET (trans). Translocation traces were recorded and filtered using a Multiclamp 700B amplifier (Molecular Devices) and DigiData 1322 A digitiser (Molecular Devices). The data was analysed using pClamp software (Molecular Devices) and a customised Matlab application (details are presented in **Chapter 2**).

4.3 Result and discussion

4.3.1 Single-molecule DNA sensing using a nexFET

NexFETs, which are nanopore-based transistors, have been fabricated by depositing conductive polymer, such as PPy, on a double-barrel nanopipette tip with real-time feedback control. The FET behaviour and pH sensitivity of these devices have been demonstrated in **Chapter 3**. To initially examine the abilities of the nexFET as a biosensor, we compared the translocation of 300 pM, 3 kbps dsDNA through a bare

dual-barrel nanopipette (each pore size is ~100 nm) and a nexFET (**Figure 4.2a**). When DNA molecules passed through the nanopore using the bare nanopipette, no translocation events were observed. This is attributed to the pore size of the initial dual-barrel nanopipette being too large to generate the current spikes when a DNA passes through it. After PPy deposition, the nanopore was shrunk to approximately 10% of the original diameter, as can be seen in the change of nanopore conductace, as shown in the *I-V* curves, **Figure 4.2b**. In this size regime (approximately 10–20 nm), single-molecule translocations could be observed. To fully study single-molecule DNA sensing using a nexFET, we varied the drain-source voltage (V_{DS}) and gate voltage (V_G) to observe different translocation features.

4.3.1.1 Voltage (drain-source) dependence

To gain insight into the basic translocation behaviour of the dsDNA through a nexFET, we varied the driving voltages from 500 mV to 900 mV, without applying V_G. As expected, nexFETs demonstrate similar trends to conventional nanopores, whereby the increase in electrical driving potentials leads to a higher capture rate (**Figure 4.2c**), a shorter dwell time (**Figure 4.2d**), and a larger peak current (**Figure 4.2e**). The exponential growth of the capture rate with increasing V_{DS} is consistent with the feature of DNA translocation through small nanopores. The trend is mainly caused by the DNA's negatively charged backbones driven by an applied EP force.

However, compared with the translocation through conventional solid-state nanopores, the current change of the 3-kbps dsDNA translocation signals through nexFETs exhibit longer dwell times and higher peak currents. This improvement of the translocation signal is attributed to the interactions between DNA molecules and the PPy layer. We believe that a variety of non-covalent interactions take place between these biopolymers and synthetic polymers, for example, hydrophobic interactions, van der Waals force, and hydrogen bonding.[27] Among these non-covalent interactions, the electrostatic force predominately contributes to slowing down the translocation. In detail, the phosphate group of DNA contributes to its polyanionic character, whereas the nanopore is surrounded by a cationic PPy surface. By using described interactions, DNA is absorbed or deposited on the PPy surface.[28-30] However, the absorption between the nanopore and the analytes are always the double edge blade: on one hand, this interaction can slow down translocation; on the other hand, the affinity between the molecules and the nanopore inner walls may cause the congestion of the transport, resulting the full block of the nanopore. Fortunately, in our case, this weak binding is not irreversible, as the DNA would fall off if the electrical driving force is large enough.

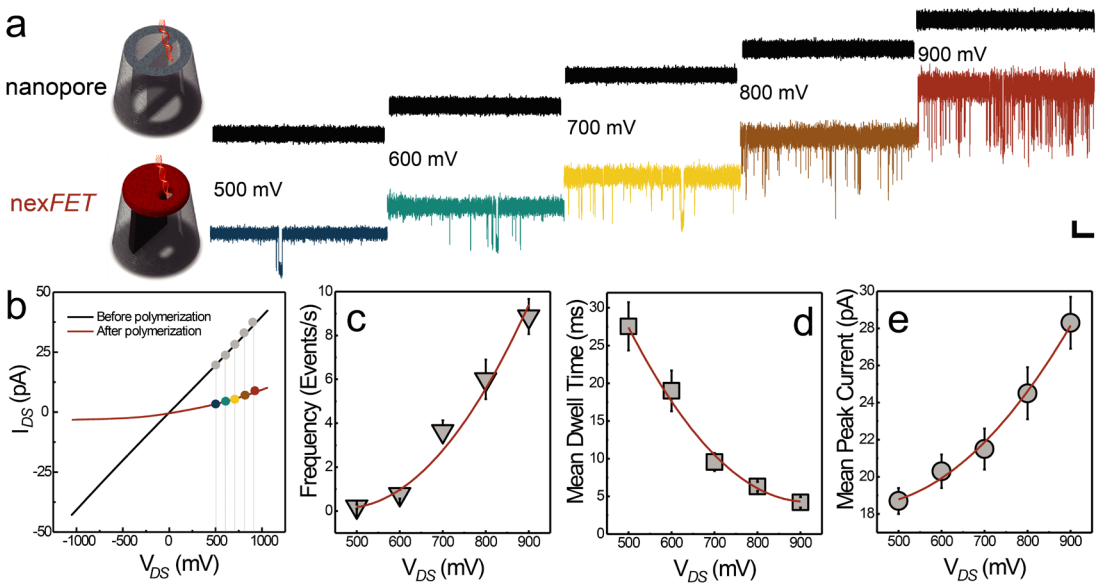


Figure 4. 2 Bias voltage study of DNA translocation through a nexFET. **(a)** The voltage dependence of DNA translocation through a quartz nanopore (approximately 100 nm) located on a bare dual-barrel nanopipette and the PPy nanopore located on the nexFET are indicated by the black traces on the top and coloured traces on the bottom, respectively. The translocation of 100 pM, 3 kbp dsDNA is measured in 100 mM of KCl and a 1 mM Tris-EDTA buffer, pH 7 solution. All traces are 10 s long and filtered by a low-pass Bessel filter with a cut-off frequency of 10 kHz. Horizontal scale bar: 1 s; vertical scale bar: 10 pA. **(b)** The *I-V* characteristics of the nanopore before and after PPy deposition, corresponding to the schematic above. Before PPy modification, the pore size is too large to sense the target DNA, which results in no events observed. **(c)**The capture rate, **(d)**the translocation time, and **(e)** the current blockage versus applied V_{DS} without any gate voltage (V_G). The nexFET behaves similarly to conventional nanopores. Error bars represent the standard deviation of three independent experimental repeats with different nexFETs.

4.3.1.2 Using the gate voltage to control the DNA transport

Many efforts have previously been made to improve the translocation throughput, including modification of the internal surface of a nanopore[31], the utilisation of bias pulses[32], and using high ionic strength solutions[33]. However, there are limitations such as low biocompatibility at ionic strength. In addition, most methods can only improve the translocation properties partially; for example, by applying a pulse voltage, the translocation frequency can be improved, but the dwell time and peak amplitude remain at the original levels. In comparison, the nexFET can be utilised to regulate transport properties, including the capture rate, dwell times, peak amplitude, and signal-to-noise ratio simply by changing the gate voltage.

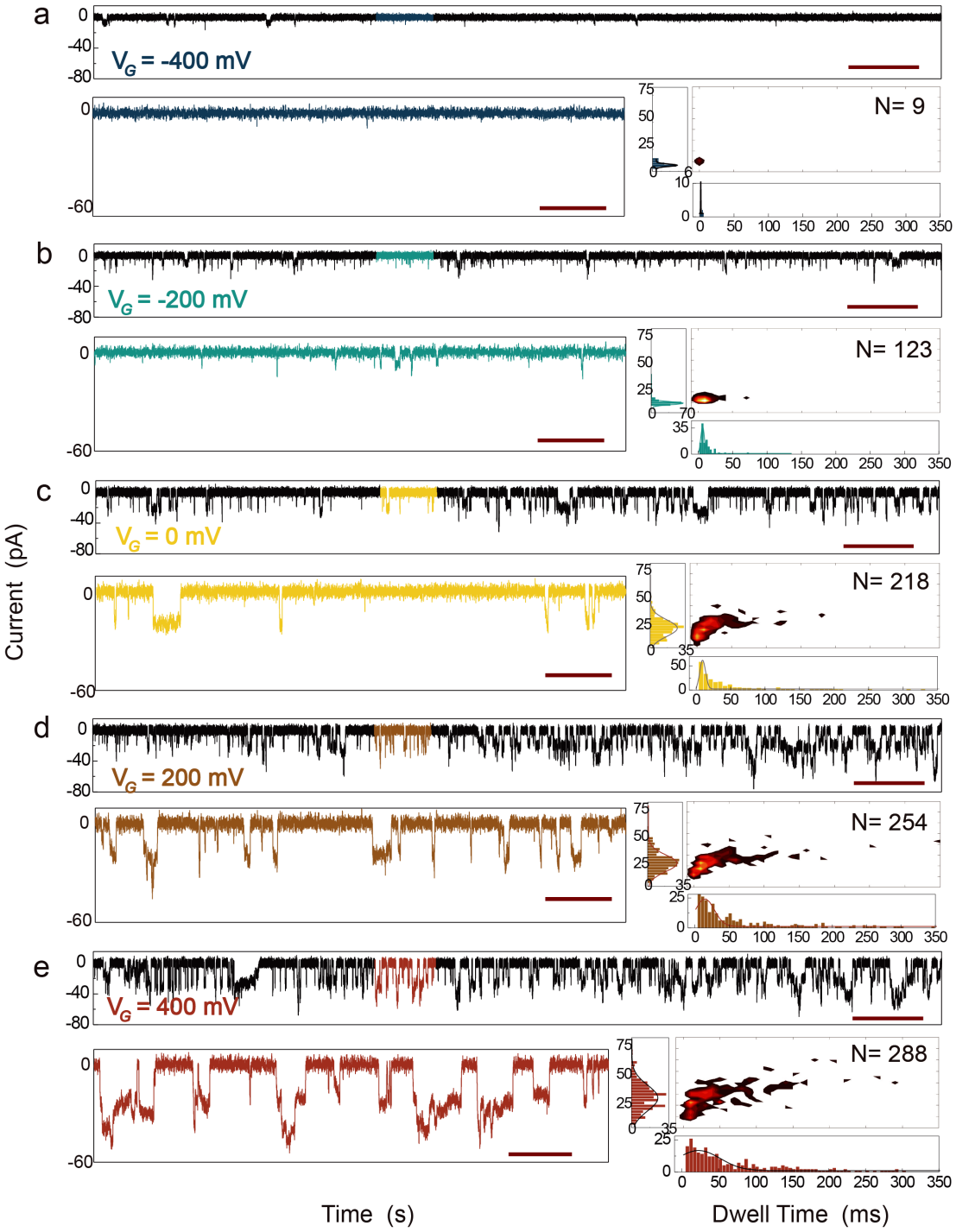


Figure 4. 3 Gate voltage dependence on dsDNA translocation through the nexFET. (a) Representative translocation recordings are shown for 300 pM 3 kbp dsDNA in 100 mM KCl and a 1 mM Tris-EDTA buffer, pH 8 with V_{DS} = 700 mV and V_G, equal to (i) -400 mV, (ii) -200 mV, (iii) 0 mV, (iv) 200 mV, and (v) 400 mV. All measurements were conducted at least three times. I-t traces are shown for a 60 s duration as well as a 4 s inset. Note that the number of events (N) is for the plotted traces. In all cases, the traces were filtered using a Bessel filter with a cut-off frequency of 10 kHz. The main trace scale bar: 5 s; partial traces scale bar: 0.5 s) The scatter plots, along with peak amplitude and translocation time histograms, are also included. Note that the count of event numbers (N) is only for the plotted traces. All measurements were conducted at least three times.

To validate the level of gate control, we varied V_G from -400 mV to 400 mV and kept the V_{DS} = 700 mV. The V_G applied was limited to lower voltages as above 1 V, PPy is prone to oxidation. Furthermore, the gate can also suffer from dielectric breakdown and unwanted leakage current.

From a series of current-time traces under different gate voltages (**Figure 4.3**), the changes in translocation signatures were evident, indicating that the applied V_G can influence the transport of DNA molecules efficiently. For example, applying a negative voltage to the gate leads to a lower frequency of events, a shorter dwell time, and a smaller peak amplitude. In contrast, a higher V_G results in higher capture rates, longer dwell times, and larger peak amplitudes, and is directly attributed to the positively charged PPy nanopore.

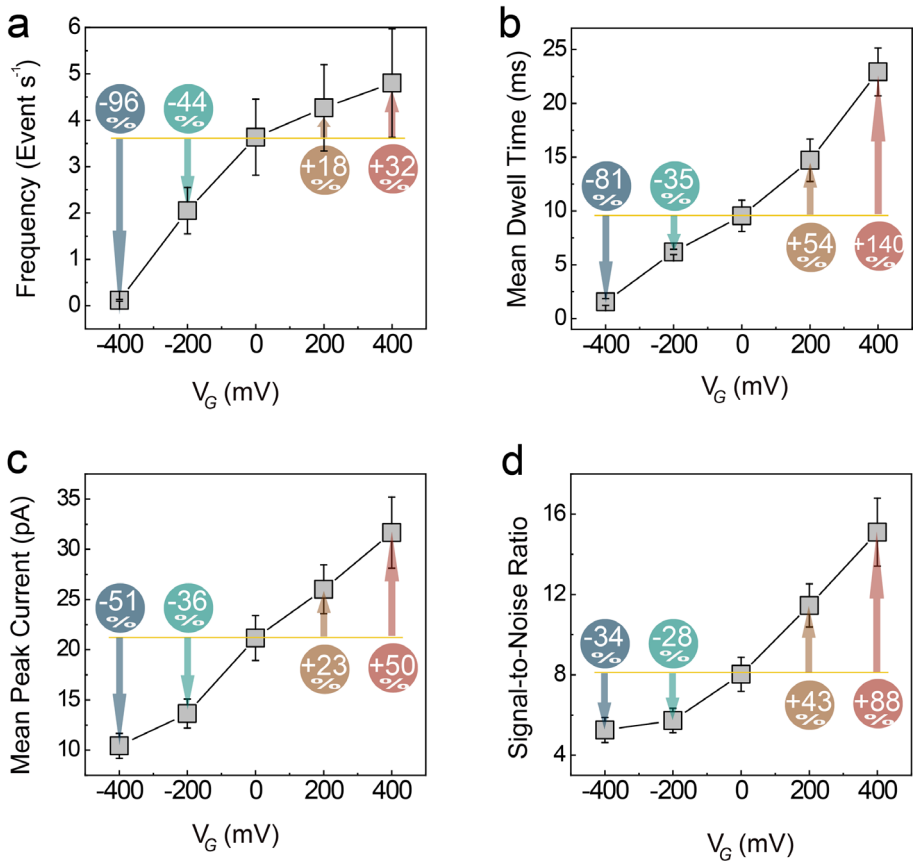


Figure 4. 4 The gate voltage dependence of DNA translocation through the nexFET. The **(a)** capture rate, **(b)** translocation dwell time, **(c)** current blockage, and **(d)** signal-to-noise ratio of 300 pM, 3 kbp dsDNA translocation versus gate voltage are measured in 100 mM of KCl and a 1 mM Tris-EDTA buffer under a 700-mV drain-source voltage. The rate of change (based on V_G = 0) in each parameter is also marked. Error bars represent the standard deviation of three independent experimental repeats with different nexFETs.

Quantitative indicators to examine the performance of this nanopore-transistor platform is shown in **Figure 4.4**. For instance, applying a -400 mV to the gate resulted in a 96% decrease in the translocation frequency, an 81% increase in dwell times, a 51%

decrease in peak amplitude, and a 34% decrease in the signal-to-noise ratio. In contrast, with a positive 400 mV applied to the gate, the results were reversed. 32% increase in the capture rate, a 140% increase in dwell times, a 50% increase in peak amplitude, and an 88% increase in the signal-to-noise ratio. More specifically, we can regulate the translocation capture rate from 0.15 to 4.8 events/s, the mean dwell time from 1.5 to 22.9 ms, the mean peak amplitude from 10.4 to 31.7 pA, and the signal-to-noise ratio from 5.3 to 15.1 by adjusting the V_G from -400 mV to 400 mV.

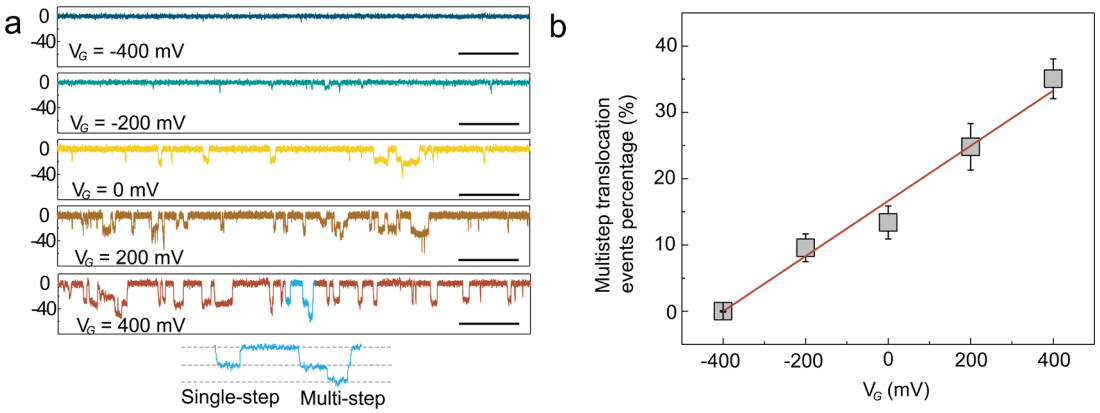


Figure 4. 5 The ratio of translocation events with multi-steps in all translocation events at different gate voltages. **(a)** Representative ionic translocation recordings demonstrate different single- or multi-step events of the 3 kbp dsDNA molecules with a 700-mV drain-source voltage and different gate voltages from -400 mV to 400 mV (from top to bottom). The measurements were conducted in 100 mM of KCl and a 1 mM Tris-EDTA buffer, pH 8, and they were recorded with a low-pass Bessel filter with a cut-off frequency of 10 kHz. Scale bars: 0.5 s. **(b)** Increasing the gate voltage results in more multi-step events. With the gate voltage increased from -400 mV to 400 mV, the ratio of multi-step events in all translocation events increased linearly. Error bars represent the standard deviation of three independent experimental repeats with different nexFETs.

The mechanism of modulating molecular transport through the nanopore by controlling the gate voltage is has two likely explanations.

The first explanation comes to the local electric field change and interactions between the DNA and the PPy nanopore walls. With $V_G > 0$, the PPy surface is positively charged, resulting in a local attraction to the negatively charged dsDNA leading to an increase in the capture rate. When the negatively charged DNA molecules travel through the nanopore, it will interact with the cationic chamber by electrostatic force, resulting in a broader distribution in the translocation time. The interaction between the biopolymer molecules and synthetic polymer walls can be confirmed by seeing a multi-step translocation signature (**Figure 4.5**). With V_G increasing, the ratio of events with multi-step behaviour to all translocation events was increased linearly. Such events are observed when there is more than one molecule entering the pore or due to the DNA being partially folded. This would be expected to increase when a stronger electrostatic force exists between the biomolecules and nanopores.

Another explanation is the electroosmotic effects. As discussed in **Chapter 1, Section 1.3.4**, when the nanopore carries opposite charge compare to the analytes, the direction of electroosmotic flow (EOF) would be similar with the electrophoretic flow (EP), leading to higher capture rate. This explanation is also in line with the experiment results (**Figure 4.4a**): when a negative gate voltage applied, the nanopore becomes neutral or slightly negative, resulting an opposite water flow; when a positive gate voltage applied, the water helps the nanopore to push the molecule pass through. However, only use electroosmotic effects cannot explain the dwell time change. Herein, I think the control of the molecule transport is a multifaceted result.

Apart from these changes, another key improvement is the signal-to-noise ratio, **Figure 4.4d**. We believe that this is mainly because of the character of PPy, which is conductive and the shape can be changed by the applied bias. Under the experimental buffer conditions, the PPy layers tend to repel the adjacent layers as they all carry moderately positive charges. As a result, the entire polymer structure would slightly swell and expand. With a negative voltage is applied to the gate, the electrons can neutralise the positive charges so that the internal repelling force would be smaller. As a result, the nanopore size would swell, leading to a lower signal-to-noise ratio. On the other hand, if a positive gate voltage is applied, then the nanopore will shrink to a smaller size, resulting in a higher signal-to-noise ratio.

4.3.1.3 Sensing short DNA fragments

The sensing of sub-100-base DNA fragments and microRNA using conventional nanopores is typically challenging because of the quick translocation times and a poor signal-to-noise ratio. Several solutions have been reported to detect these crucial biomarkers at the single-molecule level. A large proportion of these solutions involve fabricating complicated nanopore systems such as highly insulating quartz substrates[34], or locally thinning the membrane[14]. The complicated fabrication process often becomes a bottleneck. However, a nexFET, on the other hand, can slow down transport and improve the signal-to-noise ratio, allowing for the possibility to detect smaller fragments. **Figure 4.6** illustrates the detection of 18-base ssDNA molecules using a nexFET. The translocation signals are recorded clearly with long dwell times and high signal-to-noise ratios. Compared with dsDNA, the translocation of ssDNA can be improved further because of relatively stronger interactions between ssDNA and PPy. Similarly to the DNA absorption study on graphene[35, 36], the interaction between ssDNA and the substrate is stronger than that between dsDNA and the substrate because the ssDNA has a higher affinity to the PPy surface, which contains consistent heterocyclic structures, by Van der Waals interactions without the constraint of the double-helix structure.

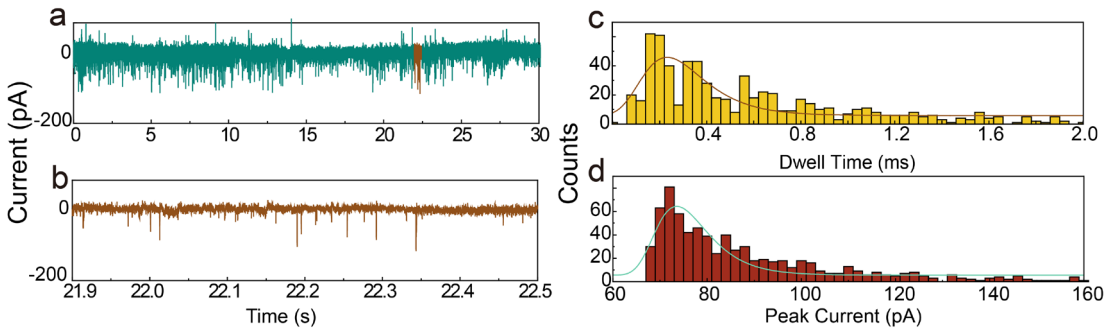


Figure 4. 6 The detection of single 18-mer ssDNA using a nexFET. **(a)** Representative ionic translocation traces of 1 nM of ssDNA (18 mer) and **(b)** partially magnified traces indicate that the small oligonucleotides can be detected using a nexFET at the single-molecule level. The translocation was measured in 100 mM of KCl and a 1 mM Tris-EDTA (pH = 8) buffer with V_{DS} = 700 mV. The **(c)** distribution of translocation time and **(d)** peak current histograms. All measurements were conducted at least three times.

4.3.2 Selective protein sensing using a nexFET

In the previous sections, the nexFET have been demonstrated to be sufficiently sensitive to control biomolecular transport at the single-molecule level. Here we show how the PPy can be modified to enable selective sensing of proteins via the introduction of receptors.[37] For this part, the insulin - anti-insulin antibody, which has central role in diabetes, was selected as a model system.

4.3.2.1 The fabrication and characterisation of an insulin-embedded nexFET

As is known, diabetes seriously affects the quality of people's lives. In diabetes treatment, early identification is important, as it can help to reduce the risks of a person developing devastating complications. The level of anti-insulin antibodies is an indicator of type 1 diabetes of people who are not previously treated with insulin. However, the detection of this antibody is challenging due to its ultra-low concentration (< 20 μU/ml)[38, 39] in human serum. Importantly as shown below an insulin-embedded nexFET has sufficient sensitivity and selectivity to detect anti-insulin antibodies.

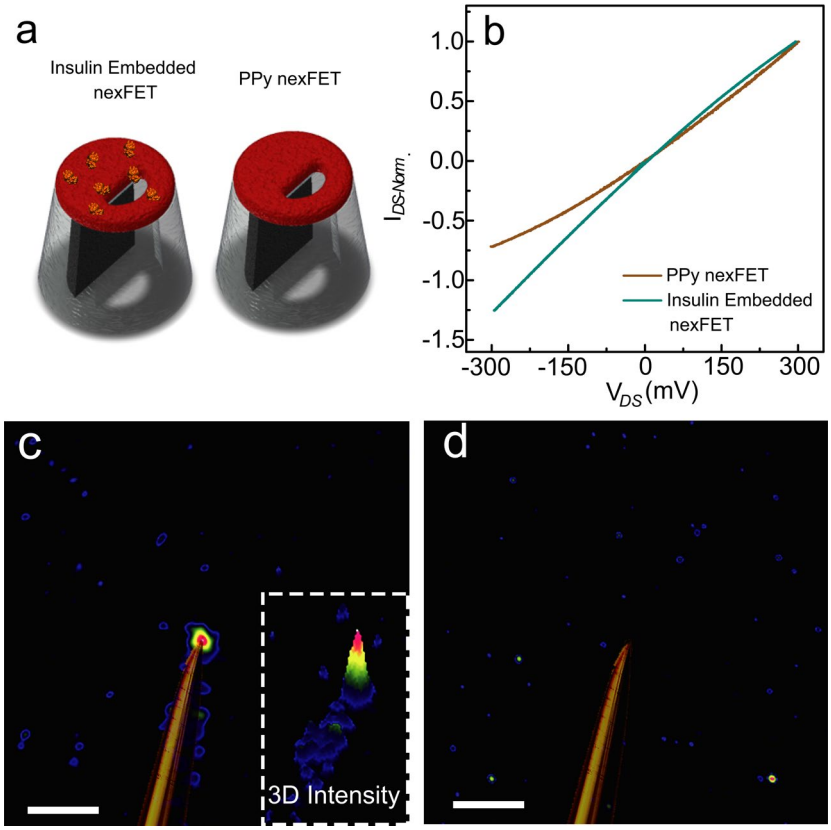


Figure 4. 7 The characterisation of a nexFET and an insulin-embedded nexFET. **(a)** Schematic of an insulin-embedded nexFET and a plain nexFET. **(b)** The I-V (drain-source) characteristics of an insulin-embedded nexFET and a plain nexFET in 100 mM of KCl and a 1 mM Tris-EDTA buffer, pH 8. Fluorescence images, which were superimposed on optical microscopy images of the nanopipette, validate that **(c)** the insulin-embedded nexFET can bind the anti-insulin antibody selectively by using a dye tagged secondary antibody, while **(d)** the plain nexFET is not able to bind the target antibody selectively.

By adding insulin proteins into the Py electropolymerization buffer, the insulin-embedded nexFET can be generated via electropolymerisation of the insulin-PPy mixture. Similar to the geometry of a plain nexFET (**Figure 4.7a**), the insulin-embedded nexFET contains the PPy nanopore with insulin proteins inlaid in the polymer layer. The *I-V* curves (**Figure 4.7b**) confirmed that the surface charges of the normal nexFET and the insulin-embedded nexFET as can be seen in the current rectification. The pristine cationic PPy layer carries positive charges, whereas the insulin-imprinted PPy layer becomes slightly negative as a result of the negatively charged insulin. To further confirm the activity of the insulin binding site, we immersed the insulin-embedded nexFETs into highly concentrated anti-insulin antibodies, and a fluorophore tagged secondary antibody of the same concentration. High fluorescence intensity was observed (**Figure 4.7c**), indicating that the binding site is active. No fluorescence was observed with the plain nexFET (**Figure 4.7d**).

4.3.2.2 Selective anti-insulin IgG antibody sensing using insulin-embedded nexFETs

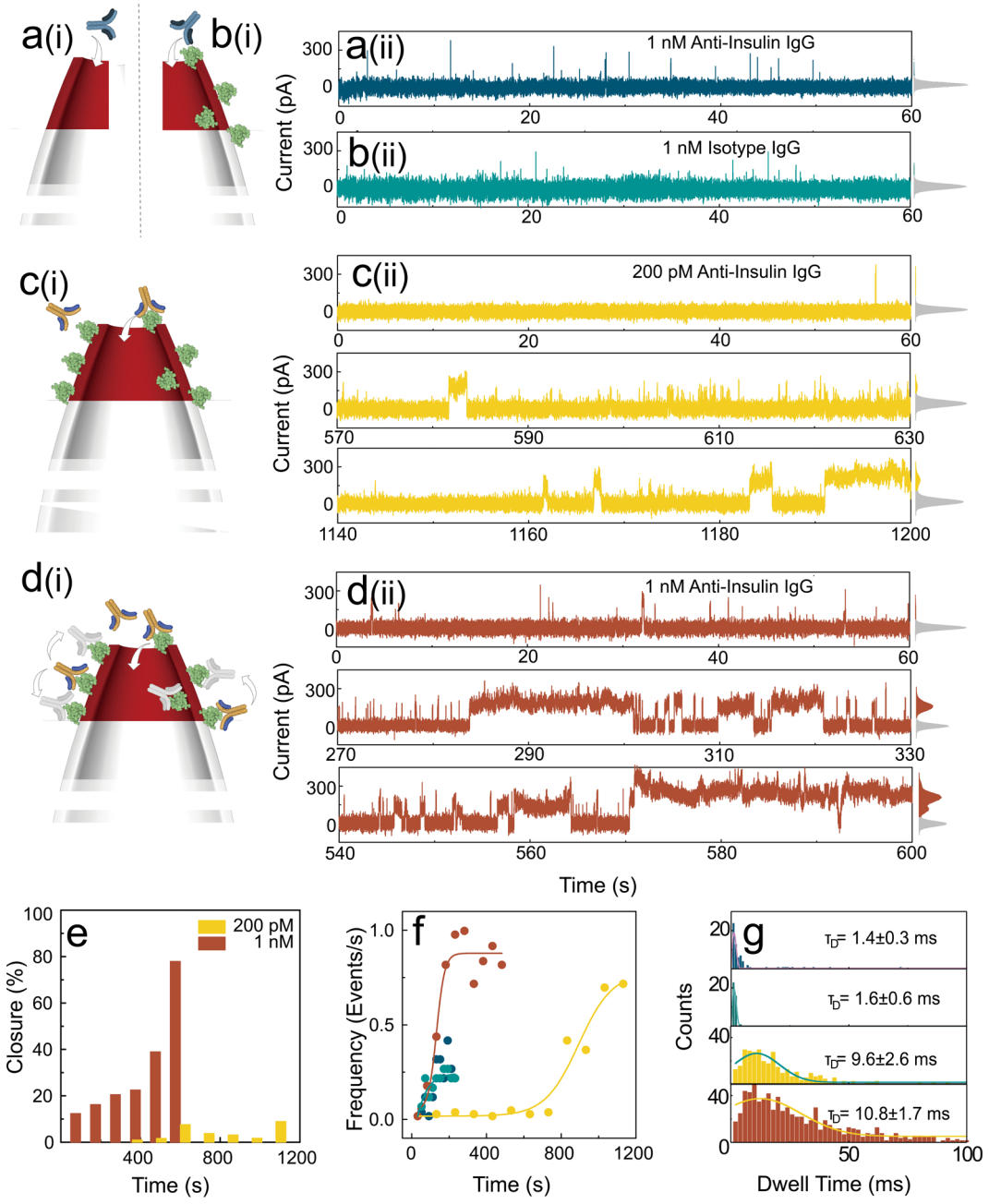


Figure 4. 8 Using an insulin-embedded nexFET to sense an anti-insulin IgG antibody. **(a–d)** Schematic of the nexFET translocation and corresponding 60 s I-t records: **(a)** the translocation of 1 nM of an anti-insulin IgG antibody through a plain nexFET, **(b)** the translocation of 1 nM of an isotype IgG antibody through an insulin-modified nexFET, **(c)** the translocation of 200 pM of an anti-insulin IgG antibody through an insulin-modified nexFET, and **(d)** the translocation of 1 nM of an anti-insulin IgG antibody through an insulin-embedded nexFET. All above translocations were measured in 100 mM of KCl, 1mM TE, pH = 7 buffer with a -800-mV drain-source voltage and recorded using a low-pass Bessel filter with a cut-off frequency of 10 kHz. For all translocation traces, the all-point data analysis is shown, including **(e)** the histogram of the pore closure ratio; **(f)** the capture rate, along with time; and **(g)** the translocation time.

Figure 4.8a–d provides a comparison of the translocation recordings of an anti-insulin IgG antibody using both plain nexFETs and insulin-imprinted nexFETs. The control experiments are presented for the translocation of 1 nM of an anti-insulin IgG antibody through a plain nexFET (**Figure 4.8a**) and the translocation of 1 nM of an isotype IgG antibody through the insulin-embedded nexFET (**Figure 4.8b**). The isotype antibody has a size and charge similar to those of the anti-insulin antibody but cannot bind to insulin. In both controls, the translocation events were sparse and sharp (τ_D = 1.4 ms for the first control, **Figure 4.8a**; τ_D = 1.6 ms for the second control, **Figure 4.8b**), indicating that there were no binding or interaction effects between these biomolecules and the wall of the nanopore chamber. From the current distribution histograms (on the right side of each current-time trace), it is evident that the baseline current dominated, indicating fast and no-binding translocation. This result is not surprising, because protein detection at the single-molecule level using nanopores is always limited by the fast translocation, low capture rate, and small signal-to-noise ratio. The low event rate is attributed to the protein concentration being significantly lower than predicted from the Smoluchowski rate equation, which often necessitates protein concentrations well over 10s–100s nM[40].

Figure 4.8c–d depicts the current-time traces of the anti-insulin IgG antibody translocation through an insulin-embedded nexFET. It is evident that both capture rate and translocation dwell time increased dramatically; this is because of the strong antibody-antigen interactions.[41, 42] Time-dependent translocation recordings for 200 pM of an anti-insulin IgG antibody are illustrated in **Figure 4.8c** (t = 0–60 s; 570–630 s; 1,140–1,200 s), and the full current-time trace is pictured in **Figure 4.9**. To better understand the mechanism of this biosensor, translocations for 1 nM of an anti-insulin IgG antibody were also performed as illustrated in **Figure 4.8d** (t = 0–60 s, 270–330 s, 540–600 s), and the full current-time trace is presented in **Figure 4.10**. Based on the time-dependent traces, a lag time exists between the initial status (t = 0, which is when the pipette is first immersed in the buffer containing target biomarkers) and the optimal operation of the biosensor. The analysis of the nanopore open/closure ratio and the capture rate, along with time, also confirmed this, as illustrated in **Figure 4.8e** and **Figure 4.8f**, respectively. This lag time is attributed to the diffusion and saturation of the analytes on the insulin-imprinted PPy layer. Another phenomenon that cannot be ignored is the antibody molecules hopping between the antigen-binding sites. It has been previously reported that the target molecules can detach and reattach to the same antigen or move to adjacent binding sites with a nanometre-sized distance.[28, 43] When many antibodies interact with an antigen-binding site at the same time, the translocation of single-site binding analytes are limited because the receptor will be occupied again soon after detachment. Therefore, compared with the translocation of 200 pM of an

antibody, the translocation of 1 nM of an analyte will take a shorter time to reach the same pore closure level. **Figure 4.8g** shows the difference between the translocation durations of the controls (1.4 ± 0.3 ms, 1.6 ± 0.6 ms) and the analytes (9.6 ± 2.6 ms, 10.8 ± 1.7 ms), demonstrating the insulin embedded nexFET is selective to detect the anti-insulin IgG antibody.

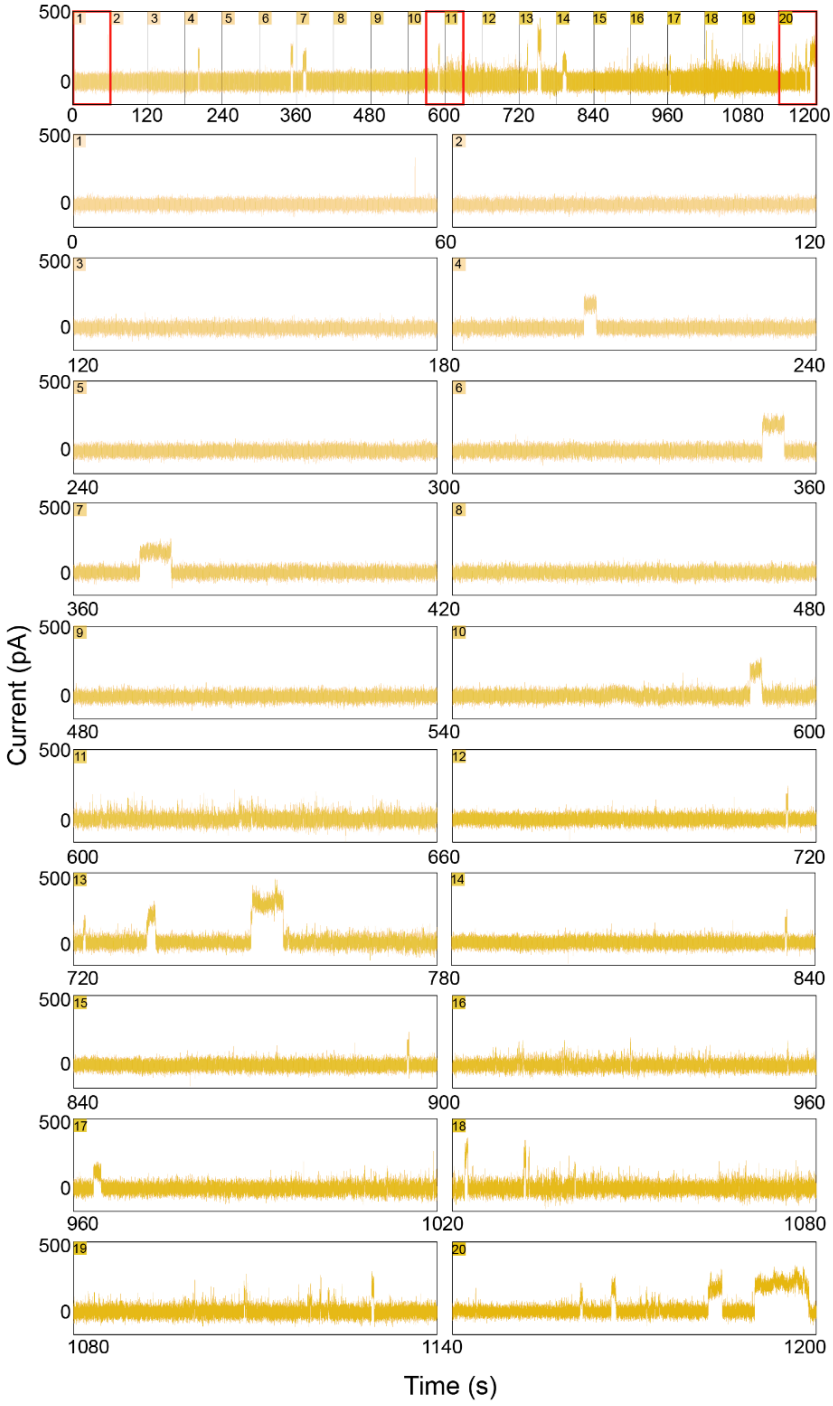


Figure 4. 9 A full translocation trace of 200 pM of an anti-insulin IgG antibody through an insulin-modified nexFET. A 1,200-s full translocation trace is demonstrated for the sensing of 200 pM of an anti-insulin IgG antibody by using an insulin-modified nexFET. This translocation experiment was

conducted in 100 mM of KCl, 1 mM TE, pH = 7 buffer under a -800-mV drain-source bias voltage. The top panel illustrates the 1,200 s full trace, and the remaining 20 panels depict magnified 60 s successive traces. The initial (0–60 s), the middle (570–630 s), and the end (1,140–1,200 s) segments of the trace are presented in Figure 4.8c. The histograms of the nanopore closure ratio (Figure 4.8e); the capture rate, along with translocation time (Figure 4.8f); and the dwell time (Figure 4.8g) for 200 pM of an anti-insulin IgG antibody were calculated from this full trace.

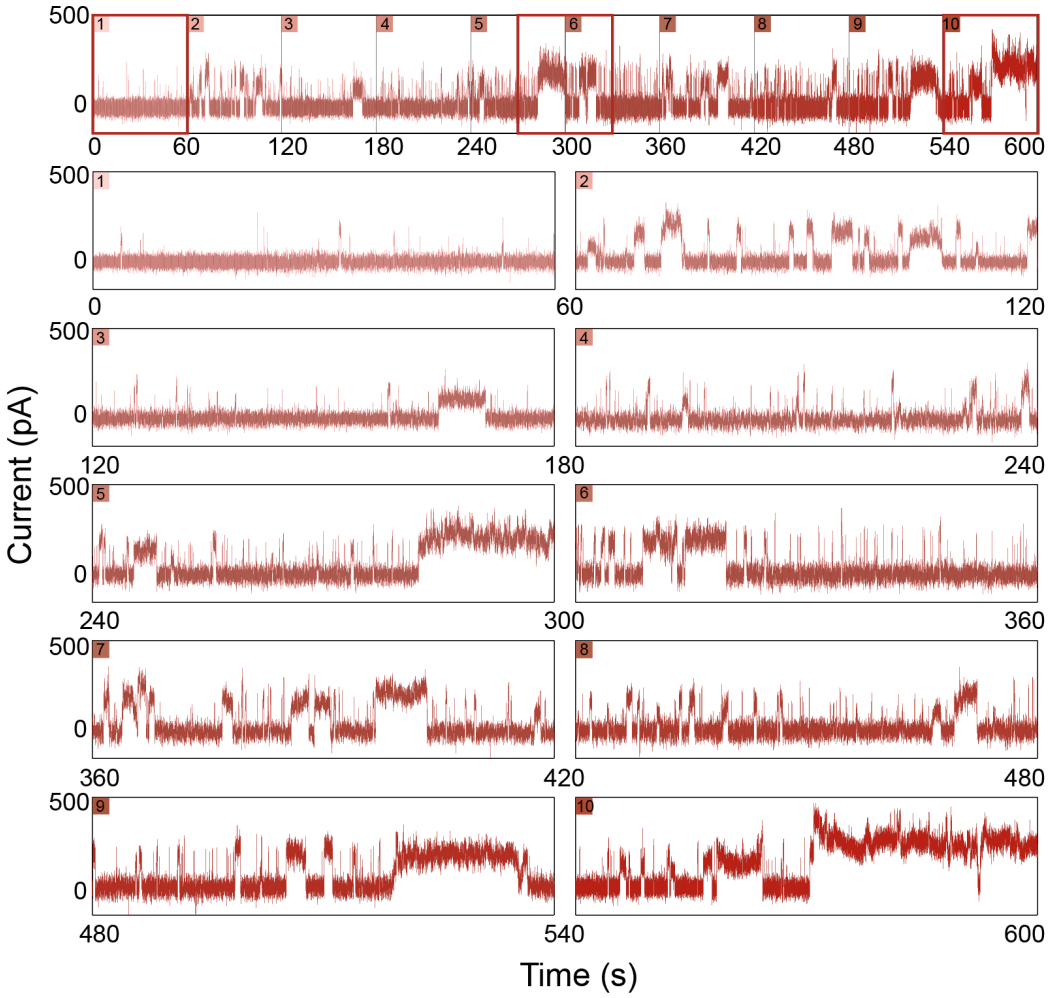


Figure 4. 10 A full translocation trace of 1 nM of an anti-insulin IgG antibody through an insulin-modified nexFET. A 600-s full translocation trace is demonstrated for the sensing of 1 nM of an anti-insulin IgG antibody by using an insulin-modified nexFET. This translocation experiment was conducted in 100 mM of KCl, 1 mM TE, pH = 7 buffer under a -800-mV drain-source bias voltage. The top panel illustrates the 600 s full trace, and the remaining 10 panels depict magnified 60 s successive traces. The initial (0–60 s), the middle (270–330 s), and the end (540–600 s) segments of the trace are presented in Figure 4.8d. The histograms of the nanopore closure ratio (Figure 4.8e); the capture rate, along with translocation time (Figure 4.8f); and the dwell time (Figure 4.8g) for 200 pM of an anti-insulin IgG antibody were calculated from this full trace.

4.4 Conclusion

In summary, nexFET biosensors display superior performance in detecting single-molecules, compared to using a FET or nanopore sensors alone. By combining these two methods, their individual advantages are also accumulated to make a highly sensitive and selective sensor. We demonstrated that the nexFET allows for the detection of translocations events with longer duration, higher signal-to-noise, and increased frequency.

Using the plain nexFET, the dsDNA translocation behaviour can be controlled by applying different potentials to the gate. With an increased gate voltage, the positively charged nanopore can slow down the translocation, increase the current amplitude, and attract more negatively charged biopolymers. Moreover, the translocation signal of the 18-mer ssDNA single-molecule, which is hard to detect by using plain nanopipettes, was observed by utilising the interactions between the PPy surface and the biomolecules.

Furthermore, the PPy surface is shown to act as a useful support material to incorporate binding sites, which can detect the target analytes selectively. Insulin-embedded nexFETs were successfully fabricated, and they demonstrate the ability to sense anti-insulin IgG antibodies selectively at trace amounts. In short, the nexFET, with an easy fabrication process and capable of controlling ionic and biomolecule transport. These results provide the first evidence suggesting that nexFET can be a versatile biosensor in the future sensing of a wide range of clinical biomarkers.

4.5 References

1. Clark, L. C., Jr.; Lyons, C., Electrode systems for continuous monitoring in cardiovascular surgery. *Annals of the New York Academy of Sciences* **1962,** *102*, 29-45.

2. Turner, A. P. F., Biosensors: sense and sensibility. *Chemical Society reviews* **2013,** *42* (8), 3184-3196.

3. Sassolas, A.; Leca-Bouvier, B. D.; Blum, L. J., DNA biosensors and microarrays. *Chemical Reviews* **2008,** *108* (1), 109-139.

4. Wang, J., Electrochemical glucose biosensors. *Chemical Reviews* **2008,** *108* (2), 814-825.

5. Miles, B. N.; Ivanov, A. P.; Wilson, K. A.; Dogan, F.; Japrung, D.; Edel, J. B., Single molecule sensing with solid-state nanopores: novel materials, methods, and applications. *Chemical Society reviews* **2013,** *42* (1), 15-28.

6. Meller, A.; Nivon, L.; Branton, D., Voltage-driven DNA translocations through a nanopore. *Physical review letters* **2001,** *86* (15), 3435-3438.

7. Wanunu, M., Nanopores: A journey towards DNA sequencing. *Physics of life reviews* **2012,** *9* (2), 125-58.

8. Ying, Y. L.; Zhang, J. J.; Gao, R.; Long, Y. T., Nanopore-Based Sequencing and Detection of Nucleic Acids. *Angewandte Chemie-International Edition* **2013,** *52* (50), 13154-13161.

9. Meller, A.; Branton, D., Single molecule measurements of DNA transport through a nanopore. *Electrophoresis* **2002,** *23* (16), 2583-2591.

10. Li, J. L.; Gershow, M.; Stein, D.; Brandin, E.; Golovchenko, J. A., DNA molecules and configurations in a solid-state nanopore microscope. *Nature Materials* **2003,** *2* (9), 611-615.

11. Fologea, D.; Gershow, M.; Ledden, B.; McNabb, D. S.; Golovchenko, J. A.; Li, J. L., Detecting single stranded DNA with a solid state nanopore. *Nano letters* **2005,** *5* (10), 1905-1909.

12. Wanunu, M.; Morrison, W.; Rabin, Y.; Grosberg, A. Y.; Meller, A., Electrostatic focusing of unlabelled DNA into nanoscale pores using a salt gradient. *Nat.Nanotechnol.* **2010,** *5* (2), 160-165.

13. Zahid, O. K.; Wang, F.; Ruzicka, J. A.; Taylor, E. W.; Hall, A. R., Sequence-Specific Recognition of MicroRNAs and Other Short Nucleic Acids with Solid-State Nanopores. *Nano letters* **2016,** *16* (3), 2033-2039.

14. Wanunu, M.; Dadosh, T.; Ray, V.; Jin, J.; McReynolds, L.; Drndic, M., Rapid electronic detection of probe-specific microRNAs using thin nanopore sensors. *Nature nanotechnology* **2010,** *5* (11), 807-814.

15. Rodriguez-Larrea, D.; Bayley, H., Multistep protein unfolding during nanopore translocation. *Nature nanotechnology* **2013,** *8* (4), 288-295.

16. Rosen, C. B.; Rodriguez-Larrea, D.; Bayley, H., Single-molecule site-specific detection of protein phosphorylation with a nanopore. *Nature biotechnology* **2014,** *32* (2), 179-181.

17. Marshall, M. M.; Ruzicka, J.; Zahid, O. K.; Henrich, V. C.; Taylor, E. W.; Hall, A. R., Nanopore Analysis of Single-Stranded Binding Protein Interactions with DNA. *Langmuir* **2015,** *31* (15), 4582-4588.

18. Lin, X. Y.; Ivanov, A. P.; Edel, J. B., Selective single molecule nanopore sensing of proteins using DNA aptamer-functionalised gold nanoparticles. *Chemical Science* **2017,** *8* (5), 3905-3912.

19. Luan, B.; Stolovitzky, G.; Martyna, G., Slowing and controlling the translocation of DNA in a solid-state nanopore. *Nanoscale* **2012,** *4* (4), 1068-1077.

20. Keyser, U. F., Controlling molecular transport through nanopores. *J.R.Soc.Interface* **2011,** *8* (63), 1369-1378.

21. Wei, R. S.; Gatterdam, V.; Wieneke, R.; Tampe, R.; Rant, U., Stochastic sensing of proteins with receptor-modified solid-state nanopores. *Nature*

nanotechnology **2012,** *7* (4), 257-263.

22. Tan, S. W.; Wang, L.; Yu, J. J.; Hou, C. R.; Jiang, R.; Li, Y. P.; Liu, Q. J., DNA-functionalized silicon nitride nanopores for sequence-specific recognition of DNA biosensor. *Nanoscale Research Letters* **2015,** *10*.

23. Haywood, D. G.; Saha-Shah, A.; Baker, L. A.; Jacobson, S. C., Fundamental Studies of Nanofluidics: Nanopores, Nanochannels, and Nanopipets. *Analytical Chemistry* **2015,** *87* (1), 172-187.

24. Nam, S.-W.; Rooks, M. J.; Kim, K.-B.; Rossnagel, S. M., Ionic Field Effect Transistors with Sub-10 nm Multiple Nanopores. *Nano letters* **2009,** *9* (5), 2044-2048.

25. Siwy, Z. S.; Powell, M. R.; Petrov, A.; Kalman, E.; Trautmann, C.; Eisenberg, R. S., Calcium-induced voltage gating in single conical nanopores. *Nano letters* **2006,** *6* (8), 1729-1734.

26. Xie, P.; Xiong, Q.; Fang, Y.; Qing, Q.; Lieber, C. M., Local electrical potential detection of DNA by nanowire-nanopore sensors. *Nature nanotechnology* **2012,** *7* (2), 119-125.

27. Vanoss, C. J., ACID-BASE INTERFACIAL INTERACTIONS IN AQUEOUS-MEDIA. *Colloids and Surfaces a-Physicochemical and Engineering Aspects* **1993,** *78*, 1-49.

28. Ghanbari, K.; Bathaie, S. Z.; Mousavi, M. F., Electrochemically fabricated polypyrrole nanofiber-modified electrode as a new electrochemical DNA biosensor. *Biosensors & Bioelectronics* **2008,** *23* (12), 1825-1831.

29. Saoudi, B.; Jammul, N.; Abel, M. L.; Chehimi, M. M.; Dodin, G., DNA adsorption onto conducting polypyrrole. *Synthetic Metals* **1997,** *87* (2), 97-103.

30. Ramanavicius, A.; Ramanaviciene, A.; Malinauskas, A., Electrochemical sensors based on conducting polymer- polypyrrole. *Electrochimica Acta* **2006,** *51* (27), 6025-6037.

31. Rincon-Restrepo, M.; Milthallova, E.; Bayley, H.; Maglia, G., Controlled Translocation of Individual DNA Molecules through Protein Nanopores with Engineered Molecular Brakes. *Nano letters* **2011,** *11* (2), 746-750.

32. Ivanov, A. P.; Actis, P.; Jonsson, P.; Klenerman, D.; Korchev, Y.; Edel, J. B., On-Demand Delivery of Single DNA Molecules Using Nanopipets. *ACS nano* **2015,** *9* (4), 3587-3595.

33. Wanunu, M.; Morrison, W.; Rabin, Y.; Grosberg, A. Y.; Meller, A., Electrostatic focusing of unlabelled DNA into nanoscale pores using a salt gradient. *Nature nanotechnology* **2010,** *5* (2), 160-165.

34. Lee, M.-H.; Kumar, A.; Park, K.-B.; Cho, S.-Y.; Kim, H.-M.; Lim, M.-C.; Kim, Y.-R.; Kim, K.-B., A Low-Noise Solid-State Nanopore Platform Based on a Highly Insulating Substrate. *Scientific Reports* **2014,** *4*.

35. Liu, B. W.; Salgado, S.; Maheshwari, V.; Liu, J. W., DNA adsorbed on graphene and graphene oxide: Fundamental interactions, desorption and applications. *Current Opinion in Colloid & Interface Science* **2016,** *26*, 41-49.

36. Park, J. S.; Goo, N. I.; Kim, D. E., Mechanism of DNA Adsorption and Desorption on Graphene Oxide. *Langmuir* **2014,** *30* (42), 12587-12595.

37. Ramanaviciene, A.; Ramanavicius, A., Molecularly imprinted polypyrrole-based synthetic receptor for direct detection of bovine leukemia virus glycoproteins. *Biosensors & Bioelectronics* **2004,** *20* (6), 1076-1082.

38. Olsen, C. L.; Chan, E.; Turner, D. S.; Iravani, M.; Nagy, M.; Selam, J. L.; Wong, N. D.; Waxman, K.; Charles, M. A., INSULIN ANTIBODY-RESPONSES AFTER LONG-TERM INTRAPERITONEAL INSULIN ADMINISTRATION VIA IMPLANTABLE PROGRAMMABLE INSULIN DELIVERY SYSTEMS. *Diabetes Care* **1994,** *17* (3), 169-176.

39. Heise, T.; Bott, S.; Tusek, C.; Stephan, J. A.; Kawabata, T.; Finco-Kent, D.; Liu, C.; Krasner, A., The effect of insulin antibodies on the metabolic action of inhaled and subcutaneous insulin - A prospective randomized pharmacodynamic study. *Diabetes Care* **2005,** *28* (9), 2161-2169.

40. Plesa, C.; Kowalczyk, S. W.; Zinsmeester, R.; Grosberg, A. Y.; Rabin, Y.; Dekker, C., Fast Translocation of Proteins through Solid State Nanopores. *Nano letters* **2013,** *13* (2), 658-663.

41. Petersen, K. G.; Storch, M. J.; Rother, K.; Licht, T.; Kerp, L., INSULIN AND ANTI-INSULIN ANTIBODY INTERACTION - EVIDENCE FOR THE FORMATION OF 7S AND 10S STRUCTURES. *Diabetes* **1985,** *34* (8), 799-802.

42. Peng, H.-P.; Lee, K. H.; Jian, J.-W.; Yang, A.-S., Origins of specificity and affinity in antibody-protein interactions. *Proceedings of the National Academy of Sciences of the United States of America* **2014,** *111* (26), E2656-E2665.

43. Preiner, J.; Kodera, N.; Tang, J.; Ebner, A.; Brameshuber, M.; Blaas, D.; Gelbmann, N.; Gruber, H. J.; Ando, T.; Hinterdorfer, P., IgGs are made for walking on bacterial and viral surfaces. *Nature Communications* **2014,** *5*.

CHAPTER 5

The nanopore sensing of AuNP-based nanostructures

Synopsis

In this chapter, gold nanoparticle (AuNP)-based structures are used for analyte detection with nanopipette platforms. I present the screening of the sub-structures within these carriers with a high-bandwidth amplifier and fine-tuning of the nanopore dimension. The translocation signatures of these structures, including AuNP monomers, dimers, and trimers, can be easily distinguished by identifying the sub-peaks corresponding to different sub-structures of the bound analytes. Besides, surface-enhanced Raman scattering (SERS) enhancement effect between the two AuNPs is exhibited in these carriers and studied at the single-molecule level.

Part of this chapter is in preparation as **Ren, R**.; Sun, M. Z.; Xu, C. L.; Ivanov, A. P.; Edel, J. B., A single molecule nanopore binding assay using nanoparticle conjugates. In this work the AuNP based structures were prepared by Prof. Maozhong Sun. The single particle SERS was measured by Dr. Pratibha Goel.

5.1 Introduction

Driven by the need for improved microelectronics and biotechnology devices, the development of conductive or semi-conductive materials-based nanostructures has been employed in a wide range of applications. Nanostructures are usually fabricated by top-down approaches such as lithography or bottom-up such as self-assembly and the chemical synthesis of complex compounds. Self-assembling structures have recently attracted more attention because of a large number of advantages compared with traditional methods: self-assembly fabrication avoids challenging steps in nanofabrication, such as a highly complex synthetic chemistry. Also, self-assembly materials can be designed to be biocompatible, defect-free, and self-healing. A wide range of self-assembly methods has recently been developed based on DNA, protein, and polymers as the nanostructure linkers. By using various synthetic routes, different nanostructures based on nanoparticles, nanorods, nanowires, nanoprisms, nanopyramids, and other nanocolloids, have been constructed. However, to use the self-assembly method to fabricate these complex superstructures with controllable feature sizes and geometry in different dimensions[1-10], an extensive, advanced synthetic toolbox is required.

A simple and efficient self-assembly method was recently reported based on the PCR[11] and antibody-antigen interaction[12]. Using these flexible and controllable processes, a series of nanostructures, such as dimers,[12-14] trimers,[15, 16] or even tetramers[17, 18] in different dimensions, have been explored. Although these nanostructures are successfully fabricated and characterised by conventional methods, for example, transmission electron microscopy (TEM), dynamic light scattering (DLS), and surface-enhanced Raman scattering (SERS) detecting these nanostructures in vitro and at the single-molecule level remains a challenge. Nanopore technology provides single-molecule sensing platform where the size of the nanopore can be optimised to discriminate between these charged superstructures. Ang et al. used solid-state nanopore detection of several nanoparticle-based superstructures to discriminate nucleotides. With the addition of nucleotides, the nanoparticles self-assembled from monomers (single AuNP) to dimers (two AuNP linked together), trimers, tetramers, or pentamers. When these charged nanostructures passed through the nanopore, the ionic current changes varied because the molecules' charges and sizes are different (**Figure 5.1**).[19] However, the ionic current signal amplitude can be often inaccurate, due to size heterogeneity of the nanoparticles and the elusive rotation of the superstructures when they pass through a nanopore. Herein, to discriminate different superstructures and to minimise false positives, the screening of the sub-structure, indicating each part of the

superstructures, is essential. However, this is often difficult to achieve because of fast analyte translocation through the nanopore, long effective length of the nanopore compared to the analyte size, and unstuffiness instrumentation bandwidth.

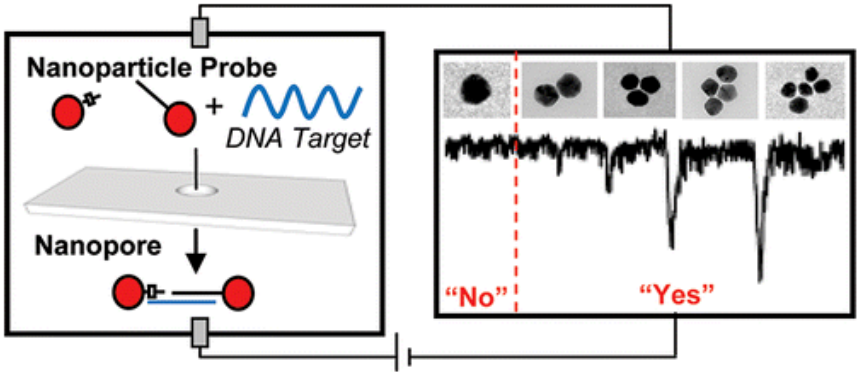


Figure 5. 1 A single-nucleotide polymorphism detection assay that integrates nanoparticle-based superstructures and a solid-state nanopore sensing platform. Different ionic signals represent different nanostructures. Figure adapted from reference 19.

In this chapter, to address the issues as mentioned above, we fabricated a series of nanoparticle-based superstructures using self-assembly methods. Their structures were measured using a high-bandwidth amplifier and fine-tuning nanopore size (**Figure 5.2**). The sub-structures of these AuNP-based nanostructures included AuNP monomers, AuNP symmetrical or asymmetrical dimers, and even AuNP trimers, were detected by a manifestation of sub-peaks of the single-molecule translocation signal. The motivation of doing this detection is to prepare for the single molecule biosensing next step. For a brief example, with adding the procalcitonin (PCT), two monomers with antibodies will be dimerised, which can be detected as the signal of monomer and dimer can be discriminated effectively (This will be discussed in **Chapter 6**).

Moreover, the single-particle surface-enhanced Raman scattering (SERS) detection was also performed, and an amplified Raman signal located in the nanogap of these plasmonic structures was observed, consistent with experimental predictions.

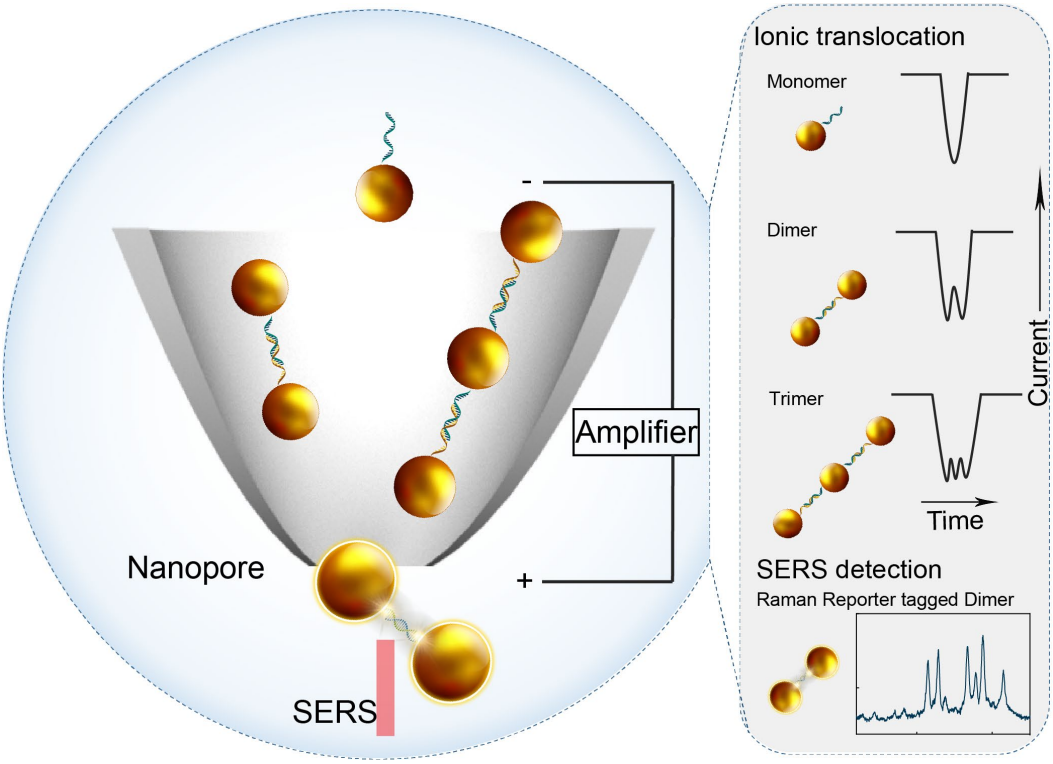


Figure 5. 2 Schematic of single-molecule detection of nanoparticle-based superstructures. From an AuNP monomer and AuNP symmetrical dimers to trimers, a range of nanoparticle-based superstructures were fabricated and sensed by the nanopore platform incorporating a high-bandwidth amplifier. The sub-peaks of the ionic translocation signal represent the sub-structures of the nanoparticle-based superstructures. In addition, single-molecule SERS detection was also applied by integrating gold-coated nanopores, SERS, and Raman reporter tagged AuNP dimers.

5.2 Methods

In this chapter, to challenge the limitation of the nanopore resolution, different AuNP-based nanostructures were designed:

- AuNP monomer, which is one AuNP linked by a ssDNA;
- AuNP symmetrical dimer (35-base linker), two 17 nm AuNPs linked by a dsDNA
- AuNP symmetrical dimer (115 base linker), two 17 nm AuNPs linked by a longer DNA linker dsDNA
- AuNP asymmetrical dimer, 20 nm AuNP and 10 nm AuNP linked by a dsDNA
- AuNP trimer, three 17 nm AuNP linked by two dsDNA to a linear shape
- 4-ATP labelled AuNP symmetrical dimer, two 4-aminothiophenol modified 35 nm AuNPs linked by a dsDNA

5.2.1 The fabrication of AuNP-based nanostructures

The fabrication of AuNP-based nanostructures is based on the interactions between thiol (SH) and Au, and the PCRs between two complementary ssDNA chains. The structures mentioned above are shown in **Figure 5.3**. All AuNP based nanostructures were fabricated by Prof. Maozhong Sun (Jiangnan University, China).

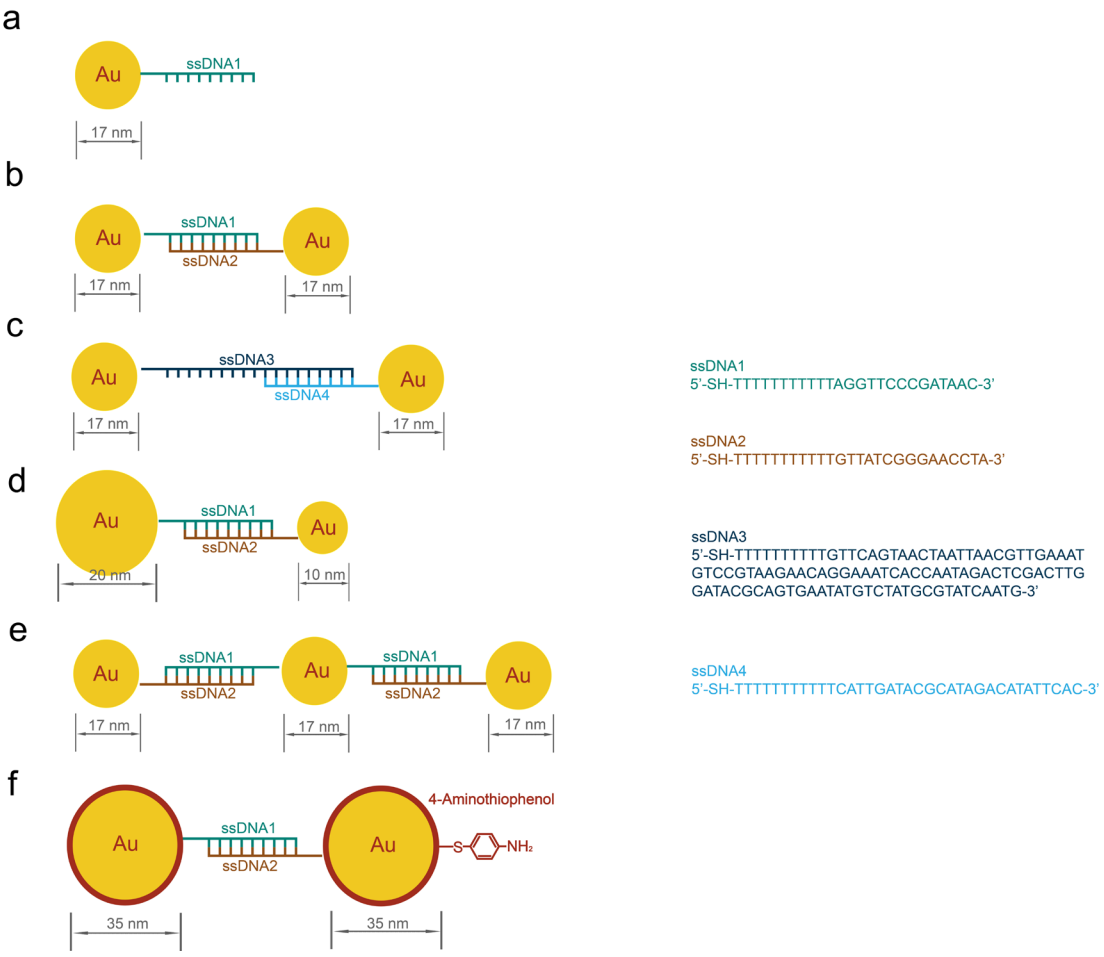


Figure 5. 3 The details of AuNP-based nanostructures. **(a)** AuNP monomer: one 17 nm AuNP modified by an ssDNA. **(b)** AuNP symmetrical dimers: two 17 nm AuNPs linked by a DNA bridge (35 bases long). **(c)** AuNP symmetrical dimers with a long linker: two 17 nm AuNPs linked by a DNA bridge (115 bases long). **(d)** AuNP asymmetrical dimers: one 20 nm AuNP and one 10 nm AuNP linked by a DNA bridge (35 bases long). **(e)** AuNP trimers: three AuNPs linked by two DNA bridges (35 bases long). **(f)** The AuNP symmetrical dimers with Raman reporter. Two 4-aminothiophenol modified 35 nm AuNPs linked by a DNA bridge (35 bases long). All fabrication details are described in the method part.

5.2.1.1 The AuNP monomers

The synthesised AuNPs (17 nm) were concentrated tenfold and resuspended in a 0.5×TBE buffer to a final concentration of 10 nM. The prepared AuNPs were then modified with the ssDNA1 (10 μM, dissolved in TE buffer), in a DNA-to-AuNP molar

ratio of 5:1. A NaCl solution (5 M) was added to the mixture to a final NaCl concentration of 50 mM, and it was left at 25 °C for 12 h. Finally, the mixture was centrifuged (three times) at 7,000 rpm for 10 mins to remove the excess DNA and then resuspended in the TBE buffer. The schematic of the AuNP monomer is presented in **Figure. 5.3a**.

5.2.1.2 The AuNP symmetrical dimers (35-base linker)

The process of fabricating AuNPs (17 nm) modified with the ssDNA2 was the same as for DNA1; 100 μL of AuNP–DNA1 and 100 μL of AuNP–DNA2 were mixed in the TBE buffer containing 50 mM of NaCl. After that, the mixture was hybridised for 12 h at room temperature with gentle stirring. The mixture was then centrifuged at 5,000 rpm for 10 mins to remove the single nanoparticles and to collect the AuNP symmetrical dimers with short linkers. The schematic of the AuNP symmetrical dimers is shown in **Figure. 5.3b**.

5.2.1.3 The AuNP symmetrical dimers (115-base linker)

The 17 nm AuNPs were concentrated tenfold and resuspended in a 0.5×TBE buffer to a final concentration of 10 nM. The prepared AuNPs were then modified with the ssDNA3 (10 μM, dissolved in TE buffer), in a DNA-to-AuNP molar ratio of 5:1. A NaCl solution (5 M) was added to the mixture to a final NaCl concentration of 50 mM, and it was left at 25 °C for 12 h. Finally, the mixture was centrifuged (three times) at 7,000 rpm for 10 mins to remove the excess DNA, and it was resuspended in the TBE buffer. The process of fabricating AuNPs (17 nm) modified with the ssDNA4 was the same as for DNA3; 100 μL of AuNP–DNA3 and 100 μL of AuNP–DNA4 were mixed in a TBE buffer containing 50 mM of NaCl. After that, the mixture was hybridised for 12 h at room temperature with gentle stirring. The mixture was then centrifuged at 5,000 rpm for 10 mins to remove the single nanoparticles and to collect the AuNP symmetrical dimers with long linkers. The schematic of the symmetrical dimers with a long linker is presented in **Figure. 5.3c**.

5.2.1.4 The AuNP asymmetrical dimers

Gold nanoparticles were concentrated tenfold and resuspended in a 0.5×TBE buffer to a final concentration of 10 nM. The prepared 20 nm AuNPs were then modified with the ssDNA1 (10 μM, dissolved in TE buffer, mixture1), and the 10 nm AuNPs were modified with the ssDNA2 (10 μM, dissolved in TE buffer, mixture2), in a DNA-to-AuNP molar ratio of 5:1. A NaCl solution (5 M) was added to the mixture to a final NaCl concentration of 50 mM, and it was left at 25 °C for 12 h. Finally, mixture1 and mixture 2 were centrifuged (three times) at 7,000 rpm and 8,500 rpm, respectively, for

10 mins to remove the excess DNA before being resuspended in the TBE buffer. Furthermore, 100 μL of 20 nm AuNP–DNA1 and 100 μL of 10 nm AuNP–DNA2 were mixed in the TBE buffer containing 50 mM of NaCl. The mixture was hybridised for 12 h at room temperature with gentle stirring. Thereafter, it was centrifuged at 5,000 rpm for 10 mins to remove the single nanoparticles and to collect the AuNP asymmetrical dimers. The schematic of the AuNP asymmetrical dimers is shown in **Figure. 5.3d**.

5.2.1.5 The AuNP trimers

100 μL of 17 nm AuNP–DNA1 and 200 μL of 17 nm AuNP–DNA2 were mixed in a TBE buffer containing 50 mM of NaCl. The mixture was hybridised for 12 h at room temperature with gentle stirring. It was then centrifuged at 4,000 rpm for 10 mins to remove the single nanoparticles and to collect the AuNP trimers. The schematic of these trimers is presented in **Figure. 5.3e**.

5.2.1.6 The 4-ATP labelled AuNP symmetrical dimers (SERS sample)

The 35 nm AuNPs were concentrated tenfold and resuspended in a 0.5×TBE buffer to a final concentration of 10 nM. The prepared AuNPs were then modified with the ssDNA1 (10 μM, dissolved in TE buffer), in a DNA-to-AuNP molar ratio of 5:1. A NaCl solution (5 M) was added to the mixture to a final NaCl concentration of 50 mM, and it was left at 25 °C for 12 h. Finally, the mixture was centrifuged (three times) at 5,000 rpm for 10 mins to remove the excess DNA before being resuspended in the TBE buffer.

Before being modified with the ssDNA2, 4-Aminothiophenol was added to the 35 nm AuNPs, with a final concentration of 10 μM. After 6 h, the AuNPs were centrifuged at 5,000 rpm for 10 mins to remove the unconnected 4-Aminothiophenol. Then, the above AuNPs were modified with ssDNA2. Finally, 100 μL of 35 nm AuNP–DNA1 and 100 μL of 35 nm AuNP–DNA2 were mixed in a TBE buffer containing 50 mM of NaCl. The mixture was hybridised for 12 h at room temperature with gentle stirring. It was then centrifuged at 3,000 rpm for 10 mins to remove the single nanoparticles and to collect the 4-ATP labelled AuNP symmetrical dimers. To increase the stability of the large AuNPs in a high salt concentration, the SERS samples were further modified by PEG-SH. The schematic of the 4-ATP labelled AuNP dimers is presented in **Figure. 5.3f**.

5.2.2 Nanostructure translocation experiments

The translocation experiments were performed from the inside of the nanopipettes (the nanopipettes for the translocation measurements were pulled by Protocol 2 in **Chapter 2**) to the outside, where the AuNPs based nanostructures are loaded in the nanopipette (cis) and an Ag/AgCl working/patch electrode was added in the pipette. At the same time, an Ag/AgCl counter/reference electrode was placed in a buffer solution in the bath (trans). The buffer used in the translocation experiments consisted of 50 mM of KCl and a 10-mM Tris-EDTA (pH = 8) unless reported otherwise. For the translocation of plain metal structures (AuNP monomer, AuNP dimers, AuNP trimers, TBA-modified dimers, AuNP monomer PCT probes), the buffer containing target analytes was simply filled inside the nanopipette. Then, a voltage was applied by a high-bandwidth amplifier VC100 (Chimera Instruments) between the electrodes on both sides of the nanopore, and the current-time trace was recorded. The data were then resampled to 1 μs and digitally filtered to 100 kHz using a low pass filter, and traces were analysed by an in-house Matlab app (details are described in **Chapter 2**).

5.2.3 Single-molecule SERS detection

To enhance the single-molecule SERS signal, a thin layer of Au (10 nm) was deposited on the nanopore located on the pulled nanopipette area (the nanopipettes for the SERS measurement were pulled by Protocol 3 in **Chapter 2**) using a sputterer (Quorum Technologies Ltd). A low concentration of Au nanoparticles (15 nM of the Au dimer) in 100 mM of KCl was used for experiments. The Au-coated nanopipettes were then filled with the 4-ATP labelled AuNP symmetrical dimers, and a blank buffer droplet was inserted, placed on a coverslip. The place of Ag/AgCl electrodes was the same as the set-up of the above electrical translocation experiment. Simultaneous translocation and Raman measurements were carried out on a custom-built Raman microscope using a HeNe 632.8 nm excitation source. The voltage was applied by an eOne amplifier (Elements, Italy) with a 10-kHz low-pass filter and 100 kHz sampling rate. The electrical translocation data and the SERS spectrums were then analysed by a homemade Matlab code.

5.3 Result and discussion

To demonstrate the screening ability of the AuNP conjugates, the initial steps were to quantify the resolution of our platform. First was confirmed the ability to differentiate between monomers and dimers linked with differing DNA lengths. AuNP monomers

were fabricated by attaching a thiol-modified 25-mer ssDNA to the surface of 17 nm in diameter AuNPs (**Figure. 5.3**). Symmetrical AuNP dimers were fabricated by self-assembly of two AuNP monomers with one consisting of a 15 bases complementary sequence. In order to probe the limits of spatial resolution achievable with the method, two kinds of AuNP symmetrical dimers were fabricated: one with 35 bases linkers and the other with 115 bases linkers. Asymmetrical dimers we also designed consisting of 10 nm AuNP monomers and 20 nm AuNPs. Finally, trimers were also quantified and could be achieved by controlling the NP to DNA ratio. Protocols and details of the synthesis can be found in **Figure 5.3** and Methods part. To avoid the unpredictable orientation of the conjugated molecules with high viscosity during translocation, all AuNPs based samples were not protected by polyethene glycol (PEG) unless otherwise stated. All NP conjugates were dispersed after fabrication and measured by UV-Vis after 24 hours stabilisation in the buffer 50 mM KCl, 10 mM Tris-EDTA and used in nanopore experiments. This ionic strength was chosen to minimise NP aggregation and at the same time maximise the signal to noise of the measurements.

5.3.1 Fine-tuned nanopipette

5.3.1.1 Nanopipette characterisation

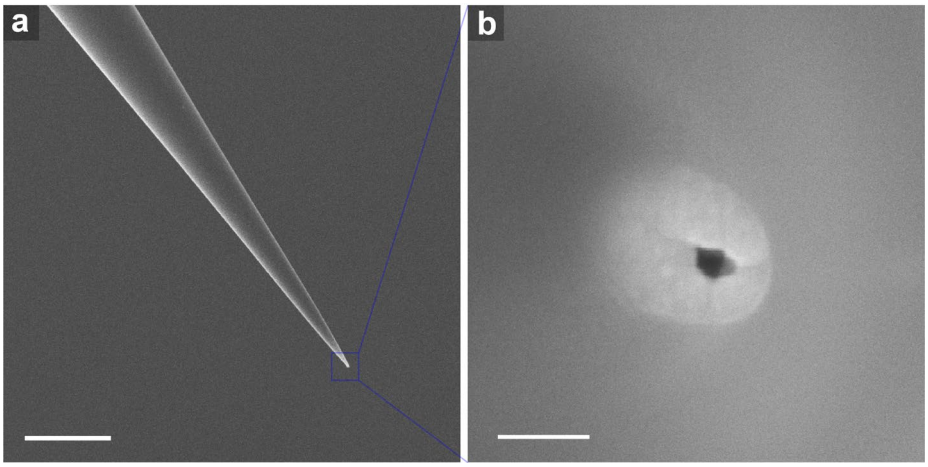


Figure 5. 4 The SEM images of a representative nanopipette. The SEM image of **(a)** a side view (scale bar: 10 μm) and **(b)** a cross-section (scale bar: 100 nm) of a nanopipette. From the images, the conical shape of the nanopipette and the nanopore located on the tip can be observed.

Nanopore experiments were done using single-barrelled nanopipettes[20, 21], which can be fabricated by laser-assisted pulling of quartz capillaries (the details and parameters are shown in **Chapter 2, Section 2.1.1.2**). The nanopores were pulled with an average diameter slightly larger than the dimensions of the nanoparticles, with an average diameter of 34 ± 5 nm, as measured by scanning electron microscope (SEM),

Figure 5.4. These dimensions closely matched the diameters estimated from nanopore conductance measurements of 15.3 ± 2.4 nS in 100 mM KCl (n = 18, **Figure 5.5**).

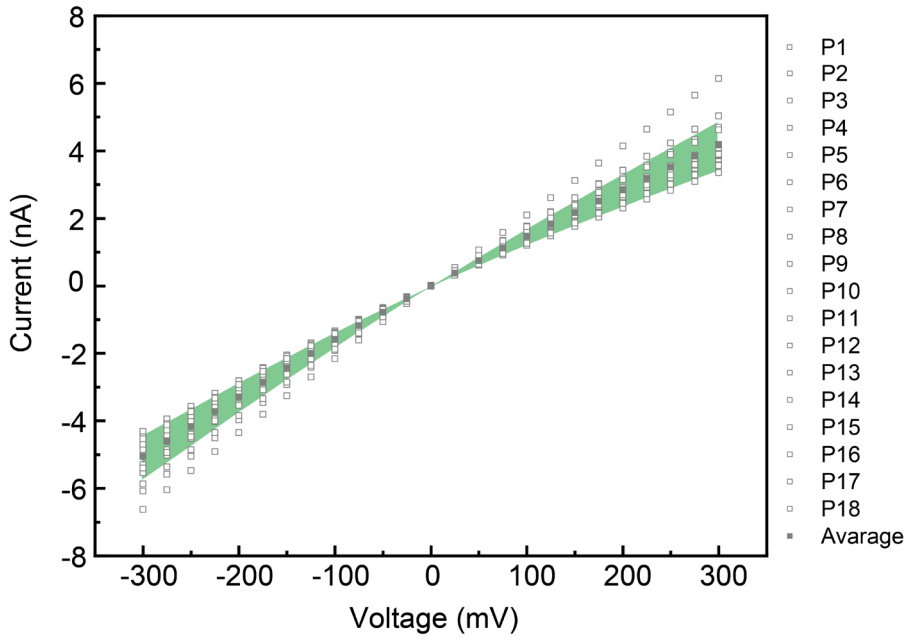


Figure 5. 5 The I-V characterisation of nanopores. Electrical nanopipette characterisation from 18 nanopipettes. The quartz nanopipettes were pulled from quartz capillaries by a laser-based pipette puller. The current-voltage curves indicate the conductance of quartz nanopores to be 15.3 ± 2.4 nS (n = 18). The measurements of the I-V characterisation were performed in 100 mM of KCl, 10-mM of Tris-EDTA, pH 8.

5.3.1.2 Effective length calculation

To improve the resolution of biosensors, several methods have been developed to fabricate nanopores with a short, effective length[22-24], which can increase small fragment readout and minimise the neighbouring effects. To confirm that the fabricated nanopipettes had a sufficient resolution to detect the sub-structures of the targets, the nanopore was electrically measured, and the effective length was estimated.

The effective length of a nanopipette is the portion of the electrolyte-filled pore over which contribute the majority of the total ionic resistance (75–80% for our calculations). In addition, the voltage drop is greatest in this area, resulting in a region along the nanopore channel where the electric field is strongest. For a cylindrical nanopore, the effective length is simply equal to length of the pore (on the solid-state nanopore, the pore length is considered the same as the thick of the membrane). Theoretically, the voltage drops linearly along the pore length in these cylindrical pores. However, for a conical nanopore, such as the one that is located on the tip of the nanopipette, a nonlinear drop in the electric field and resistance occur along with the pore length, due to the gradual increase of pore radius along the nanopore channel length.[25]

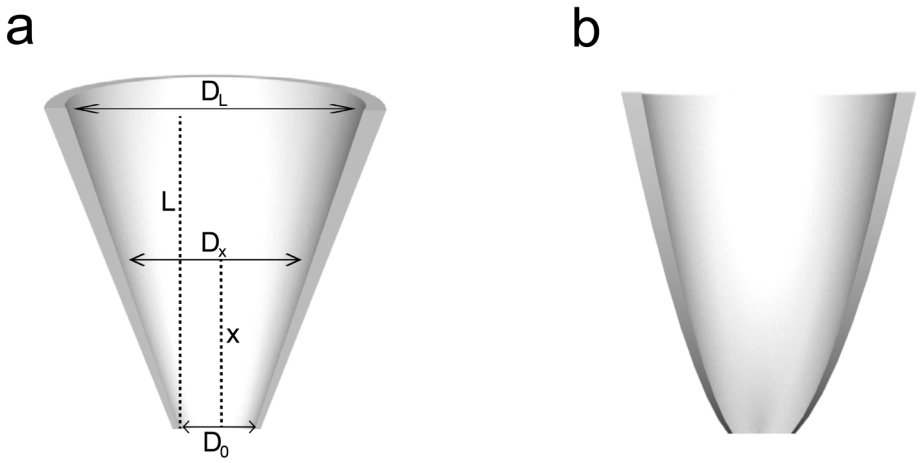


Figure 5. 6 Schematic representation of a nanopipette. **(a)** The model of the conical nanopore for effective length calculation. **(b)** The real nanopore shape model.

The nanopipette's effective length can be estimated from the resistance distribution along the nanopore channel (**Figure 5.6**). The resistance can be estimated with a different position (R_x) from the nanopore. The distance from the end, x, ranges from 0 to L, which is a long-enough length that can be measured using SEM imaging. D_0 represents the diameter of the end of the nanopipette part, and D_L represents the diameter of the area, where is a length of L from the end. The diameter, along with the distance, D_x, can be calculated. Then, the R_x can be estimated.[26, 27]

D_x can be expressed as the following function of x:

$$D_x = \frac{x(D_L - D_0) + LD_0}{L} \qquad (\mathbf{5.1})$$

In our calculation, the step of x is 1 nm.

The resistance R_x can be calculated as the following function:

$$R_x = \frac{4L\rho}{\pi D_0 D_x} \qquad (\mathbf{5.2})$$

where ρ is the specific resistance of the electrolyte, which fills the pore, and R_{tot} represents the total resistance. Therefore, combining **Equation 5.1** and **Equation 5.2**, the relationship between R_x/R_{tot} and x can finally indicate the effective length of the nanopore.

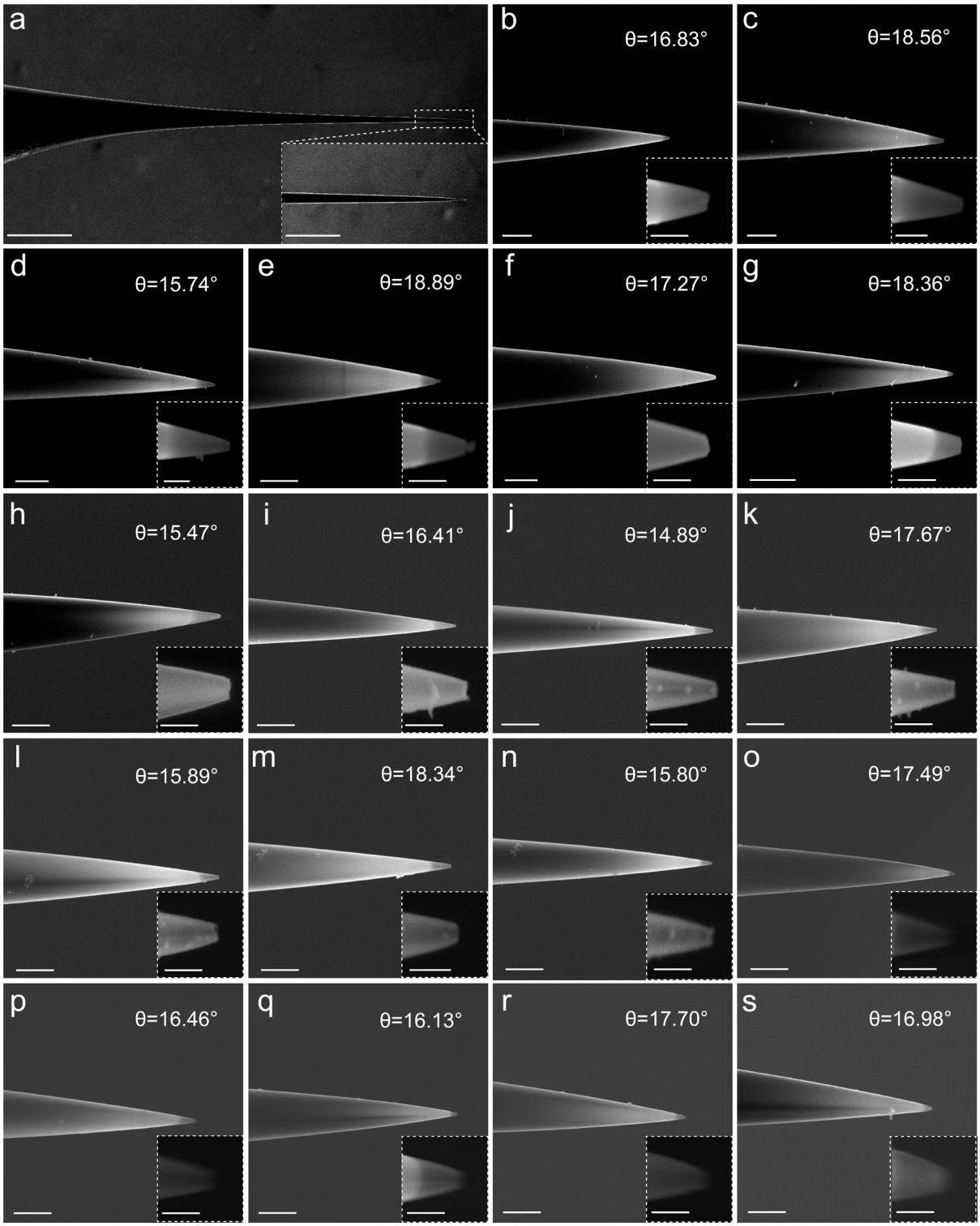


Figure 5. 7 The SEM of the nanopore and tip angle measurement. **(a)** SEM image depicts the tip length and geometry, (scale bar 100 μm, inset 20 μm) **(b–s)** The side view of the nanopore and the semi-angle of the first 100 nm of the nanopipette (scale bar 1 μm, inset 50 nm).

From the SEM image of the side view of the nanopipette, the semi angles of the tip cone were measured to be 16.9 ± 1.1 of the first 100 nm (n = 18, **Figure 5.7**). The D_L, L, and D_0 of each nanopore were measured and used for the effective length calculation.

Figure 5.8 illustrates the resistance drop, along with the distance from the pore. Considering that the effective length of a pore is the portion of the electrolyte-filled pore over which the majority (75–80% for our calculations) of its ionic resistance is focused, the effective length of the nanopores we used is approximately 25–55 nm. However, it is noteworthy that the real nanopore does not adopt a perfect conical geometry. From the SEM images in **Figure 5.7**, it can be seen that the tip radius decreases abruptly close to the pipette tip, as is illustrated in the model in **Figure 5.6b**. Compared with our calculation result, which is based on conical nanopipette geometry, the real nanopipette geometry will result in an even shorter effective length. The geometry of the nanopore is, unfortunately, always varied with different nanopipettes; therefore, simulation is difficult to achieve.

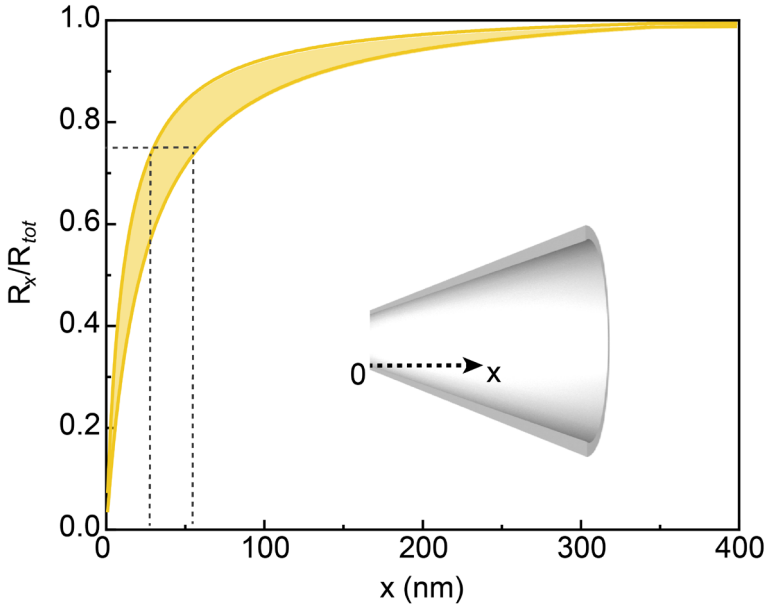


Figure 5. 8 Calculation of the nanopipette's effective length. The ratio of the resistance of 18 conical nanopores from length *x* to 500 nm, which is considered to reach the whole resistance. Considering the majority resistance (75%–80%) in our calculation, the effective length can be calculated.

5.3.2 Single-molecule sensing of nanoparticle-based nanostructures

5.3.2.1 Single-molecule translocation detection

The analyte was filled inside the nanopipette where a patch electrode (AgCl) was placed, and a ground/reference electrode (AgCl) was placed in a bath, outside the pipette. By applying a negative potential, it was possible to transport the AuNPs from inside (cis) to outside (trans) of the nanopipette. A high bandwidth amplifier (Chimera VC100) was used with a 1 μs sampling rate and 100 kHz low-pass digital filter.

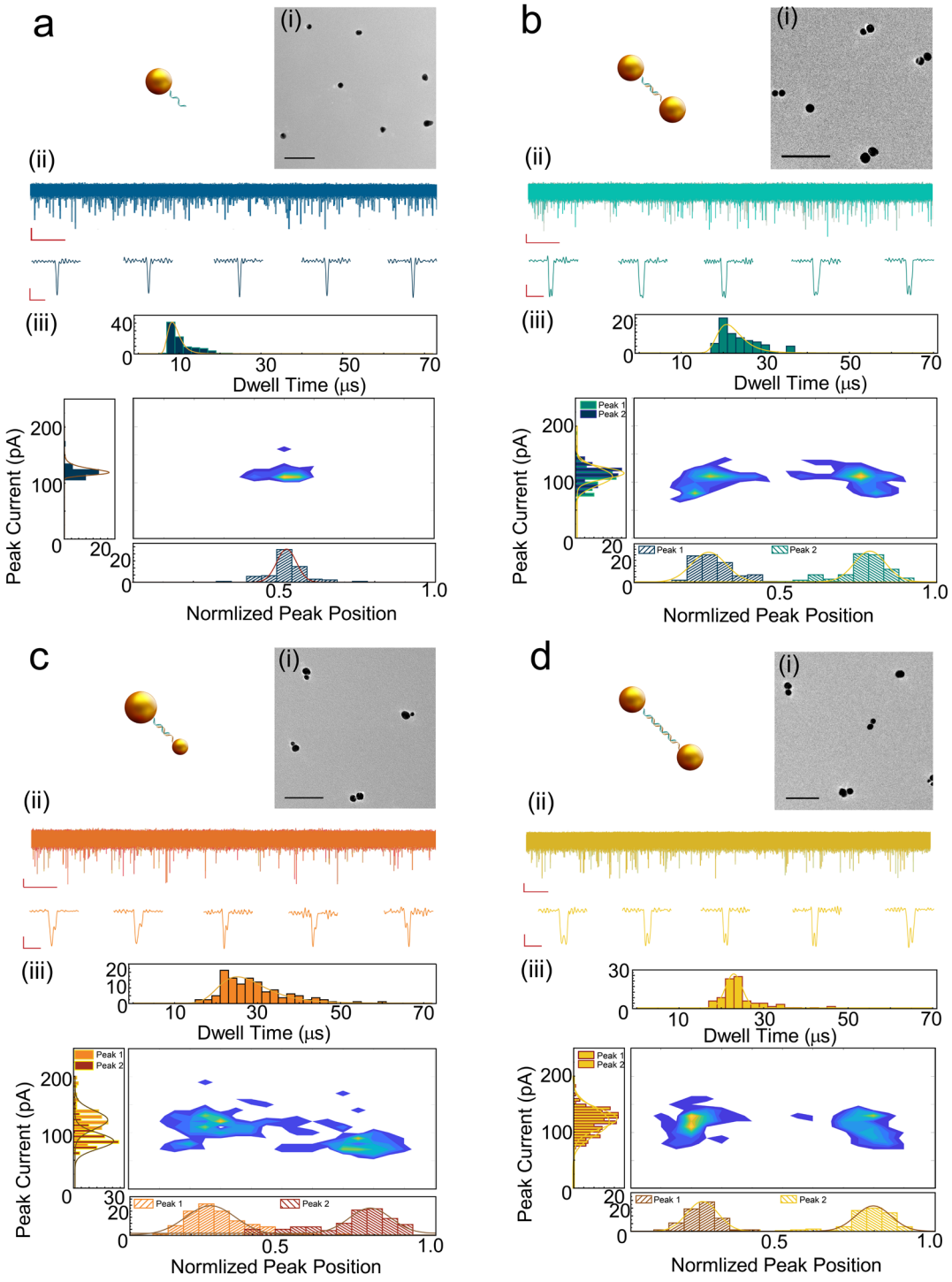


Figure 5. 9 The TEM images, current-time traces, individual events, and statistics of a series of AuNP-based nanostructures. The TEM (scale bar: 100 nm), current-time traces (scale bar: vertical 50 pA, horizontal 5 s), individual events (scale bar: vertical 50 pA, horizontal 20 μs), and statistics for **(a)** AuNP monomers, **(b)** AuNP symmetrical dimers (35-mer linker), **(c)** AuNP asymmetrical dimers, and **(d)** AuNP symmetrical dimers (115-mer linker). The schematic and TEM images in **(i)** indicate a clear geometry of the molecules. The typical translocation traces and individual translocation events of each molecule are also depicted in **(ii)**, as their signatures can be distinguished easily from others. All the translocation experiments were performed in 50 mM of KCl, 10 mM of Tris-EDTA, and at a potential of -600 mV. Each current-time trace was recorded at a 1-us sampling rate and filtered using a low-pass Bessel filter with a cut-off frequency of 100 kHz. The statistics of translocation are illustrated in **(iii)**,

including the translocation dwell time, peak current, and normalised peak position. Surface plots along with peak current and normalised peak position histograms are also presented, and they clearly indicate that the translocation signal is capable of simulating the nanostructure, the size/charge of each molecule, and even the distance between them.

Figure 5.9 shows a comparison of translocation characteristics between the different conjugates. The simplest constructs, AuNP monomers, translocated relatively quickly in a single file translocation with a single peak dwell time distribution (mean dwell time of 8.3 ± 1.4 µs at an applied potential of -600 mV), **Figure 5.9a**. In comparison symmetric and asymmetric dimers with a 35-base DNA spacer, **Figure 5.9b-5.9c** exhibited clear double-file events. The current amplitudes of each subpeak are consistent with the size of the individual AuNPs within the conjugate.

The observations are consistent with the model that the first peak appears due to the negatively charged AuNPs passing through the nanopore sensing area. This is followed by a decrease of the current due to the reduced charge on the linker. Finally, the 2nd AuNP results in a 2nd peak, **Figure 5.10**.

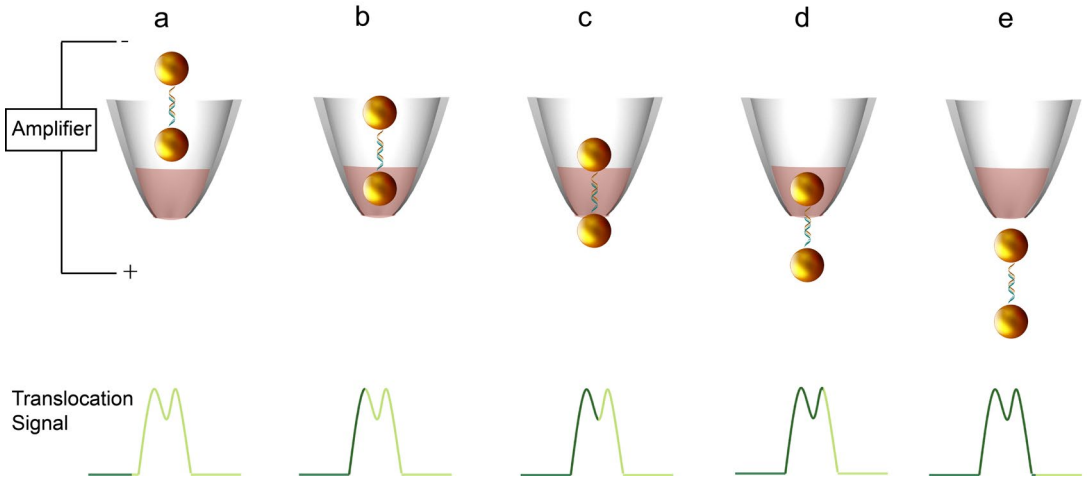


Figure 5. 10 Schematic of a nanopore sensing the sub-structures of the dimer. With applied potential, the negatively charged molecule is driven by an electrophoretic force and thus moves to the anode. **(a)** When it approaches but does not enter the nanopore sensing area, only the current baseline can be recorded. **(b)** When the first AuNP dominates the sensing part, the local conductivity is increased by the heavy, negatively charged particle. **(c)** Then, the DNA bridge passes through the sensing area, generating a trough. **(d)**The second AuNP enhances the signal again when it passes the sensing area. **(e)**The whole event finishes after the molecule is pushed out of the nanopipette.

The mean dwell time of the dimers in **Figure 5.9b** is 20.8 ± 2.7 µs which is just over twice the monomer translocation time and is consistent with linear transport through the nanopore. Importantly, one could distinguish between the peaks with high spatial resolution, as the distance between the peaks was a mere 28 nm. Voltage dependence along with current-time traces are shown in **Figure 5.11**.

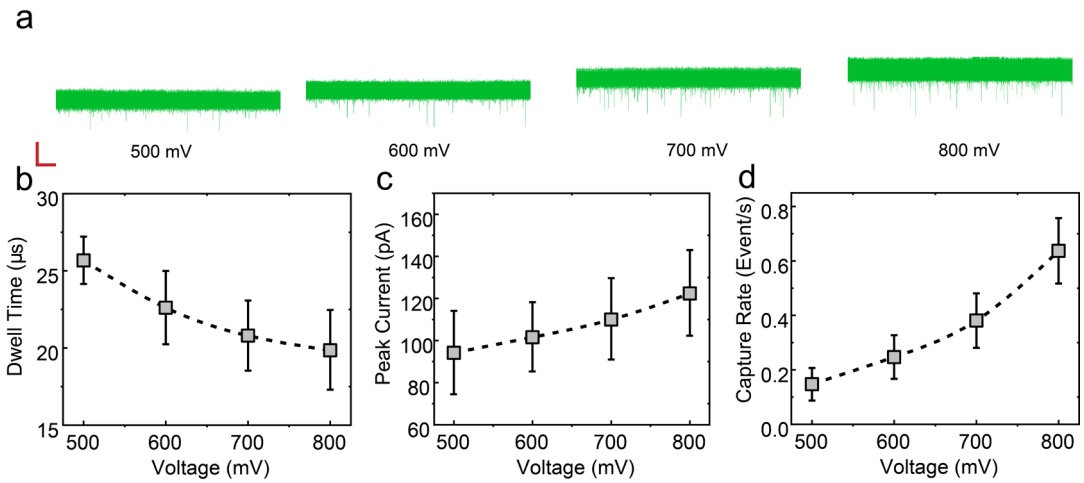


Figure 5. 11 The voltage dependence of AuNP symmetrical dimers. **(a)** The current-time traces of the AuNP symmetrical dimers with biases of 500, 600, 700, and 800 mV. **(b)** The decreasing of mean dwell times, **(c)** the increasing of mean peak currents, and **(d)** the increasing of event frequency is observed as the voltage is increased. All the translocation experiments were performed in 50 mM of KCl and 10 mM of Tris-EDTA. Each current-time trace was recorded at a 1-μs sampling rate and filtered using a low-pass Bessel filter with a cut-off frequency of 100 kHz. Error bars represent the standard deviation of three independent experimental repeats with different nanopipettes.

A comparison between AuNP symmetrical dimers with different linker lengths (35 bases and 115 bases) is also shown in **Figure 5.9b** and **Figure 5.9d**. Furthermore, it was possible to differentiate between spacers of different lengths, which correspond to a distance of 28 and 51 nm, respectively.

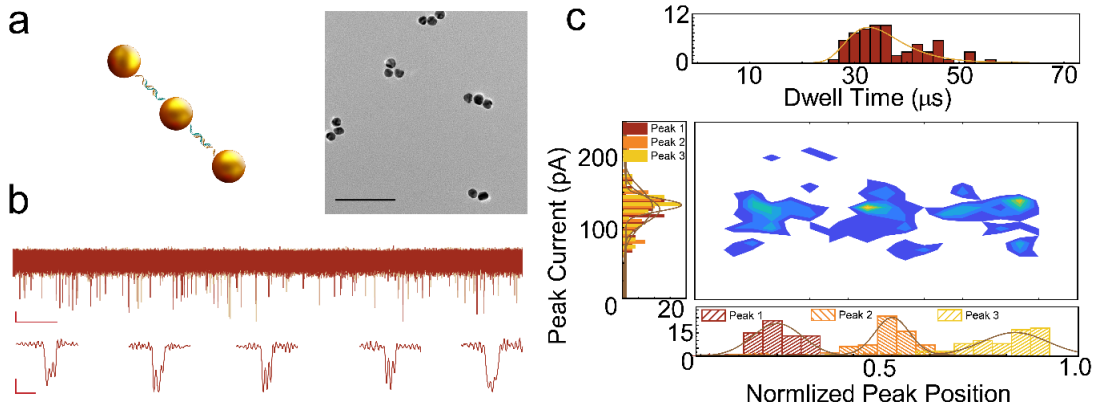


Figure 5. 12 The TEM images, current-time traces, individual events, and statistics of a series of AuNP trimers. The **(a)** TEM (scale bar: 100 nm), **(b)** current-time traces (scale bar: vertical 50 pA, horizontal 5 s), **(c)** individual events (scale bar: vertical 50 pA, horizontal 20 μs) for AuNP trimers. The translocation experiments were performed in 50 mM of KCl, 10 mM of Tris-EDTA, and at a potential of -600 mV. The current-time trace was recorded at a 1-μs sampling rate and filtered using a low-pass Bessel filter with a cut-off frequency of 100 kHz.

When asymmetric AuNPs dimers were translocated out of the nanopipette (**Figure 5.9c**), their asymmetric size was reflected in the shape of an individual event in current

time traces as well as the corresponding current peak distributions. The double peak current distributions were recorded with high peak currents of 155.51 ± 21.55 pA and 81.83 ± 13.47 pA, corresponding to translocations of 20 nm and 10 nm AuNP, respectively. Interestingly, nearly 95% of all translocation events of asymmetric dimers showed a preferential orientation with the larger NP being transported first, which was attributed to the larger NPs carrying a higher surface charge. Although this was not the focus of the present chapter, we also investigated the possibility of translocating and detecting NP trimers, **Figure 5.12**. Trimers could be detected with well-defined individual monomer signatures, and it took 32.7 ± 5.0 μs for individual trimers to translocate through the nanopore, which is 3.94-folds (4.23-folds for spatial length) longer than the monomer dwell time and 1.57-folds (1.61-folds for spatial length) longer than the dimer dwell time, respectively.

5.3.2.2 Single-particle SERS detection

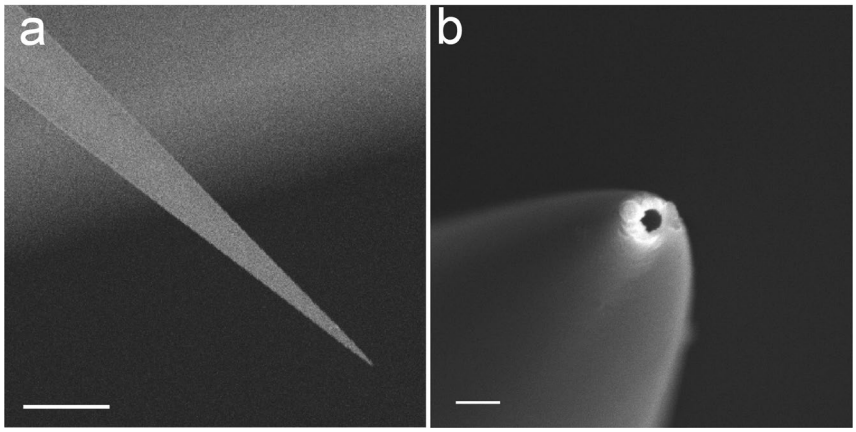


Figure 5. 13 The SEM images of Au-coated nanopipette. SEM images of nanopipette after Au 10 nm layer deposition: **(a)** side view (scale bar: 10 μm), **(b)** top-view (scale bar: 200 nm). The size of the nanopore at the tip was approximately 60 nm. A 10 nm layer of Au was deposited on the nanopore prior to translocation to enhance the SERS signal.

To further characterise the translocations of these metallic nanoparticles, single-particle surface-enhanced Raman scattering (SERS) was also performed on a modified gold-coated (10 nm thickness) nanopipette, **Figure 5.13, Figure 5.14**. Due to the coupling and proximity between dimer and metal pipette surface, this results in a significant increase in Raman signal.[28, 29]

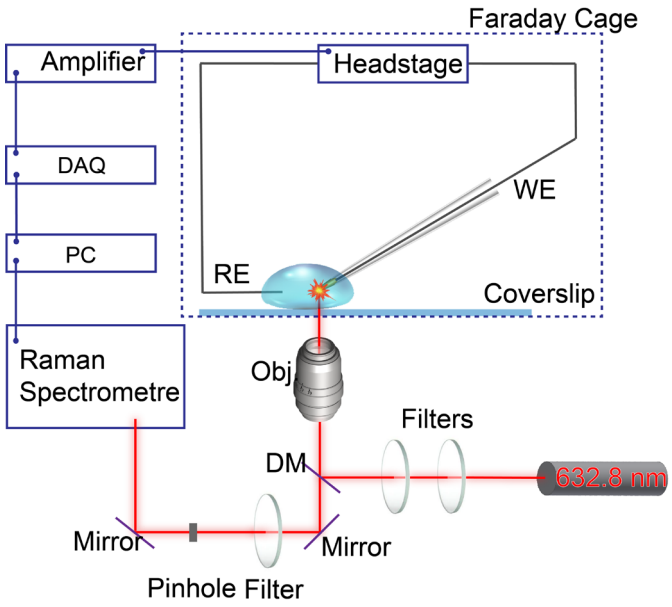


Figure 5. 14 Customised electrical detection set-up with integrated laser optics to enable Raman measurement.

To achieve single-particle SERS somewhat larger 35 nm AuNP symmetrical dimers we used due to the higher scattering cross-section. The AuNPs were functionalized with 4-aminothiophenol (ATP) dye (**Figure 5.3**). The dimer is further stabilized with PEG to ensure the particles do not aggregate at the 100 mM salt concentrations required to perform the translocations. A typical SERS spectrum of the NPs in bulk solution is shown and consists of expected peaks at 1138, 1387 and 1571 cm^{-1} (**Figure 5.15a**). This is comparable to the data obtained for single-particle SERS as can be seen from the transients in **Figure 5.15b**. The integration time for the transients was 810 µs, and translocations were obtained at -800 mV. In this example, the optical translocation times were 3.24 ms which is longer than the corresponding electrical events (0.79 ± 0.29 ms), **Figure 5.16**. This is due to the nanopore sensing region being much smaller than the diffraction-limited laser spot size (ca. 1 µm).

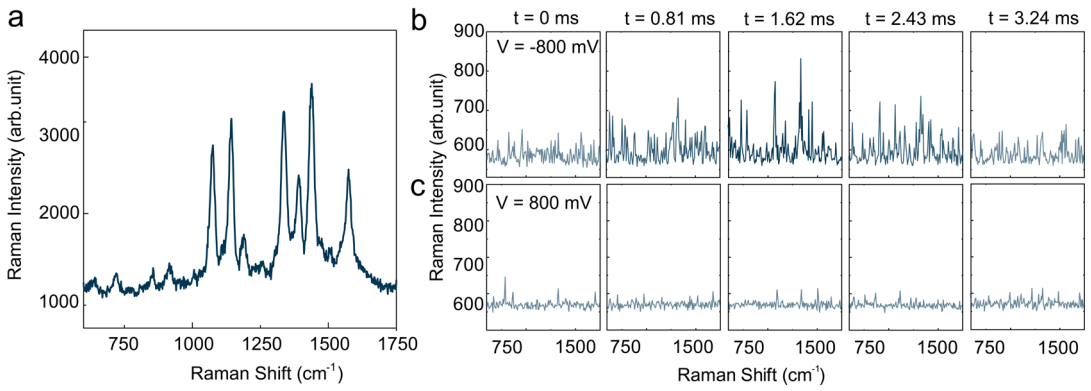


Figure 5. 15 The single-molecule Raman detection of a 4-ATP tagged AuNP symmetrical dimer. **(a)** The SERS spectrum of the 4-ATP modified AuNP symmetrical dimer in bulk solution. SERS spectrum

of 4-ATP dye present in the nanogap of the AuNP symmetrical dimer. This spectrum indicates a significant enhancement of the 1,138, 1,387, and 1,571 cm^{-1} vibrational bands of 4-ATP. **(b)** Raman spectra demonstrate the translocation of the dimers. The top panels illustrate a 4.05-ms translocation using a -800-mV potential at an 810-µs acquisition time. These spectra demonstrate that a single AuNP dimer is translocating through the nanopore over a period of 4.05 ms. **(c)** The Raman spectra of a PEG-modified 4-ATP loaded Au dimer using +800 mV potential. There is a small enhancement in vibrational bands, indicating that the Au dimer moves away from the nanopore, and no translocation takes place.

As a negative control, Raman spectra were also acquired for the event when the reverse potential is applied to diffuse the dimer away from the nanopore. In these controls, no Raman signal was observed, **Figure 5.15c**. We envisage that this method can also be used to perform molecular assays and complements the electrical work shown in this manuscript.

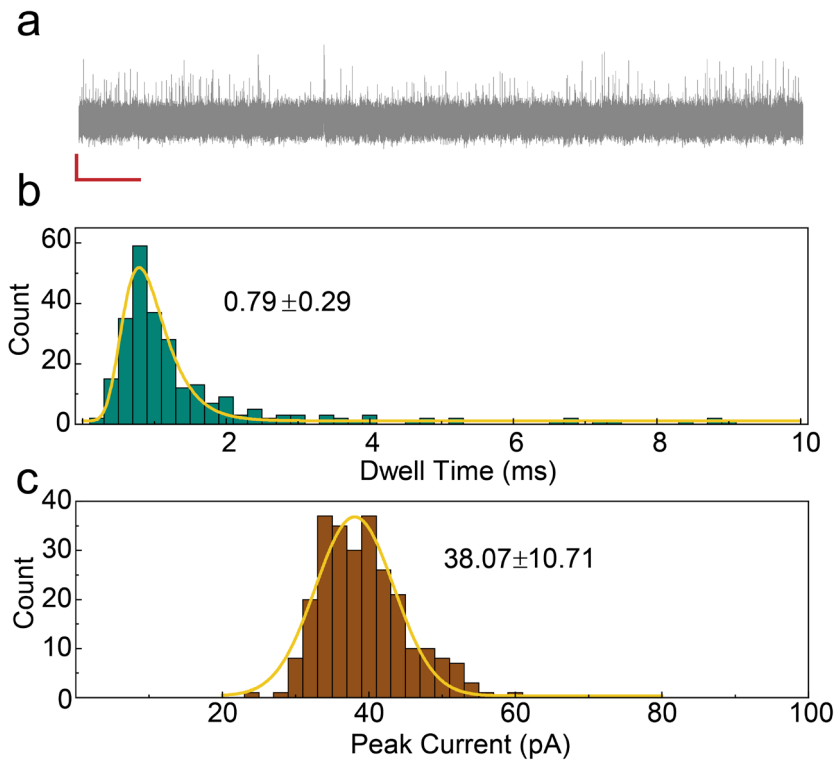


Figure 5. 16 Translocation of a PEG-stabilised 35 nm AuNP dimer functionalised with 4-ATP dye. **(a)** The current-time trace (scale bar: vertical 50 pA, horizontal 5 s) and statistics for a 1 nM Raman sample (35 nm AuNP dimer functionalised with 4-ATP dye, protected by SH-PEG). All the translocation experiments were performed in 100 mM of KCl and 10 mM of Tris-EDTA. The current-time trace was recorded at a 10-us sampling rate and filtered using a low-pass Bessel filter with a cut-off frequency of 10 kHz. **(b)** The dwell time distribution of the electrical translocation of the dimer. The translocation duration of this sample is much longer than others in this work because the PEG-modified molecules have high viscidity. Moreover, the charge of the particles is shielded, so they move slowly, and some unpredictable rotation may occur when the electric field is applied. **(c)** The amplitude statistics of the translocation.

5.4 Conclusion

Although nanoparticle-based superstructures have already been reported, and some of them are characterised by nanopore translocation, in this chapter, we demonstrate that it is possible to use a fine-tuned nanopore testing platform incorporating high-bandwidth instruments to depict the sub-structure of these molecules. I designed and fabricated a detection platform to differentiate a series of AuNP-based nanostructures, including an AuNP monomer, AuNP symmetrical dimers with different linkers, asymmetrical dimers, and AuNP trimers. When a molecule with a complicated structure passes through the nanopore, a rough shape can be identified from the peak currents observed in each translocation event. These, in turn, can reflect the charge/shape of each part of the molecule. In addition, by utilising the plasmonic effect of the dimer system, single-molecule SERS detection was also achieved by a customised SERS/electrical translocation set-up incorporating the Raman tag labelled AuNP dimers.

Inspired by the high-resolution translocation signal, we believe it is worth using this system to address the limitations of utilising nanopores to detect small biomolecules, which always pass through the pores at fast speeds and with negligible signals because of their small size and weak charge. Therefore, based on the detection of AuNP dumbbell molecules, I designed two strategies to sense the elusive biomolecules at the single-molecule level, which are presented in the next chapter.

5.5 References

1. Mirkin, C. A.; Letsinger, R. L.; Mucic, R. C.; Storhoff, J. J., A DNA-based method for rationally assembling nanoparticles into macroscopic materials. *Nature* **1996,** *382* (6592), 607-609.

2. Deng, Z. X.; Tian, Y.; Lee, S. H.; Ribbe, A. E.; Mao, C. D., DNA-encoded self-assembly of gold nanoparticles into one-dimensional arrays. *Angewandte Chemie-International Edition* **2005,** *44* (23), 3582-3585.

3. Alivisatos, A. P.; Johnsson, K. P.; Peng, X. G.; Wilson, T. E.; Loweth, C. J.; Bruchez, M. P.; Schultz, P. G., Organization of 'nanocrystal molecules' using DNA. *Nature* **1996,** *382* (6592), 609-611.

4. Claridge, S. A.; Goh, S. L.; Frechet, J. M. J.; Williams, S. C.; Micheel, C. M.; Alivisatos, A. P., Directed assembly of discrete gold nanoparticle groupings using branched DNA scaffolds. *Chemistry of Materials* **2005,** *17* (7), 1628-1635.

5. Liz-Marzan, L. M.; Mulvaney, P., The assembly of coated nanocrystal. *Journal*

of Physical Chemistry B **2003,** *107* (30), 7312-7326.

6. Niemeyer, C. M., Progress in "engineering up" nanotechnology devices utilizing DNA as a construction material. *Applied Physics a-Materials Science & Processing* **1999,** *68* (2), 119-124.

7. Nykypanchuk, D.; Maye, M. M.; van der Lelie, D.; Gang, O., DNA-guided crystallization of colloidal nanoparticles. *Nature* **2008,** *451* (7178), 549-552.

8. Taton, T. A.; Mucic, R. C.; Mirkin, C. A.; Letsinger, R. L., The DNA-mediated formation of supramolecular mono- and multilayered nanoparticle structures. *Journal of the American Chemical Society* **2000,** *122* (26), 6305-6306.

9. Qin, W. J.; Yung, L. Y. L., Nanoparticle-DNA conjugates bearing a specific number of short DNA strands by enzymatic manipulation of nanoparticle-bound DNA. *Langmuir* **2005,** *21* (24), 11330-11334.

10. Niemeyer, C. M., Nanoparticles, proteins, and nucleic acids: Biotechnology meets materials science. *Angewandte Chemie-International Edition* **2001,** *40* (22), 4128-4158.

11. Chen, W.; Bian, A.; Agarwal, A.; Liu, L. Q.; Shen, H. B.; Wang, L. B.; Xu, C. L.; Kotov, N. A., Nanoparticle Superstructures Made by Polymerase Chain Reaction: Collective Interactions of Nanoparticles and a New Principle for Chiral Materials. *Nano letters* **2009,** *9* (5), 2153-2159.

12. Wu, X. L.; Xu, L. G.; Liu, L. Q.; Ma, W.; Yin, H. H.; Kuang, H.; Wang, L. B.; Xu, C. L.; Kotov, N. A., Unexpected Chirality of Nanoparticle Dimers and Ultrasensitive Chiroplasmonic Bioanalysis. *Journal of the American Chemical Society* **2013,** *135* (49), 18629-18636.

13. Sun, M. Z.; Xu, L. G.; Banhg, J. H.; Kuang, H.; Alben, S.; Kotov, N. A.; Xu, C. L., Intracellular localization of nanoparticle dimers by chirality reversal. *Nature Communications* **2017,** *8*, 10.

14. Ma, W.; Fu, P.; Sun, M. Z.; Xu, L. G.; Kuang, H.; Xu, C. L., Dual Quantification of MicroRNAs and Telomerase in Living Cells. *Journal of the American Chemical Society* **2017,** *139* (34), 11752-11759.

15. Qu, A. H.; Wu, X. L.; Xu, L. G.; Liu, L. Q.; Ma, W.; Kuang, H.; Xu, C. L., SERS- and luminescence-active Au-Au-UCNP trimers for attomolar detection of two cancer biomarkers. *Nanoscale* **2017,** *9* (11), 3865-3872.

16. Wu, X. L.; Fu, P.; Ma, W.; Xu, L. G.; Kuang, H.; Xu, C. L., SERS-active silver nanoparticle trimers for sub-attomolar detection of alpha fetoprotein. *Rsc Advances* **2015,** *5* (90), 73395-73398.

17. Li, S.; Xu, L. G.; Sun, M. Z.; Wu, X. L.; Liu, L. Q.; Kuang, H.; Xu, C. L., Hybrid Nanoparticle Pyramids for Intracellular Dual MicroRNAs Biosensing and Bioimaging. *Advanced Materials* **2017,** *29* (19).

18. Xu, L. G.; Yan, W. J.; Ma, W.; Kuang, H.; Wu, X. L.; Liu, L. Q.; Zhao, Y.; Wang, L. B.; Xu, C. L., SERS Encoded Silver Pyramids for Attomolar Detection of Multiplexed Disease Biomarkers. *Advanced Materials* **2015,** *27* (10), 1706-+.

19. Ang, Y. S.; Yung, L.-Y. L., Rapid and Label-Free Single-Nucleotide

Discrimination via an Integrative Nanoparticle–Nanopore Approach. *ACS nano* **2012,** *6* (10), 8815-8823.

20. Ying, L. M.; White, S. S.; Bruckbauer, A.; Meadows, L.; Korchev, Y. E.; Klenerman, D., Frequency and voltage dependence of the dielectrophoretic trapping of short lengths of DNA and dCTP in a nanopipette. *Biophysical journal* **2004,** *86* (2), 1018-1027.

21. Karhanek, M.; Kemp, J. T.; Pourmand, N.; Davis, R. W.; Webb, C. D., Single DNA molecule detection using nanopipettes and nanoparticles. *Nano letters* **2005,** *5* (2), 403-407.

22. Cai, Q.; Ledden, B.; Krueger, E.; Golovchenko, J. A.; Li, J. L., Nanopore sculpting with noble gas ions. *Journal of Applied Physics* **2006,** *100* (2).

23. Venta, K.; Shemer, G.; Puster, M.; Rodriguez-Manzo, J. A.; Balan, A.; Rosenstein, J. K.; Shepard, K.; Drndic, M., Differentiation of Short, Single-Stranded DNA Homopolymers in Solid-State Nanopores. *ACS nano* **2013,** *7* (5), 4629-4636.

24. Suk, M. E.; Aluru, N. R., Ion transport in sub-5-nm graphene nanopores. *Journal of Chemical Physics* **2014,** *140* (8).

25. Lee, S.; Zhang, Y. H.; White, H. S.; Harrell, C. C.; Martin, C. R., Electrophoretic capture and detection of nanoparticles at the opening of a membrane pore using scanning electrochemical microscopy. *Analytical Chemistry* **2004,** *76* (20), 6108-6115.

26. Wang, Y. X.; Kececi, K.; Mirkin, M. V.; Mani, V.; Sardesai, N.; Rusling, J. F., Resistive-pulse measurements with nanopipettes: detection of Au nanoparticles and nanoparticle-bound anti-peanut IgY. *Chemical Science* **2013,** *4* (2), 655-663.

27. Heins, E. A.; Siwy, Z. S.; Baker, L. A.; Martin, C. R., Detecting single porphyrin molecules in a conically shaped synthetic nanopore. *Nano letters* **2005,** *5* (9), 1824-1829.

28. Nam, J. M.; Oh, J. W.; Lee, H.; Suh, Y. D., Plasmonic Nanogap-Enhanced Raman Scattering with Nanoparticles. *Accounts of Chemical Research* **2016,** *49* (12), 2746-2755.

29. Cecchini, M. P.; Wiener, A.; Turek, V. A.; Chon, H.; Lee, S.; Ivanov, A. P.; McComb, D. W.; Choo, J.; Albrecht, T.; Maier, S. A.; Edel, J. B., Rapid Ultrasensitive Single Particle Surface-Enhanced Raman Spectroscopy Using Metallic Nanopores. *Nano letters* **2013,** *13* (10), 4602-4609.

CHAPTER 6

Two strategies based on AuNP-based nanostructures for single biomolecule detection using nanopores

Synopsis

Based on the high-resolution detection of molecule sub-structures demonstrated in the previous chapter; this chapter reports two strategies to detect a wide range of biomolecules at the single-molecule level. The first strategy is implemented by a protein carrier, which can selectively identify relatively large proteins by high specificity and affinity between those proteins and aptamers. The other strategy, aiming to sense small analytes, is achieved by a pair of antigen probes. Both strategies are fully flexible by selecting a different aptamer sequence or antibody to target a specific analyte.

Part of this chapter is in preparation as **Ren, R**.; Sun, M. Z.; Xu, C. L.; Ivanov, A. P.; Edel, J. B., A single molecule nanopore binding assay using nanoparticle conjugates. In this work the AuNP based structures were prepared by Prof. Maozhong Sun.

6.1 Introduction

Early-stage and rapid diagnosis is an essential step in improving the effectiveness of therapeutic intervention. To this end, there has been a considerable drive to developing ultra-sensitive biomarker detection strategies with single-molecule sensitivity. Such tools hold the promise of screening for very low abundance targets within complex media such as serum, urine and cerebral spinal fluid. One strategy that has been gaining attention is nanopore sensing. Although DNA sequencing and DNA detection has been the primary driving force[1, 2, 3, 4, 5], more recently, there has been progress in using such platforms for the detection and sensing of protein[6, 7, 8], nanoparticles[9, 10, 11, 12, 13] and other molecules[14, 15, 16]. The popularity of the nanopore method is in large part due to the simplicity of the approach. For example, molecules are translocated one at a time, through a nanoscale-sized pore using an applied electric field across an insulating membrane. Translocations of individual analytes are detected by observing changes in the transients of the ionic current; the magnitude and dwell time of these transients and their frequency provide information on the size of the analytes and their concentration.

However, the selective detection of protein analytes is often challenging, especially for small molecules. For example, unlike DNA, proteins have a heterogeneous charge and often translocate faster than can be detected and with a low signal-to-noise ratio. Most importantly, if nanopore sensing is to be used as a realistic tool for screening, methods are needed to be able to distinguish molecules with a very similar size but different biological function. To date, many efforts have been made to remedy these issues which include, functionalization of the nanopore lumen with binding moities[17, 18, 19], incorporation of field-effect-transistors[20, 21, 22], or use of high bandwidth instruments[23, 24]. Perhaps one of the most promising strategies is based around the use of molecular carriers such as nanoparticles or DNA. These carriers can be designed to bind a target biomarker selectively (usually using a grafted aptamer or an antibody), and subsequently translocate through the nanopore for detection. The biomarker no longer becomes difficult to detect as the carrier is often designed to have a distinct shape and charge, which slows down translocation and improves the signal-to-noise ratio. When a biomarker bound to the molecular carrier passes through the nanopore, a multilevel current signal is often observed with a first-level originating from the carrier occupying the nanopore, and a secondary level in the ionic current, caused by the bound biomarker. A number of research groups have already utilised the DNA based molecular carrier to detect specific biomolecules with high sensitivity.[25, 26, 27, 28, 29] However, it is often difficult to distinguish the target analyte between the secondary

signal that arises due to a partially folded DNA carrier, or DNA knots, from that of the target analyte. Also, when the size of the target is small or comparable to the size of the recognition element (for example when grafted antibodies are used) the secondary level can be masked by background noise. To address these limitations, we have designed two classes of molecular carriers based around the use of gold nanoparticle (AuNP) dimers.

The first strategy involves designing a dumbbell-shaped AuNP dimer linked by a DNA bridge incorporating an aptamer sequence, **Figure 6.1a**. This is in part inspired by the literature which has shown it is possible to design dumbbell-shaped nanoparticles linked by either dsDNA[30] or an antigen-antibody bridge[31]. Aptamers are ssDNA or RNA oligonucleotides that are capable of binding target molecules with high specificity and affinity, where the sequence can be selected via systematic evolution of ligands by exponential enrichment (SELEX). We show that we can differentiate between the translocation signals from the dimer with and without the presence of bound protein. Using this strategy, thrombins, as multifunctional proteases, were detected by thrombin aptamers engineered AuNP dimer protein carriers. The second strategy relies on the dimerisation of two monomeric NPs decorated with primary and secondary antibodies in the presence of antigen, **Figure 6.1b**. Using this strategy, the sensing of procalcitonin (PCT), an important biomarker for infection and sepsis, were achieved. A unique advantage of this strategy is that it becomes possible to sense very small molecules via differentiating between the signals arising from monomers and dimers, respectively. Both strategies are fully flexible by simply changing the aptamer sequence or antibody for different targets. Moreover, we show that these strategies can not only detect a variety of biomarkers at the single-molecule level with high sensitivity and selectivity but also can quantify concentrations via screening assays.

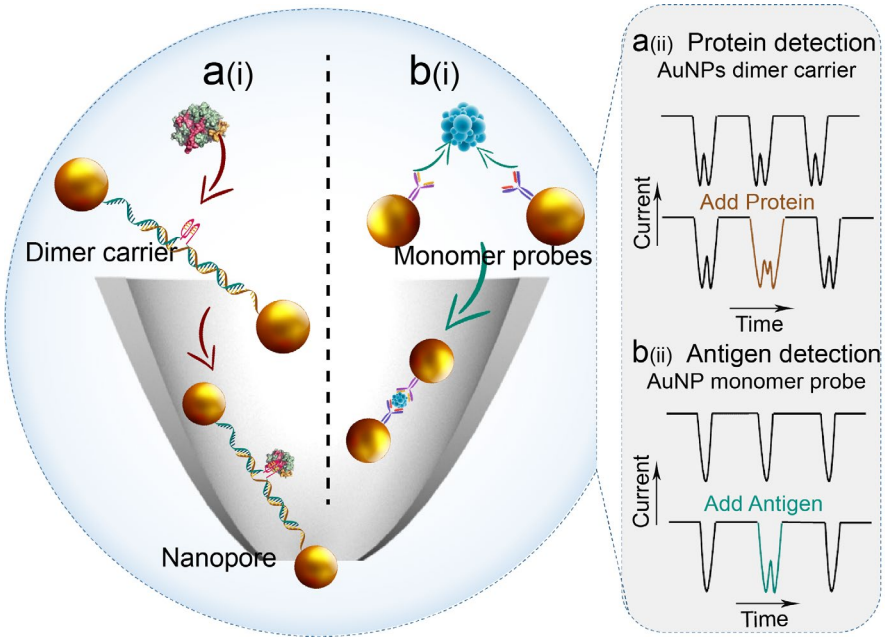


Figure 6. 1 Schematic of AuNP dimer protein carrier and AuNP antigen probes. **(a)** The dimer carrier is based on a dumbbell system where two Au nanoparticles (17–20 nm) are linked by a ~115-mer DNA bridge, which is engineered to contain an aptamer sequence that binds to target protein molecules. **(b)** For the second strategy, two monomer AuNP probes are modified with different antibodies. These form a dimer in the presence of the target antigen. In both strategies, the bound dimers are transported by the applied electric field from inside the nanopipette to outside. Bound analytes are identified at the single-molecule level by changes in the shape of individual events. Counting statistics of these individual signatures can reveal significant information on the fraction of bound vs unbound analytes, and the analyte concentration.

6.2 Methods

6.2.1 The fabrication of TBA-modified AuNP dimers

The 17 nm AuNPs were concentrated tenfold and resuspended in a 0.5×TBE buffer to a final concentration of 10 nM. The prepared AuNPs were then modified with the ssDNA5 (10 μM, dissolved in a TE buffer) in a DNA-to-AuNP molar ratio of 5:1. A NaCl solution (5 M) was added to the mixture to a final NaCl concentration of 50 mM, and it was left at 25 °C for 12 h. Finally, the mixture was centrifuged (three times) at 7,000 rpm for 10 mins to remove the excess DNA, and it was resuspended in the TBE buffer. The process of AuNPs (17 nm) modified with the ssDNA6 was the same as that for DNA5. 100 μL of AuNP–DNA5 and 100 μL of AuNP–DNA6 were mixed in a TBE buffer containing 50 mM of NaCl. The mixture was hybridised for 12 h at room temperature with gentle stirring. The mixture was then centrifuged at 5,000 rpm for 10 mins to remove the single nanoparticles and to collect the AuNP dimer thrombin carrier (**Figure 6.2**).



Figure 6. 2 Details of the AuNP dimer thrombin carrier. The AuNP dimer thrombin carrier is self-assembled by an AuNP with a 115-mer ssDNA containing a 15-mer TBA sequence and an AuNP with the complementary part to the sequence aside from the aptamer part. After self-assembling, the protein carrier can be used to sense the thrombin selectively in complex solutions. It is noteworthy that there are eight random bases close to the aptamer sequence to minimise the steric hindrance. The binding affinity between two DNA are strong enough so there's no need of ligation.

6.2.2 The fabrication of the monomer PCT probes

First, 2 mL AuNPs (20 ± 3 nm) were centrifuged for 10 mins at 8,000 rpm and then resuspended in 200 µL of a 10-mM phosphate buffer (PB) solution, which was adjusted to pH 9 with 0.1 M of K_2CO_3. Next, 100 µL of the AuNPs were conjugated with anti-PCT mAb (10 µL, 100 µg/mL), and the other 100 µL of AuNPs were modified with anti-PCT smAb (10 µL, 100 µg/mL). Then, the solutions were blocked by BSA (10 µL, 500 µg/mL) for 30 mins after incubation of 1h. After that, the functionalised AuNP solutions were centrifuged for 10 mins at 7,500 rpm, so that the final product could be collected as the monomer PCT probes.

6.2.3 UV-Vis measurement

Ultraviolet-visible spectroscopy (UV-Vis) was used to examine the stability of the metallic structures under different salt concentrations. The UV-Vis was recorded by Nanodrop 2000c (Thermo Scientific), scanning from 200 nm to 800 nm.

6.2.4 Nanostructure translocation experiments

The experiments were performed with translocation direction from inside of the nanopipettes (the nanopipettes for translocation measurements were pulled according to Protocol 2 detailed in **Chapter 2**) to the outside. The AuNP-based nanostructures were loaded in the nanopipette (cis chamber, where an Ag/AgCl working/patch electrode was placed), and an Ag/AgCl counter/reference electrode was placed in the blank buffer located in the bath (trans chamber). The buffer used in the translocation experiments consisted of 50 mM of KCl and 10 mM of Tris-EDTA (pH = 8) unless reported otherwise. For the binding assay of thrombin or PCT using corresponding strategies, 1 nM of thrombin carriers or PCT probes were incubated with target analytes at different concentrations for at least 2 hrs. The buffer containing target analytes was

filled inside the nanopipette along with the electrode. Then, a voltage was applied by a high-bandwidth amplifier VC100 (Chimera Instruments, US) between the electrodes on both sides of the nanopore, and the current-time trace could be recorded. The data were then resampled to 1 μs and digitally filtered to 100 kHz, and it was analysed by a customised Matlab app (details are described in **Chapter 2**).

6.3 Result and discussion

Two strategies for sensing molecules of different sizes at the single-molecule level were used. The first strategy is a dimer system that can deliver and sense relatively larger proteins. The other strategy is based on a dimer formation by the target analyte binding two different monomer probes that allows detecting small antigens indirectly.

6.3.1 Sensing protein using AuNP dimer protein carriers

The first strategy for biosensing is to utilise the dimer molecule as a carrier to drive and detect specific protein molecules. This dimer carrier is based on an AuNP symmetrical dumbbell system with a DNA bridge. The DNA was engineered to contain part of an ssDNA overhang with an aptamer sequence.

We use a model system of thrombin analyte and thrombin binding analyte, which is well established in the literature[32, 33]. Human alpha thrombin (α-thrombin) (M.W. 37.5 kDa; pI of 7.0–7.4), is a multifunctional protease in the bloodstream and has a significant role in physiological and pathological processes, such as blood coagulation, thrombosis, and angiogenesis. It is essential to detect thrombin at trace amounts with high sensitivity; however, using plain nanopipettes to sense this biomarker with such a small size and heterogeneous charge is difficult to achieve. **Figure 6.3** shows that no signal when the thrombin itself translocate through the nanopore. Therefore, an AuNP dimer thrombin carrier was designed to for thrombin detection at the single-molecule level.



Figure 6. 3 The sensing of 1 nM thrombin natively. The current-time trace of thrombin (1 nM) nanopore sensing (scale bar: vertical 50 pA, horizontal 5 s) at a bias of -600 mV. The translocation experiments were performed in 50 mM of KCl, 10 mM of Tris-EDTA, and at a potential of -600 mV. The current-

time trace was recorded at a 1-µs sampling rate and filtered using a low-pass Bessel filter with a cut-off frequency of 100 kHz. No events were observed under these circumstances because of a fast transient and a low capture rate.

The thrombin-binding aptamer (TBA), which binds to thrombin selectively and compactly ($K_d \sim 35–100$ nM in solid-phase assays[34]), is a 15-mer (5'-GGTTGGTGTGGTTGG-3') ssDNA folding into a stable intramolecular G-quadruplex in the presence of K^+.[32, 33] As the binding site of thrombin, the TBA sequence was anchored on a protuberance of the 115-mer DNA bridges of the dimer. All details regarding the fabrication and sequence of the DNA bridge are described in the method part. Before nanopore measurements, the efficiency of the binding between thrombin and the corresponding carriers was confirmed by UV-vis (**Figure 6.4**). By adding 4 nM of thrombin to 1 nM of AuNP dimer thrombin carrier dispersions with 50 mM of KCl and 10 mM of Tris-EDTA at pH 8, the AuNP-based molecules started oligomerisation as a result of the weakening of the holistic charge of the molecule (this is a result of specific binding). As a control, the pristine AuNP dimer molecules (two AuNPs linked by a dsDNA bridge without any binding site) of the same ionic strength would not aggregate until the concentration of thrombin reached 100 nM, which masked the surface of the dimer molecules (this is a result of unspecific binding).

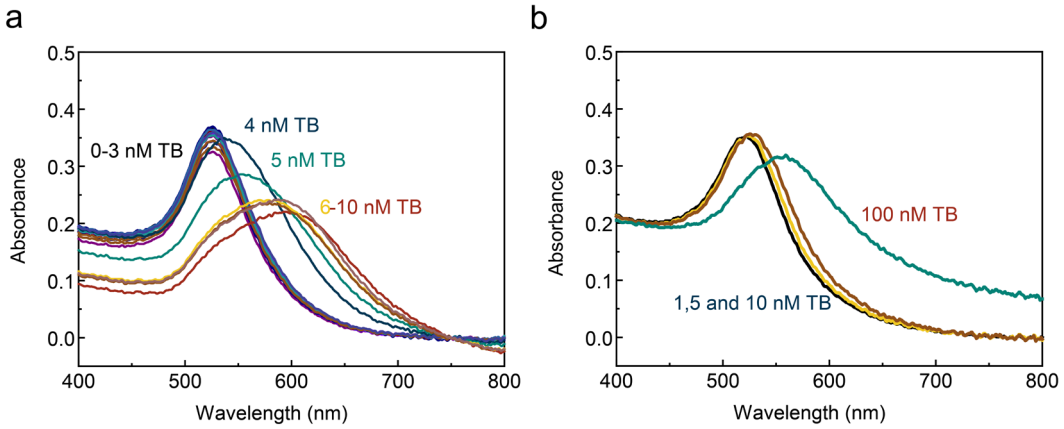


Figure 6. 4 The UV-vis spectrum of thrombin/dimer complexes. **(a)** By adding 4 nM of thrombin to 1 nM of AuNP dimer thrombin carrier dispersions with 50 mM of KCl and 10 mM of Tris-EDTA at pH 8, the AuNP-based molecules started oligomerisation as a result of the weakening of the whole charge of the molecule. **(b)** The pristine AuNP dimer molecules of the same ionic strength would not aggregate until the concentration of thrombin reached 100 nM, which masked the surface of the dimer molecules.

The working principle of using the AuNP thrombin carrier to detect thrombin is illustrated in **Figure 6.5**. The targets, as well as the working electrode (AgCl), were filled inside the nanopipette, and a counter/reference electrode (AgCl) was placed outside of the pipette. With applied negative potential, the AuNP carrier or the carrier/protein complex was pushed from inside (cis) to outside (trans) of the nanopipette. With the translocation of these molecules, a current enhancement could be

observed when the electrolyte is 50 mM of KCl at pH 8. A high-bandwidth amplifier was used to record the data at a 1-μs sampling rate and with a 100-kHz low-pass filter.

As a control, the translocation of the AuNP dimer carrier without binding thrombin was recorded, as **Figure 6.5b** depicts. Evident translocation and double-peak events were observed. Comparing the translocation events of TBA-modified AuNP dimers (**Figure 6.5b**) and plain AuNP dimer (**Chapter 5, Figure 5.10b**) of the same particle size and with the same linker length, the difference in dwell time (24.77 vs 23.01 ms), peak current (113.05/121.10 vs 118.99/123.55 pA), and fraction position (0.26/0.80 vs 0.23/0.80) are negligible. The reason the aptamer overhang did not generate a measurable change in the ionic current is that the charge and size of the 23-base ssDNA overhang (a 15-base aptamer and an eight-random-base linker) are too small to generate an observable signal.

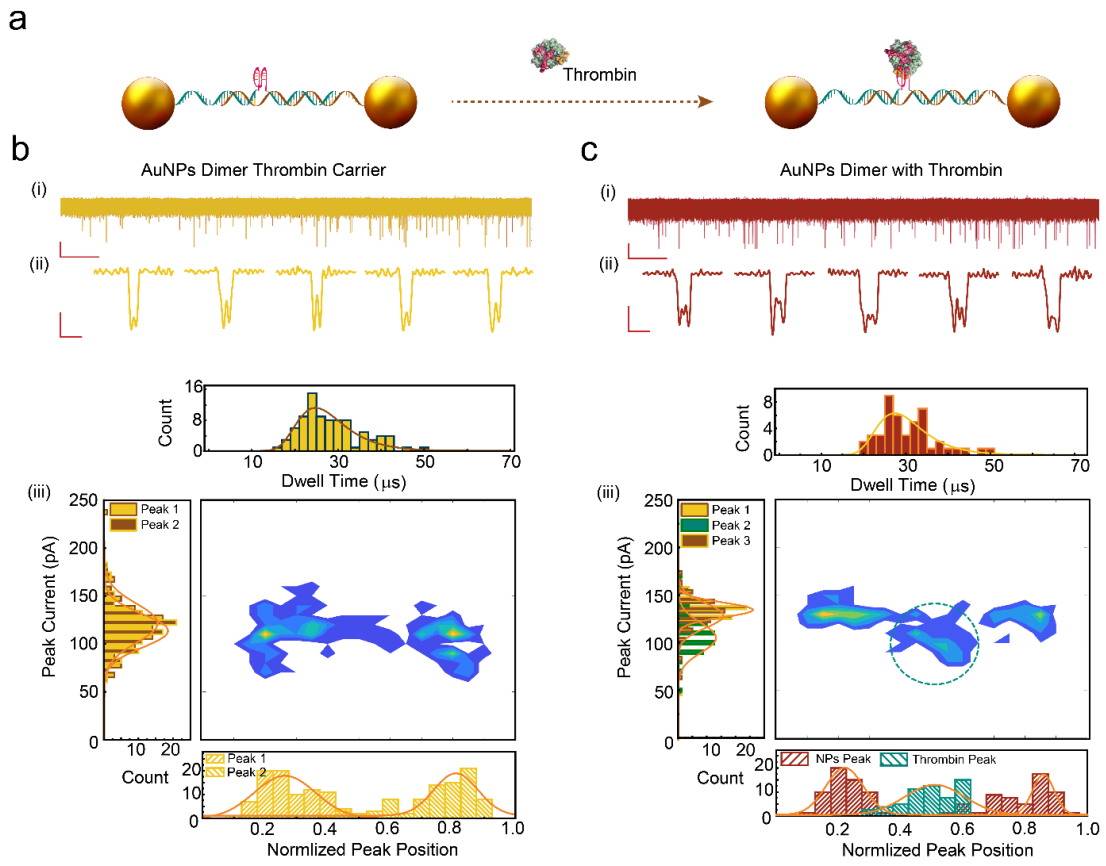


Figure 6. 5 Nanopore sensing of thrombin with AuNP dimer thrombin carriers. **(a)** Schematic of the dimer carriers, which were engineered to contain aptamer sequences, delivering and sensing the target protein. **(b—c)** The representative current-time trace (scale bar: vertical 50 pA, horizontal 5 s), individual translocation events (scale bar: vertical 50 pA, horizontal 20 μs), and statistics (translocation dwell time, and the scatter plot, along with peak current and normalised peak position histograms) for AuNP dimer thrombin carriers and AuNP dimers with thrombin complex. The translocation experiments were performed in 50 mM of KCl, 10 mM of Tris-EDTA, and at a potential of -600 mV. Each trace is recorded at a 1-us sampling rate and filtered using a low-pass Bessel filter with a cut-off frequency of 100 kHz.

With the addition of 1 nM of thrombin into 1 nM of the TBA-modified AuNP dimers, some triple-peak events were observed when these complexes are driven by a potential of -600 mV (**Figure 6.5c**). Unlike the triple peaks of the AuNP trimers (**Chapter 5, Figure 5.10d**), the triple-peak events of the protein-bound dimers revealed a distinct signature: the second peak (located at 0.51 of the normalised peak position) was always smaller than the first and third peaks (located at 0.22 and 0.86 of the normalised peak position, respectively). As discussed in the previous chapter, the peaks are generated when the nanopore conductance is changed by the different part of the nanostructures. In the pH 8 environment, the thrombin and TBA part are negatively charged, which is ascribable to the deprotonation of the amino acid, although it is not comparable with the charge of the AuNPs. Therefore, the small enhancement peak, with an 80% magnitude of the AuNPs peaks, occurred in the middle of the events, corresponding to the thrombin-anchored DNA bridges. However, as demonstrated by the UV-Vis, the total charge of the molecular carrier was reduced after the addition of thrombin, thereby leading to a 1.1-fold increase in the translocation dwell time.

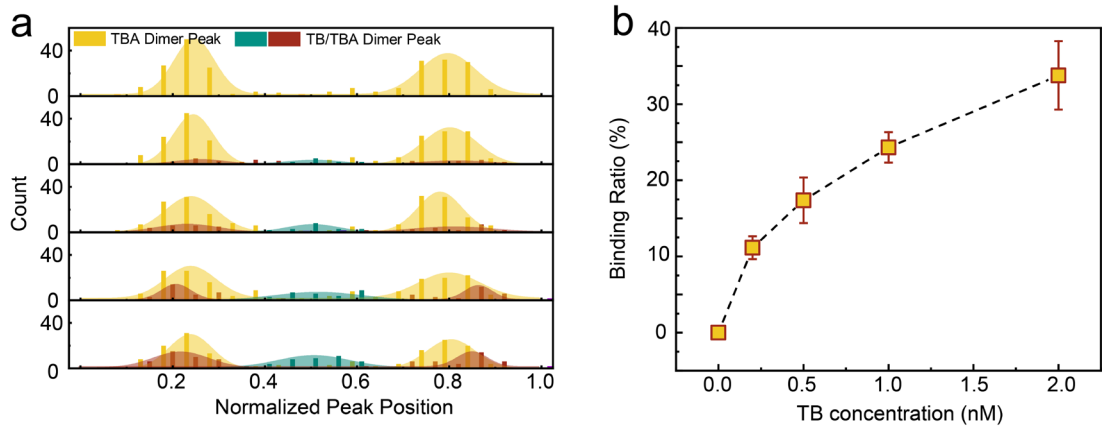


Figure 6. 6 The binding assay for thrombin using AuNP dimer thrombin carriers through nanopipettes. **(a)** The normalised peak position of the dimer carriers or the carrier and target protein complexes, under different concentrations of thrombin (from top to bottom, 0 nM, 0.2 nM, 0.5 nM, 1 nM, and 2 nM). **(b)** Binding assay for a 1 nM dimer carrier concentration incubated with increasing thrombin concentrations ranging from 0 to 2 nM. Error bars represent the standard deviation of three independent experimental repeats with different nanopipettes.

By counting the percentage of triple-peak events of all triple- and double-peak events, the binding ratio can be calculated (**Figure 6.6**). As expected, the proportion of the triple-peak signature increased with the addition of thrombin. In this experiment, we varied the concentration of thrombin from 0 to 2 nM, while the concentration of the dimer remained at 1 nM. From the statistics of the normalised peak position (**Figure 6.6b**), it is evident that no triple-peak events occurred without the addition of thrombin, and the middle peak then appeared stepwise with the increasing of the thrombin concentration. By counting the percentage of triple peaks in the total number of double-

and triple-peak events, the subtle change in the concentration of thrombin can be monitored. With an approximate 50-pM change in the thrombin concentration, the triple- or double-peak ratio will change by 1%. Furthermore, to validate the selectivity of the AuNP dimer thrombin carrier, 1 nM lysozyme was incubated with a 1 nM thrombin carrier, and subsequent nanopore detection of the mixture was performed (**Figure 6.7**). There was no indication of a triple-peak; however, the double-peak events were visible, corresponding to unbounded dimer carriers.

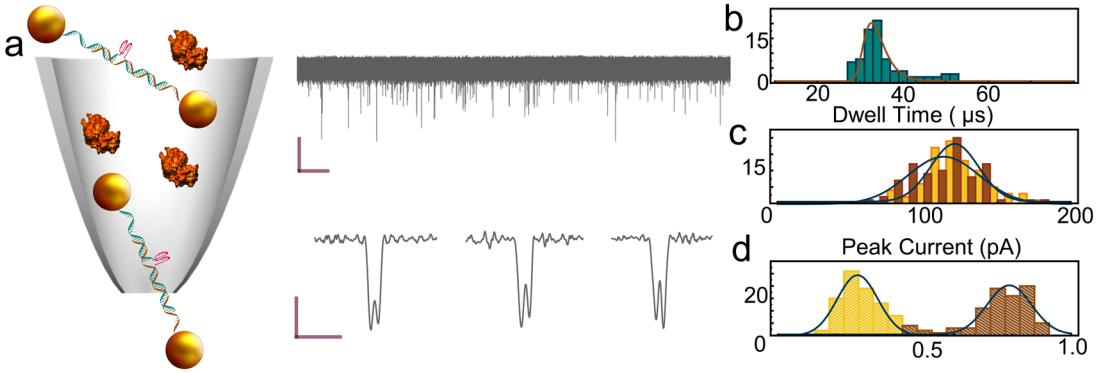


Figure 6. 7 The control experiment of AuNP dimer thrombin carrier. **(a)** The current-time trace (scale bar: vertical 50 pA, horizontal 5 s), individual events (scale bar: vertical 50 pA, horizontal 20 μs), and **(b–d)** statistics for 1 nM of AuNP dimer thrombin carrier incubated with 1 nM of lysozyme. All the translocation experiments were performed in 50 mM of KCl and 10 mM of Tris-EDTA. The current-time trace was recorded at a 1-μs sampling rate and filtered using a digital low-pass Bessel filter with a cut-off frequency of 100 kHz. There are no triple-peak events; however, double-peak events are present, corresponding to unbound thrombin carriers.

6.3.2 Sensing small antigens using AuNP monomer antigen probes

The AuNP dimer protein carriers demonstrated the ability to sense a corresponding protein with high sensitivity and selectivity. However, the aptamer-modified carriers, including most carriers reported previously, cannot sense smaller targets (< 15kDa). Moreover, with the decreasing of the biomolecule size, the signatures become progressively more challenging to detect because of the lowering of the signal-to-noise ratio.

Herein, based on our previous work, a universal strategy of sensing small antigen molecules was performed. In detail, half of the AuNPs are modified by the corresponding antibody (mAb) of the target antigen, while the rest are modified with a complementary secondary antibody (smAb). With the presence of the antigen, the monomers will self-assemble to dimers with a ‘sandwich’ formation, and this changing can be recorded when the molecules pass through the nanopore.



Figure 6. 8 The sensing of 1 nM PCT natively. The current-time trace of PCT (100 nM) nanopore sensing (scale bar: vertical 50 pA, horizontal 5 s). The translocation experiments were performed in 50 mM of KCl, 10 mM of Tris-EDTA, and at a potential of -600 mV. The current-time trace was recorded at a 1-us sampling rate and filtered using a low-pass Bessel filter with a cut-off frequency of 100 kHz. Even with this high concentration of PCT, there is no translocation signal, because of the poor signal-to-noise ratio. The PCT molecules are too small to be detected natively.

In this case, our target biomarker molecule is procalcitonin (PCT, M.W. 12.8 kDa; pI of 6.5), which is a peptide precursor of the hormone calcitonin. Given the PCT level variance between healthy and microbial infected individuals, it has become an important biomarker to improve bacterial infection identification and guide antibiotic therapy. However, this crucial biomarker cannot be efficiently detected by conventional solid-state nanopores because of the fast translocation and negligible signal-to-noise ratio (**Figure 6.8**).

Herein, a pair of AuNP monomer PCT probes were fabricated to sense PCT at the single-molecule level (**Figure 6.9a**). To ensure that the intramolecular nanostructure can be distinguished by the nanopore in this case, we increased the AuNP size to 20 nm. Therefore, with an antibody-antigen-antibody sandwich linker of approximately 10 nm, the nanostructure of the dumbbell molecule (the distance from the centre of one AuNP to the other is around 30 nm) can be distinguished by nanopores with an effective length of sub-30 nm.

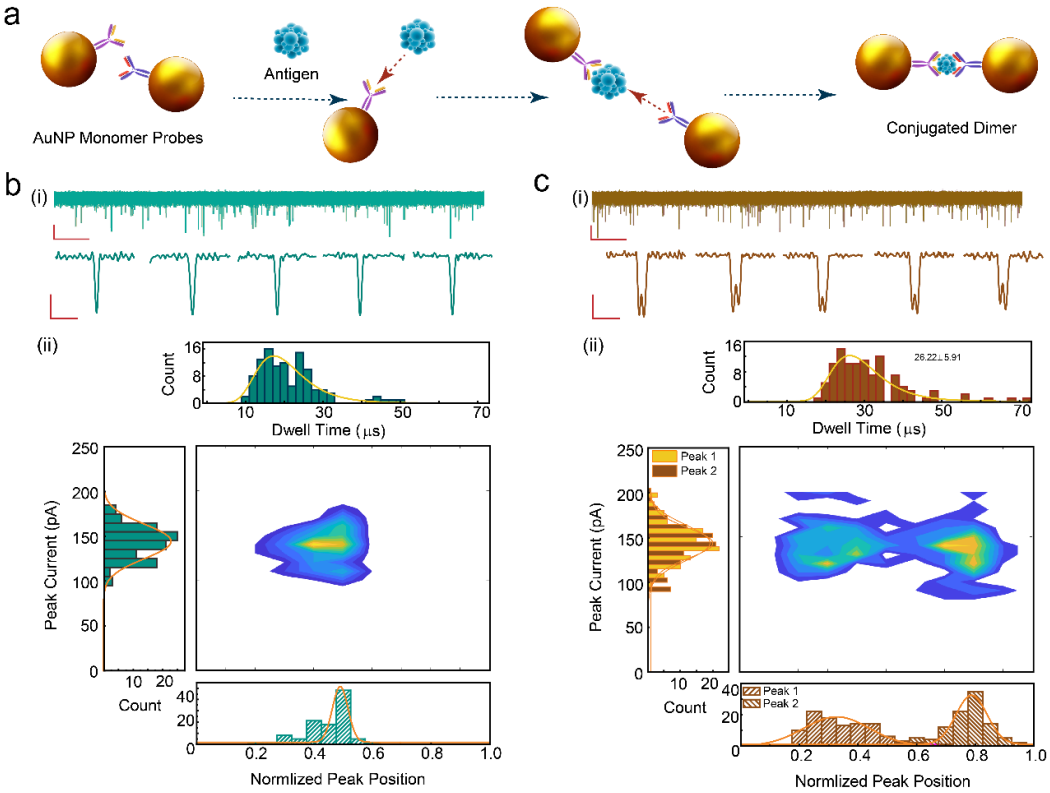


Figure 6. 9 Nanopore sensing of PCT via a pair of AuNP monomer probes. **(a)** Schematic of two AuNP monomer probes with different antibodies self-assembling to a dimer in the presence of an antigen (PCT). **(b–c)** The representative current-time trace (scale bar: vertical 50 pA, horizontal 5 s), individual translocation events (scale bar: vertical 50 pA, horizontal 20 μs), and statistics (the translocation dwell time, and the scatter plot, along with peak current and normalised peak position histograms) of conjugated dimers, which are linked by antibody-antigen-antibody sandwich bridges. All the translocation experiments were performed in 50 mM of KCl, 10 mM of Tris-EDTA, and at a potential of -600 mV. The data was recorded at a 1-μs sampling rate and filtered using a low-pass Bessel filter with a cut-off frequency of 100 kHz.

A comparison between the translocation of 1 nM of AuNP monomers (50% are functionalised by PCT mAb, and the remaining 50% are functionalised by smAb) and the assembled dumbbell complex after adding 20 nM of PCT, is presented in **Figure 6.9b–c**. Without the presence of PCT, there was no double-peak signal, but the single-peak signal was observed during the translocation of 1 nM of AuNP monomers with 50 mM of KCl, pH 8. With the addition of 20 nM of PCT, approximately 15% of the single peaks transformed to clear double-peak events. Each peak is the result of the translocation of AuNP, whereas the trough is because of the translocation of the weak and uniform charged sandwich linker (PI of mAb, smAb is 6.6-7.2). As a negative control, no double-peak signatures were observed when PCT was replaced by other antigens; for example, insulin (**Figure 6.10**).

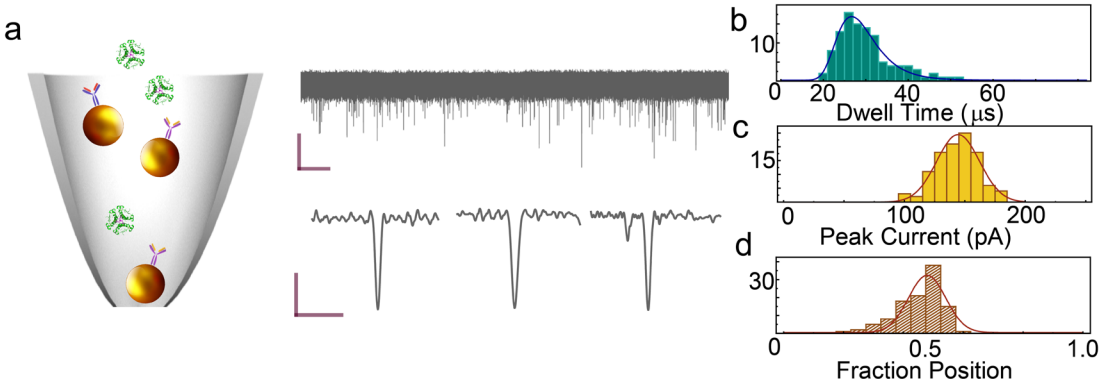


Figure 6. 10 The control experiment of AuNP monomer PCT probes. The current-time trace (scale bar: vertical 50 pA, horizontal 5 s), individual events (scale bar: vertical 50 pA, horizontal 20 μs), and statistics for 1 nM of AuNP monomer PCT probes incubated with 1 nM of insulin. All the translocation experiments were performed in 50 mM of KCl and 10 mM of Tris-EDTA. The current-time trace was recorded at a 1-μs sampling rate and filtered using a low-pass Bessel filter with a cut-off frequency of 100 kHz. While there are no double-peak events, single-peak events occurred, corresponding to free PCT probes.

To validate this mode, similar to sandwich immunoassay, can be used in the clinical diagnosis level, nanopore sensing studies of AuNP monomer probes with different concentrations of PCT were performed. In this case, the concentration of the probes was kept at 1 nM, while the concentration of PCT ranged from 0 to 200 nM. As expected, the percentage of the single peak (located at 0.49 of the normalised peak position) decreased, whereas the proportion of double-peak signatures (located at 0.30 and 0.78 of the normalised peak position) raised with the increasing concentration of PCT (**Figure 6.11**).

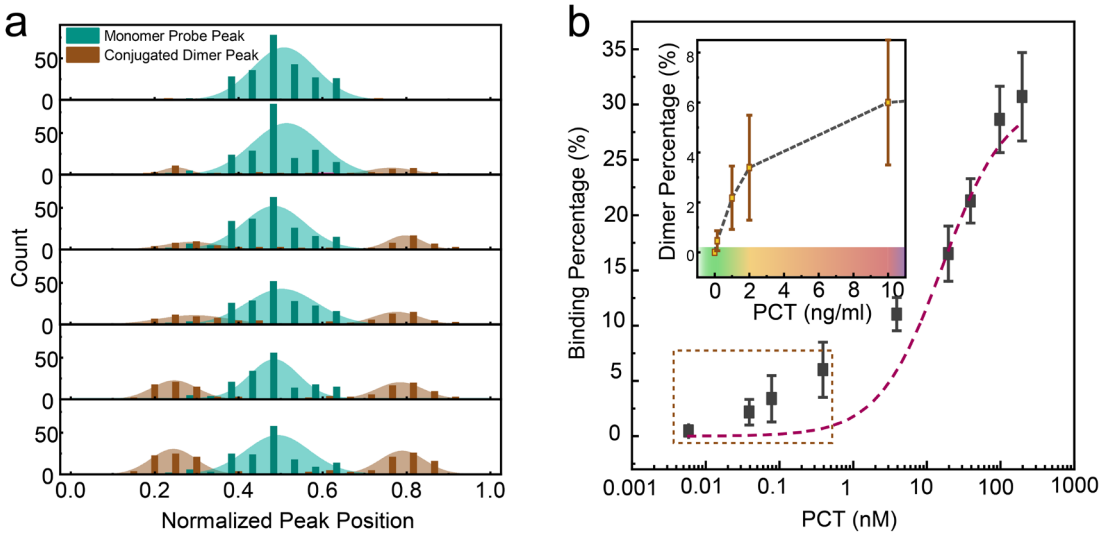


Figure 6. 11 The binding assay for thrombin by using AuNP monomer probes through nanopipettes. **(a)** The normalised peak position of the monomer probe and conjugated dimer with different concentrations of PCT (from top to bottom: 0 nM, 80 pM, 20 nM, 40 nM, 100 nM, and 200 nM). **(b)** The binding curve of 1 nM of AuNP monomer PCT probes incubating with PCT ranging from 0 to 400 nM. The inset is the

sensing of PCT in a clinical diagnostic range. The error bars of the binding ratio analysis represent the standard deviation of three independent experimental repeats.

In bacterial infections, sepsis, severe sepsis, and septic shock, PCT in plasma concentrations increase from 0.15 to more than 10 ng/ml. This increase often correlates with the severity of the disease and with mortality. At the same time, PCT has also been used to guide antibiotic therapy; for example, if the PCT level < 0.1 ng/ml, then antibiotic therapy is strongly discouraged, and if that level > 1 ng/ml, then such therapy is strongly encouraged. With high sensitivity, the PCT monomer probe is capable of sensing this important biomarker in this range (**Figure 6.11b** inset).

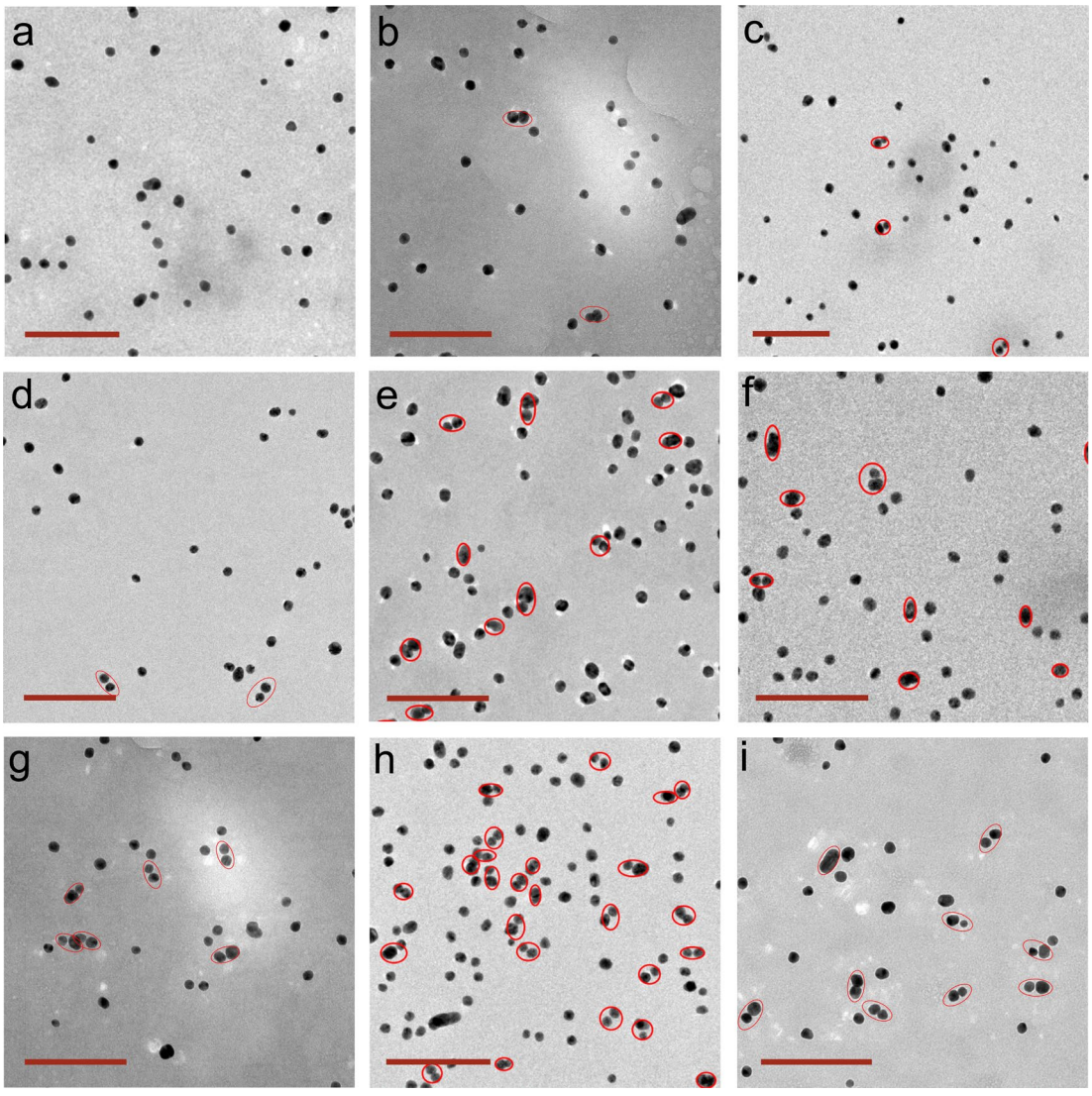


Figure 6. 12 The TEM of AuNP monomer probes incubating with different levels of PCT. The TEM images (scale bars: 200 nm) of AuNP monomer probes incubated with **(a)** no PCT or **(b)** 40 pM, **(c)** 80 pM, **(d)** 400 pM, **(e)** 4 nM, **(f)** 20 nM, **(g)** 40 nM, **(h)** 100 nM, and **(i)** 200 nM PCT.

The binding assays were further confirmed by TEM (**Figure 6.12**). **Figure 6.12a** demonstrates that the AuNP monomers are well-dispersed single particles when there is no PCT. **Figure 6.12b–i** provides visualised evidence that the proportion of the dimer increased with the further addition of PCT. **Figure 6.13** illustrates both the nanopore translocation and the TEM statistics of the binding ratio versus the PCT concentration, which are consistent, validating the accuracy of PCT single-molecule detection using fine-tuned nanopores incorporating AuNP monomer antigen carriers.

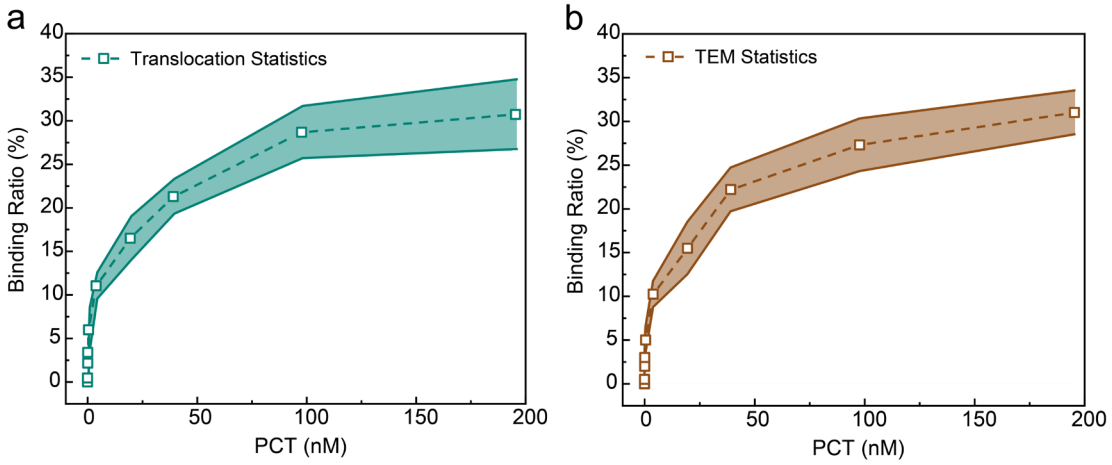


Figure 6. 13 The binding assay confirmed by translocation and TEM counting statistics. The binding assay of 1 nM of PCT monomer probes with PCT ranging from 0 to 200 nM. **(a)** The binding ratio calculated from the percentage of double-peak translocation signatures in all signals. Error bars represent the standard deviation of three independent experimental repeats with different nanopipettes. **(b)** The binding ratio achieved by counting the dimer out of all particles. Error bars represent the standard deviation of three independent experimental repeats.

6.4 Conclusion

In summary, based on the success of the high-resolution sensing sub-structures of single molecules using nanopores in **Chapter 5**, we built two strategies of sensing biomolecules at the single-molecule level. These strategies can bring nanopores sensing closer to applications such as early disease diagnosis for time-critical conditions such as sepsis.

Both strategies are fully flexible in detecting a number of biomolecules simply by changing the aptamer sequence or antibodies. The excellent selectivity and affinity of aptamer-proteins or antibody-antigens allow for the possibility to apply these strategies to diagnostics for detecting biomarkers in trace amounts. Importantly, for different biomolecules, a different strategy can be chosen. For example, to sense some large proteins, the aptamer-modified carrier can be used because of a signature in the ionic current associated with the bound target. Statistical analysis of this additional peak can

provide information about the size and charge of the target. Otherwise, if the analyte is too small to generate measurable change in the electric signal, then the second strategy, involving an indirect detection at the single-molecule level, can be applied. Importantly, both strategies are capable of validating the presence of the specific targets and have shown promise in quantifying the concentration of those targets at the clinical diagnosis level.

6.5 References

1. Miles BN, Ivanov AP, Wilson KA, Dogan F, Japrung D, Edel JB. Single molecule sensing with solid-state nanopores: novel materials, methods, and applications. *Chemical Society reviews* **42**, 15-28 (2013).

2. Meller A, Nivon L, Branton D. Voltage-Driven DNA Translocations through a Nanopore. *Physical review letters* **86**, 3435-3438 (2001).

3. Wanunu M. Nanopores: A journey towards DNA sequencing. *Physics of life reviews* **9**, 125-158 (2012).

4. Ying YL, Zhang JJ, Gao R, Long YT. Nanopore-Based Sequencing and Detection of Nucleic Acids. *Angewandte Chemie-International Edition* **52**, 13154-13161 (2013).

5. Wanunu M. Nanopores: A journey towards DNA sequencing. *Physics of life reviews* **9**, 125-158 (2012).

6. Plesa C, Kowalczyk SW, Zinsmeester R, Grosberg AY, Rabin Y, Dekker C. Fast Translocation of Proteins through Solid State Nanopores. *Nano letters* **13**, 658-663 (2013).

7. Li W*, et al.* Single Protein Molecule Detection by Glass Nanopores. *ACS nano* **7**, 4129-4134 (2013).

8. Steinbock LJ*, et al.* Probing the size of proteins with glass nanopores. *Nanoscale* **6**, 14380-14387 (2014).

9. Lan WJ, Holden DA, Zhang B, White HS. Nanoparticle Transport in Conical-Shaped Nanopores. *Analytical Chemistry* **83**, 3840-3847 (2011).

10. Tsutsui M, Hongo S, He Y, Taniguchi M, Gemma N, Kawai T. Single-Nanoparticle Detection Using a Low-Aspect-Ratio Pore. *ACS nano* **6**, 3499-3505 (2012).

11. Lan W-J, Holden DA, Liu J, White HS. Pressure-Driven Nanoparticle Transport across Glass Membranes Containing a Conical-Shaped Nanopore. *Journal of Physical Chemistry C* **115**, 18445-18452 (2011).

12. Davenport M*, et al.* The Role of Pore Geometry in Single Nanoparticle Detection. *ACS nano* **6**, 8366-8380 (2012).

13. Wang YX, Kececi K, Mirkin MV, Mani V, Sardesai N, Rusling JF. Resistive-

pulse measurements with nanopipettes: detection of Au nanoparticles and nanoparticle-bound anti-peanut IgY. *Chemical Science* **4**, 655-663 (2013).

14. Zahid OK, Wang F, Ruzicka JA, Taylor EW, Hall AR. Sequence-Specific Recognition of MicroRNAs and Other Short Nucleic Acids with Solid-State Nanopores. *Nano letters* **16**, 2033-2039 (2016).

15. Cai H*, et al.* Resistive-Pulse Measurements with Nanopipettes: Detection of Vascular Endothelial Growth Factor C (VEGF-C) Using Antibody-Decorated Nanoparticles. *Analytical Chemistry* **87**, 6403-6410 (2015).

16. Heins EA, Siwy ZS, Baker LA, Martin CR. Detecting single porphyrin molecules in a conically shaped synthetic nanopore. *Nano letters* **5**, 1824-1829 (2005).

17. Luan B, Stolovitzky G, Martyna G. Slowing and controlling the translocation of DNA in a solid-state nanopore. *Nanoscale* **4**, 1068-1077 (2012).

18. Keyser UF. Controlling molecular transport through nanopores. *Journal of the Royal Society Interface* **8**, 1369-1378 (2011).

19. Wei R, Gatterdam V, Wieneke R, Tampe R, Rant U. Stochastic sensing of proteins with receptor-modified solid-state nanopores. *Nature nanotechnology* **7**, 257-263 (2012).

20. Xue L*, et al.* Gated Single-Molecule Transport in Double-Barreled Nanopores. *ACS applied materials & interfaces* **10**, 38621-38629 (2018).

21. Ren R*, et al.* Nanopore extended field-effect transistor for selective single-molecule biosensing. *Nature Communications* **8**, (2017).

22. Ai Y, Liu J, Zhang BK, Qian S. Field Effect Regulation of DNA Trans location through a Nanopore. *Analytical Chemistry* **82**, 8217-8225 (2010).

23. Larkin J, Henley RY, Muthukumar M, Rosenstein JK, Wanunu M. High-Bandwidth Protein Analysis Using Solid-State Nanopores. *Biophysical journal* **106**, 696-704 (2014).

24. Rosenstein JK, Wanunu M, Merchant CA, Drndic M, Shepard KL. Integrated nanopore sensing platform with sub-microsecond temporal resolution. *Nature Methods* **9**, 487-U112 (2012).

25. Singer A, Wanunu M, Morrison W, Kuhn H, Frank-Kamenetskii M, Meller A. Nanopore Based Sequence Specific Detection of Duplex DNA for Genomic Profiling. *Nano letters* **10**, 738-742 (2010).

26. Bell NAW, Keyser UF. Digitally encoded DNA nanostructures for multiplexed, single-molecule protein sensing with nanopores. *Nature nanotechnology* **11**, 645-+ (2016).

27. Sze JYY, Ivanov AP, Cass AEG, Edel JB. Single molecule multiplexed nanopore protein screening in human serum using aptamer modified DNA carriers. *Nature Communications* **8**, (2017).

28. Beamish E, Tabard-Cossa V, Godin M. Identifying Structure in Short DNA Scaffolds Using Solid-State Nanopores. *Acs Sensors* **2**, 1814-1820 (2017).

29. Loh AYY*, et al.* Electric Single-Molecule Hybridization Detector for Short

DNA Fragments. *Analytical chemistry*, (2018).

30. Chen W*, et al.* Nanoparticle Superstructures Made by Polymerase Chain Reaction: Collective Interactions of Nanoparticles and a New Principle for Chiral Materials. *Nano letters* **9**, 2153-2159 (2009).

31. Wu XL*, et al.* Unexpected Chirality of Nanoparticle Dimers and Ultrasensitive Chiroplasmonic Bioanalysis. *Journal of the American Chemical Society* **135**, 18629-18636 (2013).

32. Bock LC, Griffin LC, Latham JA, Vermaas EH, Toole JJ. SELECTION OF SINGLE-STRANDED-DNA MOLECULES THAT BIND AND INHIBIT HUMAN THROMBIN. *Nature* **355**, 564-566 (1992).

33. Kelly JA, Feigon J, Yeates TO. Reconciliation of the X-ray and NMR structures of the thrombin-binding aptamer d(GGTTGGTGTGGTTGG). *Journal of Molecular Biology* **256**, 417-422 (1996).

34. Deng B*, et al.* Aptamer binding assays for proteins: The thrombin example-A review. *Analytica Chimica Acta* **837**, 1-15 (2014).

CHAPTER 7

Conclusion and future work

Synopsis

This chapter concludes the PhD work, with the key aims and conclusions being highlighted. Future work, including potential improvement to device design and detection strategy, will be described.

7.1 Aims and achievements

This thesis aimed to explore novel methods to address the existing limitations of nanopore analytics and thus increase the practicality of nanopore techniques towards future applications such as early-stage diagnosis of biomarkers such as PCT. These methods included the development of new tools and single-molecule biosensing strategies. The purpose of fabricating comprehensive novel tools with a simple and less-costly process was to address the limitations of the existing functionalised nanopore devices. Furthermore, the aim of designing new strategies incorporating molecular carriers and molecular probes can facilitate the detection of a wide range of biomarkers at trace levels. A summary of the key conclusions is as follows:

Chapter 2 outlined the primary materials, instruments, and methods used in this thesis. I illustrated the detailed fabrication and characterisation steps of both single- and double-barrel nanopipettes, as well as the set-up and data analysis of single-molecule translocation experiments.

Chapter 3 presented a novel device, namely the nexFET, combining the principle of solid-state nanopores and FETs. Unlike conventional functionalised nanopores, this device is easy to fabricate and less-costly compared to more typical approaches. The nexFET was designed using double-barrel nanopipettes, where one barrel was filled with a carbon nanoelectrode, and the other barrel was left empty. A ring-like PPy layer covered the carbon electrode and encompassed the open barrel which acted as a gate and a nanopore. The extent of PPy deposition was used to control the nanopore size. By recording the open pore current, the degree of PPy polymerisation was monitored in real-time, and the size of the generated nanopore channel was thus controlled precisely. Through this real-time deposition and feedback-controlled process, a large number of nanopipettes could be used with similar properties, even with different initial nanopipette starting dimensions. I also demonstrated that the generated device showed strong FET performance and high pH sensitivity.

In **Chapter 4**, I demonstrated high sensitivity, specificity and capability to detect analyte at the single-molecule level. I showed that it is possible to combine the benefits of nanopore and FET performance into a single platform. The nexFET improved the sensitivity and selectivity even further for single-molecule DNA and protein sensing. By controlling the gate voltage of the nexFET, the translocation signals of DNA through the PPy nanopore were comprehensively improved. For example, a higher capture rate, a longer dwell time, and a larger signal-to-noise ratio was achieved. As a

result of the positively charged PPy nanopore inner wall, the nexFET was also capable of detecting translocation events from ultra-short nucleic acids (e.g. 18-base ssDNA). Furthermore, selective sensing of an anti-insulin IgG antibody at picomolar concentrations was also achieved using an insulin-embedded nexFET, which can be fabricated through a facile and efficient process.

In **Chapter 5**, I demonstrated that it is possible to use a fine-tuned nanopore testing platform incorporating high-bandwidth instruments to depict the sub-structure of different objectives. In this case, a series of AuNP-based nanostructures, including an AuNP monomer, AuNP symmetrical dimers with different linkers, asymmetrical dimers, and AuNP trimers, were differentiated based on their translocation signal. When a molecule with a complicated structure passes through the nanopore, a rough shape can be expressed as the peak, and the trough of the translocation events can reflect the charge of each part of the molecule. Also, by utilising the plasmonic effect of the dimer, single-molecule SERS detection was also achieved using a custom-built Raman microscope.

Chapter 6 describes methods to address the limitations of the molecular carrier for use in single-molecule biosensing. For example, folded DNA can often generate false positives, and often, it is difficult to detect small targets. In this thesis, two strategies were reported to circumvent these challenges. The first strategy relies on protein binding to dumbbell-shaped AuNP's. The second strategy was developed based on antibody functionalised AuNP's forming dumbbells only when the target analyte is bound. Both strategies are fully flexible and can be adapted for different targets by changing the aptamer sequence or antibody. Moreover, not only can these strategies detect a variety of biomolecules at the single-molecule level with high sensitivity and selectivity, but they can also quantify the trace amounts at concentrations below 10 pM.

7.2 Future works

As with any other technique, nanopipette based nanopores have proven to hold great promise, although they have their limitations. In terms of future possibilities for further refinement, there are several avenues that can be explored ranging from the design of novel carriers to testing and validating experimental outcomes of this thesis using human serum and clinical samples.

In the previous chapters, different strategies have been shown that can improve the sensitivity and selectivity of the solid-state nanopore. Recently, multiple functionalized

nanopipette works have been reported such as Au functionalized nanopipette transistor[1], hydrogel functionalized glass nanopore[2], novel wireless nanopipette electrodes[3]. Inspired by these previous works, I designed a new approach, which expands the fabricated nanopore extended field-effect transistor, to sense small biomolecules.

Another valuable method to improve the sensitivity and selectivity for nanopore is via the molecular carrier. A number of delicate aptamers modified molecular carriers have been reported[4-6]. As I discussed in previous chapters, DNA is not a perfect molecular carrier as their folding sub-peak signal would cause false positive. To replace the soft biopolymer carriers, DNA origami nanorods have emerged as a rigid cylindrical carrier. Herein, a novel DNA origami nanorod carrier which can detect up to four proteins, have been designed.

7.2.1 Improvement of receptor-embedded nexFETs

7.2.1.1 Experiment outline

Although I successfully fabricated an insulin-embedded nexFET, many crucial proteins are smaller than the IgG antibody (150 kDa) and difficult to detect/discriminate using conventional nanopore methods. nexFET platform can be adapted for use with smaller proteins, such as thrombin (37 kDa). To achieve this, a thrombin aptamer (TBA) embedded nanopore was designed (**Figure 7.1**). Different from the insulin-embedded nexFET, the aptamer-embedded nexFET includes two layers to form the gating and sensing area: a normal PPy layer, which is attached on the carbon area, and an aptamer/PPy layer, which covered the sensing area.

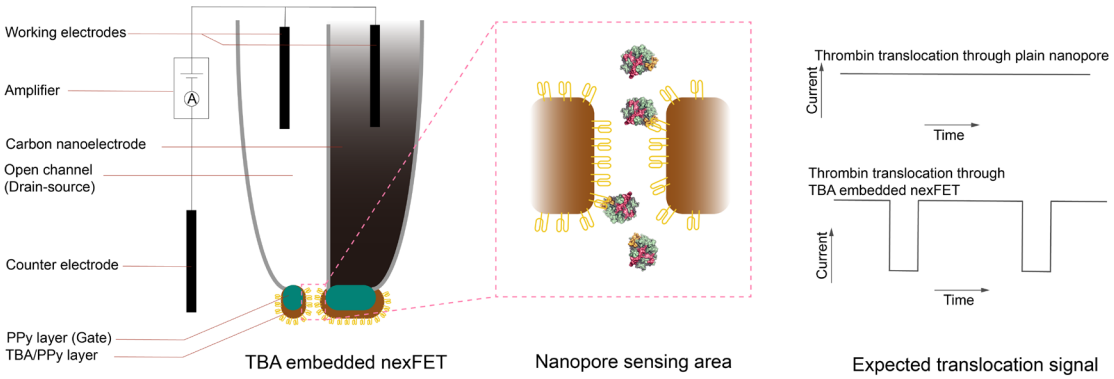


Figure 7. 1 Schematic of a TBA-embedded nexFET. This nexFET is a nanopore-based transistor, which is located on a dual-barrel nanopipette tip. By applying the voltage from the carbon nanoelectrode, the drain-source current across the nanopipette can be changed. The nanopore sensing area, which is the TBA-modified PPy nanopore inner wall, is capable of identifying and detecting thrombin selectively. The detection of thrombin by plain glass nanopore is always challenging due to its small size, heterogeneous charge, and fast translocation. This is the limitation I can address by the TBA-embedded nexFET.

7.2.1.2 The preliminary results

Proof of principle experiments have been successfully performed using aptamer-embedded nexFETs. Briefly, the thrombin aptamer was mixed with pyrrole, and the mixture was deposited on the dual-barrel nanopipette tip. **Figure 7.2** illustrates the schematic and *I-V* characterisation the TBA-embedded nexFET. Compared with the insulin-embedded nexFET, the TBA-modified one displays more negative current rectification due to the negatively charged aptamer fragments attached to the PPy.

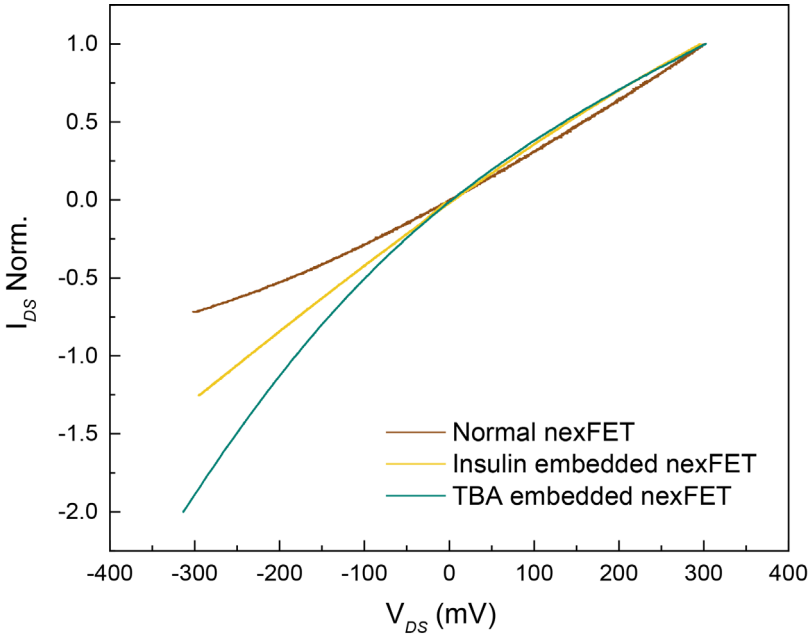


Figure 7. 2 The *I-V* characteristics of different nexFETs. **(a)** Schematic of the plain nexFET, the insulin-embedded nexFET, and the TBA-embedded nexFET. **(b)** The *I-V* measurements of those three types of nexFETs in a solution of 100 mM of KCl and 10 mM of Tris-EDTA (pH = 8).

Translocation experiments were compared using plain a quartz nanopipette and a TBA-embedded nexFET (**Figure 7.3**). Not surprisingly, no signal was observed when translocating thrombin through a plain nanopipette (**Figure 7.3a[i]**). In contrast, numerous clear translocation events were observed when the TBA-embedded nexFET was used (**Figure 7.3a[ii]**, **Figure 7.3b**).

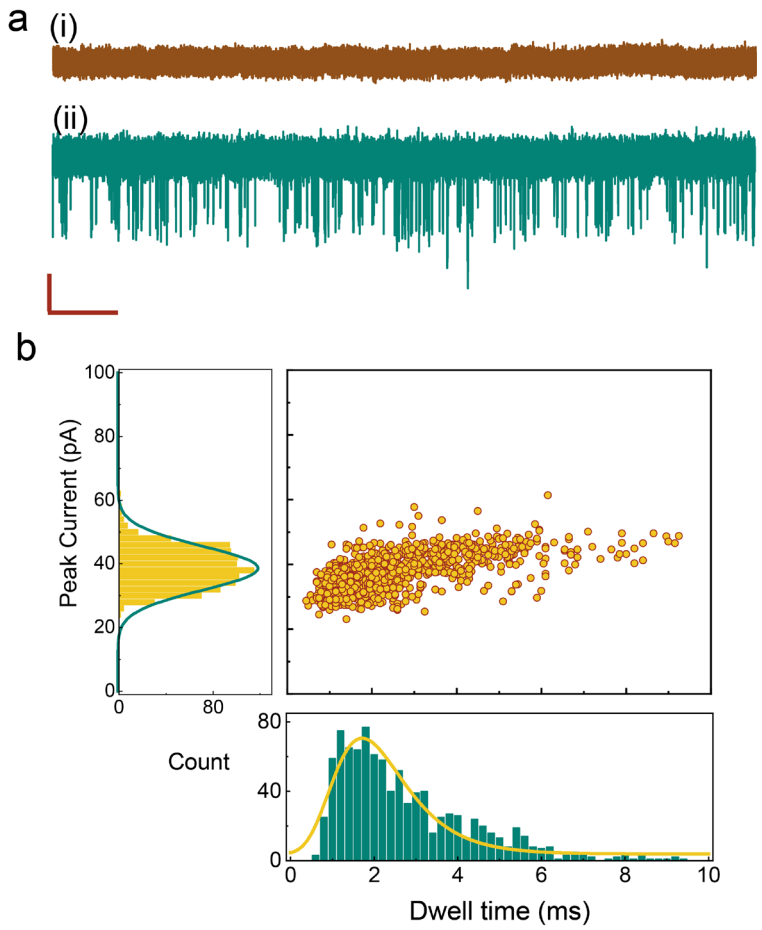


Figure 7. 3 Thrombin single-molecule sensing by using a TBA-embedded nanopore. **(a)** The translocation recordings of 30 nM thrombin translocation through **(i)** a 15 nm plain quartz nanopipette and **(ii)** a TBA-embedded nexFET, with 100 mM of KCl and 10 mM of Tris-EDTA (pH = 8), V_{DS} = 700 mV. Scale bar: horizontal 1 s; vertical 20 pA. **(b)** The scatter plot (peak current along with dwell time) of the thrombin translocation.

However, at high thrombin concentrations, the lifetime of the TBA-embedded nexFET was shorter compared to the one presented in **Chapter 4** due to electrostatic interaction between the nanopore and the analyte. I also found that the sensitivity and selectivity of the nanopore decayed when I ran the sample in serum and was likely a result of non-specific binding. To reset the sensor, a positive/negative voltage was applied to the gate to attempt repelling electrostatically attached molecules to the PPy layer. However, in these devices, a diminished FET response was observed (**Figure 7.4a**), attributed to the excess of negative charge of the functional aptamer layer embedded in the PPy.

To address this issue, a double PPy layer design was implemented, as illustrated in **Figure 7.1**. The inner layer, which is made of pure PPy, and has high conductance, while the outer layer, which consists of TBA-embedded PPy, can selectively detect targets. As expected, the FET performance of this double-layer system was improved significantly (**Figure 7.4b**).

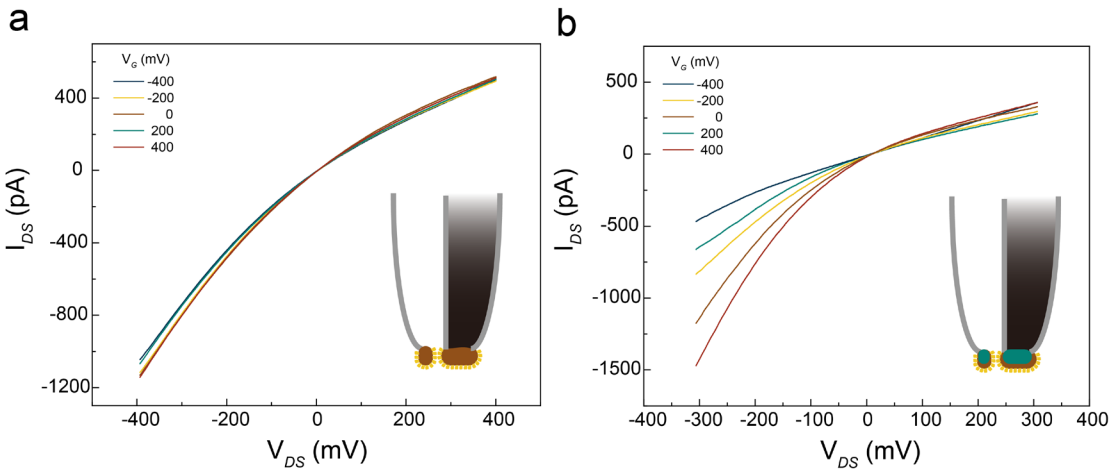


Figure 7. 4 The FET performance of two types of TBA-embedded nexFETs. The I_{DS}-V_{DS} characteristics with different gate voltages in **(a)** a one-layer TBA-embedded nexFET and **(b)** a two-layer TBA-embedded nexFET. The I-V measurements were conducted in a solution of 100 mM of KCl and 10 mM of Tris-EDTA (pH = 7).

7.2.1.3 Future experimental strategy

Based on the preliminary work, there are two key remaining objectives that require completion: sensing thrombin at different gate voltages and sensing thrombin in human serum. In **Chapter 4**, I explained how to use the gate voltage to control the translocation behaviour of DNA transport. With further optimisation, it is expected that it would also be possible to improve and control the transport of proteins. To date, only preliminary studies have been performed using complex biological fluids. To fully take advantage of the platform, it will be important to assess the capability of the nexFET under an extensive range of conditions. I believe this will enable a route towards early-stage diagnosis or therapeutics.

7.2.2 Detecting multiple targets using molecular carriers

7.2.2.1 Experiment outline

I want to improve the molecular carrier strategy by incorporating the ability to sense multiple targets simultaneously. This can be achieved by incorporating more binding sites and using more complex carriers which could include DNA origami and carbon nanotubes. In both cases, binding sites can be introduced via incorporation of aptamer sequences. An example of a strategy using DNA is shown in **Figure 7.5**. The main body of this carrier is a six-helix-bundle DNA origami with a biotinylated end. This origami rod is expected to remain in a linear shape, which will only result in a single step translocation signature. Four aptamers for different proteins can be attached to the DNA carrier. The sub-peaks can then be used to determine the presence of a target analyte.

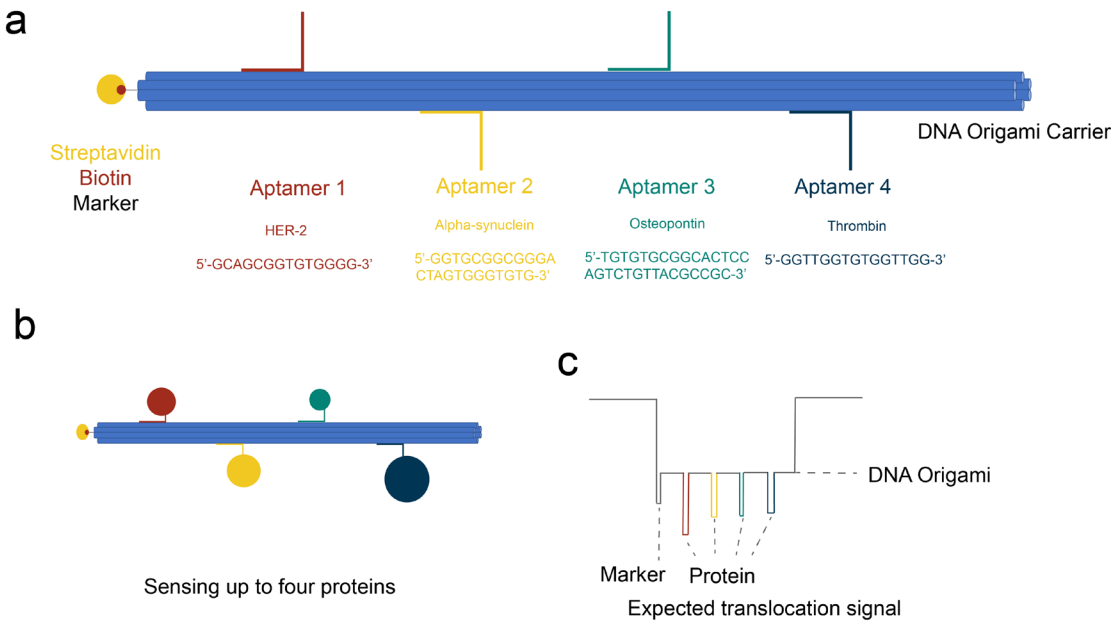


Figure 7. 5 Schematic of a DNA origami protein carrier. The main carrier is a six-helix-bundle DNA origami with a biotinylated end. In the protein carrier, four different aptamers were engineered on the DNA origami carrier to bind specific proteins. The proteins can be identified by the sub-peaks of the translocation signal. The origami sample was provided by Prof. Yang Yang (Shanghai Jiaotong University, China) and Prof. Chenxiang Lin (Yale University, US).

7.2.2.2 The preliminary results

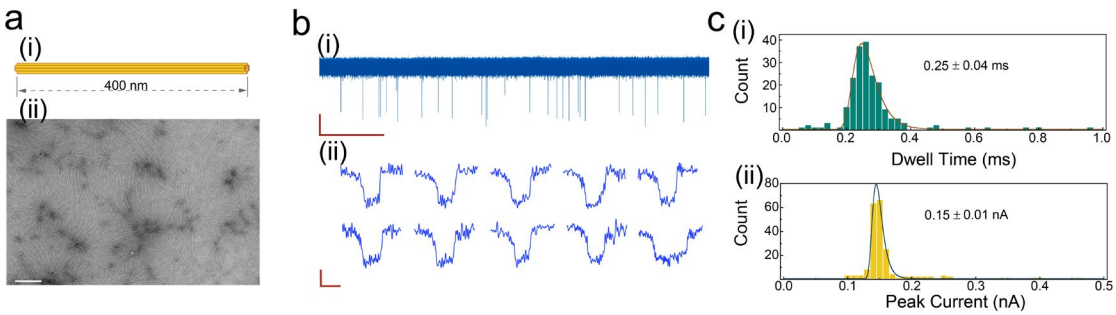


Figure 7. 6 The translocation of unmodified six-helix-bundle DNA origami molecules. **(a)** Schematic of the DNA origami, which is a cylindrical shape that is 400 nm long. **(b) (i)** The translocation recording trace and **(ii)** randomly picked events of 200 pM DNA origami in 2 M of LiCl and 10 mM of Tris-EDTA (pH = 8) under 600 mV. Scale bar: **(i)** horizontal 5 s, vertical 50 pA and **(ii)** horizontal 0.2 μs; vertical 50 pA. **(c)** The dwell time and peak current of the translocation of DNA origami.

The aim of the first and crucial experiment is to verify the translocation behaviour of the DNA origami rod. From the TEM imaging, a clear DNA origami rod shape can be observed (**Figure 7.6a**). The translocation recordings and the events illustrate that all peaks are at one level, which is also validated by the statistics (**Figure 7.6b–c**). This means that the DNA origami will pass through the nanopore in a linear configuration.

7.2.2.3 Future works

I have demonstrated that the DNA origami rod structure is a highly suitable molecule carrier, where the signal itself would not interfere with the target signal. The next step is to integrate the aptamers onto the DNA origami rod structure. The generated DNA origami protein carrier is expected to test up to four different proteins simultaneously.

For example, the aptamers HER-2 binding aptamer, alpha-synuclein oligomer binding aptamer, osteopontin binding aptamer and thrombin binding aptamer can be hybridised on the DNA origami nanorod carrier. The binding curve for each protein will then be achieved.

7.3 Conclusion

Nanopores, which are powerful single-molecule analytical tools, are limited at times by low sensitivity and selectivity when detecting small biomolecules such as proteins. In this PhD work, I used novel tools and strategies to tackle these fundamental problems. A series of new devices, combining nanopores and FETs, were fabricated. The movement of biomolecules when passing through the nanopore could be manipulated, and the translocation signals were thus improved. By introducing binding sites within the inner walls of the nanopore, it becomes possible to sense proteins selectively. Alternatively, rather than modifying the nanopore, it is also possible to introduce carriers, which is another possible route towards selective sensing using nanopores. One strategy is to use dumbbell-shaped nanoparticle dimers and based on the translocation signature; one can detect the presence of protein targets with high efficiency. Overall, from the research presented in this thesis, I reported different strategies to overcome the limitations of nanopore-based single-molecule biosensing techniques, leading to a step closer to improve the quality of life by enabling early-stage diagnostics and at the same time reducing costs associated with medical implementation.

7.4 References

1. Xue, L.; Cadinu, P.; Paulose Nadappuram, B.; Kang, M.; Ma, Y.; Korchev, Y.; Ivanov, A. P.; Edel, J. B., Gated Single-Molecule Transport in Double-Barreled Nanopores. *ACS applied materials & interfaces* **2018,** *10* (44), 38621-38629.

2. Al Sulaiman, D.; Cadinu, P.; Ivanov, A. P.; Edel, J. B.; Ladame, S., Chemically Modified Hydrogel-Filled Nanopores: A Tunable Platform for Single-Molecule Sensing. *Nano letters* **2018,** *18* (9), 6084-6093.

3. Gao, R.; Lin, Y.; Ying, Y.-L.; Hu, Y.-X.; Xu, S.-W.; Ruan, L.-Q.; Yu, R.-J.; Li, Y.-J.; Li, H.-W.; Cui, L.-F.; Long, Y.-T., Wireless nanopore electrodes for analysis of single entities. *Nature protocols* **2019,** *14* (7), 2015-2035.

4. Sze, J. Y. Y.; Ivanov, A. P.; Cass, A. E. G.; Edel, J. B., Single molecule multiplexed nanopore protein screening in human serum using aptamer modified DNA carriers. *Nature Communications* **2017,** *8*.

5. Kong, J.; Zhu, J.; Chen, K.; Keyser, U. F., Specific Biosensing Using DNA Aptamers and Nanopores. *Advanced Functional Materials* **2019,** *29* (3), 1807555.

6. Cai, S. L.; Sze, J. Y. Y.; Ivanov, A. P.; Edel, J. B., Small molecule electro-optical binding assay using nanopores. *Nature Communications* **2019,** *10*.

Appendix

Copyright Permission

Figure No.	Source	Copyright Holder	Permission	License No.	Approval No.
1.2	Song, L. Z.; Hobaugh, M. R.; Shustak, C.; Cheley, S.; Bayley, H.; Gouaux, J. E., Structure of staphylococcal alpha-hemolysin, a heptameric transmembrane pore. Science 1996, 274 (5294), 1859-1866.	The American Association for the Advancement of Science	Granted	4646590936855	1
1.3	Miles, B. N.; Ivanov, A. P.; Wilson, K. A.; Dogan, F.; Japrung, D.; Edel, J. B., Single molecule sensing with solid-state nanopores: novel materials, methods, and applications. Chemical Society reviews 2013, 42 (1), 15-28.	Royal Society of Chemistry	Granted	4646671221146	2
1.4	Li, J.; Stein, D.; McMullan, C.; Branton, D.; Aziz, M. J.; Golovchenko, J. A., Ion-beam sculpting at nanometre length scales. *Nature* **2001,** *412* (6843), 166-169.	Springer Nature	Granted	4646651225878	3
1.9	Firnkes, M.; Pedone, D.; Knezevic, J.; Doblinger, M.; Rant, U., Electrically Facilitated Translocations of Proteins through Silicon Nitride Nanopores: Conjoint and Competitive Action of Diffusion, Electrophoresis, and Electroosmosis. Nano letters 2010, 10 (6), 2162-2167.	American Chemical Society	Granted	N/A	4
1.10	Steinbock, L. J.; Lucas, A.; Otto, O.; Keyser, U. F., Voltage-driven transport of ions and DNA through nanocapillaries. Electrophoresis 2012, 33 (23), 3480-3487.	John Wiley and Sons	Granted	4646660153453	5
1.11	Kowalczyk, S. W.; Wells, D. B.; Aksimentiev, A.; Dekker, C., Slowing down DNA Translocation through a Nanopore in Lithium Chloride. Nano letters 2012, 12 (2), 1038-1044.	American Chemical Society	Granted	N/A	6
1.12	Liu, Y. F.; Yobas, L., Slowing DNA Translocation in a Nanofluidic Field-Effect Transistor. ACS nano 2016, 10 (4), 3985-3994.	American Chemical Society	Open Access	N/A	N/A
1.13	Al Sulaiman, D.; Cadinu, P.; Ivanov, A. P.; Edel, J. B.; Ladame, S., Chemically Modified Hydrogel-Filled Nanopores: A Tunable Platform for Single-Molecule Sensing. Nano letters 2018, 18 (9), 6084-6093.	American Chemical Society	Granted	N/A	7
1.14	Venkatesan, B. M.; Bashir, R., Nanopore sensors for nucleic acid analysis. *Nature nanotechnology* **2011,** *6* (10), 615-624.	Springer Nature	Granted	4646670061964	8
1.15	Steinbock, L. J.; Krishnan, S.; Bulushev, R. D.; Borgeaud, S.; Blokesch, M.; Feletti, L.; Radenovic, A., Probing the size of proteins with glass nanopores. Nanoscale 2014, 6 (23), 14380-14387.	Royal Society of Chemistry	Granted	4646670299579	9
1.16a	Li, Q.; Ying, Y. L.; Liu, S. C.; Lin, Y.; Long, Y. T., Detection of Single Proteins with a General Nanopore Sensor. Acs Sensors 2019, 4 (5), 1185-1189.	American Chemical Society	Granted	N/A	10

1.16b	Yu, R. J.; Ying, Y. L.; Hu, Y. X.; Gao, R.; Long, Y. T., Label-Free Monitoring of Single Molecule Immunoreaction with a Nanopipette. Analytical Chemistry 2017, 89 (16), 8203-8206.	American Chemical Society	Granted	N/A	11
1.17	Wei, R.; Gatterdam, V.; Wieneke, R.; Tampe, R.; Rant, U., Stochastic sensing of proteins with receptor-modified solid-state nanopores. Nature nanotechnology 2012, 7 (4), 257-263.	Springer Nature	Granted	4646670565047	12
1.18	Sze, J. Y. Y.; Ivanov, A. P.; Cass, A. E. G.; Edel, J. B., Single molecule multiplexed nanopore protein screening in human serum using aptamer modified DNA carriers. Nature Communications 2017, 8.	Springer Nature	Open Access	N/A	N/A
3.1a	Cai, B. J.; Wang, S. T.; Huang, L.; Ning, Y.; Zhang, Z. Y.; Zhang, G. J., Ultrasensitive Label-Free Detection of PNA-DNA Hybridization by Reduced Graphene Oxide Field-Effect Transistor Biosensor. ACS nano 2014, 8 (3), 2632-2638.	American Chemical Society	Granted	N/A	13
3.1b	Zhang, C.; Xu, J. Q.; Li, Y. T.; Huang, L.; Pang, D. W.; Ning, Y.; Huang, W. H.; Zhang, Z. Y.; Zhang, G. J., Photocatalysis-Induced Renewable Field-Effect Transistor for Protein Detection. Analytical Chemistry 2016, 88 (7), 4048-4054.	American Chemical Society	Granted	N/A	14
5.1	Ang, Y. S.; Yung, L.-Y. L., Rapid and Label-Free Single-Nucleotide Discrimination via an Integrative Nanoparticle–Nanopore Approach. *ACS nano* **2012,** *6* (10), 8815-8823.	American Chemical Society	Granted	N/A	15
Chapter 3	Ren, R.; Zhang, Y. J.; Nadappuram, B. P.; Akpinar, B.; Klenerman, D.; Ivanov, A. P.; Edel, J. B.; Korchev, Y., Nanopore extended field-effect transistor for selective single-molecule biosensing. *Nature Communications* **2017,** *8*.	Springer Nature	Open Access	N/A	N/A
Chapter 4	Ren, R.; Zhang, Y. J.; Nadappuram, B. P.; Akpinar, B.; Klenerman, D.; Ivanov, A. P.; Edel, J. B.; Korchev, Y., Nanopore extended field-effect transistor for selective single-molecule biosensing. *Nature Communications* **2017,** *8*.	Springer Nature	Open Access	N/A	N/A

Approval 1

THE AMERICAN ASSOCIATION FOR THE ADVANCEMENT OF SCIENCE LICENSE TERMS AND CONDITIONS

Aug 12, 2019

This Agreement between Imperial College London -- Ren Ren ("You") and The American Association for the Advancement of Science ("The American Association for the Advancement of Science") consists of your license details and the terms and conditions provided by The American Association for the Advancement of Science and Copyright Clearance Center.

License Number	4646590936855
License date	Aug 12, 2019
Licensed Content Publisher	The American Association for the Advancement of Science
Licensed Content Publication	Science
Licensed Content Title	Structure of Staphylococcal α-Hemolysin, a Heptameric Transmembrane Pore
Licensed Content Author	Langzhou Song,Michael R. Hobaugh,Christopher Shustak,Stephen Cheley,Hagan Bayley,J. Eric Gouaux
Licensed Content Date	Dec 13, 1996
Licensed Content Volume	274
Licensed Content Issue	5294
Volume number	274
Issue number	5294
Type of Use	Thesis / Dissertation
Requestor type	Scientist/individual at a research institution
Format	Print and electronic
Portion	Figure
Number of figures/tables	2
Order reference number	
Title of your thesis / dissertation	Novel tools and strategies of nanopore single-molecule biosensing
Expected completion date	Aug 2019
Estimated size(pages)	200
Requestor Location	Imperial College London Imperial College London South Kensington London, SW7 2AZ United Kingdom Attn: Imperial College London
Total	**0.00 GBP**

Terms and Conditions

American Association for the Advancement of Science TERMS AND CONDITIONS
Regarding your request, we are pleased to grant you non-exclusive, non-transferable permission, to republish the AAAS material identified above in your work identified above, subject to the terms and conditions herein. We must be contacted for permission for any uses other than those specifically identified in your request above.
The following credit line must be printed along with the AAAS material: "From [Full Reference Citation]. Reprinted with permission from AAAS."
All required credit lines and notices must be visible any time a user accesses any part of the AAAS material and must appear on any printed copies and authorized user might make.
This permission does not apply to figures / photos / artwork or any other content or materials included in your work that are credited to non-AAAS sources. If the requested material is sourced to or references non-AAAS sources, you must obtain authorization from that source as well before using that material. You agree to hold harmless and indemnify AAAS against any claims arising from your use of any content in your work that is credited to non-AAAS sources.

Approval 2

Welcome To RightsLink

Aug 12, 2019

This is a License Agreement between Imperial College London -- Ren Ren ("You") and Royal Society of Chemistry ("Royal Society of Chemistry") provided by Copyright Clearance Center ("CCC"). The license consists of your order details, the terms and conditions provided by Royal Society of Chemistry, and the payment terms and conditions.

All payments must be made in full to CCC. For payment instructions, please see information listed at the bottom of this form.

License Number	4646671221146
License date	Aug 12, 2019
Licensed Content Publisher	Royal Society of Chemistry
Licensed Content Title	Chemical Society reviews
Licensed Content Date	Jan 1, 1972
I would like to...	Thesis/Dissertation
Requestor type	Academic institution
Format	Print, Electronic
Portion	image/photo
Number of images/photos requested	4
The requesting person/organization is:	Ren Ren
Title or numeric reference of the portion(s)	Novel tools and strategies of nanopore single-molecule biosensing
Title of the article or chapter the portion is from	Chapter 1
Editor of portion(s)	N/A
Author of portion(s)	Ren Ren
Volume of serial or monograph.	N/A
Page range of the portion	200
Publication date of portion	08/2019
Rights for	Main product
Duration of use	Life of current edition
Creation of copies for the disabled	yes
With minor editing privileges	no
For distribution to	Worldwide
In the following language(s)	Original language of publication
With incidental promotional use	no
The lifetime unit quantity of new product	Up to 499
Title	Novel tools and strategies of nanopore single-molecule biosensing
Institution name	Imperial College London
Expected presentation date	Aug 2019
Total (may include CCC user fee)	**0.00 USD**
Terms and Conditions	

Approval 3

SPRINGER NATURE LICENSE TERMS AND CONDITIONS

Aug 12, 2019

This Agreement between Imperial College London -- Ren Ren ("You") and Springer Nature ("Springer Nature") consists of your license details and the terms and conditions provided by Springer Nature and Copyright Clearance Center.

License Number	4646651225878
License date	Aug 12, 2019
Licensed Content Publisher	Springer Nature
Licensed Content Publication	Nature
Licensed Content Title	Ion-beam sculpting at nanometre length scales
Licensed Content Author	Jiali Li et al
Licensed Content Date	Jul 12, 2001
Type of Use	Thesis/Dissertation
Requestor type	academic/university or research institute
Format	print and electronic
Portion	figures/tables/illustrations
Number of figures/tables/illustrations	2
Will you be translating?	no
Circulation/distribution	<501
Author of this Springer Nature content	no
Title	Novel tools and strategies of nanopore single-molecule biosensing
Institution name	Imperial College London
Expected presentation date	Aug 2019
Portions	Chapter 1, Figure 1.4
Requestor Location	Imperial College London Imperial College London South Kensington London, SW7 2AZ United Kingdom Attn: Imperial College London
Total	**0.00 GBP**
Terms and Conditions	

Springer Nature Customer Service Centre GmbH
Terms and Conditions

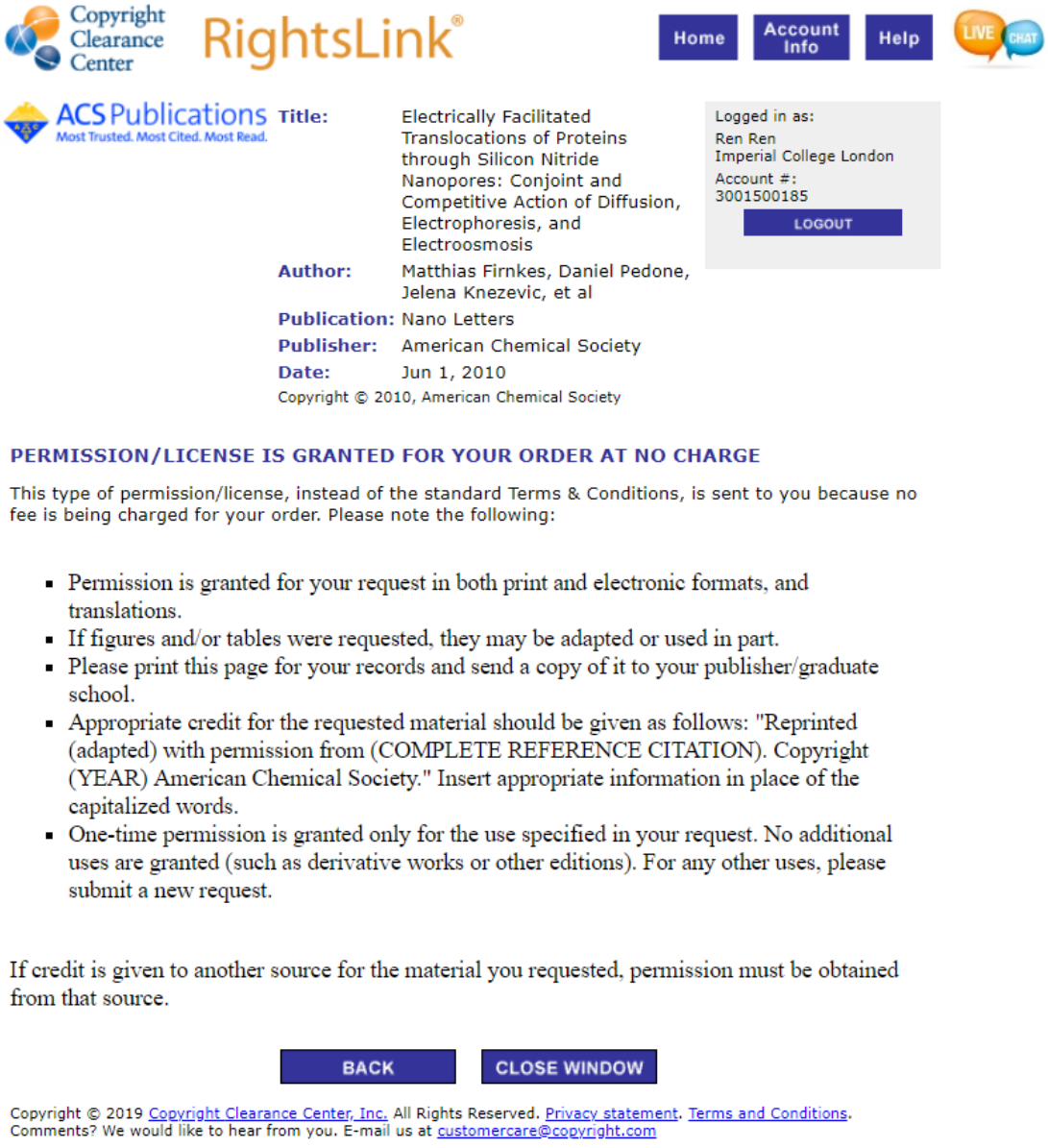
This agreement sets out the terms and conditions of the licence (the **Licence**) between you and **Springer Nature Customer Service Centre GmbH** (the **Licensor**). By clicking 'accept' and completing the transaction for the material (**Licensed Material**), you also confirm your acceptance of these terms and conditions.

1. Grant of License

1. 1. The Licensor grants you a personal, non-exclusive, non-transferable, world-wide licence to reproduce the Licensed Material for the purpose specified in your order only. Licences are granted for the specific use requested in the order and for no other use, subject to the conditions below.

1. 2. The Licensor warrants that it has, to the best of its knowledge, the rights to license reuse of the Licensed Material. However, you should ensure that the material you are requesting is original to the Licensor and does not carry the

Approval 4



Copyright Clearance Center RightsLink®

Home | Account Info | Help | LIVE CHAT

ACS Publications
Most Trusted. Most Cited. Most Read.

Title: Electrically Facilitated Translocations of Proteins through Silicon Nitride Nanopores: Conjoint and Competitive Action of Diffusion, Electrophoresis, and Electroosmosis

Author: Matthias Firnkes, Daniel Pedone, Jelena Knezevic, et al

Publication: Nano Letters

Publisher: American Chemical Society

Date: Jun 1, 2010

Copyright © 2010, American Chemical Society

Logged in as:
Ren Ren
Imperial College London
Account #:
3001500185
LOGOUT

PERMISSION/LICENSE IS GRANTED FOR YOUR ORDER AT NO CHARGE

This type of permission/license, instead of the standard Terms & Conditions, is sent to you because no fee is being charged for your order. Please note the following:

- Permission is granted for your request in both print and electronic formats, and translations.
- If figures and/or tables were requested, they may be adapted or used in part.
- Please print this page for your records and send a copy of it to your publisher/graduate school.
- Appropriate credit for the requested material should be given as follows: "Reprinted (adapted) with permission from (COMPLETE REFERENCE CITATION). Copyright (YEAR) American Chemical Society." Insert appropriate information in place of the capitalized words.
- One-time permission is granted only for the use specified in your request. No additional uses are granted (such as derivative works or other editions). For any other uses, please submit a new request.

If credit is given to another source for the material you requested, permission must be obtained from that source.

BACK | CLOSE WINDOW

Copyright © 2019 Copyright Clearance Center, Inc. All Rights Reserved. Privacy statement. Terms and Conditions.
Comments? We would like to hear from you. E-mail us at customercare@copyright.com

Approval 5

JOHN WILEY AND SONS LICENSE TERMS AND CONDITIONS

Aug 12, 2019

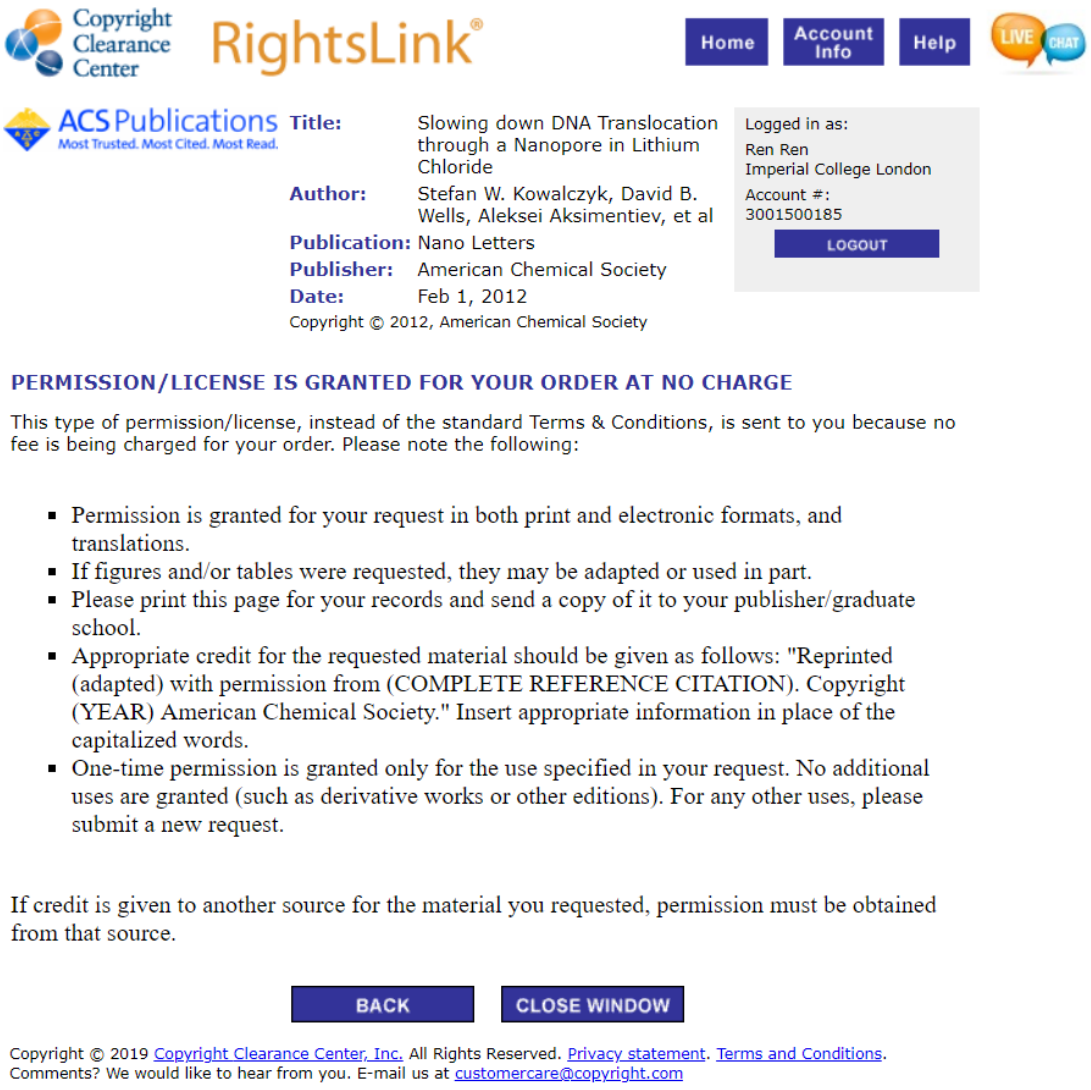
This Agreement between Imperial College London -- Ren Ren ("You") and John Wiley and Sons ("John Wiley and Sons") consists of your license details and the terms and conditions provided by John Wiley and Sons and Copyright Clearance Center.

License Number	4646660153453
License date	Aug 12, 2019
Licensed Content Publisher	John Wiley and Sons
Licensed Content Publication	Electrophoresis
Licensed Content Title	Voltage-driven transport of ions and DNA through nanocapillaries
Licensed Content Author	Lorenz J. Steinbock, Alex Lucas, Oliver Otto, et al
Licensed Content Date	Nov 12, 2012
Licensed Content Volume	33
Licensed Content Issue	23
Licensed Content Pages	8
Type of use	Dissertation/Thesis
Requestor type	University/Academic
Format	Print and electronic
Portion	Figure/table
Number of figures/tables	4
Original Wiley figure/table number(s)	Figure 4
Will you be translating?	No
Title of your thesis / dissertation	Novel tools and strategies of nanopore single-molecule biosensing
Expected completion date	Aug 2019
Expected size (number of pages)	200
Requestor Location	Imperial College London Imperial College London South Kensington London, SW7 2AZ United Kingdom Attn: Imperial College London
Publisher Tax ID	EU826007151
Total	0.00 GBP
Terms and Conditions	

TERMS AND CONDITIONS

This copyrighted material is owned by or exclusively licensed to John Wiley & Sons, Inc. or one of its group companies (each a"Wiley Company") or handled on behalf of a society with which a Wiley Company has exclusive publishing rights in relation to a particular work (collectively "WILEY"). By clicking "accept" in connection with completing this licensing transaction, you agree that the following terms and conditions apply to this transaction (along with the billing and payment terms and conditions established by the Copyright Clearance Center Inc., ("CCC's Billing and Payment terms and conditions"), at the time that

Approval 6



Copyright Clearance Center RightsLink®

Home | Account Info | Help | LIVE CHAT

ACS Publications
Most Trusted. Most Cited. Most Read.

Title:	Slowing down DNA Translocation through a Nanopore in Lithium Chloride
Author:	Stefan W. Kowalczyk, David B. Wells, Aleksei Aksimentiev, et al
Publication:	Nano Letters
Publisher:	American Chemical Society
Date:	Feb 1, 2012

Copyright © 2012, American Chemical Society

Logged in as:
Ren Ren
Imperial College London
Account #:
3001500185
LOGOUT

PERMISSION/LICENSE IS GRANTED FOR YOUR ORDER AT NO CHARGE

This type of permission/license, instead of the standard Terms & Conditions, is sent to you because no fee is being charged for your order. Please note the following:

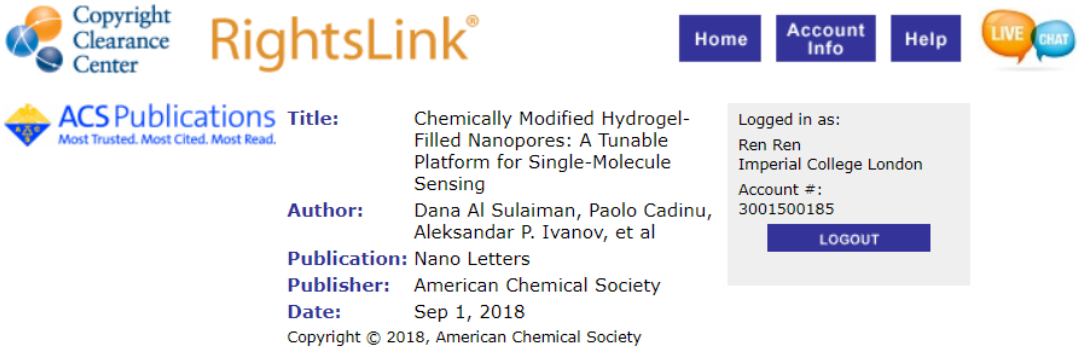
- Permission is granted for your request in both print and electronic formats, and translations.
- If figures and/or tables were requested, they may be adapted or used in part.
- Please print this page for your records and send a copy of it to your publisher/graduate school.
- Appropriate credit for the requested material should be given as follows: "Reprinted (adapted) with permission from (COMPLETE REFERENCE CITATION). Copyright (YEAR) American Chemical Society." Insert appropriate information in place of the capitalized words.
- One-time permission is granted only for the use specified in your request. No additional uses are granted (such as derivative works or other editions). For any other uses, please submit a new request.

If credit is given to another source for the material you requested, permission must be obtained from that source.

BACK | CLOSE WINDOW

Copyright © 2019 Copyright Clearance Center, Inc. All Rights Reserved. Privacy statement. Terms and Conditions.
Comments? We would like to hear from you. E-mail us at customercare@copyright.com

Approval 7



PERMISSION/LICENSE IS GRANTED FOR YOUR ORDER AT NO CHARGE

This type of permission/license, instead of the standard Terms & Conditions, is sent to you because no fee is being charged for your order. Please note the following:

- Permission is granted for your request in both print and electronic formats, and translations.
- If figures and/or tables were requested, they may be adapted or used in part.
- Please print this page for your records and send a copy of it to your publisher/graduate school.
- Appropriate credit for the requested material should be given as follows: "Reprinted (adapted) with permission from (COMPLETE REFERENCE CITATION). Copyright (YEAR) American Chemical Society." Insert appropriate information in place of the capitalized words.
- One-time permission is granted only for the use specified in your request. No additional uses are granted (such as derivative works or other editions). For any other uses, please submit a new request.

If credit is given to another source for the material you requested, permission must be obtained from that source.

BACK CLOSE WINDOW

Copyright © 2019 Copyright Clearance Center, Inc. All Rights Reserved. Privacy statement. Terms and Conditions.
Comments? We would like to hear from you. E-mail us at customercare@copyright.com

Approval 8

SPRINGER NATURE LICENSE
TERMS AND CONDITIONS

Aug 12, 2019

This Agreement between Imperial College London -- Ren Ren ("You") and Springer Nature ("Springer Nature") consists of your license details and the terms and conditions provided by Springer Nature and Copyright Clearance Center.

License Number	4646670061964
License date	Aug 12, 2019
Licensed Content Publisher	Springer Nature
Licensed Content Publication	Nature Nanotechnology
Licensed Content Title	Nanopore sensors for nucleic acid analysis
Licensed Content Author	Bala Murali Venkatesan, Rashid Bashir
Licensed Content Date	Sep 18, 2011
Licensed Content Volume	6
Licensed Content Issue	10
Type of Use	Thesis/Dissertation
Requestor type	academic/university or research institute
Format	print and electronic
Portion	figures/tables/illustrations
Number of figures/tables/illustrations	5
High-res required	no
Will you be translating?	no
Circulation/distribution	<501
Author of this Springer Nature content	no
Title	Novel tools and strategies of nanopore single-molecule biosensing
Institution name	Imperial College London
Expected presentation date	Aug 2019
Portions	Chapter 1, Figure 1.14
Requestor Location	Imperial College London Imperial College London South Kensington London, SW7 2AZ United Kingdom Attn: Imperial College London
Total	0.00 GBP

Terms and Conditions

Springer Nature Customer Service Centre GmbH
Terms and Conditions

This agreement sets out the terms and conditions of the licence (the **Licence**) between you and **Springer Nature Customer Service Centre GmbH** (the **Licensor**). By clicking

Approval 9

Welcome To RightsLink

Aug 12, 2019

This is a License Agreement between Imperial College London -- Ren Ren ("You") and Royal Society of Chemistry ("Royal Society of Chemistry") provided by Copyright Clearance Center ("CCC"). The license consists of your order details, the terms and conditions provided by Royal Society of Chemistry, and the payment terms and conditions.

All payments must be made in full to CCC. For payment instructions, please see information listed at the bottom of this form.

License Number	4646670299579
License date	Aug 12, 2019
Licensed Content Publisher	Royal Society of Chemistry
Licensed Content Title	Nanoscale
Licensed Content Date	Jan 1, 2009
I would like to...	Thesis/Dissertation
Requestor type	Academic institution
Format	Print, Electronic
Portion	image/photo
Number of images/photos requested	3
The requesting person/organization is:	Ren Ren
Title or numeric reference of the portion(s)	Novel tools and strategies of nanopore single-molecule biosensing
Title of the article or chapter the portion is from	Chapter 1
Editor of portion(s)	N/A
Author of portion(s)	Ren Ren
Volume of serial or monograph.	N/A
Page range of the portion	200
Publication date of portion	08/2019
Rights for	Main product
Duration of use	Life of current edition
Creation of copies for the disabled	yes
With minor editing privileges	no
For distribution to	Worldwide
In the following language(s)	Original language of publication
With incidental promotional use	no
The lifetime unit quantity of new product	Up to 499
Title	Novel tools and strategies of nanopore single-molecule biosensing
Institution name	Imperial College London
Expected presentation date	Aug 2019
Total (may include CCC user fee)	**0.00 USD**
Terms and Conditions	

Approval 10



Copyright Clearance Center RightsLink®

Home | Account Info | Help | LIVE CHAT

ACS Publications
Most Trusted. Most Cited. Most Read.

Title: Detection of Single Proteins with a General Nanopore Sensor
Author: Qiao Li, Yi-Lun Ying, Shao-Chuang Liu, et al
Publication: ACS Sensors
Publisher: American Chemical Society
Date: May 1, 2019
Copyright © 2019, American Chemical Society

Logged in as:
Ren Ren
Imperial College London
Account #:
3001500185
LOGOUT

PERMISSION/LICENSE IS GRANTED FOR YOUR ORDER AT NO CHARGE

This type of permission/license, instead of the standard Terms & Conditions, is sent to you because no fee is being charged for your order. Please note the following:

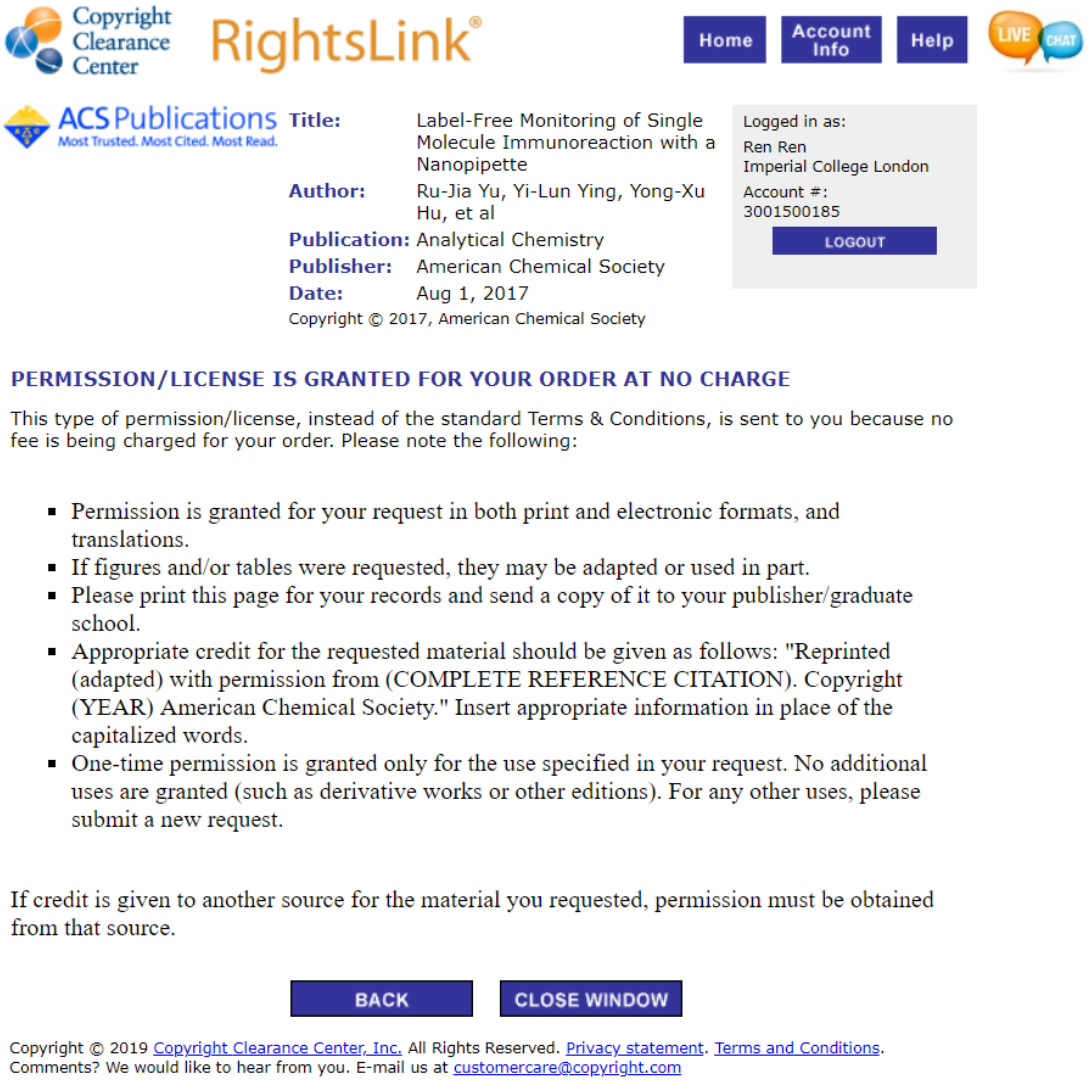
- Permission is granted for your request in both print and electronic formats, and translations.
- If figures and/or tables were requested, they may be adapted or used in part.
- Please print this page for your records and send a copy of it to your publisher/graduate school.
- Appropriate credit for the requested material should be given as follows: "Reprinted (adapted) with permission from (COMPLETE REFERENCE CITATION). Copyright (YEAR) American Chemical Society." Insert appropriate information in place of the capitalized words.
- One-time permission is granted only for the use specified in your request. No additional uses are granted (such as derivative works or other editions). For any other uses, please submit a new request.

If credit is given to another source for the material you requested, permission must be obtained from that source.

BACK | CLOSE WINDOW

Copyright © 2019 Copyright Clearance Center, Inc. All Rights Reserved. Privacy statement. Terms and Conditions.
Comments? We would like to hear from you. E-mail us at customercare@copyright.com

Approval 11



Copyright Clearance Center RightsLink®

Home | Account Info | Help | LIVE CHAT

ACS Publications
Most Trusted. Most Cited. Most Read.

Title: Label-Free Monitoring of Single Molecule Immunoreaction with a Nanopipette
Author: Ru-Jia Yu, Yi-Lun Ying, Yong-Xu Hu, et al
Publication: Analytical Chemistry
Publisher: American Chemical Society
Date: Aug 1, 2017
Copyright © 2017, American Chemical Society

Logged in as:
Ren Ren
Imperial College London
Account #:
3001500185
LOGOUT

PERMISSION/LICENSE IS GRANTED FOR YOUR ORDER AT NO CHARGE

This type of permission/license, instead of the standard Terms & Conditions, is sent to you because no fee is being charged for your order. Please note the following:

- Permission is granted for your request in both print and electronic formats, and translations.
- If figures and/or tables were requested, they may be adapted or used in part.
- Please print this page for your records and send a copy of it to your publisher/graduate school.
- Appropriate credit for the requested material should be given as follows: "Reprinted (adapted) with permission from (COMPLETE REFERENCE CITATION). Copyright (YEAR) American Chemical Society." Insert appropriate information in place of the capitalized words.
- One-time permission is granted only for the use specified in your request. No additional uses are granted (such as derivative works or other editions). For any other uses, please submit a new request.

If credit is given to another source for the material you requested, permission must be obtained from that source.

BACK | CLOSE WINDOW

Copyright © 2019 Copyright Clearance Center, Inc. All Rights Reserved. Privacy statement. Terms and Conditions.
Comments? We would like to hear from you. E-mail us at customercare@copyright.com

Approval 12

SPRINGER NATURE LICENSE
TERMS AND CONDITIONS

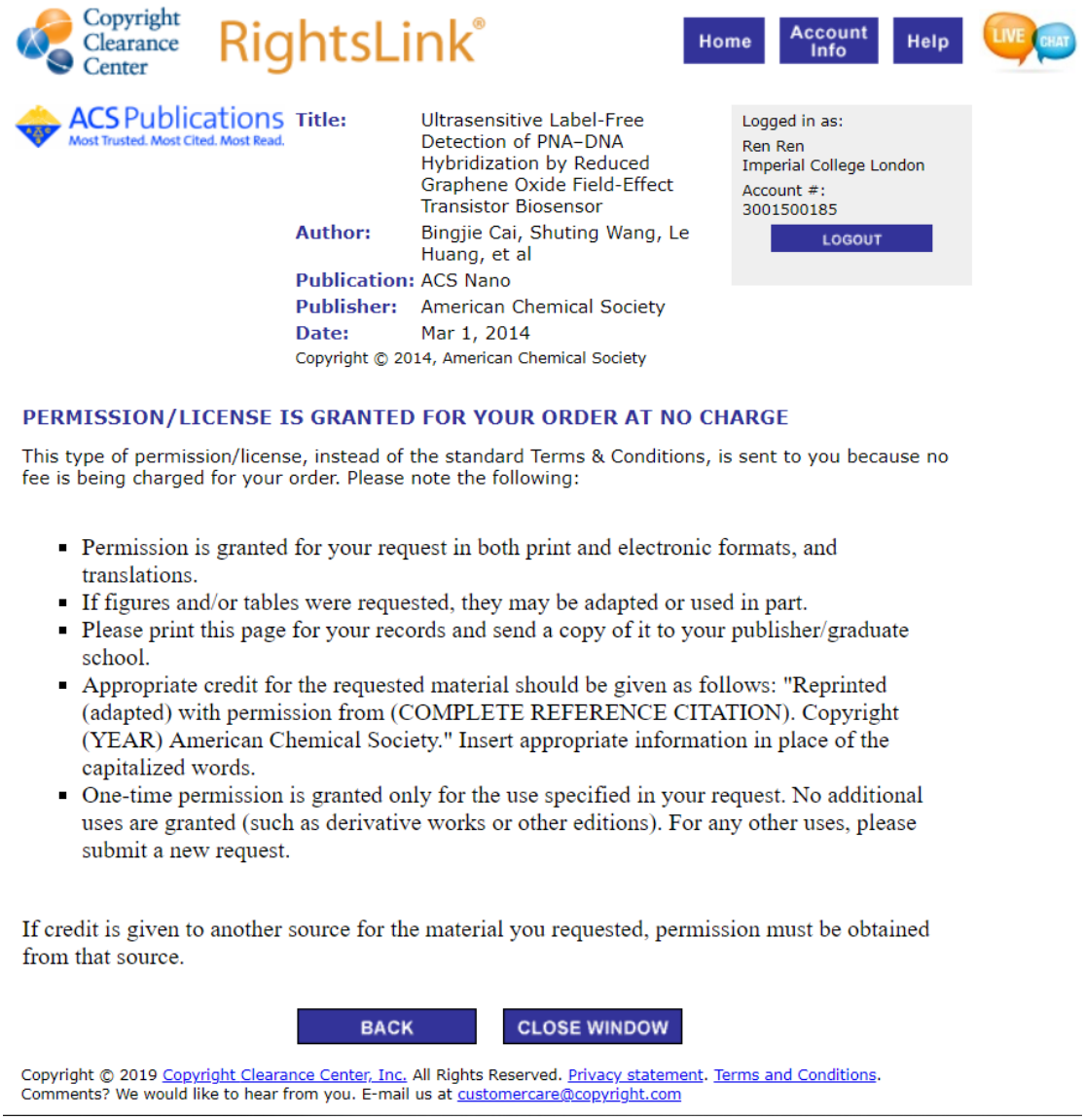
Aug 12, 2019

This Agreement between Imperial College London -- Ren Ren ("You") and Springer Nature ("Springer Nature") consists of your license details and the terms and conditions provided by Springer Nature and Copyright Clearance Center.

License Number	4646670565047
License date	Aug 12, 2019
Licensed Content Publisher	Springer Nature
Licensed Content Publication	Nature Nanotechnology
Licensed Content Title	Stochastic sensing of proteins with receptor-modified solid-state nanopores
Licensed Content Author	Ruoshan Wei, Volker Gatterdam, Ralph Wieneke, Robert Tampé, Ulrich Rant
Licensed Content Date	Mar 11, 2012
Licensed Content Volume	7
Licensed Content Issue	4
Type of Use	Thesis/Dissertation
Requestor type	academic/university or research institute
Format	print and electronic
Portion	figures/tables/illustrations
Number of figures/tables/illustrations	1
High-res required	no
Will you be translating?	no
Circulation/distribution	<501
Author of this Springer Nature content	no
Title	Novel tools and strategies of nanopore single-molecule biosensing
Institution name	Imperial College London
Expected presentation date	Aug 2019
Portions	Chapter 1, Figure 1.17
Requestor Location	Imperial College London Imperial College London South Kensington London, SW7 2AZ United Kingdom Attn: Imperial College London
Total	0.00 GBP
Terms and Conditions	

Springer Nature Customer Service Centre GmbH
Terms and Conditions

Approval 13



Copyright Clearance Center RightsLink®

Home | Account Info | Help | LIVE CHAT

ACS Publications
Most Trusted. Most Cited. Most Read.

Title: Ultrasensitive Label-Free Detection of PNA–DNA Hybridization by Reduced Graphene Oxide Field-Effect Transistor Biosensor

Author: Bingjie Cai, Shuting Wang, Le Huang, et al

Publication: ACS Nano

Publisher: American Chemical Society

Date: Mar 1, 2014

Copyright © 2014, American Chemical Society

Logged in as:
Ren Ren
Imperial College London
Account #:
3001500185
LOGOUT

PERMISSION/LICENSE IS GRANTED FOR YOUR ORDER AT NO CHARGE

This type of permission/license, instead of the standard Terms & Conditions, is sent to you because no fee is being charged for your order. Please note the following:

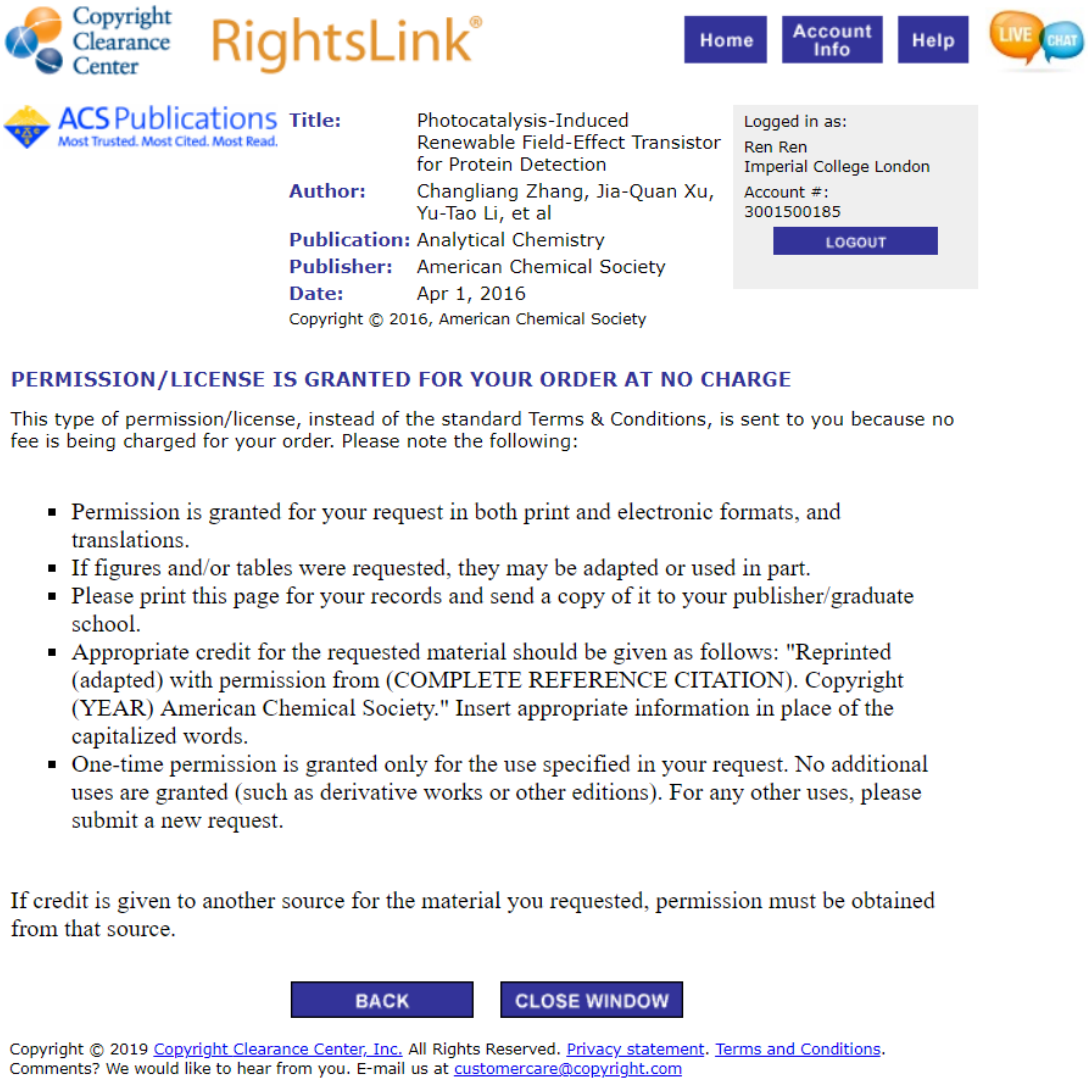
- Permission is granted for your request in both print and electronic formats, and translations.
- If figures and/or tables were requested, they may be adapted or used in part.
- Please print this page for your records and send a copy of it to your publisher/graduate school.
- Appropriate credit for the requested material should be given as follows: "Reprinted (adapted) with permission from (COMPLETE REFERENCE CITATION). Copyright (YEAR) American Chemical Society." Insert appropriate information in place of the capitalized words.
- One-time permission is granted only for the use specified in your request. No additional uses are granted (such as derivative works or other editions). For any other uses, please submit a new request.

If credit is given to another source for the material you requested, permission must be obtained from that source.

BACK | CLOSE WINDOW

Copyright © 2019 Copyright Clearance Center, Inc. All Rights Reserved. Privacy statement. Terms and Conditions.
Comments? We would like to hear from you. E-mail us at customercare@copyright.com

Approval 14



Copyright Clearance Center RightsLink®

Home | Account Info | Help | LIVE CHAT

ACS Publications
Most Trusted. Most Cited. Most Read.

Title:	Photocatalysis-Induced Renewable Field-Effect Transistor for Protein Detection
Author:	Changliang Zhang, Jia-Quan Xu, Yu-Tao Li, et al
Publication:	Analytical Chemistry
Publisher:	American Chemical Society
Date:	Apr 1, 2016

Copyright © 2016, American Chemical Society

Logged in as:
Ren Ren
Imperial College London
Account #:
3001500185
LOGOUT

PERMISSION/LICENSE IS GRANTED FOR YOUR ORDER AT NO CHARGE

This type of permission/license, instead of the standard Terms & Conditions, is sent to you because no fee is being charged for your order. Please note the following:

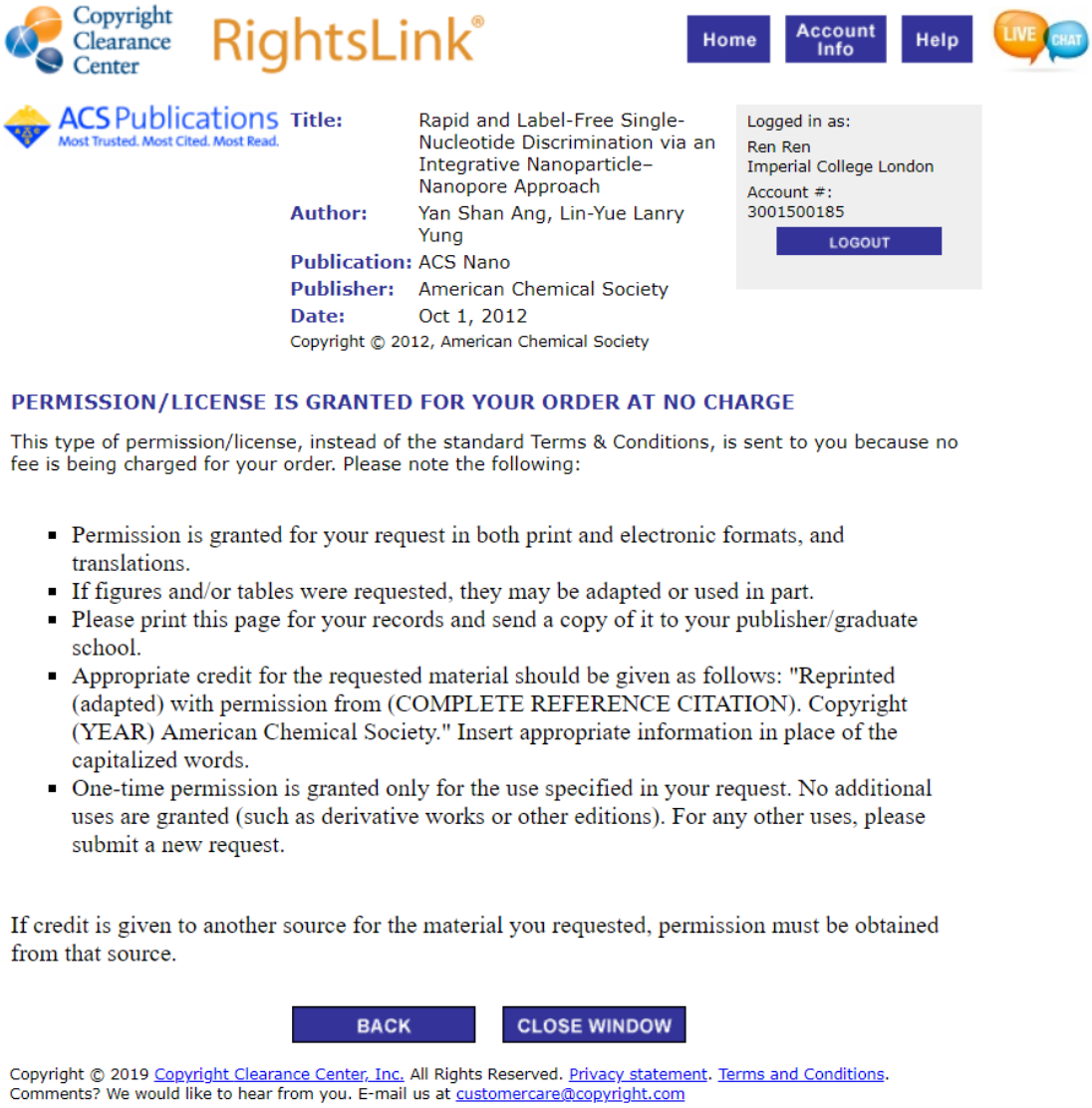
- Permission is granted for your request in both print and electronic formats, and translations.
- If figures and/or tables were requested, they may be adapted or used in part.
- Please print this page for your records and send a copy of it to your publisher/graduate school.
- Appropriate credit for the requested material should be given as follows: "Reprinted (adapted) with permission from (COMPLETE REFERENCE CITATION). Copyright (YEAR) American Chemical Society." Insert appropriate information in place of the capitalized words.
- One-time permission is granted only for the use specified in your request. No additional uses are granted (such as derivative works or other editions). For any other uses, please submit a new request.

If credit is given to another source for the material you requested, permission must be obtained from that source.

BACK | CLOSE WINDOW

Copyright © 2019 Copyright Clearance Center, Inc. All Rights Reserved. Privacy statement. Terms and Conditions.
Comments? We would like to hear from you. E-mail us at customercare@copyright.com

Approval 15



Copyright Clearance Center RightsLink®

Home | Account Info | Help | LIVE CHAT

ACS Publications Most Trusted. Most Cited. Most Read.

Title: Rapid and Label-Free Single-Nucleotide Discrimination via an Integrative Nanoparticle–Nanopore Approach

Author: Yan Shan Ang, Lin-Yue Lanry Yung

Publication: ACS Nano

Publisher: American Chemical Society

Date: Oct 1, 2012

Copyright © 2012, American Chemical Society

Logged in as:
Ren Ren
Imperial College London
Account #:
3001500185
LOGOUT

PERMISSION/LICENSE IS GRANTED FOR YOUR ORDER AT NO CHARGE

This type of permission/license, instead of the standard Terms & Conditions, is sent to you because no fee is being charged for your order. Please note the following:

- Permission is granted for your request in both print and electronic formats, and translations.
- If figures and/or tables were requested, they may be adapted or used in part.
- Please print this page for your records and send a copy of it to your publisher/graduate school.
- Appropriate credit for the requested material should be given as follows: "Reprinted (adapted) with permission from (COMPLETE REFERENCE CITATION). Copyright (YEAR) American Chemical Society." Insert appropriate information in place of the capitalized words.
- One-time permission is granted only for the use specified in your request. No additional uses are granted (such as derivative works or other editions). For any other uses, please submit a new request.

If credit is given to another source for the material you requested, permission must be obtained from that source.

BACK | CLOSE WINDOW

Copyright © 2019 Copyright Clearance Center, Inc. All Rights Reserved. Privacy statement. Terms and Conditions.
Comments? We would like to hear from you. E-mail us at customercare@copyright.com